RADAR AND SATELLITE CHARACTERIZATION OF THE IONOSPHERE UNDER STRONG ELECTRIC FIELD CONDITIONS

A Thesis Submitted to the
College of Graduate and Postdoctoral Studies
in Partial Fulfillment of the Requirements
for the degree of Doctor of Philosophy
in the Department of Physics and Engineering Physics
University of Saskatchewan
Saskatoon

By
Lindsay Victoria Goodwin

Permission to Use

In presenting this thesis in partial fulfilment of the requirements for a Postgraduate degree from the University of Saskatchewan, I agree that the Libraries of this University may make it freely available for inspection. I further agree that permission for copying of this thesis in any manner, in whole or in part, for scholarly purposes may be granted by the professor or professors who supervised my thesis work or, in their absence, by the Head of the Department or the Dean of the College in which my thesis work was done. It is understood that any copying or publication or use of this thesis or parts thereof for financial gain shall not be allowed without my written permission. It is also understood that due recognition shall be given to me and to the University of Saskatchewan in any scholarly use which may be made of any material in my thesis.

Requests for permission to copy or to make other use of material in this thesis in whole or part should be addressed to:

Head of the Department of Physics and Engineering Physics
163 Physics Building
116 Science Place
University of Saskatchewan
Saskatoon, Saskatchewan S7N 5E2
Canada

OR

Dean
College of Graduate and Postdoctoral Studies
University of Saskatchewan
116 Thorvaldson Building, 110 Science Place
Saskatoon, Saskatchewan S7N 5C9
Canada

ABSTRACT

It is now well established that strong electric fields can distort high-latitude ion velocity distributions to the point that this affects Incoherent Scatter Radar (ISR) observations, and therefore the ion and electron temperatures inferred through those observations. Until now, studies of this topic have focused on first order, semi-empirical ion velocity distribution descriptions. However, a precise description has been lacking, notably along directions parallel or near-parallel to the magnetic field. To remedy these shortcomings and provide the best possible tools to analyze ISR observations, this thesis uses a state-of-the-art Monte-Carlo (MC) simulation to retrieve accurate ion velocity distributions for any electric field, ion-neutral particle interaction, and direction relative to the magnetic field. Through these improvements, a number of important points have been made, such as: 1) for the most part simulated NO^+ ISR observations can be modeled using Maxwellian velocity distributions having the same line-of-sight ion temperature as the simulated MC distribution, 2) although simulated O^+ ISR observations parallel to the magnetic field are similar to those produced from Maxwellian velocity distributions they reflect an erroneous increase in electron temperature due to a wide O^+ velocity distribution, and 3) signatures of toroidal ion velocity distributions in IS spectra are possibly the easiest to identify near 20° with respect to the magnetic field. Based on these results, accurate distorted ion velocity distributions are currently being incorporated into IS spectral fitting routines.

In the logical next step, this thesis turns to radar observations to characterize the ion temperature anisotropy, which is particularly important for Joule heating studies. Using ISR observations from a particularly strong heating event reported by *Clauer et al.* (2016), it is found that the O^+-O collision cross-section from *Knof et al.* (1964) represents the anisotropy of the ionosphere fairly accurately, but still suggests the ionosphere to be slightly more anisotropic than expected. Knowing this allows for the preliminary determination of the effective electric field (the electric field in the neutral frame of reference). To obtain the electric field vector at a given latitude and longitude this thesis has explored a novel technique that employs multi-altitude measurements. This method combined with a knowledge of the effective electric field from the ion temperature studies opens up the possibility of a determination of the neutral wind in future work.

Finally, to study the impact electric field strength has on Swarm satellites observations and on the upper ionosphere in general, a time-dependent gyro-kinetic O^+ model of the motion of ions above a discontinuous boundary between fully collisional and collisionless plasmas has been revisited. This upgraded model uses descriptions of the ion velocity distribution provided by the MC simulation for the boundary velocity distribution as a function of electric field. As well, it incorporates a variable boundary plasma density and can describe any temporal variation of the ion velocity distribution at the boundary without complications. The results agree with the observations of highly distorted ion velocity distributions at high altitudes, as well as explain heretofore unpredictable anisotropic ion temperatures, attributing them to changing boundary conditions propagating upwards along a given flux tube, away from strongly-collisional regions.

ACKNOWLEDGEMENTS

I would first like to thank my supervisor, Jean-Pierre St-Maurice, who dramatically changed my life by giving me the opportunity to complete both an MSc and PhD at the University of Saskatchewan. Jean-Pierre has not only taught me much and given me incredible advice over the years, but thanks to him I moved to Saskatoon, which allowed me to connect with my grandfather and meet my partner of 4.5 years. I would next like to thank Raymond Spiteri, who gave me much of his time and energy over the course of my PhD, as well as Kathryn McWilliams, through whom I enrolled in the 2014 Canada-Norway Student Sounding Rocket program. I would next like to thank Jean-Pierre's postdoctoral researcher, William Archer, who has given me great advice ever since we first met in 2006 (when I was an undergrad at the University of Calgary). I would also like to thank Hassan Akbari, for his collaborations and guidance during my PhD and Ashton Reimer for recalibrating the long pulse Resolute Bay Incoherent Scatter Radar-North data used in Chapter 5 and creating Figure 3.6.

Several organizations and groups have made my research possible. I would like to thank the University of Saskatchewan for providing me with the resources I needed to become both a researcher and a teacher. I wish to thank the National Science Foundation (NSF), the Natural Sciences and Engineering Research Council of Canada, and the Canadian Space Agency for funding my research in one form or another. Additionally, I would like to thank the NSF for providing me funding to attend multiple Coupling, Energetics and Dynamics of Atmospheric Regions (CEDAR) meetings, and the International Union of Radio Science (URSI) for awarding me a 2017 Young Scientist Award (allowing me to attend the 2017 URSI General Assembly and Scientific Symposium). For providing equipment and data vital to this work, I wish to thank the people behind the Advanced Modular Incoherent Scatter Radar instruments at Stanford Research Institute International, and the team behind the Swarm spacecraft.

Last but not least, I wish to thank my family for their love and support. I also wish to thank my friends in Calgary, my friends in Saskatoon, Saskatoon Historical Fencing (who has helped me stay somewhat healthy during my graduate studies), the CEDAR community

(especially Leda Sox, Josh Semeter and Richard Behnke who let me become a CEDAR student representative), and, of course, the members of the Physics and Engineering Physics Graduate Students Association of Students at the University of Saskatchewan (simply referred to as PEGASUS).

Dedicated to my parents, my grandparents, Kimberly, and Kelly.

CONTENTS

LIST OF TABLES

List of Figures

LIST OF ABBREVIATIONS

AC	Alternating Code
AMISR	Advanced Modular Incoherent Scatter Radar
CRC	Canada Research Chair
CSR	Coherent Scatter Radar
EFI	Electric Field Instruments
EISCAT	European Incoherent SCATter scientific association
e-POP	Enhanced Polar Outflow Probe
EUV	Extreme Ultra-Violet
FAC	Field-Aligned Current
GSFC/SPDF	Goddard Space Flight Center/Space Physics Data Facility
HF	High-Frequency
IMF	Interplanetary Magnetic Field
IS	Incoherent Scatter
ISR	Incoherent Scatter Radar
KMV	Knof, Mason, and Vanderslice
MC	Monte-Carlo
MLAT	Magnetic LATitude
MLT	Magnetic Local Time
MSIS	Mass Spectrometer Incoherent Scatter radar
NSERC	Natural Sciences and Engineering Research Council of Canada
PFISR	Poker Flat Incoherent Scatter Radar
POH	Pesnell, Omidvar, and Hoegy
RADAR	RAdio Detection And Ranging
RCE	Resonant Charge Exchange
RCM	Relaxation Collision Model
RISR-C	Resolute Bay Incoherent Scatter Radar-Canada
RISR-N	Resolute Bay Incoherent Scatter Radar-North
RPA	Retarding Potential Analyzers
SAID	Sub-Auroral Ion Drift
SAPS	Sub-Auroral Polarization Stream
SSEBIT	Special Study of E/B and Ion Temperature
SuperDARN	Super Dual Auroral Radar Network
TII	Thermal Ion Imager
TOI	Tongue of Ionization
UT	Universal Time
VFM	Vector Field Magnetometer

List of Nomenclature

A_e	Electron dielectric function for a Maxwellian distribution
A_i	Ion dielectric function for a Maxwellian distribution
a	Electron thermal speed
a_{gp}	Acceleration due to gravity and the polarization electric field
$\mathbf{B}$	Magnetic field, where the magnitude is B and the direction is $\hat{b}$
$\mathbf{B}_i$	Magnetic field of incident plane monochromatic wave
b	Ion thermal speed
C_s	Ion acoustic speed
c	Speed of light
D^*	Modified ion mach number
d_{pw}	Depth of potential well
$\mathbf{E}$	Electric field, where the magnitude is E
$\mathbf{E}'$	Electric field in the frame of a given neutral species
$\mathbf{E}_i$	Electric field of incident plane monochromatic wave
E_{i0}	Incident electric field amplitude
$\mathbf{E}_s$	Electric field of scattered radiation
e	Elementary charge
f	Frequency shift
f_e	Electron velocity distributions
f_i	Ion velocity distributions
f_{in}	MC simulated ion velocity distribution
f_n	Neutral velocity distributions
f_T	Total ion velocity distribution (includes ion-ion, ion-neutral and ion-electron collisions)
f_{1i}	Isotropic Maxwellian velocity distribution with a temperature equal to the electron temperature
f_{2i}	Isotropic Maxwellian velocity distribution with a temperature equal to the average ion temperature
G_e	Electron dielectric function
G_i	Ion dielectric function
G_{iM}	G_i for a Maxwellian ion velocity distribution
G_{iR}	The real component of G_i
$\mathbf{g}$	Acceleration due to gravity
g_{0e}	One-dimensional electron velocity distribution
g_{0i}	One-dimensional ion velocity distribution
H	Scale height
H_e	Electron dielectric function for magnetized plasmas
H_i	Ion dielectric function for magnetized plasmas
I_0	Modified Bessel function of order zero
I_λ	Photon Flux

$\mathbf{J}$	Current density
J	Bessel function
$\mathbf{k}$	Wavevector shift, $\mathbf{k}_s - \mathbf{k}_i$
k_b	Boltzmann constant
$\mathbf{k}_i$	Incident wavevector
$\mathbf{k}_s$	Scattered wavevector
m_e	Electron mass
m_i	Ion mass
m_n	Neutral mass
n_e	Electron number density
n_i	Ion number density
n_n	Neutral number density
$\mathbf{P}$	Stress tensor
p_i	Ion pressure
Q_T^{ex}	Effective RCE cross-section
$\mathbf{q}$	Heat flow
q	Charge
$q(z^*)$	The production function of the Chapman profile as a function of z^*
q_{max}	the maximum peak production
R	Distance from charge
$\mathbf{r}$	Position vector
r_m	Separation when $V(r)$ is a minimum
S	Backscatter spectra
T^*	Effective temperature
T_e	Electron temperature
T_i	Ion temperature
$T_{i\phi}$	Ion temperature along a line-of-sight
T_n	Neutral temperature
T_r	Average of the neutral and ion temperatures
T_x	Temperature along the x-direction
t	Time
t'	Retarded time
t_s	The time being simulated
U	Potential energy
u	Complex envelope of the signal
$V(r)$	Potential of interaction
$\mathbf{V}_n$	Volume in velocity space
$\mathbf{v}_e$	Electron velocity
v_f	Chosen final velocity
$\mathbf{v}_i$	Ion velocity
v_{in}	Relative speed of colliding ion and neutral particles
$\mathbf{v}_n$	Neutral velocity
$v_{th\kappa}$	Thermal speed of charge κ
v_x	Velocity along the x-direction

v_0	Initial velocity
v_ϕ	Line-of-sight velocity
w	Plasma dispersion relation
w_j	Gaussian quadrature weight
X	Ambiguity function
x_e	Normalized frequency, $\omega/(ka)$
x_i	Normalized frequency, $\omega/(kb)$
x_j	Gaussian quadrature location
y	Normalized ion velocity along the x-direction, v_x/b
z	altitude
z^*	the reduced altitude
z_0	Reference altitude
α	$1/(k\lambda_D)$
β	Partition coefficient
γ_s	Measure of the relative strengths of different attractive forces
ϵ	Longitudinal dielectric function
ϵ_e'	Current flow conductivity due to thermal gradients $(n_e e k_B/(m_e \nu_e)$
ϵ_0	Permittivity of free space
η	Ionization efficiency factor
Θ	Scattering angle in centre-of-mass frame
θ	Angle (solar zenith angle, angle between the $\mathbf{E}\times\mathbf{B}$ and $\mathbf{v}-\dfrac{\mathbf{E}\times\mathbf{B}}{B^2}$ in velocity space, angle between the $\mathbf{E}\times\mathbf{B}$ drift and the line-of-sight)
λ	Radar wavelength
λ_D	Debye length
ν_e	Total electron momentum transfer collision frequency
ν_{en}	Electron-neutral momentum transfer collision frequency
ν_i,ν_T	Ion momentum transfer collision frequency
ν_{ie}	Ion-electron collision frequency
ν_{ii}	Ion-ion momentum transfer collision frequency
ν_{in}	Ion-neutral momentum transfer collision frequency
$\rho(\mathbf{r})$	Charge density of a swarm of charges being attracted and repelled
ρ_i	Ion cyclotron radius
ρ_e	Electron cyclotron radius
σ	Collision cross-section
σ_e	Electron conductivity, $n_e e^2/(m_e \left(\sum_n \nu_{en}\right))$
$\sigma_{e\|\|}$	Parallel electrical conductivity $(n_e e^2/(m_e \nu_e)$
σ_H	Hall conductivity
σ_i	Ion conductivity, $n_i q_i^2/(m_i \left(\sum_n \nu_{in}\right))$
σ_{in}	Differential scattering cross-section
σ_P	Pedersen conductivity
τ	Optical depth

τ^*	Optical depth when $\theta = 0°$
τ_d	Time delay
ϕ	Aspect angle
ϕ_E	Electric potential
χ	Minimized difference
Ω	Solid angle
Ω_e	Electron gyrofrequency, eB/m_e
$\vec{\Omega}_i$	Ω_i along the magnetic field
Ω_i	Ion gyrofrequency, q_iB/m_i
ω	Frequency shift, $\omega_s - \omega_i$
ω_i	Incident frequency
ω_{pi}	Ion plasma frequency, $\sqrt{4\pi n_{i0}e^2/m_i}$
ω_s	Scattered frequency
Subscript $\perp$	Perpendicular to the magnetic field
Subscript $\|\|$	Parallel to the magnetic field

Chapter 1

INTRODUCTION

According to Nobel Laureate Hannes Alfvén, “more than 99 percent of the Universe consists of plasma” (*Alfvén*, 1986). Plasma is so ubiquitous in the universe that Alfvén coined the term “Plasma Universe” in 1986 to underline its importance in everyday physics. Plasma is generated through a very wide variety of processes, and exists on many scale-sizes. Arguably the largest known accumulation of plasma is the intergalactic medium, which is a low density plasma medium that exists between galaxies. Meanwhile, plasma also exists in much smaller quantities, such as the gas within fluorescent and neon lights. Somewhere between these two scale-sizes is the plasma accumulation located in the Earth’s ionosphere.

Above 90 km altitude, the ionized gas in the Earth’s atmosphere is considered a plasma. Although both ionized gases and plasmas are accumulations of ions and electrons, what distinguishes a plasma from an ionized gas is Debye shielding, which obscures the electric field of individual particles over distances exceeding the Debye length (discussed further in Chapter 3). Nevertheless, plasmas are subject to electromagnetic fields, both those produced from collective interactions within the plasma and the ambient fields that are imposed on the plasma. Collective interactions and the organized motions within a given plasma create large amplitude waves and turbulence, and are often associated with plasma instabilities that develop when external fields force a plasma to depart from a state of equilibrium. However, the main focus of this thesis is the impact of large-scale, ambient electromagnetic fields on ionospheric plasmas, where the ambient magnetic field is taken to be the Earth’s geomagnetic field and the electric field of interest is that imposed on the ionosphere through the interaction of the solar wind with the magnetosphere (as opposed to the generally weaker dynamo electric fields introduced by neutral winds).

Electric fields imposed by the solar wind have a wide variety of consequences on the ionosphere. For example, there is the mid-latitude trough, which is a late evening latitudinally narrow region of reduced plasma density located at sub-auroral latitudes (typically between 55° and 75° latitudes) (*Muldrew*, 1965; *Sharp*, 1966). Three proposed mechanisms by which the midlatitude trough is formed are: 1) a reversal in plasma convection on the Earth's nightside leading to plasma stagnation and a decrease in photoionization (e.g., *Collis and Häggström* (1988); *Hedin et al.* (2000); *Knudsen* (1974); *Spiro et al.* (1978)), 2) Sub-Auroral Ion Drifts (SAIDs) causing plasma depletions through enhanced recombination rates (*Schunk et al.*, 1976), or 3) substorm onsets or Sub-Auroral Polarization Stream (SAPS) events transporting plasma from the dusk sector during summer conditions (*Goodwin et al.*, 2014; *Richards et al.*, 2014). A second example of how electric fields imposed by the solar wind impact the ionosphere is Joule heating, which originates in frictional heating between ions and neutrals. The results for the ions is a large increase in their temperature under strong electric field conditions to the point that it becomes much larger than either the electron or the neutral temperature (as discussed further in Chapter 2). By contrast, Joule heating does not markedly increase the neutral temperature. Instead, it creates an upwelling of the gas. This increases spacecraft drag in the Earth's upper atmosphere, accelerating the decay of satellite orbits over time (e.g. *Lühr et al.* (2004)).

This thesis studies the combined role strong electric fields and ion-neutral collisions have on distorting ion velocity distributions from their thermal equilibrium configuration and the impact this has on the high-latitude retrieval of ionospheric plasma parameters. This topic is now introduced in more detail, after which an outline of this thesis is provided.

1.1 The Combined Effect of Strong Electric Fields and Ion-Neutral Collisions

There is an abundance of literature detailing how, through ion-neutral collisions, strong electric fields distort the ion velocity distributions of plasmas in weakly-ionized, magnetized regions from isotropic Maxwellian shapes into anisotropic toroidal shapes (e.g. *St.-Maurice and Schunk* (1977)). In this context, weakly-ionized regions are defined as regions in which the ion-neutral momentum transfer collision frequency, ν_{in}, is much greater than the ion-ion collision frequency, ν_{ii}, and a magnetized region is one in which the ion collision frequency, ν_i, is less than the ion gyrofrequency, Ω_i. The consequences of this have been explored on a semi-qualitative basis for instruments like Retarding Potential Analyzers (RPAs) (*St-Maurice et al.*, 1976) and for RAdio Detection And Ranging (radar) systems (*Raman et al.*, 1981). For moderate electric fields up to 25 mV/m these distortions appear not to be too significant, but there is an increasing interest in characterizing the impact of strong localized electric fields on the Joule heating budget given the finding that Joule heating plays a local role in producing neutral density enhancements. However, studies into strong electric field events are further complicated by the instrumentation itself. For example, current Incoherent Scatter Radar (ISR) spectral analysis techniques rely heavily on the inference that ionospheric ion velocity distributions have an isotropic Maxwellian shape, which potentially leads to falsely characterizing plasma parameters (e.g. *Raman et al.*, 1981; *Suvanto*, 1988). Therefore this thesis pursues a more precise description of velocity distributions in weakly-ionized, magnetized regions than has been characterized previously to allow for more accurate and quantitative studies of large electric fields and Joule heating.

The electric field strength also plays a role in the evolution of plasma properties. For example, through plasma transport, heated plasma from strongly collisional regions move into collision-free regions and evolve strong departures from equilibrium in directions parallel to the magnetic field (e.g. *Loranc and St-Maurice* (1994); *Wilson* (1994)). The impact of this is far reaching, influencing high-altitude in-situ observations of ion velocity distributions (such as those performed by the Swarm Electric Field Instruments (EFI) (*Archer et al.*, 2015)), as well as creating ion upflows and introducing temperature anisotropies that have observable implications for radar spectra. Past work on this that has been based on kinetic theory lacked realistic temporal and spatial variations (*Loranc and St-Maurice*, 1994; *Wilson*, 1994), while work that has been based on transport models relied heavily on predominately Maxwellian velocity distributions (*Heelis et al.*, 2009; *Sydorenko and Rankin*, 2013). There is a need to re-examine and update the kinetic approach used in the past by incorporating more powerful computing technology.

1.2 Outline of Current Work

Chapter 2 first describes the formation of the ionosphere through chemical processes and transport, and then discusses the creation of high-latitude electric fields and plasma convection through the magnetospheric generator and the role these electric fields have on the ion temperature and ion velocity distributions in weakly-ionized, magnetized regions. Next, Chapter 3 discusses ISRs from both a theoretical and practical perspective.

After these preliminary chapters, Chapters 4, 5, and 6 all explore the combined role electric field strength and ion-neutral collisions have on distorting ion velocity distributions, and the impact this has on high-latitude ionospheric plasma parameters. First, from highly accurate Monte-Carlo (MC) simulations of ion velocity distributions in weakly-ionized, magnetized regions, Chapter 4 describes in quantitative terms the impact of electric field strength and ion-neutral collisions on ion velocity distributions, line-of-sight ion temperatures, and Incoherent Scatter (IS) spectra. Chapter 5 uses ground-based ISR observations in a specific arrangement to preliminarily characterize ion temperature anisotropy, determine the correct O^+-O collision cross-section, and resolve the electric field vector at a specific geomagnetic latitude during a large electric field event. Chapter 6 discusses mapping the effect of ion-neutral frictional heating in strongly-collisional regions into weakly-collisional regions, and how this impacts high-altitude plasma parameters and the interpretation of Swarm spacecraft observations. Here, only temporal variations are addressed, leaving the gradual change from collisional to collision-free for future work.

The final chapter gives a summary of this research, along with concluding remarks and potential future studies.

Chapter 2
BACKGROUND

In order to understand the impact that high-latitude electric fields have on the ionosphere, it is important to first establish how the ionosphere is formed and modified, as well as how electric fields in the ionosphere are generated and manipulate plasma. This chapter begins by discussing plasma creation and depletion in the ionosphere, as well as the different regions of the ionosphere and several processes that affect ionospheric plasma. It then describes the magnetospheric generator and discusses how convection electric fields impact the ion temperature and the ion velocity distribution in weakly-ionized, magnetized regions. Lastly, this chapter discusses high-latitude currents in the Earth's ionosphere, since these current systems also play a significant role in modifying ionospheric plasma properties.

2.1 Origin of the Ionosphere and Different Altitude Regions

Simply put, an ionosphere is a portion of a planet's upper atmosphere that is ionized by solar EUV and X-ray radiation to produce plasma that is further controlled through chemistry and transport. For the Earth, the ionosphere normally has a plasma density greater than 10^9 m^{-3}. In this section, the creation of the Earth's ionosphere is detailed, followed by an overview of the different ionospheric altitude regions and their basic variability.

2.1.1 Photoionization of the High-Altitude Atmosphere

The Sun's atmosphere extends beyond 10 solar radii and is divided into three regions (*Schunk and Nagy*, 2009). Closest to the sun is the photosphere, which decreases from approximately

6000 K to 4500 K near the photosphere-chromosphere boundary. The next closest layer is the chromosphere, where the temperature increases rapidly from 4500 K to about 25000 K near the base of the corona. Lastly there is the corona, which contains a very tenuous, roughly 10^6 K, ionized plasma. The corona is of particular importance to the ionosphere because it is the only region of the sun that is able to produce and emit Extreme Ultra-Violet (EUV) radiation into the solar system, therefore it is the only region of the sun that is capable of emitting in abundance the energy needed to ionize the upper atmosphere. When EUV radiation enters the high-altitude atmosphere it ionizes neutral particles and creates ions and free electrons, mostly above 100 km. Through this process, plasma produced by solar EUV radiation and x-rays establishes the ionosphere in the upper atmosphere.

Photoionization is dominated by atomic oxygen, O, between roughly 150 km and 250 km, giving [*Rees* (1989), Chapter 2]:

$$\mathrm{O} + h\nu \rightarrow \mathrm{O}^{+} + \mathrm{e}^{-}$$

where e^{-} is a single electron, $h\nu$ represents a photon, and O has an ionization threshold of 13.62 eV (91.03 nm). Between roughly 110 km and 150 km, photoionization is dominated by molecular Nitrogen, $\mathrm{N_2}$, giving [*Rees* (1989), Chapter 2]:

$$\mathrm{N_2} + h\nu \rightarrow \mathrm{N_2^{+}} + \mathrm{e}^{-}$$

where $\mathrm{N_2}$ has an ionization threshold of 15.58 eV (79.58 nm). Since molecular oxygen, $\mathrm{O_2}$ also has a relatively high density between 110 km and 150 km, there is also [*Rees* (1989), Chapter 2]:

$$\mathrm{O_2} + h\nu \rightarrow \mathrm{O_2^{+}} + \mathrm{e}^{-}$$

and:

$$\mathrm{O_2} + h\nu \rightarrow \mathrm{O}^{+} + \mathrm{O}^{+} + \mathrm{e}^{-}$$

where $\mathrm{O_2}$ has an ionization threshold of 12.06 eV (102.8 nm). During the photoionization process, hot photoelectrons are created that raise the overall electron temperature of a given plasma. These photoelectrons provide the main source of energy for thermal electrons, increasing the electron temperature above the ion and neutral temperatures above 150 km in regions visible to the Sun (*Schunk and Nagy*, 1978).

As the neutral density increases with decreasing altitude, the ion and photoelectron production rates increase as solar radiation becomes incident on more neutral particles. However, eventually an altitude is reached at which there are enough neutral particles to absorb all of the available photons, forcing the production rate to drop off abruptly. This creates the nose-like altitude production rate profile seen in Figure 2.1, known as the “Chapman profile”. The production function of the Chapman profile is described by [*Schunk and Nagy* (2009), Chapter 9]:

$$q(z^*) = q_{max} \exp\left(1 - z^* - e^{-z^*} \sec\theta\right) \tag{2.1}$$

where $q(z^*)$ is the production rate for a given reduced height, θ is the solar zenith angle, z^* is the reduced altitude given as:

$$z^* = \frac{z - z(\tau^* = 1)}{H} = \frac{z - z_0}{H} \tag{2.2}$$

and where q_{max} is the maximum peak production, given by:

$$q_{max} = I_\lambda(\infty)\sigma n_n(z^* = 0)\eta e^{-1} \tag{2.3}$$

where

$$n_n(z) = n_n(z_0) \exp\left[-z^*\right] \tag{2.4}$$

while I_λ is the photon flux, η is the efficiency factor, z is the altitude, z_0 is the reference altitude, H is the scale height (the distance over which the density depletes by a factor of e, which in this case is the density of the neutrals being ionized), τ^* is the optical depth, τ, when $\theta = 0°$ (where $\tau = \sigma n_n H \sec\theta$), σ is the cross-section, and n_n is the density of the neutral species being ionized. Since Equation 2.1 depends strongly on the solar zenith angle, there is a strong diurnal variation in the production rates of chemically controlled regions (typically, below 250 km altitude). However, ionization also strongly depends on the efficiency factor, which describes the probability of producing ions. Although the efficiency factor includes photon interaction, note that it is dominated by secondary ionization through photoelectrons. The wavelength-dependence of ionization rates in the ionosphere are shown in Figure 2.2 as a function of altitude, where each slice in wavelength is essentially a Chapman production curve, with the peak altitude determined by the total of the major species cross-sections. This figure is somewhat similar for both quiet and active solar conditions.

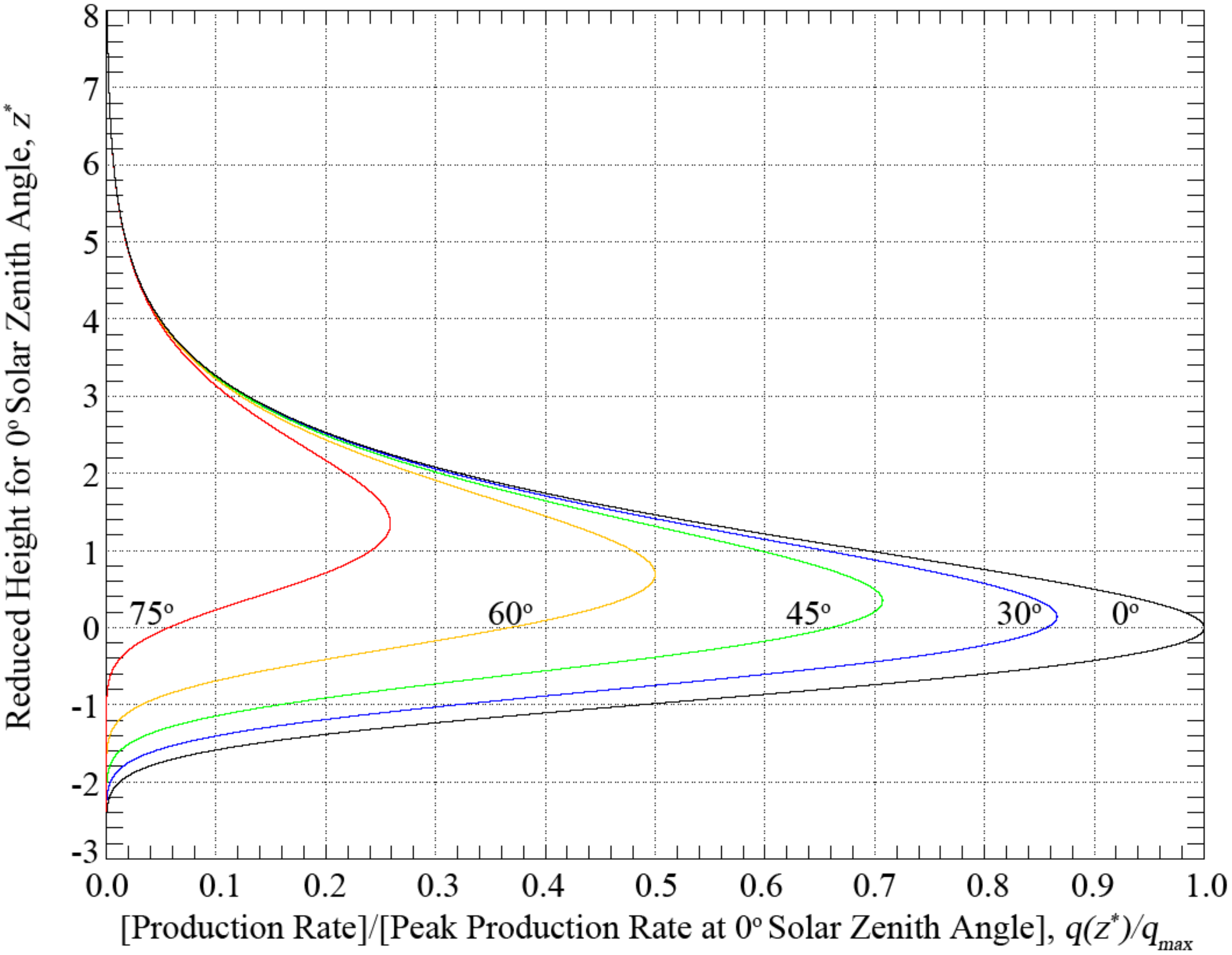

Figure 2.1: Chapman production curves, where each color represents a different solar zenith angles.

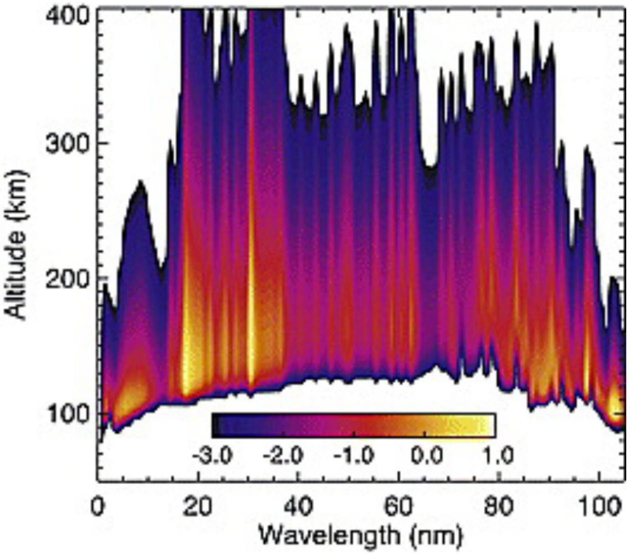

Figure 2.2: Deposition of solar EUV energy in the thermosphere as a function of wavelength and altitude in $\log_{10}(\mathrm{Wm}^4)$ for low solar activity (*Solomon and Qian*, 2005).

2.1.2 Regions of the Ionosphere

The photoionization reactions on Earth, as well as their resulting interaction reactions and recombination reactions are seen in Figure 2.3. However, as Figure 2.4 shows, different neutral compositions only exist in abunbance over limited altitude ranges. For this reason the Earth's ionosphere is categorized into three sub-regions: the *D*-, *E*-, and *F*-regions. Existing between 60 km and 100 km, the main sources of ions in the *D*-region are Lyman alpha photoionization of O_2 and NO. This region is quite complex, containing dissociative recombination, ion recombination, ion-ion neutralization, three-body reactions, photo-detachment, associative detachment, both positive and negative ions, and water cluster ions [*Schunk and Nagy* (2009), Chapter 11]. Cluster ions (hydrated protons, mostly) dominate this region below about 85 km, and are formed through hydration starting from the primary ions NO^+ and O_2^+.

The *E*-region is between 100 and 150 km. Through the photoionization of O_2 and N_2 this region contains a high density of O_2^+ and NO^+. As seen in Figure 2.3, through interaction reactions NO^+ replaces N_2^+ as the dominant molecular ion species, particularly in the higher *E*-region. The plasma density is roughly 10^{11} m^{-3} and the neutral density is greater than 10^{17} m^{-3}. The *E*-region is weakly-ionized and the influence of Coulomb collisions is negli-

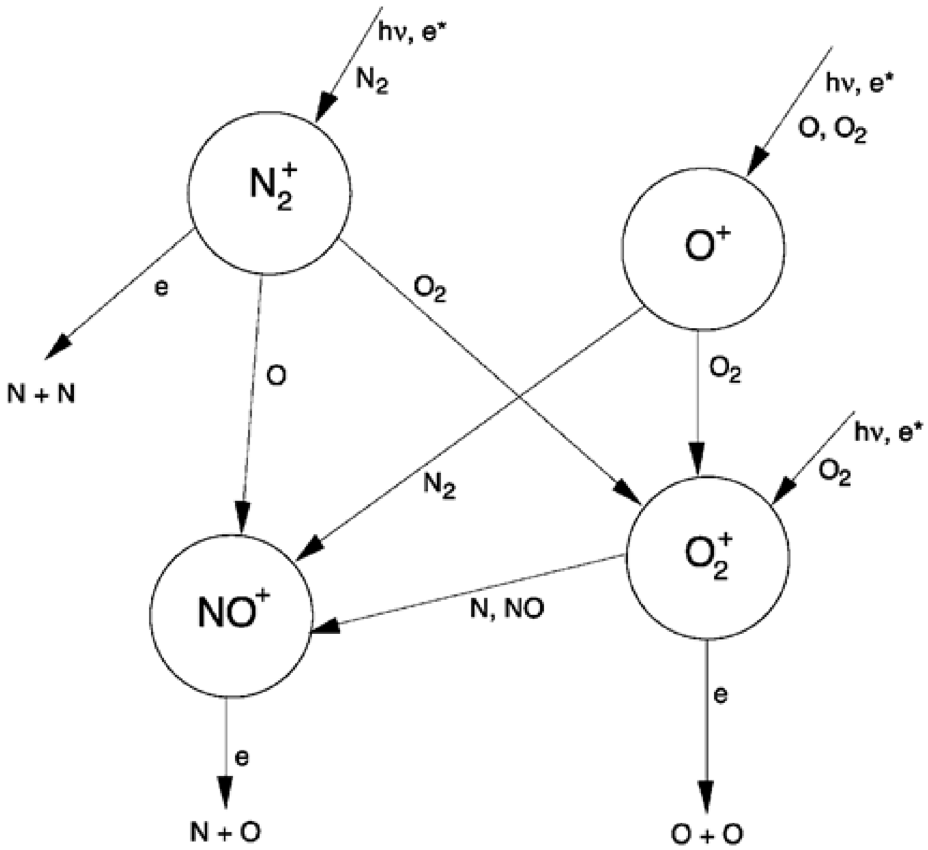

Figure 2.3: Photoionization reactions, interaction reactions, and recombination reactions above approximately 110 km (*Solomon*, 2007).

gible [*Schunk and Nagy* (2009), Chapter 11]. In both the D- and E-regions, molecular ions dominate and chemical processes are critical.

From 150 km to the edge of the ionosphere (roughly 1000 km) exists the F-region, which is further divided into the F_1 layer, between 150 km to 250 km, and the F_2 layer, above 250 km [*Schunk and Nagy* (2009), Chapter 11]. In the F-region, O dominates, and O^+ is the dominant ion through photoionization. This region is also typified by Resonant Charge Exchange (RCE) collisions which frequently turn O into O^+ and O^+ into O. The peak F-region density is approximately 10^{12} m^{-3} and the neutral density is roughly 10^{14} m^{-3} [*Schunk and Nagy* (2009), Chapter 11]. This region is weakly-ionized below roughly 400 km, but becomes more ionized with increasing altitude, meaning both ion-neutral collisions and Coulomb collisions must be considered in the F-region, but in varying degrees depending on the altitude. An important feature of this region is a density peak. Since O^+ does not readily recombine with electrons, O^+ in the ionosphere must first become NO^+ or O_2^+ in order to recombine. However, to do this O^+ must first interact with N_2 or O_2. As a result, the O^+ production rate decreases with the decrease with altitude in O density while the conversion to molecular ions decreases with the N_2 or O_2 densities. The O^+ density therefore increases with increasing altitude even though the peak O^+ production region is near 150 km. Put another way, O^+ production is slow (on the scale of hours) and becomes slower with altitude given the decreasing O density. The central point is that, by 250 km, particle diffusion, which is inversely proportional to the atmospheric density, overcomes production and the plasma density starts to decrease with altitude to achieve a diffusive equilibrium profile.

By approximately 700 km the decrease in plasma density with altitude becomes less rapid, as lighter atomic ions, such as H^+ and He^+, begin to dominate. In this region, called the protonosphere, H^+ is produced from RCE with O^+. This not only prevents H from leaving the ionosphere (due to its large scale height), but also forces O^+ and H^+ to have approximately the same density (but not quite, due to transport). In this region, the plasma is strongly-ionized (where the ion-ion collision frequency, ν_{ii}, is much greater than the ion-neutral collision frequency, ν_{in}), even though the neutral density is still larger than the plasma density (*Schunk and Nagy*, 2009).

The above reactions and accompanying transport processes result in the electron, ion,

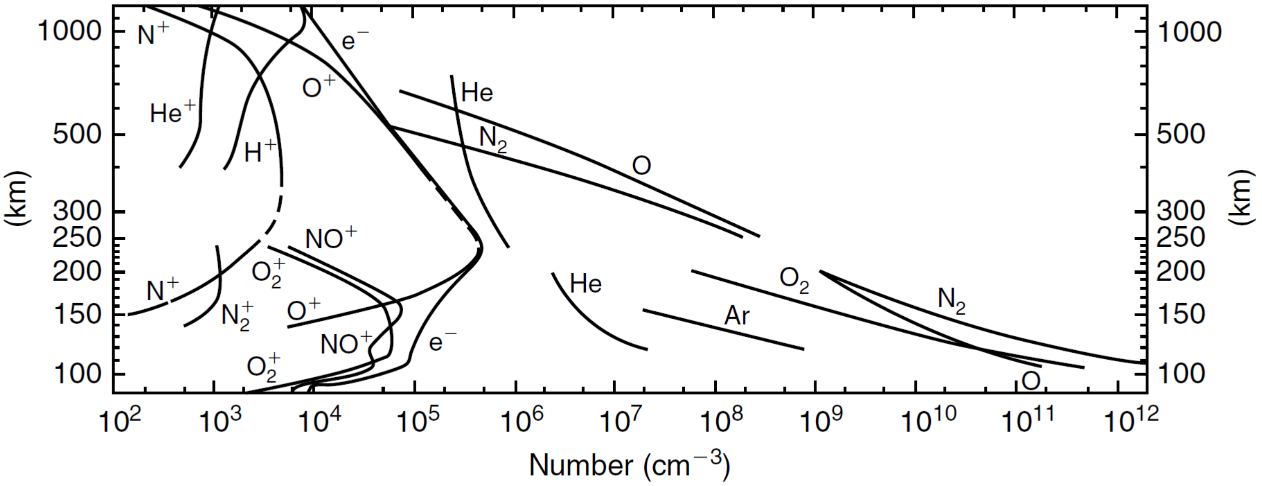

Figure 2.4: Combined measurements from daytime mass spectrometer measurements above White Sands, New Mexico (32° N, 106° W) from the International Quiet Solar Year, Elektron 11 satellite results of *Istomin* (1966), and Explorer XVII results of *Reber and Nicolet* (1965). The helium distribution is from a nighttime measurement. Taken from *Kelley* (2009) [Chapter 1] and modified in *Johnson* (1969).

and neutral density profiles shown in Figure 2.4. Meanwhile, Figure 2.5 shows the average neutral temperatures in these regions. Up until 90 km, the neutral temperature decreases with altitude due to a combination of adiabatic and radiative cooling. At higher altitudes, EUV radiation decomposes infrared radiators while depositing substantial amounts of energy per unit volume, therefore increasing the neutral temperature with altitude.

Lastly, it is important to note that below approximately 120 km (at high-latitudes) the ionosphere is considered to be unmagnetized ($\nu_i/\Omega_i > 1$), while regions above 120 km are considered to be strongly magnetized ($\nu_i/\Omega_i < 1$) (*Sangalli et al.*, 2009). This means that plasma in the E-region is strongly subject to the motion of neutral particles, while plasma in the F-region is strongly subject to the combined drift of the electric and magnetic fields, also called the "$\mathbf{E} \times \mathbf{B}$ drift" (*Schunk and Nagy*, 2009).

2.1.3 Density Variability

Recalling the Chapman curves in Figure 2.1 and Equation 2.1, it is clear that the solar zenith angle plays an important role in ionospheric plasma creation. However, the solar zenith angle also leads to daily changes in density, as well as seasonal and latitudinal variations, where regions that have experienced less photoionization in general have lower densities. Therefore

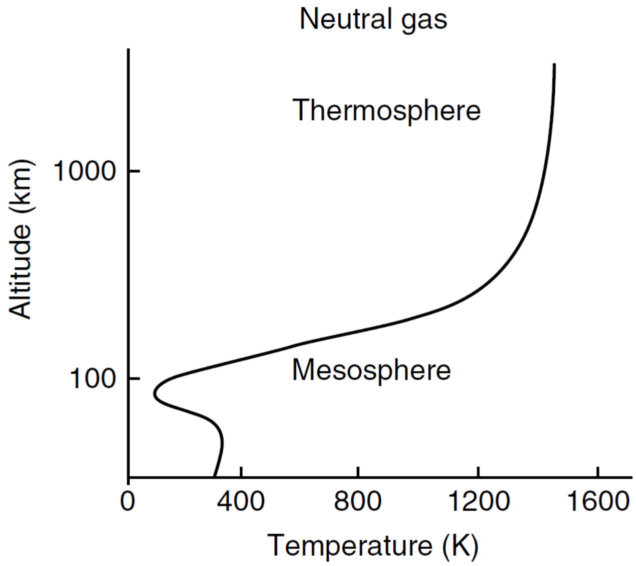

Figure 2.5: Neutral temperature as a function of altitude [*Kelley* (2009), Chapter 1].

the plasma density on the nightside of the Earth is typically lower than the density on the dayside of the Earth. Likewise, winter months typically have lower plasma densities than summer months, and latitudes experiencing little photoionzation have lower plasma densities than other regions. However, photoionization and density variations becomes more complicated when plasma motion and altitude variations are taken into consideration. As is discussed below in Section 2.2.1, F-region plasma convects and moves with magnetic flux tubes that map into the ionosphere. This means that the plasma density at a given region and time can be controlled by the motion and history of a given flux tube. For example, if a given flux tube remains on the nightside of the Earth longer than a neighboring flux tube, it is possible that a decrease in plasma density will be seen (*Richards et al.*, 2014; *Spiro et al.*, 1978). Conversely, this can also lead to high-density dayside plasma being pulled into the nightside ionosphere, leading to plasma density structures, such as the Tongue of Ionization (TOI) and polar cap patches. However, the effects of plasma convection are not nearly as noticeable in the E-region. This is not only because it is a highly collisional region whose motion is strongly controlled by the neutral winds, but is also because the E-region density peak quickly disappears at night (on the order of minutes). This is due to the rapid recombination rates of NO^+ and O_2^+, the dominant ions in the E-region. Since the dominant ion in the F-region is O^+, and O^+ must first turn into NO^+ before it can recombine (which is challenging given the relatively low N_2 density), the F-region peak density only decreases very slowly at night.

Besides convection, plasma density variations can also be clearly affected by the electric field strength. As the electric field increases, and subsequently increases the ion-neutral relative drift, recombination reaction rates of O^+ with O_2 and N_2 increase, leading to plasma density depletions (*Pitout and Blelly*, 2003; *St-Maurice and Laneville*, 1998; *St-Maurice and Torr*, 1978). Interestingly, this process is relatively simple to identify in data, because increases in the ion-neutral relative drift also lead to increases in the ion temperature (as discussed in Section 2.2.2). As mentioned previously this process is also believed to be one of the possible creation mechanisms behind the midlatitude trough (*Schunk et al.*, 1976).

A final mechanism worth mentioning here that introduces plasma density variations is particle impact ionization. Precipitation is made up of energetic particles that move into the ionosphere from the magnetosphere (the region directly above the ionosphere). This precipitation (typically involving kilo-electron volt, keV electrons) leads to particle impact ionization, creating secondary ion-electron pairs. When these ionized species undergo de-excitation, light is released and the aurora is formed (although similar, this process is not to be confused with the de-excitation of solar photoionized species, which leads to airglow (*Schunk and Nagy*, 2009)). This process results in the high-latitude oval-shaped region known as the "auroral oval", which is depicted in Figure 2.6 along with different types of particle impact ionization. Typically, particle precipitation in the auroral oval is structured and highly time-dependent, creating structured plasma densities in space and time in the ionosphere (*Schunk and Nagy*, 2009).

Figures 2.7 and 2.8 show the altitude profiles of the ionization rates produced by precipitation as a function of energy at the top of the atmosphere for precipitating ions (protons mostly) and electrons, respectively. In both figures the ionization rates increase with decreasing altitude until a density limit is reached, making this process maximized between the E-region and the F_1 layer (*Schunk and Nagy*, 2009). Hard precipitation (on the order of keVs) produces ionization in the E-region that often and rapidly comes and goes, while soft precipitation (on the order of a few hundred eV), produces ionization that remains in the F-region for longer periods. This is, once again, because NO^+ in the E-region is able to

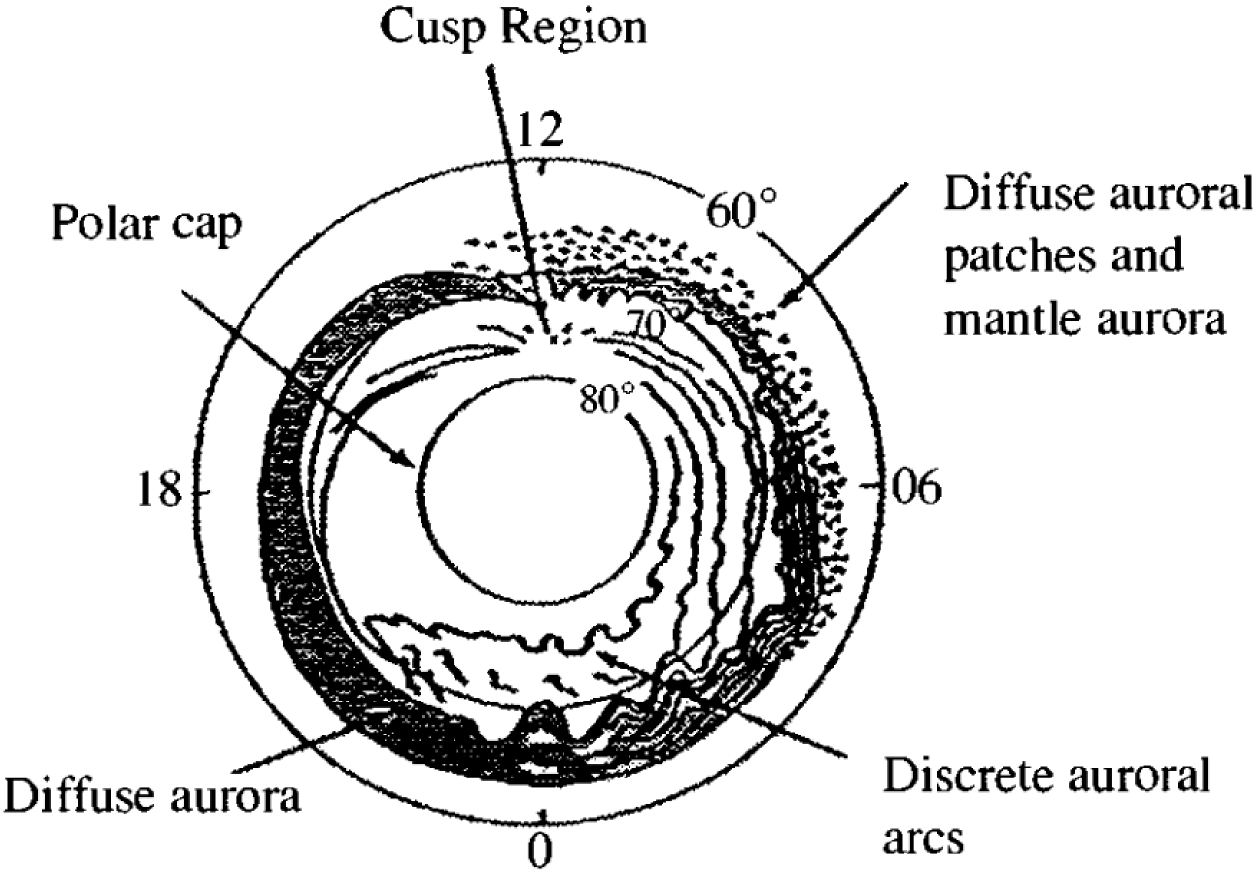

Figure 2.6: Schematic diagram showing the main particle precipitation regions and auroral displays for a southward Interplanetary Magnetic Field [*Akasofu* (1976), modified in *Schunk and Nagy* (2009), Chapter 12]

recombine easily, unlike O^+ in the F-region.

The highest precipitating ion energies occur at dusk, while the highest electron energies occur at dawn and poleward of the ions at dusk. Near the equatorward side of the dusk sector, the ion integral energy flux exceeds the electron integral energy flux, but in the rest of the auroral oval the ion energy flux is comparable to, but smaller than, the electron energy flux even though the average energy of the precipitating ions is far greater than that for the precipitating electrons (*Schunk and Nagy*, 2009). During quiet magnetic conditions, the maximum energy flux of precipitation is about 1 erg cm^{-2} s^{-1} and occurs typically in the midnight-dawn sector of the auroral oval. As geomagnetic activity increases, the auroral oval moves equatorward, the latitudinal width of the auroral oval increases, and the precipitation intensifies, with the maximum energy flux typically being 8 ergs cm^{-2} s^{-1} (*Fukunishi*, 1975; *Jones et al.*, 1982; *Montbriand*, 1971; *Schunk and Nagy*, 2009). Precipitation and current systems associated with precipitation are discussed further in Section 2.3.

2.2 High-Latitude Electric Fields

In the high-latitude F-region, plasma is subject to convecting magnetic field lines that establish a high-latitude electric field pattern, due to the merging of the solar wind with the magnetosphere. This section discusses the plasma convection and electric fields that result from this merging, along with how this impacts plasma energy and the ion velocity distribution.

2.2.1 Origin of High-Latitude Electric Fields

Electric fields in the ionosphere are produced by either charge separation or time-varying magnetic fields. There are a number of mechanisms by which electric fields are generated within the ionosphere, but arguably the most important two are: 1) dynamos, and 2) interactions between the solar wind and the magnetosphere, also known as the magnetospheric generator. Ionospheric dynamos are established by a variety of different process depending on altitude and latitude, but simply put they are created when ionospheric winds move charges at different rates (depending on their mass and charge) across magnetic field lines (*Pudovkin*,

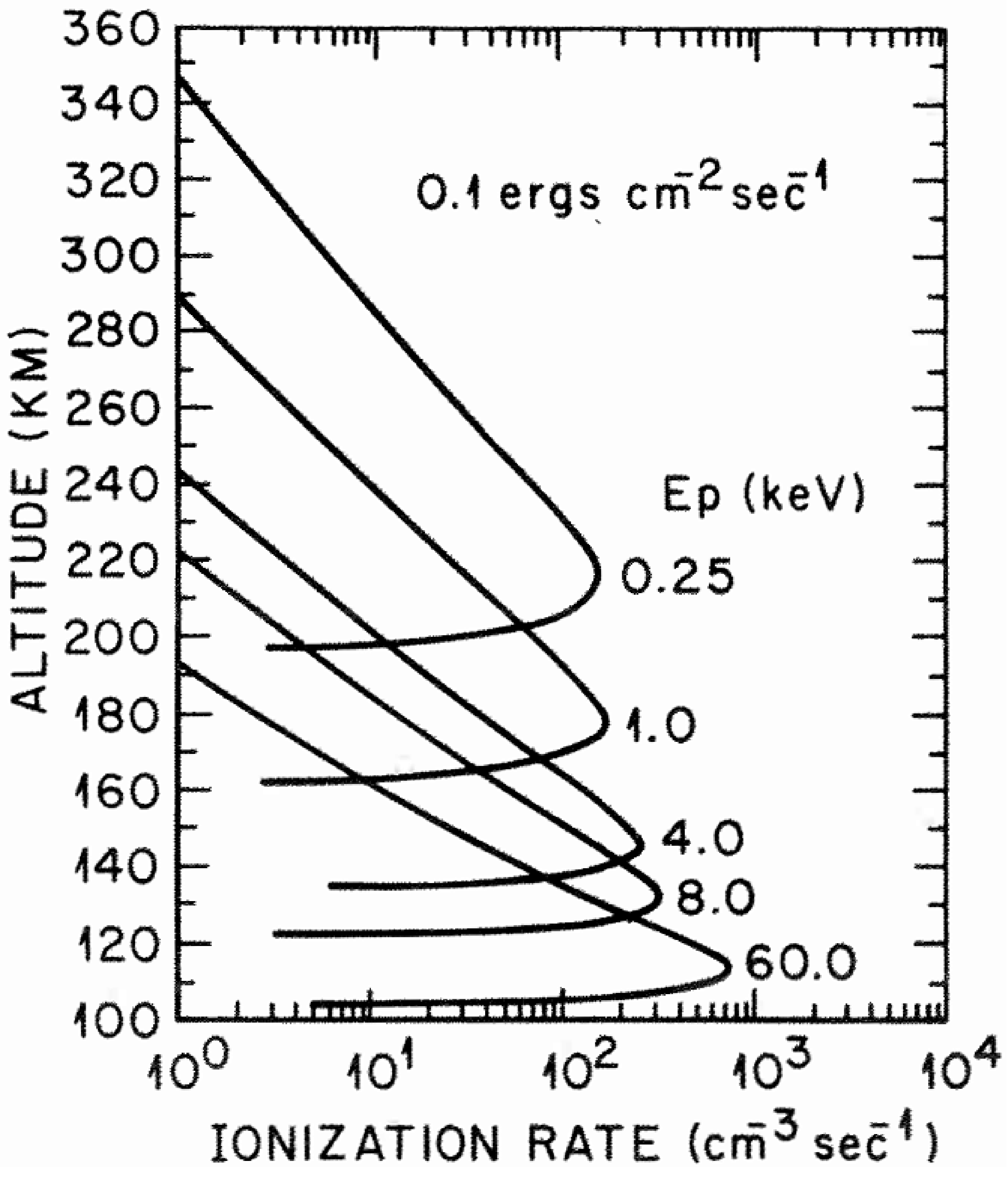

Figure 2.7: Profile plot of ionization rates produced by precipitating primary proton fluxes with energy E_p at the top of the atmosphere. Note that this figure assumes isotropic flux and an energy flux of 0.1 erg cm^{-2} s^{-1} [*Rees* (1989), Chapter 3].

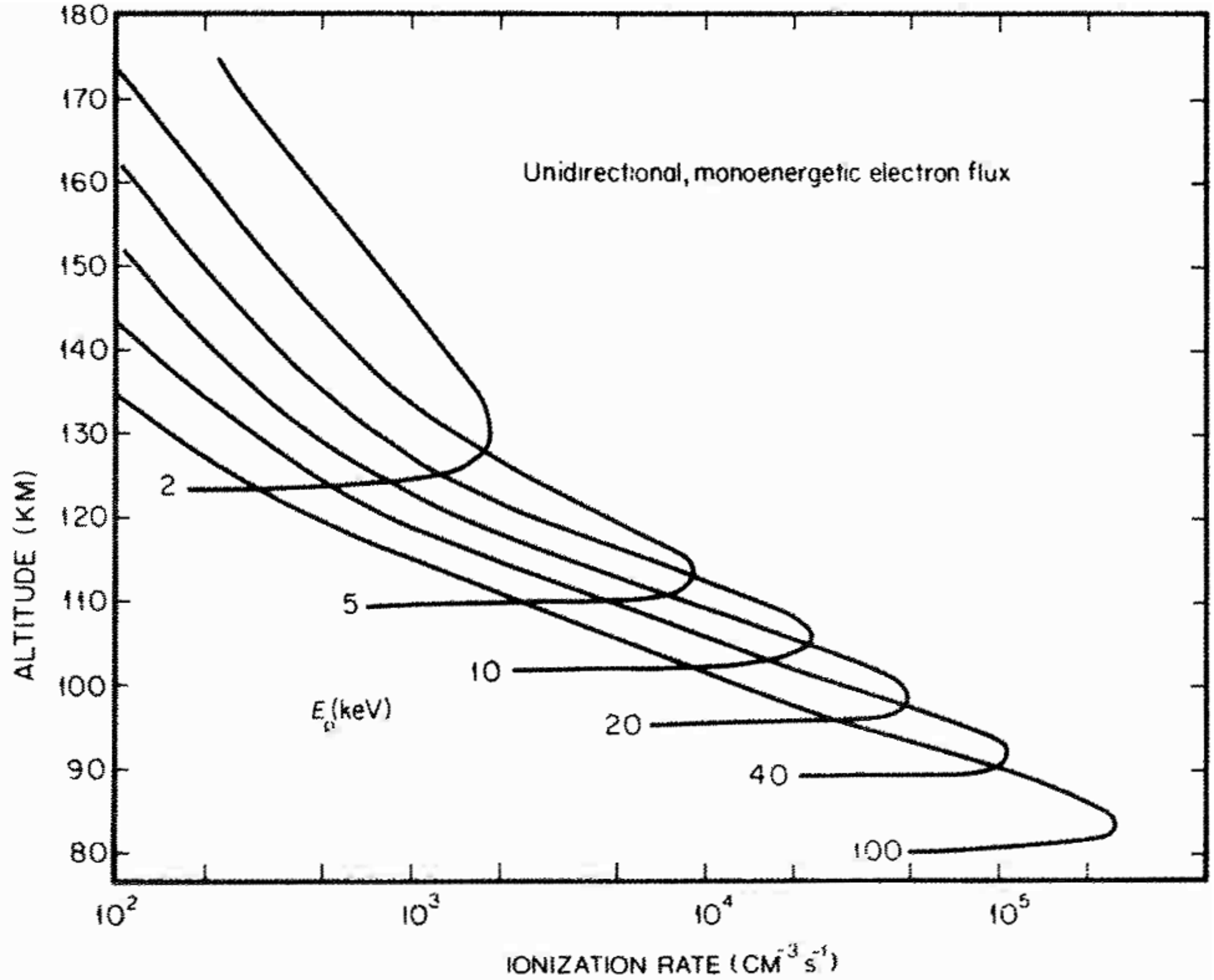

Figure 2.8: Profile plot of ionization rates produced by a flux of 10^8 electrons cm^2 s^{-1} precipitating along the magnetic field lines into the Earth's atmosphere. A variety of different initial rates in keVs are shown [*Rees* (1989), Chapter 3].

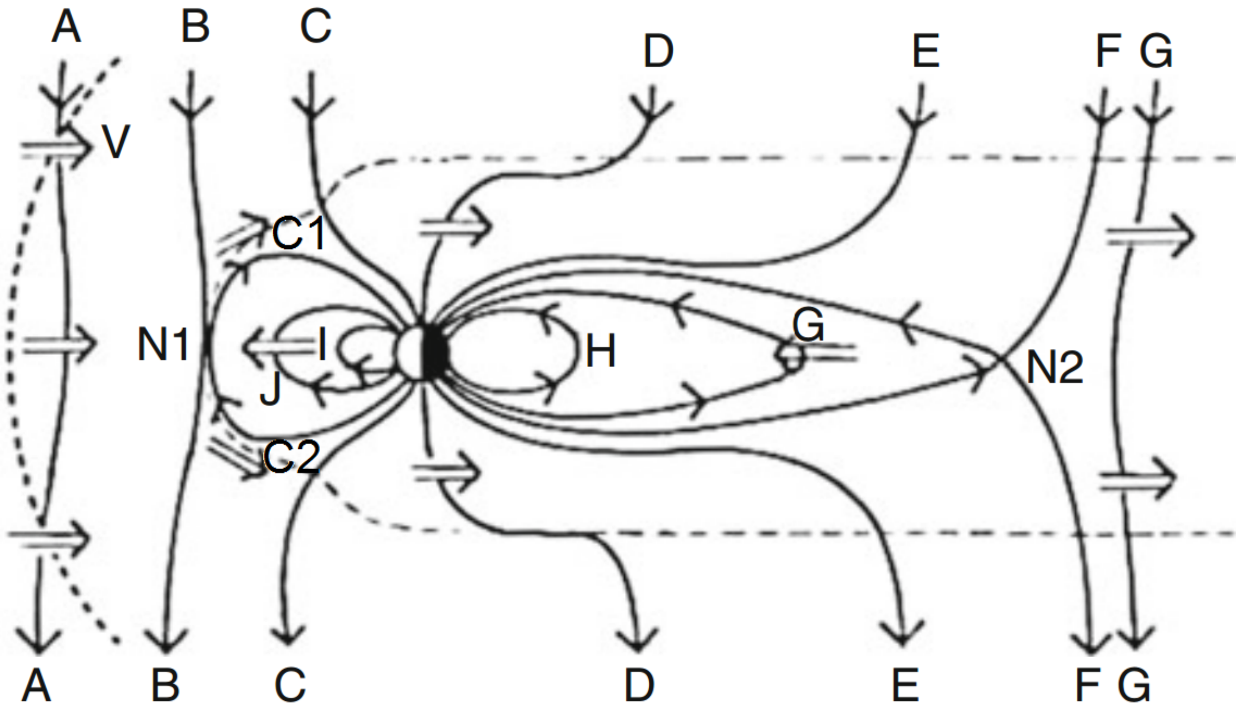

Figure 2.9: Cartoon of magnetospheric convection. Letters indicate the order of events, N1 and N2 indicate the location of the merging events, and C1 and C2 indicate the polar cusps [*Zarka* (2011), Chapter 13].

1974). Meanwhile, electric fields are generated when the magnetic field lines of the solar wind merge with those of the magnetosphere.

As the solar wind approaches the Earth from the Sun, the magnetic field of the solar wind, also known as the Interplanetary Magnetic Field (IMF), merges with that of the Earth, opening flux tubes in a process called dayside merging. These open magnetic flux tubes continue moving from the dayside to the nightside of the Earth. On the nightside, the antiparallel field lines from north and south of the magnetic equator reconnect, closing the flux tubes in a process called nightside merging, or reconnection. These newly closed stretched geomagnetic field lines then move earthward around the polar cap, and the process repeats itself. This process is sketched in Figure 2.9 for a purely southward (-B_z direction) IMF. Figure 2.9 also indicates the cusps, which are narrow dayside regions of recently opened magnetic flux tubes that map into the high-latitude ionosphere just poleward of the next flux tube to open.

The motion of the solar wind establishes a series of perpendicular electric fields that map into the ionosphere and push ionospheric plasma. Two regions in the ionosphere that are defined in the context of merging magnetic field lines are the polar cap region and the auroral region [*Harra and Mason* (2004), Chapter 9]. Assuming a purely southward IMF, field lines that map into the ionosphere from the solar wind pull plasma antisunward by a dawn-to-dusk electric field (*Heelis*, 1984). Meanwhile, in the auroral region, plasma convects along the dawn and dusk sides of the Earth back to the dayside through a radial electric field (*Reiff*, 1982). This convection establishes two large cells in the ionosphere, called the dawn and dusk convection cells. At latitudes below the auroral region lies the co-rotation region, where plasma moves with the Earth's rotation [*Harra and Mason* (2004), Chapter 9]. The polar cap, the auroral region, and the corotation region are labeled in Figure 2.10, but Figure 2.11 shows a more accurate illustration of basic polar cap and auroral region convection.

The high-latitude convection pattern deviates from the basic, average pattern shown in Figure 2.11 when the IMF is not strictly southward. For example, if the southward IMF is tilted towards dawn ($+B_y$ direction) dayside merging will occur more on the dusk side of the northern hemisphere (dawn side of the southern hemisphere), and if the IMF is tilted towards the dusk side ($-B_y$ direction) dayside merging will occur more on the dawn side of the northern hemisphere (dusk side of the southern hemisphere). This then leads to anti-symmetric convection cells, where one cell is somewhat circular and the other cell is shaped like a banana, as is seen in Figure 2.12 (*Reiff and Burch*, 1985).

The north-south component of the IMF also plays an important role in the high-latitude convection pattern. As discussed, when the IMF is southwards the average convection pattern is like those in Figures 2.11 and 2.12. However, when the IMF is northwards the pattern becomes disordered, and the two-cell convection pattern seen during southward IMF conditions may become dramatically shifted and warped, as reflected in Figure 2.13 through several example Super Dual Auroral Radar Network (SuperDARN) convection maps. In spite of this, Figure 2.14 shows the average convection patterns that result from a variety of IMF directions, including northward IMF conditions.

Both the total IMF and the pressure of the solar wind will increase when the sun becomes more active and more solar energy is released into the solar wind. However, this increase in solar activity and IMF does not necessarily change the shape of the convection pattern. For

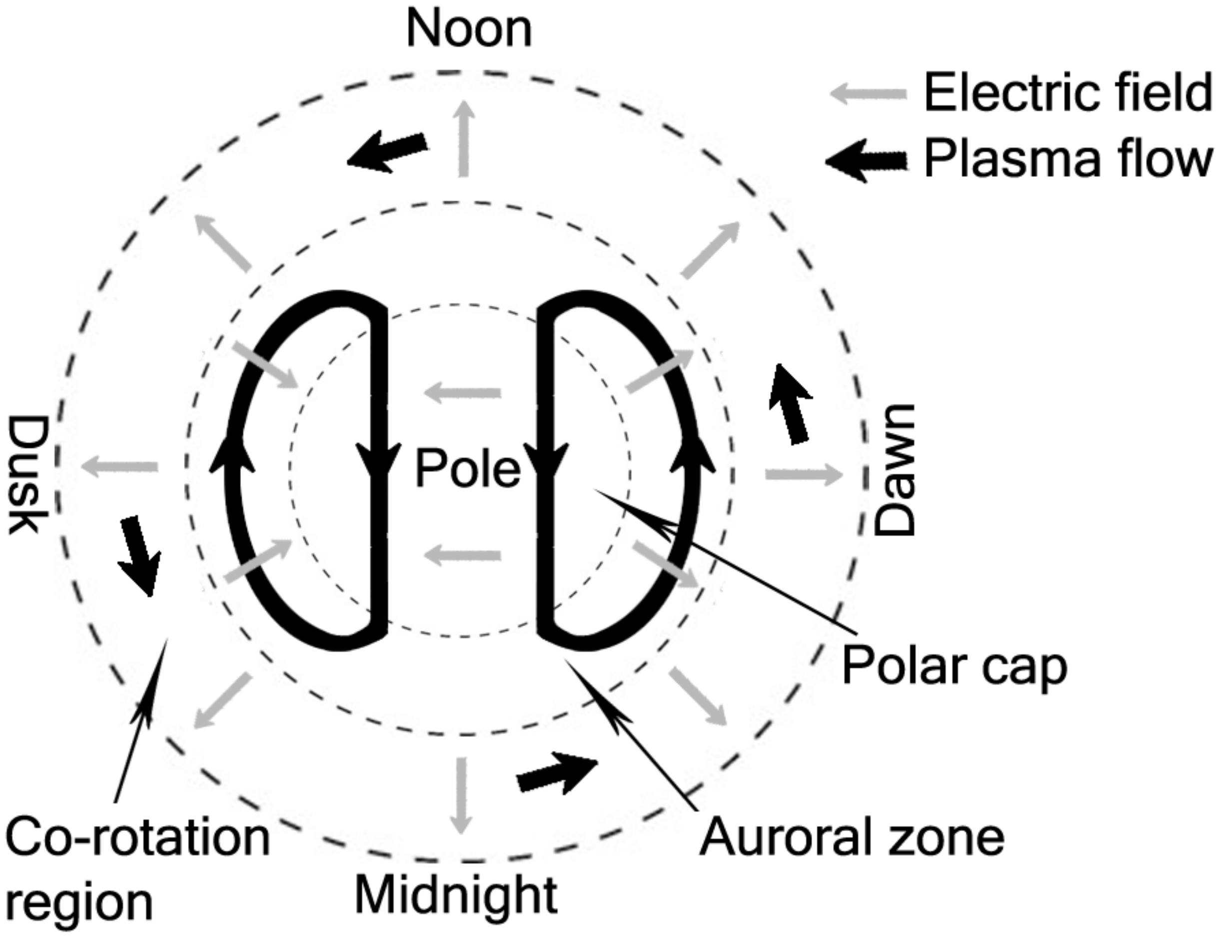

Figure 2.10: Cartoon of the convection pattern seen in the Earth's northern ionosphere when the IMF is purely southward [*Harra and Mason* (2004), Chapter 4].

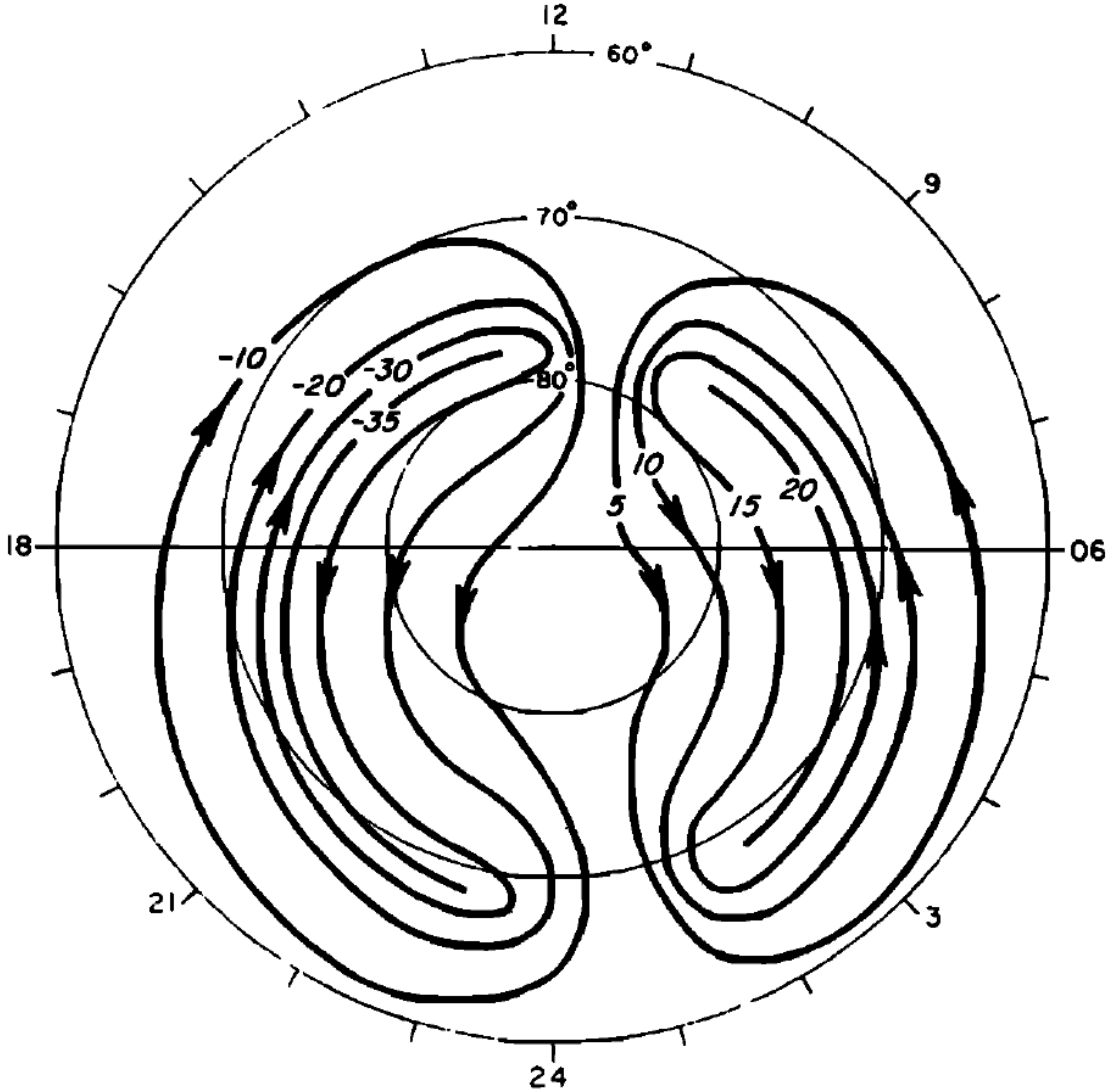

Figure 2.11: A more precise illustration of the convection pattern seen in the Earth's northern ionosphere when the IMF is purely southward. Values represent electric potential, and arrows give convection direction (*Heelis et al.*, 1982).

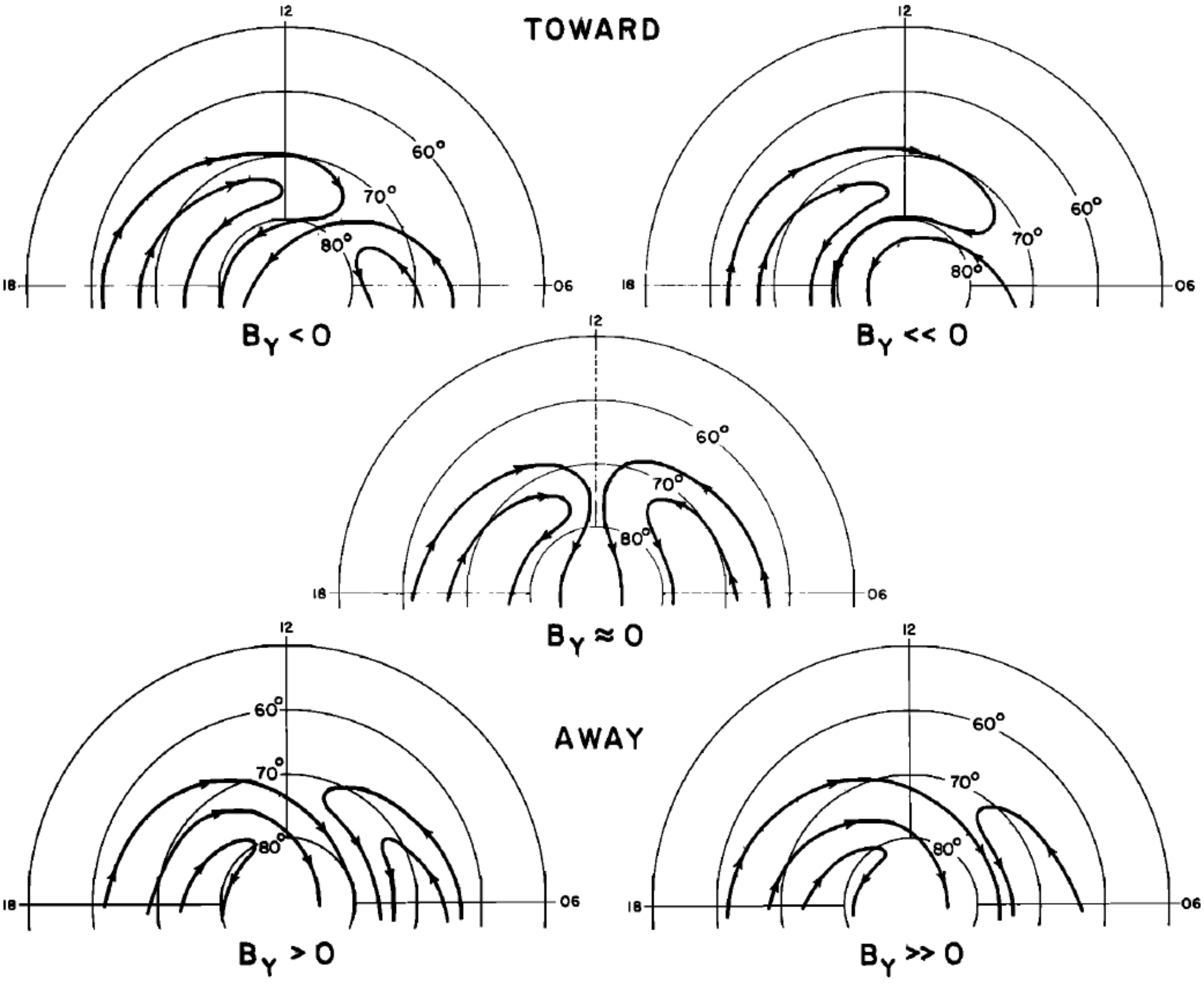

Figure 2.12: A schematic representation of the flow geometries observed in the dayside northern hemisphere for different magnitudes of B_y when B_z is negative and $|B_x|$ is constant (*Heelis*, 1984).

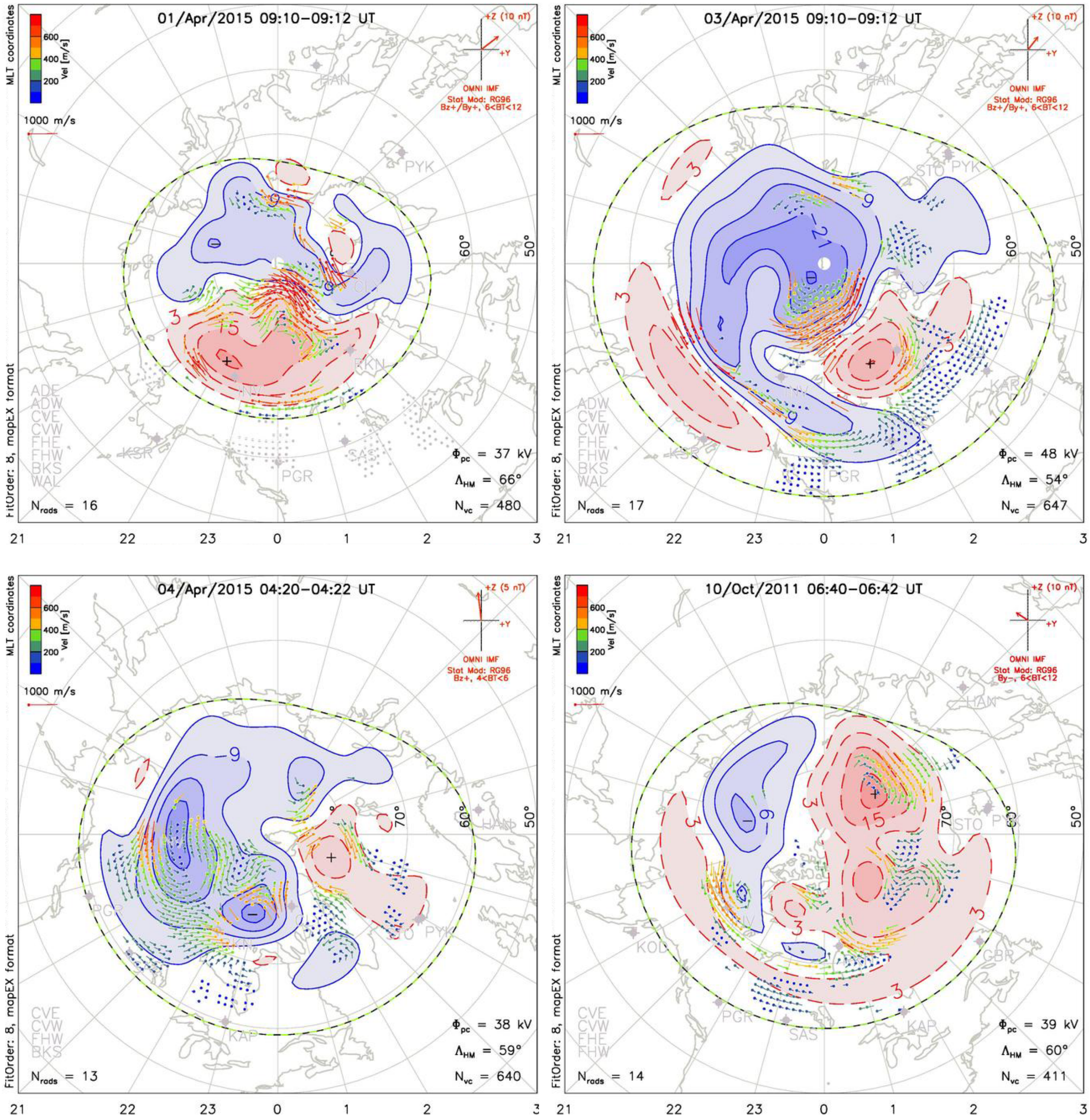

Figure 2.13: Four example convection patterns inferred by SuperDARN in the Earth's northern ionosphere during a northward IMF (data for figure and figure available through http://vt.superdarn.org).

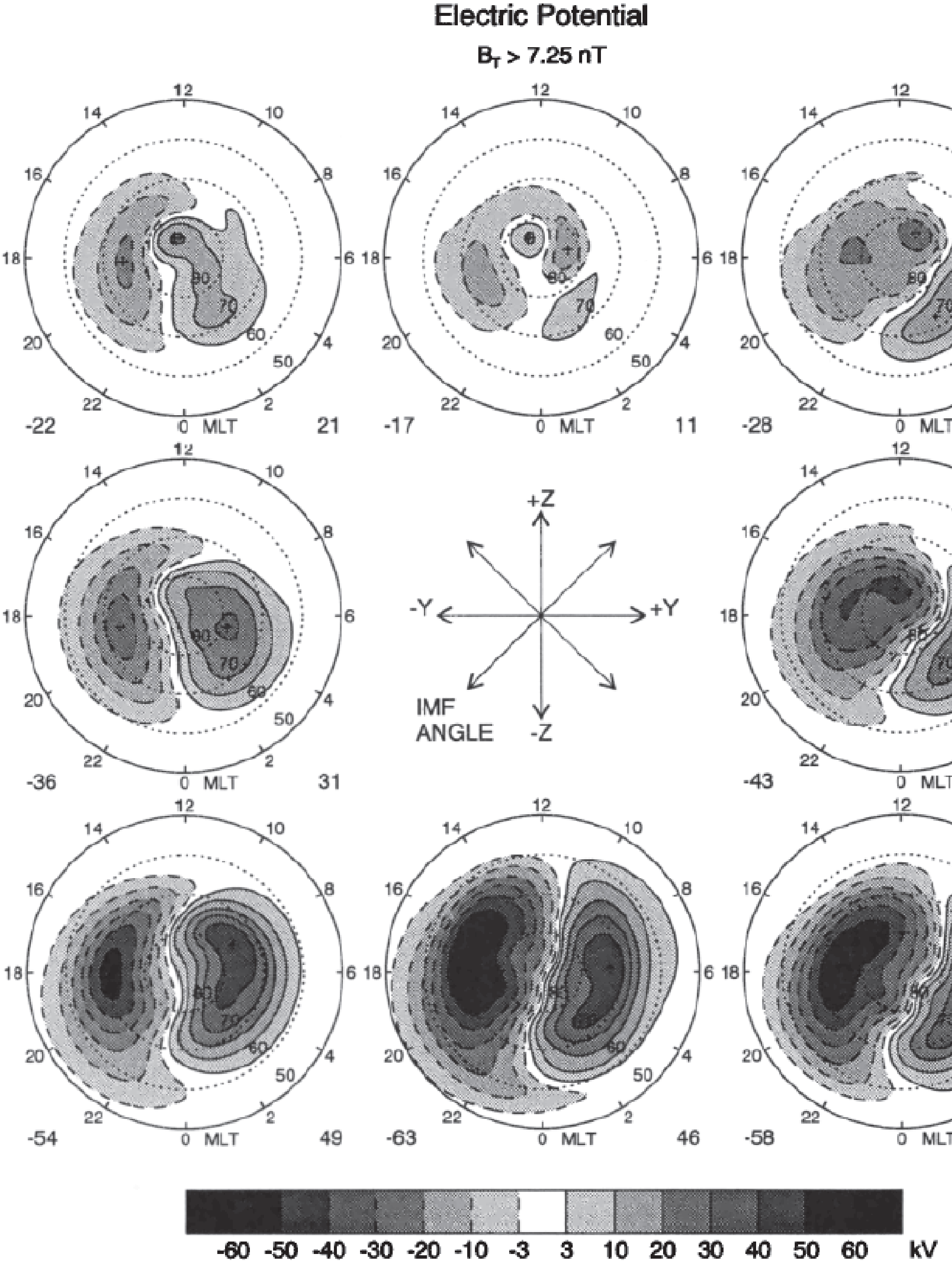

Figure 2.14: Electric potential from an empirical convection model when the magnitude of the IMF is greater than 7.25 nT (*Weimer*, 1995).

example, Figure 2.15 shows a SuperDARN convection map that uses observations of the 2015 St. Patrick's day storm, which had a large, southward IMF. Even during this period of strong activity, the high-latitude plasma convection pattern still roughly follows the southward IMF pattern shown in Figures 2.11 and 2.12, even though the pattern is considerably larger than normal. An increase in solar activity may also lead to the injection of particles into the magnetosphere from the ionosphere, as well as increases in precipitation (as discussed in Section 2.1.3).

2.2.2 Plasma Temperature and Energy

Electric fields not only play a role in plasma convection, but also change the energy in a plasma. From *St-Maurice and Hanson* (1982), the general ion energy equation is given by:

$$\frac{3}{2}\left(\frac{D}{Dt}p_i + p_i\nabla\cdot\mathbf{v}_i\right) + \nabla\cdot\mathbf{q}_i + \mathbf{P}_i : \nabla\mathbf{v}_i = \sum_n \frac{n_i m_i \nu_{in}}{m_i + m_n}\left[3k_b(T_n - T_i)\psi_{in} + m_n(\mathbf{v}_i - \mathbf{v}_n)^2\phi_{in}\right] + n_i\nu_{ie}3k_b(T_e - T_i) + n_i\nu_{ie}m_e\left(\mathbf{v}_i - \mathbf{v}_e\right)^2 \tag{2.5}$$

where t is time, p is the pressure, D/Dt is the convective derivative ($\partial/\partial t + \mathbf{v}_i \cdot \nabla$), $\mathbf{v}_i$ is ion velocity, $\mathbf{v}_n$ is neutral velocity, $\mathbf{v}_e$ is electron velocity, $\mathbf{q}$ is the heat flow, $\mathbf{P}$ is the stress tensor, n_i is the ion number density (which by assuming plasma quasineutrality is the same as the electron number density, n_e), m_i is the ion mass, m_n is the neutral mass, m_e is the electron mass, ν_{ie} is the ion-electron collision frequency (where $\nu_{ie} \approx 54.5 n_e T_e^{-3/2}$), k_b is the Boltzmann constant, T_i is the (average) ion temperature, T_e is the electron temperature, T_n is the neutral temperature, $\sum_n$ is the sum over different neutrals, and ψ_{in} and ϕ_{in} are dimensionless functions of order 1. The left-hand side of Equation 2.5 contains the rate of change of internal energy, adiabatic heating and cooling, ion heat flow and viscous heating, while the right-hand side contains the heat exchange between neutrals and ions, frictional heating through the relative drift between ions and neutrals, heat exchange between electrons and ions, and frictional heating through the relative drift between ions and electrons.

Equation 2.5 is reduced considerably for the weakly-ionized F-region ionosphere. First, assuming a large ν_{in} means $\partial/\partial t$ is negligible (zero after a few seconds at most), as well as heat advection, conduction, and viscous heating, making $\mathbf{v}_i \cdot \nabla p_i$, $\nabla \cdot \mathbf{q}_i$ and $\mathbf{P}_i : \nabla\mathbf{v}_i$ all

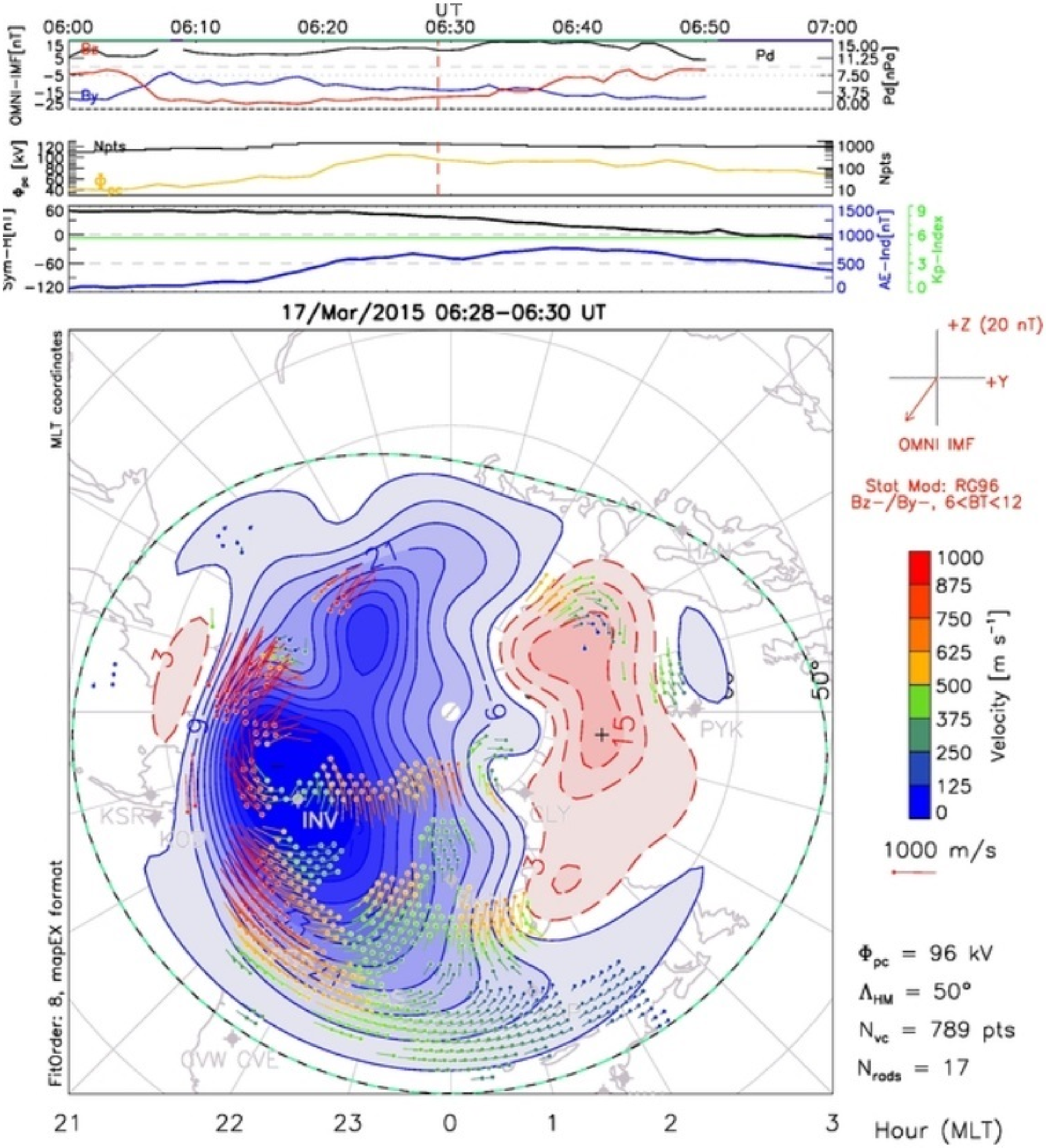

Figure 2.15: The convection pattern inferred by SuperDARN in the Earth's northern ionosphere during the 2015 St. Patrick's day storm (data for figure and figure available through http://vt.superdarn.org).

relatively small (*Schunk*, 1975; *Schunk and Sojka*, 1982). Then, for $\mathbf{O}^+$ and $\mathbf{O}$ dominant environments ψ_{in} and ϕ_{in} are approximately 1 (*St-Maurice and Hanson*, 1982), and since $\partial\mathbf{B}/\partial t$ is assumed to be small, where $\mathbf{B}$ is the magnetic field, $\nabla \cdot \mathbf{v}_i$ is negligible (*Rishbeth and Hanson*, 1974). By lastly taking the mass of electrons to be negligible, to leading order the F-region ion temperature is (*Banks*, 1980; *Banks and Kockarts*, 1973; *Schunk*, 1977; *St-Maurice and Hanson*, 1982, 1984):

$$T_i \approx \frac{\dfrac{m_n}{3k_b}(\mathbf{v_i} - \mathbf{v}_n)^2 + T_n + \dfrac{m_i + m_n}{m_i}\dfrac{\nu_{ie}}{\nu_{in}}T_e}{1 + \dfrac{m_i + m_n}{m_i}\dfrac{\nu_{ie}}{\nu_{in}}} \tag{2.6}$$

This shows that the leading factors affect the F-region ion temperature, are: the electron temperature, the neutral temperature, the mean neutral mass, and the relative drift between ions and neutrals. Additionally, since ion heating and cooling comes from elastic collisions, the ions heat up at the same rate as they cool down, namely over a time scale of $1/\nu_{in}$, which is seconds below 400 km (*Schunk*, 1975). In Equation 2.6, the relative drift between ions and neutrals has the strongest impact on the F-region ion temperature whenever the relative drift exceeds 200 m/s, and the term that depends on the relative drift is specifically referred to as ion-neutral frictional heating. A key driver for frictional heating is electric fields because when an electric field is introduced, charged particles will move with an $\mathbf{E} \times \mathbf{B}$ drift relative to the neutral particles, which at times can be quite large (several km/s at times). Since this process depends on the collision frequency between ions and neutrals, it is most effective below roughly 400 km because at higher altitudes the collision frequency is not large enough and other processes compete with the simple notion of local friction. In fact, as this research and that of *Loranc and St-Maurice* (1994), and *Wilson* (1994) shows, during periods of particularly strong frictional heating this heating can affect higher regions through transport.

2.2.3 Ion Velocity Distributions

As discussed above, electric fields move plasma with the $\mathbf{E} \times \mathbf{B}$ drift and heat plasma through frictional heating. However, electric fields also alter the ion velocity distribution of the plasma. To understand the ion velocity distribution in the F-region, and by extension the influence of electric field strength on the velocity distribution of a weakly-ionized, magnetized plasma, first consider the Lorentz force on an individual ion:

$$\frac{d\mathbf{v}_i}{dt} = \Omega_i \frac{\mathbf{E}}{B} + \mathbf{v}_i \times \vec{\Omega}_i \tag{2.7}$$

which is re-written as (*St.-Maurice and Schunk*, 1977):

$$\frac{d}{dt}\left(\mathbf{v}_i - \frac{\mathbf{E} \times \mathbf{B}}{B^2}\right) = \left(\mathbf{v}_i - \frac{\mathbf{E} \times \mathbf{B}}{B^2}\right) \times \vec{\Omega}_i \tag{2.8}$$

where $\mathbf{E}$ is a uniform electric field, $\mathbf{B}$ is a uniform magnetic field, and $\vec{\Omega}_i$ is a vector along the magnetic field that has a magnitude of Ω_i. From this expression it is clear that in velocity-space charged particles drift in a circular motion centered on $\mathbf{E} \times \mathbf{B}/B^2$, regardless of their initial velocity. A two-dimensional cartoon of this is provided in Figure 2.16, where the red rings indicate the motions of independent ions. However, through ion-neutral collisions (particularly RCE collisions) the ions tend to acquire the Maxwellian neutral particle velocity distribution represented by a blue disk in Figure 2.16 (note that $\mathbf{E} \times \mathbf{B}/B^2$ is chosen to be much greater than the neutral thermal speed). In the case of pure RCE collisions the ions are injected randomly one by one into the blue disk, and then drift in a circular orbit. This results in the ion velocity distribution described by the purple ring in Figure 2.16, while Figure 4.3 in Chapter 4 gives a more precise example of an ion velocity distribution subject to a 150 mV/m electric field. This motion gives the ions an overall toroidal velocity distribution in a strong electric field and a Maxwellian distribution in a weak to negligible electric field. Furthermore, not only does the distribution become more toroidal through ion-neutral collisions as the electric field increases, but since the width of the distribution is larger in the directions perpendicular to the magnetic field, the temperature perpendicular to the magnetic field is greater than the temperature along the magnetic field. This is known as temperature anisotropy, and is discussed in more detail in Chapter 4.

For a more mathematical approach, consider the Boltzmann equation in the $\mathbf{E} \times \mathbf{B}$ frame of reference, for a steady-state with no gradients (*St-Maurice and Schunk*, 1979):

$$\left(\mathbf{v} - \frac{\mathbf{E} \times \mathbf{B}}{B^2}\right) \times \vec{\Omega}_i \cdot \nabla_{\mathbf{v}} f_i = \frac{\delta f_i}{\delta t} \tag{2.9}$$

where f_i is the ion velocity distribution, and $\frac{\delta f_i}{\delta t}$ accounts for the rate of change of f_i due to

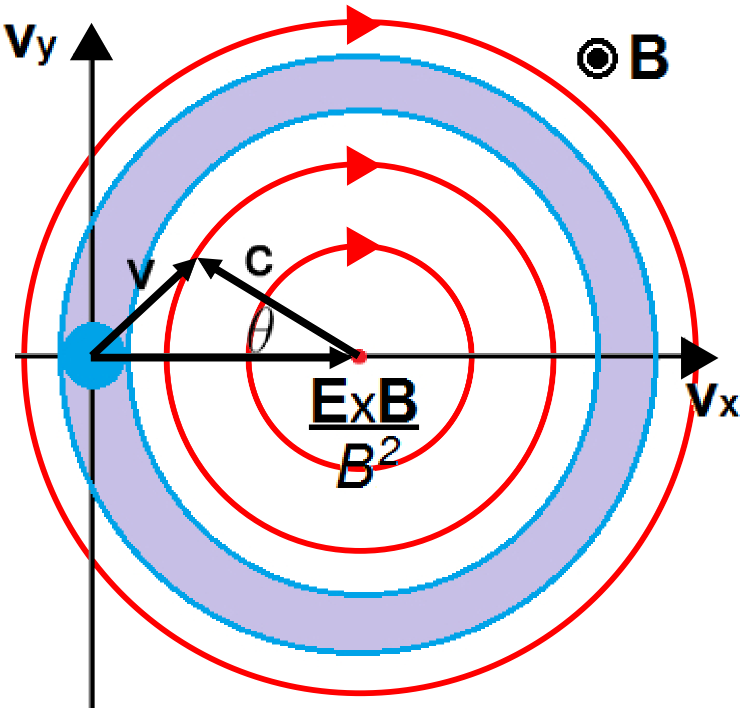

Figure 2.16: A cartoon of the ion velocity distribution subject to a strong electric field. The red circle indicates the motion of independent ions in velocity space, the blue circle centred on the origin indicates the neutral velocity distribution, and the purple ring is the ion velocity distribution centred on $\mathbf{E} \times \mathbf{B}/B^2$ that results through collisions. The $\mathbf{V}_y$ direction is parallel to the electric field, the $\mathbf{V}_x$ is perpendicular to both the electric and magnetic fields, and the magnetic field is directed out of the page.

ion-neutral collisions. By next defining $\mathbf{c} = \mathbf{v} - \frac{\mathbf{E} \times \mathbf{B}}{B^2}$, it can be easily shown that:

$$\mathbf{c} \times \vec{\Omega}_i \cdot \nabla_{\mathbf{c}} f_i = \Omega_i \frac{\partial f_i}{\partial \theta} = \frac{\delta f_i}{\delta t} \tag{2.10}$$

where θ is the angle shown in Figure 2.16.

For binary elastic collisions between ions and neutrals, the Boltzmann's collision integral reads:

$$\frac{\delta f_i}{\delta t} = \sum_n \int d\mathbf{V}_n d\Omega v_{in} \sigma_{in}(v_{in}, \Theta)(f_i' f_n' - f_i f_n) \tag{2.11}$$

where Θ is the scattering angle in the center-of-mass system, $d\mathbf{V}_n$ is the volume element in velocity space, $d\Omega$ is an element of solid angle in the center-of-mass reference frame, v_{in} is the relative speed of the colliding particles i and n (a neutral species), σ_{in} is the differential scattering cross section, f_n is a Maxwellian distribution at the neutral temperature and drift, and primed variables denote quantities evaluated after a collision. However, *St.-Maurice and Schunk* (1977) showed that if:

$$\sigma_{in} = C_{RC} \frac{\delta(\Theta - \pi)}{v_{in}} \tag{2.12}$$

where C_{RC} is a constant, then

$$\frac{\delta f}{\delta t} = -\nu_{in}(f_i - f_n) \tag{2.13}$$

where ν_{in} by virtue of Equation 2.12 describes a Maxwell molecule interaction where the ion-neutral collision frequency is independent of velocity (*St-Maurice and Schunk*, 1979). This model is referred to as the Relaxation Collision Model (RCM) or the Langevin model, and is often confused with the *Bhatnagar et al.* (1954) model. The effect of the RCM is to push the ion velocity distribution towards the Maxwellian neutral distribution at a rate controlled by the relaxation time ($1/\nu_{in}$). To find a solution:

$$\frac{\partial f_i}{\partial \theta} = -\frac{\nu_{in}}{\Omega_i}(f_i - f_n) \tag{2.14}$$

However, in the case of a magnetized plasma the ratio ν_{in}/Ω_i is much less than 1, and the distribution is expanded in powers of ν_{in}/Ω_i, so that to leading order:

$$f_i = f_0 + \frac{\nu}{\Omega} f_1 \tag{2.15}$$

where the subscript *in* is dropped from ν_{in} and the subscript i is dropped from Ω_i from now on. As a result:

$$\frac{\partial f_0}{\partial \theta} = 0 \tag{2.16}$$

which has an infinite number of possible solutions. But:

$$\frac{\partial f_1}{\partial \theta} = f_0 - f_n(\theta) \tag{2.17}$$

However, through cyclic continuity $f_1(0) = f_1(2\pi)$, and therefore:

$$\int_0^{2\pi} \frac{\partial f_1}{\partial \theta} d\theta = 0 \tag{2.18}$$

giving

$$f_0 = \frac{1}{2\pi} \int_0^{2\pi} f_n(\theta) d\theta \tag{2.19}$$

where

$$f_n(0) = \exp\left(-v(\theta)^2\right) \tag{2.20}$$

and $\mathbf{v}$ is normalized with respect to the neutral thermal speed. Using

$$v^2 = v_{||}^2 + v_x^2 + v_y^2 \tag{2.21}$$

where $\mathbf{c} = \mathbf{v} - \mathbf{D}$ and $\mathbf{D} = \dfrac{\mathbf{E} \times \mathbf{B}}{B^2}$:

$$c_{||} = v_{||} \tag{2.22}$$

$$c_x = v_x - D \tag{2.23}$$

$$c_y = v_y \tag{2.24}$$

Therefore:

$$v_x = D + c_\perp \cos\theta \tag{2.25}$$

$$v_y = c_\perp \sin\theta \tag{2.26}$$

giving:

$$v^2 = c_{||}^2 + D^2 + c_\perp^2 + 2c_\perp D \cos\theta \tag{2.27}$$

Since this final term is the only one with a θ:

$$f_0 = \frac{1}{2\pi} \exp\left(-c_{||}^2 - c_\perp^2 - D^2\right) \int_0^{2\pi} \exp\left(-2c_\perp D \cos\theta\right) d\theta \tag{2.28}$$

where the integral is a modified Bessel function of order zero, I_0. Therefore, for the RCM,

$$f_0 = \exp\left(-c_{||}^2 - [c_\perp - D]^2\right) \exp\left[-2c_\perp D\right] I_0\left[2c_\perp D\right] \tag{2.29}$$

This implies that f_0 peaks when $c_{||} = 0$ and $c_\perp = D$. The RCM is useful because of its simplicity, and how it is able to clarify ion velocity distributions. However, *St-Maurice et al.* (1976) found from in-situ satellite observations of the ion velocity distribution in a direction perpendicular to the magnetic field that the results of the RCM needed to at least be scaled down. Nevertheless, the ion velocity distributions did retain a large enough toroidal characteristics that the scaled RCM results were found to be useful in IS spectral fitting routines, since the resulting spectra were indeed strongly affected by the scaled-down toroidal character (e.g. *Raman et al.* (1981)).

Researchers returned to the Boltzmann collision operator to obtain better solutions using more realistic collisional cross-sections. Ultimately the Boltzmann collision operator was integrated through the use of Monte-Carlo simulations that required a large number of collisions (e.g. *Barakat et al.* (1983); *Winkler et al.* (1992)). For elastic collisions, scattering from ion-neutral collisions is adequately modeled using both long-range polarization interactions, and short range repulsion interactions (*Mason*, 1970). Following *Mason and Schamp Jr* (1958), the potential of interaction is then chosen to be given by (*Winkler et al.*, 1992):

$$V(r) = \frac{d_{pw}}{2}\left[(1+\gamma_s)\left(\frac{r_m}{r}\right)^{12} - 4\gamma_s\left(\frac{r_m}{r}\right)^{6} - 3(1-\gamma_s)\left(\frac{r_m}{r}\right)^{4}\right] \tag{2.30}$$

where r is the separation, r_m is the value of r for which $V(r)$ is a minimum, d_{pw} is the depth of the potential well, and γ_s is a measure of the relative strengths of the different attractive forces. The fourth-power term represents the attraction between an ion and the dipole it induces in the neutral molecule, the sixth-power term represents the combined contributions from the charge-induced quadrupole and the London dispersion energy, and the 12-power term is the repulsion potential (*Mason*, 1970). However, *Winkler et al.* (1992) allowed $\gamma_s = 0$ to simplify these calculations, while they incorporated RCE effects into their MC simulations of O^+ ion velocity distributions. Their results not only show the ion velocity distribution evolving into a toroid as the electric field increases (as seen in Figure 2.17), but they can also be used to characterize the anisotropy of O^+ velocity distributions.

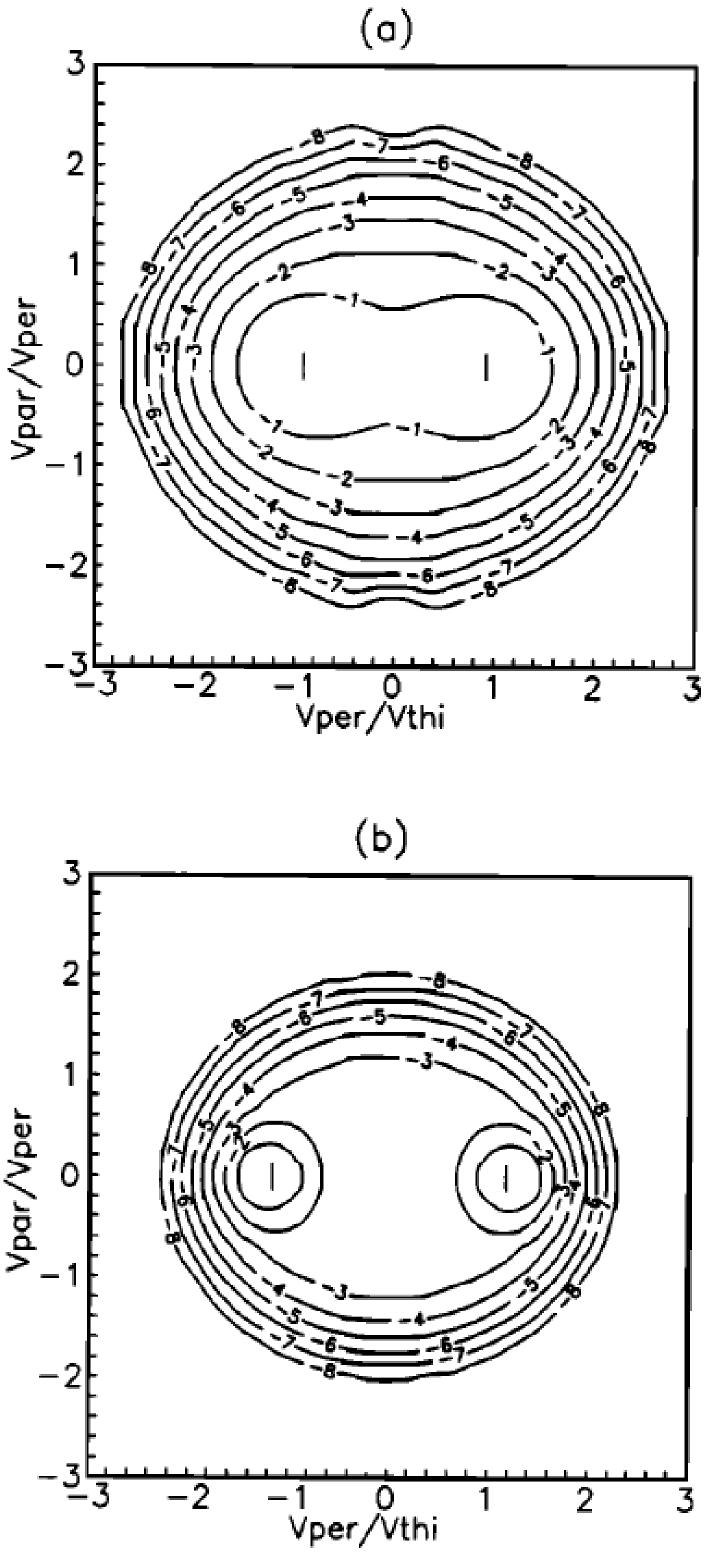

Figure 2.17: Contours indicating the log of the ratio O^+-O velocity distributions to the peak value, where the y-axis is the parallel ion velocity to the perpendicular ion velocity, and the x-axis is the perpendicular ion velocity to the ion thermal velocity. The top plot is for an electric field of 100 mV/m, and the bottom plot if for 250 mV/m. Taken from *Winkler et al.* (1992).

The focus of *Winkler et al.* (1992) is on the impact ion-neutral collisions have on the ion velocity distribution, which is accurate in weakly-ionized regions. However, as the altitude increases and the neutral density decreases, the ion-neutral collision frequency decreases and Coulomb collisions become more relevant. The influence of Coulomb collisions on the ion velocity distribution is handled in *Tereshchenko et al.* (1991) through a simplified technique. Their work showed that although in the presence of a strong electric field the ion velocity distribution is still anisotropic when both ion-neutral and ion-ion collisions are incorporated, ion-ion collisions will reduce the anisotropy of the ion velocity distribution. This is discussed in more detail in Chapter 4.

2.3 High-Latitude Currents

Since the current systems of the high-latitude ionosphere are related to precipitation, electric fields and, by extension, the magnetospheric generator, it is important to briefly discuss current systems in the high-latitude ionosphere. As discussed previously, plasma flows between the ionosphere and the magnetosphere along magnetic field lines that map into the auroral oval. The electrons that precipitate into the ionosphere lead to upward Field-Aligned Currents (FACs), and the ionospheric electrons that flow up into the magnetosphere lead to a downward FAC. Note that ions also precipitate into the ionosphere, but since the integral number flux of the precipitating ions is usually much less than that of the electrons, the current carried by the precipitating ions is relatively negligible (*Schunk and Nagy*, 2009).

The FACs system that emerges is sketched in Figure 2.18, which also distinguishes the "Region 1" currents and "Region 2" currents. Region 1 currents are the FACs that flow into the ionosphere in the morning sector, and away from the ionosphere in the evening sector. Region 2 currents are equatorward of the Region 1 currents, and flow in the opposite direction. As seen in Figure 2.18, the Region 1 and Region 2 currents are closed through horizontal currents in the lower ionosphere. Figure 2.19 shows statistical patterns of FACs for southward IMF during both quiet and active geomagnetic conditions (*Iijima and Potemra*, 1978; *Iijima et al.*, 1984).

FAC systems, particle precipitation, and convection electric fields, all impact the conduc-

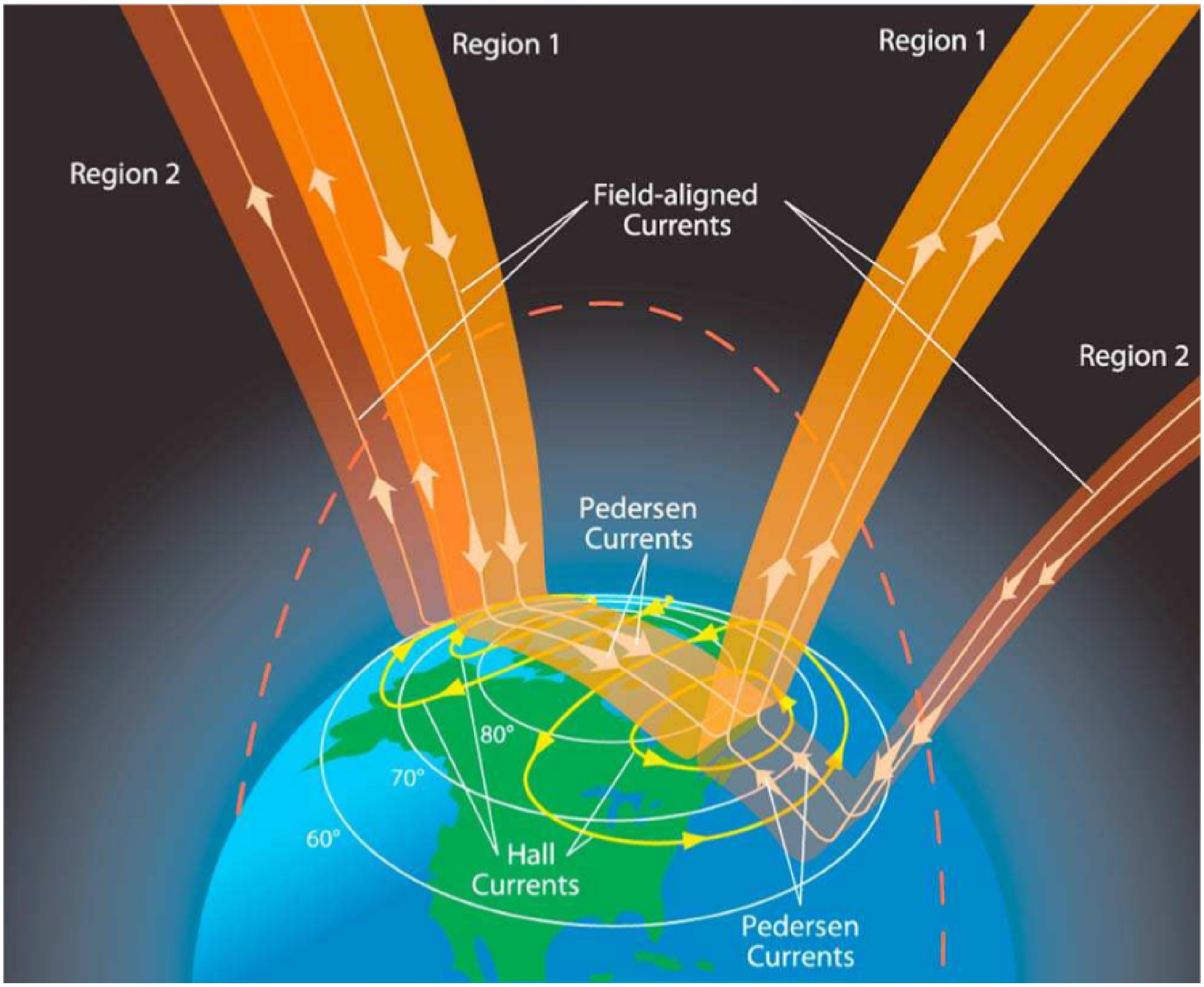

Figure 2.18: A cartoon showing Region 1 and Region 2 FACs, as well as the Hall and Pedersen currents. Taken from *Le et al.* (2010).

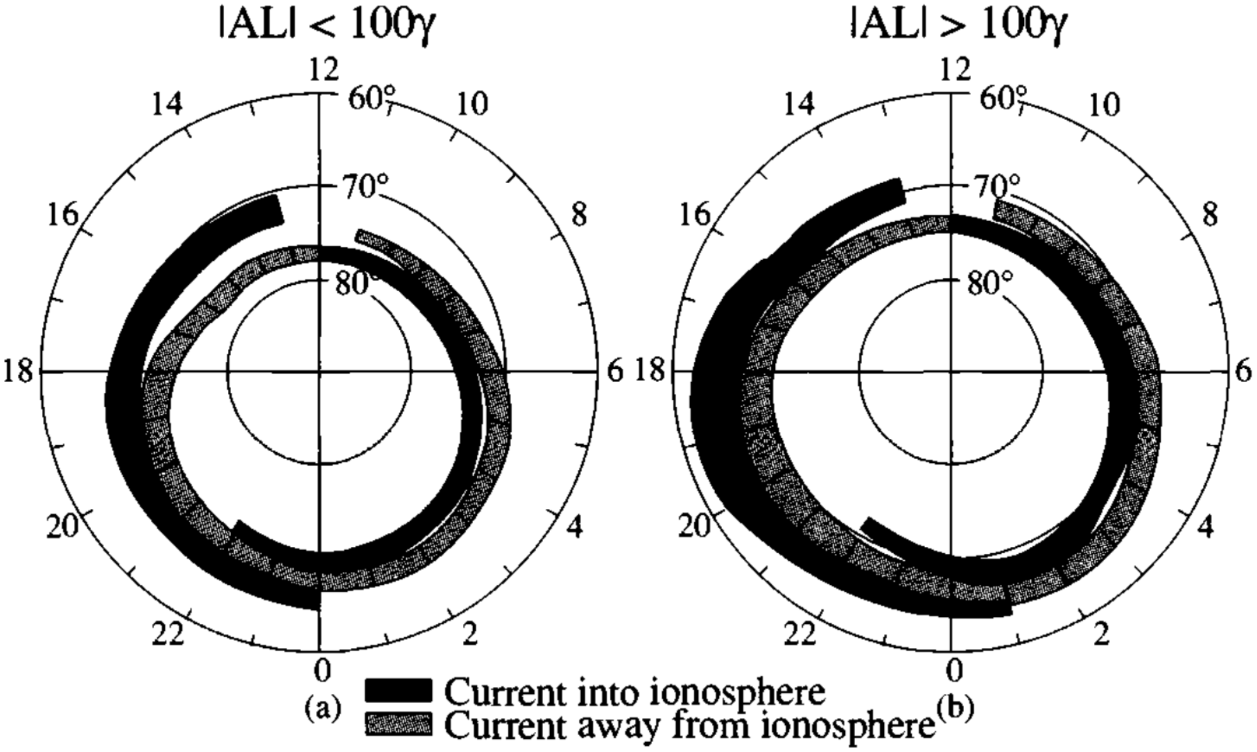

Figure 2.19: Statistical distribution and flow directions of large-scale FACs. (a) The distribution and flow directions during weakly disturbed geomagnetic conditions (taken from 439 passes of the Triad satellite) (b) The distribution and flow directions during active geomagnetic conditions (taken from 366 Triad passes). Taken from *Iijima and Potemra* (1978).

tivity of the ionosphere and current systems perpendicular to the magnetic field, namely the Pedersen currents and Hall currents. Pedersen currents act perpendicular to the magnetic field and along the convection electric fields. As seen in Figure 2.18, Pedersen currents connect the Region 1 and Region 2 currents horizontally in the ionosphere. Meanwhile, Hall currents, which are also shown in Figure 2.18, flow around the locations where the Region 1 currents map into the ionosphere. These currents flow perpendicular to both the magnetic field and the convection electric fields, following the high-latitude plasma convection pattern shown in Figure 2.10.

The total current density perpendicular to the magnetic field is given by [*Schunk and Nagy* (2009), Chapter 5]:

$$\mathbf{J}_\perp = \sigma_P \left(\mathbf{E}_\perp + \mathbf{v}_n \times \mathbf{B}\right) + \sigma_H \hat{b} \times \left(\mathbf{E}_\perp + \mathbf{v}_n \times \mathbf{B}\right) \tag{2.31}$$

where σ_P is the Pedersen conductivity, given by:

$$\sigma_P = \sum_i \sigma_i \frac{\left(\sum_n \nu_{in}\right)^2}{\left(\sum_n \nu_{in}\right)^2 + \Omega_i^2} + \sigma_e \frac{\left(\sum_n \nu_{en}\right)^2}{\left(\sum_n \nu_{en}\right)^2 + \Omega_e^2} \tag{2.32}$$

σ_H is the Hall conductivity, given by:

$$\sigma_H = -\sum_i \sigma_i \frac{\left(\sum_n \nu_{in}\right)\Omega_i}{\left(\sum_n \nu_{in}\right)^2 + \Omega_i^2} + \sigma_e \frac{\left(\sum_n \nu_{en}\right)\Omega_e}{\left(\sum_n \nu_{en}\right)^2 + \Omega_e^2} \tag{2.33}$$

where e is the elementary charge, ν_{en} is the electron-neutral collision frequency, σ_i is the ion conductivity $(n_i q_i^2/(m_i \left(\sum_n \nu_{in}\right))$, where q_i is the ion charge), Ω_e is the electron gyrofrequency, and σ_e is the electron conductivity $(n_e e^2/(m_e \left(\sum_n \nu_{en}\right)))$. Knowing this, and that $\sum_n \nu_{en}$ is usually much less than Ω_e:

$$\sigma_P = \sum_i \sigma_i \frac{\nu_i^2}{\left(\sum_n \nu_{in}\right)^2 + \Omega_i^2} \tag{2.34}$$

and:

$$\sigma_H = -\sum_i \sigma_i \frac{\left(\sum_n \nu_{in}\right)\Omega_i}{\left(\sum_n \nu_{in}\right)^2 + \Omega_i^2} + \frac{\left(\sum_n \nu_{en}\right)\sigma_e}{\Omega_e} \tag{2.35}$$

Meanwhile, parallel to the magnetic field, the current density is given by [*Schunk and Nagy* (2009), Chapter 5]:

$$\mathbf{J}_{||} = \sigma_{e||} \left(\mathbf{E}_{||} + \frac{k_B T_e}{e n_e} \nabla_{||} n_e\right) + \epsilon_e' \nabla_{||} T_e \tag{2.36}$$

where $\sigma_{e||}$ is the parallel electrical conductivity ($n_e e^2/(m_e \nu_e)$, ν_e is the sum of electron-ion and electron-neutral collision frequencies), and ϵ'_e is the current flow conductivity due to thermal gradients ($n_e e k_B/(m_e \nu_e)$). One important difference between the parallel electrical conductivity and the perpendicular electrical conductivity is that the parallel electrical conductivity is dominated by electron mobility.

Chapter 3

INCOHERENT SCATTER RADARS

Ionospheric electrodynamics are probed in a variety of ways with satellites, rockets, drift measurements of chemical releases, Fabry-Perot interferometers, and/or radars (*Park*, 1976). In addition, ISRs are particularly useful because temperatures from ground-based instruments are generally difficult to obtain, and ISRs provide more detailed electron density profiles than other instruments, like ionosondes. High-resolution measurements in both time (down to second scales) and space (as low as kilometer scales) of ion temperature, line-of-sight ion velocity, electron temperature, and plasma density are obtained from ISRs by sending out radio waves that probe small wave amplitudes and receive backscatter echoes that have bounced off high-altitude plasma. Therefore, although ISRs are expensive, power hungry, and their data require complex fitting routines (when compared to most other ground-based instruments that observe the ionosphere), they relay precious detailed plasma diagnostics, give data for a wide variety of scale sizes, and the scatter is always present. Retrieved radar parameters are used to infer changes in the F-region density, neutral atmosphere motion, and electric fields for a finite region (*Evans*, 1972).

In this chapter ISR theory is first examined, after which the more technical challenges of ISRs are discussed.

3.1 Theory

The bulk of ISR plasma theory was developed in the 1960s (*Dougherty and Farley*, 1960; *Fejer*, 1960; *Salpeter*, 1960), and then refined further to include collisions (*Dougherty and Farley*, 1963) and a magnetic field (*Farley et al.*, 1961; *Fejer*, 1961; *Hagfors*, 1961; *Rosenbluth and Rostoker*, 1962; *Salpeter*, 1961a). Using the parameters derived from ISR radio wave echoes, one can infer changes in the motion in the neutral atmosphere, and electric fields (*Evans*, 1972). This section first highlights the differences between incoherent and coherent scatter, and then discusses IS spectra. Lastly, IS spectral features are discussed in a general sense.

3.1.1 Incoherent Scatter versus Coherent Scatter

When an electromagnetic wave interacts with a cloud of quasi-neutral plasma, the incident electric field of the transmitted pulse wave accelerates the charged particles, which then emit scattered radiation at a Doppler shifted frequency. Letting the position of the charged particle be described by $\mathbf{r}(t')$ and the velocity by $\mathbf{v}(t')$ (note, $\mathbf{r}(t') = \mathbf{r}(0) + \mathbf{v}t'$), consider a plane monochromatic wave incident on a charged particle, where the electric field incident on the particle is described by:

$$\mathbf{E}_i(\mathbf{r}, t') = \mathbf{E}_{i0} \cos\left(\mathbf{k}_i \cdot \mathbf{r} - \omega_i t'\right) \tag{3.1}$$

and the magnetic field is given by:

$$\mathbf{B}_i(\mathbf{r}, t') = \hat{\imath} \times \mathbf{E}_i \tag{3.2}$$

where E_{i0} is amplitude of the electric field, $\mathbf{k}_i$ is the incident wavevector, ω_i is the incident frequency, and $\hat{\imath}$ is the direction of the incident radiation. The electric field at a distance R from the charge at a time t is related to the behavior of the charge at the previous time t', the retarded time, given by:

$$t' \approx t - \frac{R'}{c} \tag{3.3}$$

where c is the speed of light. Meanwhile, the radiation of a moving charge is given by:

$$\mathbf{E}(\mathbf{R}', t) = q\left[\frac{(\hat{s} - [\mathbf{v}/c])(1 - [\mathbf{v}/c]^2)}{(1 - \hat{s} \cdot [\mathbf{v}/c])^3 R'^2}\right]_{\text{ret}} + \frac{q}{c}\left[\frac{\hat{s} \times \{(\hat{s} - [\mathbf{v}/c]) \times (1/c)(d\mathbf{v}/dt')\}}{(1 - \hat{s} \cdot [\mathbf{v}/c])^3 R'}\right]_{\text{ret}} \tag{3.4}$$

where $\hat{s}$ is from the observer to the charge (*Jackson*, 2007). The observing point is at a large distance from the charge compared to the length over which the motion of the charge is observed. Therefore the first term is negligible to the second term, R is approximately R', and:

$$t' \approx t - (|R - \hat{s} \cdot \mathbf{r}|/c) \tag{3.5}$$

For a low-velocity charge ($v/c \ll 1$) with no acceleration other than that due to $\mathbf{E}_i$ acting on the charged particles, the scattered electric field by a single free charge is thus given by:

$$\mathbf{E}_s(R,t) = \frac{q^2}{c^2 m R}\left[\hat{s} \times (\hat{s} \times \mathbf{E}_{i0})\right] \cos\left[k_s R - \omega_s t - (\mathbf{k}_s - \mathbf{k}_i) \cdot \mathbf{r}(0)\right] \tag{3.6}$$

where m is the mass of the charge, and the charge radiates a Doppler-shifted electromagnetic wave whose frequency and wavevector are:

$$\omega_s = \omega_i \frac{(c - \hat{\imath} \cdot \mathbf{v})}{(c - \hat{s} \cdot \mathbf{v})} \tag{3.7}$$

and

$$\mathbf{k}_s = \frac{\omega_s}{c}\hat{s} \tag{3.8}$$

Note that the shift in frequency and wave number is given by:

$$\mathbf{k} = \mathbf{k}_s - \mathbf{k}_i \tag{3.9}$$

and

$$\omega = \omega_s - \omega_i = (\mathbf{k}_s - \mathbf{k}_i) \cdot \mathbf{v} \tag{3.10}$$

From Equation 3.6 it is clear that the magnitude of the electric field scattered in the ionosphere by ions is negligible compared to the field scattered by electrons, due to the considerably lighter mass of electrons. This scattered radiation, or “echo”, is then intercepted by the ISR and analyzed to probe ionospheric parameters (described in more detail in Section 3.1.2 and 3.2.2).

In a conductor such as a plasma, electrons surround and shield a positive charged particle from electric fields. The radius of this shield is called the Debye length and is derived by finding the total potential that results from a point charge in a “swarm” of moving charges that are being attracted and repelled by the point charge. Following *Ichimaru* (1973), we can derive the Debye sphere using Poisson’s equation, where the point charge is expressed as a delta function charge density and the charge density of the charges being attracted and repelled is $\langle \rho(\mathbf{r}) \rangle$:

$$\nabla^2 \phi_E(\mathbf{r}) = -\frac{q_0}{\epsilon_0}\delta(\mathbf{r}) - \frac{1}{\epsilon_0}\langle \rho(\mathbf{r}) \rangle \tag{3.11}$$

where ϕ_E is the potential, q_0 is the charge of the point charge, and ϵ_0 is the permittivity of free space. The statistical distribution of charges around the point charge is based on a thermodynamical equilibrium $\exp(-U/k_BT_e)$ arrangement about the mean, meaning:

$$\langle\rho(\mathbf{r})\rangle = en_e - en_e \exp\left(\frac{-U}{k_BT_e}\right) \tag{3.12}$$

where U is the electrostatic potential energy. For electrons, $U = -e\phi_E$. So :

$$\langle\rho(\mathbf{r})\rangle = -en_e \left[\exp\left(\frac{e\phi_E}{k_BT_e}\right) - 1\right] \tag{3.13}$$

For ordinary plasmas, the potential energy is much smaller than the kinetic energy. Therefore:

$$\langle\rho(\mathbf{r})\rangle = -en_e \left[1 + \left(\frac{e\phi_E}{k_BT_e}\right) - 1\right] \tag{3.14}$$

So, from Equation 3.11:

$$\nabla^2\phi_E = -\frac{q_0}{\epsilon_0}\delta(\mathbf{r}) + \frac{n_e e^2 \phi_E}{\epsilon_0 k_B T_e} \tag{3.15}$$

This resulting equation has the screened Coulomb potential as a solution:

$$\phi_E = \frac{q_0}{r}e^{-\eta r} \tag{3.16}$$

where:

$$\eta = \sqrt{\frac{n_e e^2}{\epsilon_0 k_B T_e}} = \frac{1}{\lambda_D} \tag{3.17}$$

and λ_D is the Debye length for electrons:

$$\lambda_D = \sqrt{\frac{\epsilon_0 k_B T_e}{n_e e^2}} \tag{3.18}$$

This shielding is such that the total charge rapidly goes to zero for distances larger than the Debye length, meaning that Coloumb interactions do not extend much beyond the Debye length due to the screening of a central charge by surrounding charges.

When an ionospheric radar probes inside of the Debye sphere (i.e. the radar wavelength is much less than a Debye length) there is no constructive interference or collective features. In that case instead, the radiation scattered from the electrons is randomly phased. This is often referred to as "incoherent scatter" (*Sheffield*, 1975) and it describes electrons traveling freely and independently. William E. Gordon, who pioneered ISRs, originally assumed ISRs would be subject to this form of scatter (*Gordon*, 1958). However, ISRs instead probe outside of the Debye sphere (i.e. the radar wavelength is much larger than a Debye length). This means that

ISRs probe electron clouds around ions, themselves subject to collective structures like ion-acoustic waves. As a result the radiation scattered from the electrons depends on their phase in large-scale waves. This is referred in the present context as "coherent scatter" meaning electrons that are organized in structures. At low frequencies the electrons are orbiting and shielding ions and reveal ion structures [*Chen* (2006), Chapter 1]. When a plane wave transmitted by an ISR is incident on ionospheric plasma where the ions are structured by plasma wave irregularities (e.g. sound waves), the electrons shielding those ions produce coherent scatter [(*Sheffield*, 1975), Chapter 1]. Due to constructive interference, signals backscattered from irregularities with a spacing of half the radar wavelength in the direction towards the radar produce signals that are in phase and can be detected. In other words, a radar of wavelength λ will effectively single out irregularities of wavelength $\lambda/2$ along the radar beam from the scattering medium in backscattering experiments.

All ISR's are extracting a spectrum from the stable waves present in the ionospheric plasma. Near thermodynamical equilibrium low frequency ion-acoustic waves and high frequency electron plasma waves can be probed. These waves dominate the plasma because they decay more slowly than other waves and are constantly excited by thermal broadband noise (these waves produce the ion and plasma lines, discussed further in Section 3.1.2). Alternatively, unstable plasmas can produce large amplitude waves that are detectable by low power radars. These unstable structures are usually field-aligned, meaning that they are only visible perpendicular to the magnetic field.

It is worth clarifying that even though ISRs examine coherent scatter, there still exist Coherent Scatter Radars (CSRs) which also examine coherent scatter (*Häggström*, 2012). The biggest difference between CSRs and ISRs is that the latter probe the much smaller wave amplitudes from stable plasmas in near thermal equilibrium. For this reason, ISRs use much more power than CSRs (∼10 kW, while ISRs operate at roughly ∼1 MW) [*Hagfors* (1995), Chapter 1]. CSRs also generally observe field aligned irregularities because all the other waves decay more rapidly.

3.1.2 Spectra

In general, ISRs probe all kinds of ionospheric waves that may or may not be affected by the magnetic field or by collisions, but for most situations it is possible to ignore both the magnetic field and collisional effects in spectral formulations. When the effect of collisions is neglected (generally appropriate above 105 km altitude), the general expression for an arbitrary backscatter spectrum, $S(\mathbf{k}, \omega)$, from an unmagnetized, low-temperature, singly-ionized plasma is given by [*Sheffield* (1975), Chapter 7]:

$$S(\mathbf{k}, \omega) = \frac{2\pi}{k} \left| \frac{1 + G_i}{\epsilon} \right|^2 g_{0e} \left(\frac{\omega}{k} \right) + \frac{2\pi}{k} \left| \frac{G_e}{\epsilon} \right|^2 g_{0i} \left(\frac{\omega}{k} \right), \tag{3.19}$$

where g_{0i} and g_{0e} are the one-dimensional velocity distributions of ions and electrons, respectively, evaluated at the velocity $\mathbf{k}\omega/k^2$, and G_e and G_i are the electron and ion dielectric functions, respectively, and where ϵ is the longitudinal dielectric function given by:

$$\epsilon(\mathbf{k}, \omega) = 1 + G_e(\mathbf{k}, \omega) + G_i(\mathbf{k}, \omega), \tag{3.20}$$

The electron dielectric function is given by:

$$G_e(\mathbf{k}, \omega) = \frac{4\pi e^2 n_{e0}}{m_e k^2} \int_{-\infty}^{+\infty} d\mathbf{v} \frac{\mathbf{k} \cdot \dfrac{\partial f_{0e}}{\partial \mathbf{v}}}{\omega - \mathbf{k} \cdot \mathbf{v} - i\gamma} \tag{3.21}$$

and for the singly ionized species of interest here, the ion dielectric function is given by:

$$G_i\left(\mathbf{k}, \omega\right) = \frac{4\pi e^2 n_{i0}}{m_i k^2} \int_{-\infty}^{\infty} d\mathbf{v} \frac{\mathbf{k} \cdot \dfrac{\partial f_{0i}}{\partial \mathbf{v}}}{\omega - \mathbf{k} \cdot \mathbf{v} - i\gamma}, \tag{3.22}$$

where γ is asymptotically small, real, and positive, and is used to describe analytically continuous functions that give rise to Landau damping effects. In these expressions n_{i0} and n_{e0} are the ion and electron number densities, respectively, and f_{0i} and f_{0e} are the normalized ion and electron velocity distributions, respectively. Defining the x-direction to be along the scattered wavevector, the above is rewritten as:

$$G_\kappa\left(k, \omega\right) = \frac{\omega_{p\kappa}^2}{k^2} \int_{-\infty}^{\infty} dv_x \frac{k \dfrac{\partial g_{0\kappa}}{\partial v_x}}{\omega - k v_x - i\gamma}. \tag{3.23}$$

where $\omega_{p\kappa}$ is the plasma frequency of species κ, i.e., $\omega_{p\kappa}^2 = 4\pi n_{\kappa 0}e^2/m_\kappa$. The analytical solution for a Maxwellian velocity distribution is given by (*Sheffield*, 1975):

$$G_{\kappa M} = \alpha^2 \frac{T_e}{T_\kappa}\left[1 - 2x_\kappa \exp\left(-x_\kappa^2\right)\int_0^{x_\kappa}\exp(p^2)dp - x_\kappa i\pi^{1/2}\exp(-x_\kappa^2)\right]. \tag{3.24}$$

where $\alpha = 1/(k\lambda_D)$, $x_\kappa = \omega/(kv_{th\kappa})$, and $v_{th\kappa}$ is the thermal speed. Note that this treatment implies that the eigenfrequency must have an imaginary part that describes a decaying wave, so that ϵ has complex roots and is not zero. Otherwise, if the root is real and it matches the radar frequency, ϵ becomes zero and the amplitude in Equation 3.19 becomes infinite. This highlights the fact that the analysis refers to damped waves only, and not even waves with a zero growth rate. The spectrum becomes truly incoherent when α approaches 0 (for coherent scattering $\alpha \geq 1$) and Equation 3.19 becomes:

$$S(\mathbf{k},\omega)|_{\alpha\to 0} \to \frac{2\pi}{k} f_{e0}\left(\frac{\omega}{k}\right) \tag{3.25}$$

which simply states that the spectrum would reveal the electron velocity distribution along the line-of-sight through the superposition of individual Doppler shifts.

In general for $\alpha \neq 0$ and for a Maxwellian distribution function applicable to plasmas in near thermal equilibrium, $S(\mathbf{k},\omega)$ becomes:

$$S(\mathbf{k},\omega) = \frac{2\pi^{1/2}}{ka}\left\{\frac{A_e}{|\epsilon|^2} + \frac{A_i}{|\epsilon|^2}\right\} \tag{3.26}$$

where a is the electron thermal speed, and A_κ are given by:

$$A_e = \exp\left(-x_e^2\right)\left[\left(1 + \alpha^2\frac{T_e}{T_i}\mathrm{R}w(x_i)\right)^2 + \left(\alpha^2\frac{T_e}{T_i}\mathrm{I}w(x_i)\right)^2\right] \tag{3.27}$$

and

$$A_i = \left(\frac{m_i T_e}{m_e T_i}\right)^{1/2}\exp\left(-x_i^2\right)\left[\left(\alpha^2\mathrm{R}w(x_e)\right)^2 + \left(\alpha^2\mathrm{I}w(x_e)\right)^2\right] \tag{3.28}$$

and:

$$|\epsilon|^2 = \left[1 + \alpha^2\left(\mathrm{R}w(x_e) + \frac{T_e}{T_i}\mathrm{R}w(x_i)\right)\right]^2 + \left[\alpha^2\mathrm{I}w(x_e) + \frac{\alpha^2 T_e}{T_i}\mathrm{I}w(x_i)\right]^2 \tag{3.29}$$

where Rw is the real component of the plasma dispersion relation (*Fried and Conte*, 1961):

$$\mathrm{R}w(x) = 1 - 2x\exp(-x^2)\int_0^x \exp(p^2)dp \tag{3.30}$$

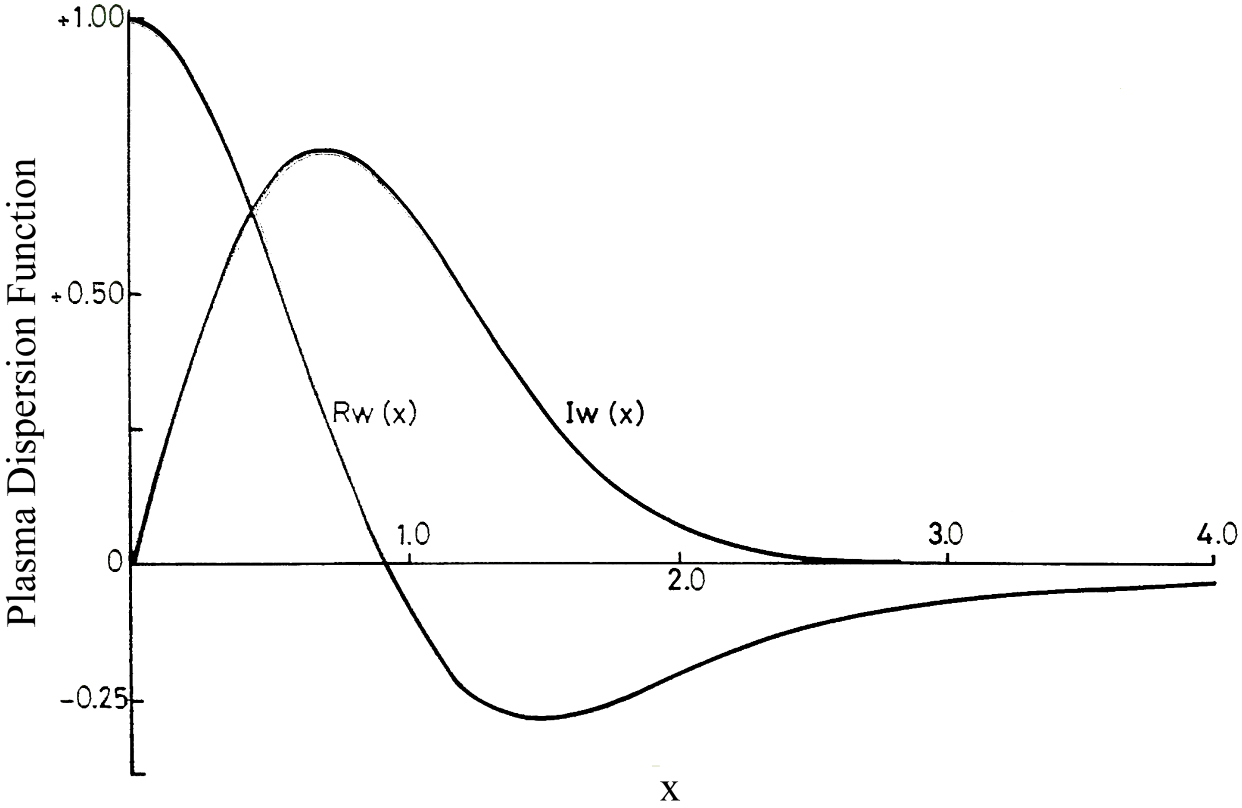

Figure 3.1: Real and imaginary components of the plasma dispersion function [(*Sheffield*, 1975), Chapter 7].

and Iw is the imaginary component of the plasma dispersion relation:

$$\mathrm{I}w(x) = \pi^{1/2} x \exp(x^2) \tag{3.31}$$

Figure 3.1 shows both the real and imaginary components of the plasma dispersion function.

An example of backscatter spectrum from a Maxwellian velocity distribution is given in Figure 3.2. At higher Doppler-shifted frequencies, x_i approaches infinity, $A_i/|\epsilon|^2$ approaches zero, and x_e is small, leaving Equation 3.26 largely dependent on $A_e/|\epsilon|^2$. This produces the "electron lines", and under appropriate conditions it is possible to observe that they consist of two sets of symmetric pairs of resonance lines at different offsets from the center frequency, called the "plasma line" and the "gyro line" (see below). Meanwhile, at lower frequencies $A_i/|\epsilon|^2$ is greater when the electron to ion temperature ratio is approximately 1 and $A_e/|\epsilon|^2$ is greater when the electron to ion temperature ratio is much greater than 1. This is the "ion line" (*Sheffield* (1975), Chapter 7). These spectral peaks are affiliated

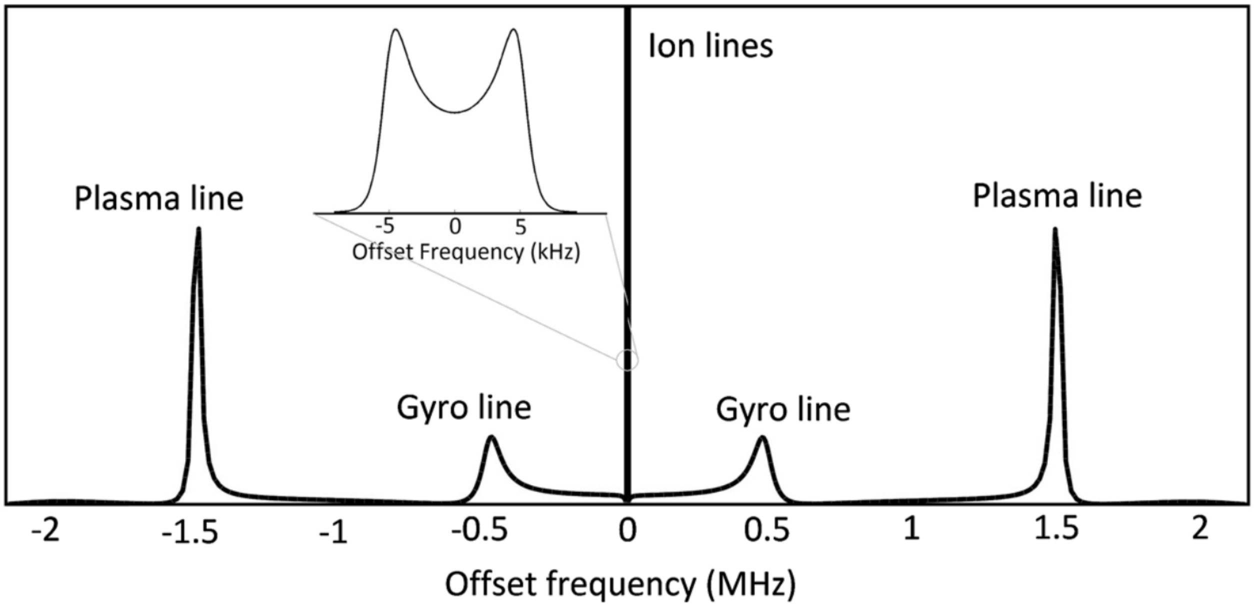

Figure 3.2: An example of a backscatter spectrum received by an ISR (*Akbari et al.*, 2017a).

with the solutions to the electrostatic dispersion relation of cold magnetized plasmas: the ion acoustic mode for the ion line, and upper hybrid/Langmuir mode for the plasma line (*Bernstein*, 1958; *Gross*, 1951; *Landau*, 1946; *Perkins et al.*, 1965; *Salpeter*, 1960, 1961a; *Sedgemore-Schulthess and St-Maurice*, 2001). The height and width of these lines depends on the intensity and the damping rate of the corresponding waves, and various scattering processes. The displacements of the lines from the radar transmitting frequency depend on the Doppler shift associated with the waves phase velocity, where positive shifts indicate the wave is propagating towards the radar and negative shifts indicate the wave is propagating away.

In most of the work done with ISRs the ion line is used. Since the ion line is produced by Bragg scattering from ion-acoustic waves it is controlled by the ion thermal motion and from collisionless Landau damping, a process in which a particle tends to synchronize their velocity to the wave phase velocity. Landau damping broadens the frequencies of two independent peaks, causing them to overlap and create a double-humped shape. The vertical distance from the tip of the peak to the bottom of the trough in Figure 3.3 depends on the electron to ion temperature ratio, which further relates to the inference of Landau damping. As the electron temperature increases, larger peaks appear and the trough becomes deeper (*Ichimaru*, 1973).

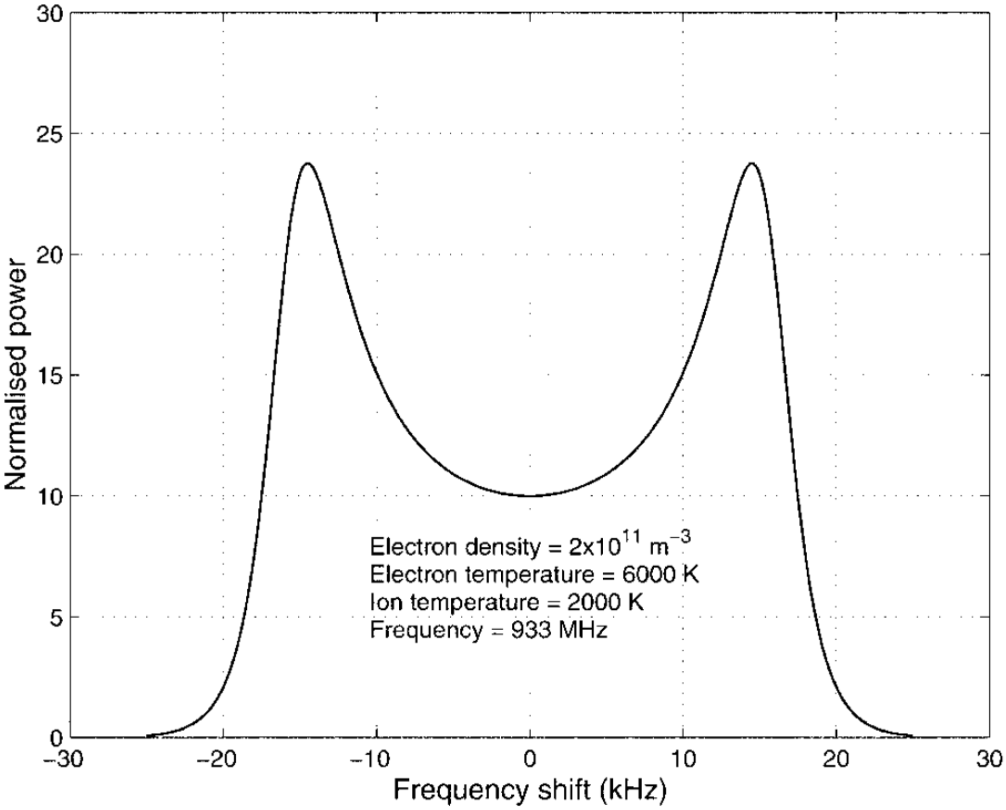

Figure 3.3: An example of the ion line in a backscatter spectrum received by an ISR (*Sedgemore-Schulthess and St-Maurice*, 2001).

In some instances, the electron temperature is so much greater than the ion temperature that two well-developed, almost separate, peaks occur (*Wickwar et al.*, 1981). Conversely, when the electron temperature is equal to the ion temperature, as expected at lower altitudes due to strong collisional coupling, there is only one large hump instead of two peaks and a trough. The ion acoustic speed is found through the ion line displacement, given by $\omega = \pm C_s k$, where C_s is the ion acoustic speed. The shift of the central frequency from the signal to the echo reflects the Doppler shift, which infers the line-of-sight ion velocity. Lastly, the integrated spectral power is approximately equal to $n_e/(1 + T_e/T_i)$, which allows the electron density to be extracted (given that the electron to ion temperature ratio is determined from the spectral shape).

Below 110 km, where the effect of ion-neutral collisions is significant (*Hagfors and Brockelman*, 1971), it is also possible to derive the ion-neutral collision frequency from the width of the ion line (e.g. *Wand and Perkins* (1968)). Through ion-neutral collisions the motion of the ion density fluctuations changes, making the power spectrum narrower (*Dougherty and Farley*, 1963). However, to calculate the ion-neutral collision frequency it is generally assumed that the ion and electron temperatures are equal, which is not always correct and restricts these studies to relatively low electric field values.

There are two important complications that need to be addressed with the spectral calculations presented so far. The first is that Equation 3.24, as well as the general spectral treatment performed in Equations 3.26 to 3.31, require the ion velocity distribution to be Maxwellian. However, during strong electric fields the velocity distribution evolves towards a toroidal distribution. In these cases, the analysis presented in Equations 3.19 through 3.23 must be calculated based on a toroidal description of the ion distribution function. This becomes particularly complicated for Equations 3.21, 3.22 and 3.23, given the integrations needed and the lack of accurate, complete descriptions of distorted ion velocity distributions. This work is done in Chapter 4.

The second complication that must be addressed is that the spectral calculations presented so far are incorrect when the line-of-sight is perpendicular or near perpendicular to the magnetic field. Within 3° of perpendicularity to the magnetic field, ISR spectra are dramatically different than those found at any other angle, as is shown in Figure 3.4 (e.g., *Sheffield*, 1975; *Woodman*, 2004, and references therein). This is because parallel to the magnetic field electrons are highly mobile and are able to form clouds around low frequency ions which are not moving (relative to the much lighter electrons) and are attached to the magnetic field. Perpendicular to the magnetic field, the electron velocity is roughly equal to, or less, than that of the ions because the electrons gyrate tightly around the geomagnetic field lines. This motion makes the electrons look heavier than the ions perpendicular to the magnetic field, making the low frequency portion of the IS spectra in that direction narrower than at any other angle (*Woodman*, 1967, 1971). These aspect angles also show the gyro line, affiliated with electron magnetization and the lower hybrid/whistler mode solution to the electrostatic dispersion relation of cold magnetized plasmas.

When the effect of the magnetic field on the motion of charged particles matter, the spectral formulations seen previously (Equations 3.19 to 3.23) become instead (*Bernstein*,

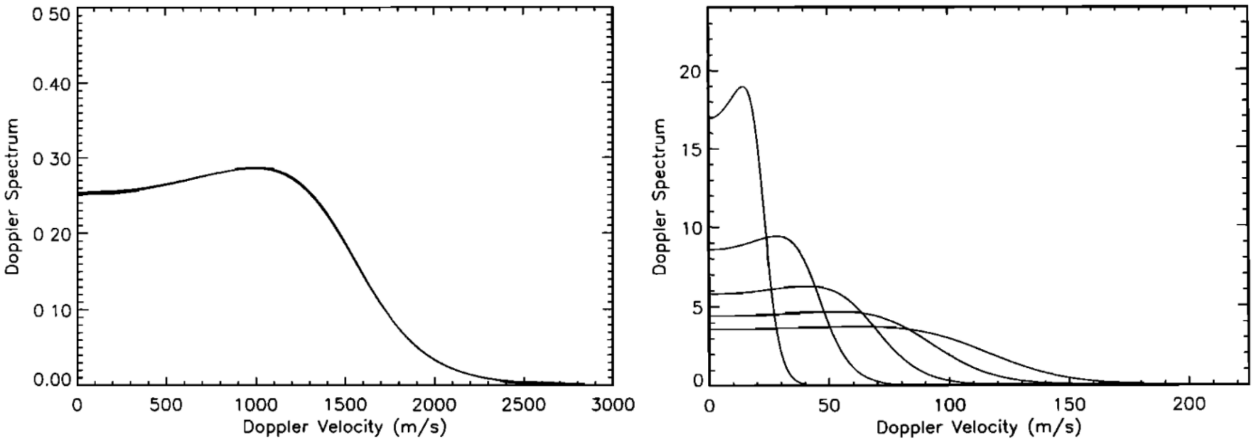

Figure 3.4: Incoherent scatter Doppler spectra from O$^+$ plasma above the Jicamarca Radio Observatory from (*Kudeki et al.*, 1999). All the curves possess an ion and electron temperature of 1000 K, and a radar carrier frequency of 50 MHz. Letting β be the angle between the radar wavevector and perpendicularity to the magnetic field, the panel on the left shows spectra from $\beta = 30°$, $\beta = 60°$, and $\beta = 90°$ (they are superimposed and indistinguishable at the scale of the plot). The panel on the right is the same as the panel on the left, but with $\beta = 0.005°$, $\beta = 0.01°$, $\beta = 0.015°$, and $\beta = 0.02°$. The tallest curve corresponds to $\beta = 0.005°$ and the broadest curve to $\beta = 0.02°$. Note the scale change between the left and right panels.

1958; *Dougherty and Farley*, 1963; *Farley et al.*, 1961; *Salpeter*, 1961a,b):

$$S(\mathbf{k},\omega) = 2\lim_{\gamma\to 0}\left|\frac{1+H_i}{\epsilon_L}\right|^2 \int_{-\infty}^{+\infty} \frac{d\mathbf{v}\sum_l J_l^2(k_\perp\rho_e) f_{0e}(\mathbf{v})}{(\omega - k_{||}v_{||} - l\Omega_e)^2+\gamma^2} + \left|\frac{H_e}{\epsilon_L}\right|^2 \int_{-\infty}^{+\infty} \frac{d\mathbf{v}\sum_m J_m^2(k_\perp\rho_i) f_{0i}(\mathbf{v})}{(\omega - k_{||}v_{||} - m\Omega_i)^2+\gamma^2} \tag{3.32}$$

The longitudinal dielectric function is now:

$$\epsilon_L(\mathbf{k},\omega) = 1 + H_e(\mathbf{k},\omega) + H_i(\mathbf{k},\omega) \tag{3.33}$$

and the ion and electron dielectric functions are:

$$H_i(\mathbf{k},\omega) = \frac{4\pi e^2 n_{i0}}{m_i k^2}\int_{-\infty}^{+\infty} d\mathbf{v}\sum_m \frac{J_m^2(k_\perp\rho_i)\mathbf{k}\cdot\dfrac{\partial f_{0i}}{\partial\mathbf{v}^*}}{\omega - k_{||}v_{||} - m\Omega_i - i\gamma} \tag{3.34}$$

and

$$H_e(\mathbf{k},\omega) = \frac{4\pi e^2 n_{e0}}{m_e k^2}\int_{-\infty}^{+\infty} d\mathbf{v}\sum_l \frac{J_l^2(k_\perp\rho_e)\mathbf{k}\cdot\dfrac{\partial f_{0e}}{\partial\mathbf{v}^*}}{\omega - k_{||}v_{||} - l\Omega_e - i\gamma} \tag{3.35}$$

where J is a Bessel function, $k_\perp$ is the perpendicular component of $\mathbf{k}$, $k_{||}$ is the parallel component of $\mathbf{k}$, $v_{||}$ is the parallel component of $\mathbf{v}$, ρ_e is the electron cyclotron radius, ρ_i is the ion cyclotron radius, and $\mathbf{k}\cdot\dfrac{\partial F_{0q}}{\partial\mathbf{v}^*} \equiv k_{||}\dfrac{\partial F_{0q}}{\partial v_{||}} + \dfrac{1}{\rho_q}\dfrac{\partial F_{0q}}{\partial v_\perp}$. It is important to note that these expressions reduce to the expressions seen earlier when they are applied to any direction more than

5° away from perpendicularity to the magnetic field. Additionally, it should be mentioned that these spectral formulations are for a stable plasma near thermodynamic equilibrium, and that large amplitude (i.e. linearly unstable) waves are often seen perpendicular to the magnetic field, in which case there is no predictable spectral behavior.

At any rate, for the present work, the impact of magnetization is not taken into consideration because it only applies to a small range of aspect angles that are not easily accessible at high latitudes. Still, it should be remembered that when the spectral analysis in Chapter 4 is describing angles perpendicular to the magnetic field, it actually represents spectra closer to 85°.

3.2 Technical Aspects of ISRs

The previous section has discussed ISRs theoretically and from the perspective of plasma physics. However, ISR observations and studies are also quite technically involved. This section highlights several technical aspects of ISRs, including the antenna design and the properties of ISR signals and echoes.

3.2.1 Antennas Designs: Dishes vs Phased Arrays

Since ISRs typically only receive about 200^{+} dB attentuation of the power transmitted, it is incredibly important to have a large, well-designed antenna. There are two antenna designs used by ISRs: 1) dish and 2) phased array. A dish antenna is simply a large single parabolic dish that emits and receives radio signals. This design is used by such ISRs as the Arecibo ISR, the Millstone Hill ISR, the European Incoherent SCATter scientific association (EISCAT) ISRs, and the Sondrestrom ISR. Meanwhile, a phased array is made of a collection of numerous smaller element antennas. An array design is used by the Jicamarca ISR, as well as the three AMISR sites. A single dish antenna is able to point at many positions in the sky, but has to integrate at each position before moving, since the power has to be concentrated at one location. Meanwhile, a phased array antenna, such as one seen at an AMISR site, has a field-of-view that is ±20° from a fixed direction, and performs a simultaneous integration over multiple positions.

Although there are many important differences between these two types of antennas, arguably one of the biggest differences is how they "look" in different directions. A dish antenna collects data from different directions by physically moving and/or turning. However, a phased array antenna collects data from any direction within their field-of-view by varying the phasing of the different elements, therefore modifying the radiation pattern to be maximized or minimized in certain directions (*Chau et al.*, 2012). Since phased array designs use pulse-to-pulse beam positioning and do not need to physically move, they are able to look in multiple directions much more quickly than dish antennas. Additionally, inertia-less steering requires less infrastructure, increases spatial sampling flexibility, reduces spatial and temporal ambiguities in data, removes antenna dwell times and predetermined integration periods, and also opens possibilities for in-beam imaging through interferometry (*Chau et al.*, 2012). These features also allow for remote operations, graceful degradation, and continual operations. Phased arrays also possess distributed, solid-state transmitters as opposed to single radio frequency sources, meaning the warm-up time is reduced, there is no need for a complex feed system, and single-point failures are less frequent. These differences are likely why ISRs developed more recently are generally phased array designs.

3.2.2 ISR Signal and Echo Properties

Since ISRs send signals that probe large groups of charged particles, the echoes detected by these radars are different than those that observe a single hard target. An ISR echo contains a range of shifted frequencies, instead of a single shifted frequency (as would be seen with a single hard target), due to thermal fluctuations within the plasma. These fluctuations contain (among other things) features associated with ion-acoustic waves driven by random motions within the plasma. This motion, occurring in a group of charged particles moving with a variety of line-of-sight velocities with respect to the radar wavevector, causes a wide spectrum of waves (*Sedgemore-Schulthess and St-Maurice*, 2001). This means that when a radar sends out a radio wave into the atmosphere, it receives more than one Doppler shifted frequency because the waves move about the mean Doppler shift. The radar then recovers the waves that decay the least, namely the ion acoustic waves at lower frequencies (*Sheffield et al.*, 2010).

Knowing how the different plasma parameters relate to the different spectral shapes and offsets, Equation 3.26 can be fit to the received spectrum using a chi squared function:

$$\chi^2 = \sum_{j=1}^{n} \frac{|y(x_j) - \text{model}(x_j; \mathbf{p})|^2}{\sigma_j^2} \tag{3.36}$$

where y is the data, $\mathbf{p}$ is the parameter vector, x_j is the independent variable and σ_j is the uncertainty. By minimizing χ, the model comes closest to the data. This process is often simplified by assuming an ion composition, or by even using other instruments to approximate parameters. However, this process becomes complicated when large coherent echoes from large-scale irregularities contaminate ISR data and mask the desired spectrum.

Before transmitting a signal into the ionosphere, other instrumental factors affecting the spectral shape also must be considered. When a radar sends signals into the ionosphere it does not send a continuous stream of waves, but rather a "pulse" of waves, as shown in Figure 3.5. The size and frequency of the pulses (not the frequency of the waves) is determined by parameters such as the power and the desired range in order to maximize the attainable signal-to-noise when both the signal and the noise are applied to the input. The pulse phase is used to determine the Doppler shift of the measurements, the pulse length determines the range resolution of the measurements, and the amplitude, determined by the transmitted power, relates to the received power.

An important factor in pulse coding is ambiguity, which is a distortion in the returned pulse introduced by the receiver matched filter (*Woodward*, 2014). More precisely, it is the absolute value of the output envelope of a matched filter when the input is a Doppler shifted echo of the original signal (*He et al.*, 2012):

$$|X(\tau_d, f)| = \left| \int_{-\infty}^{\infty} u(t)u^*(t - \tau_d) \exp(j2\pi f t) dt \right| \tag{3.37}$$

where $u(t)$ is a complex envelope of the signal, τ_d is the additional time delay, and f is the frequency shift. An example is shown in Figure 3.6, which displays the ambiguity related to sensing a hard target with an uncoded pulse. In Figure 3.6, the Doppler domain is rather narrow, and the range domain is more spread out. This means that when there is a Doppler-shifted, point target return at 0 kHz there will be a central peak and little ambiguity in the Doppler shift. However, the range will have a larger ambiguity if the Doppler shift is 50kHz because there is no clear peak there.

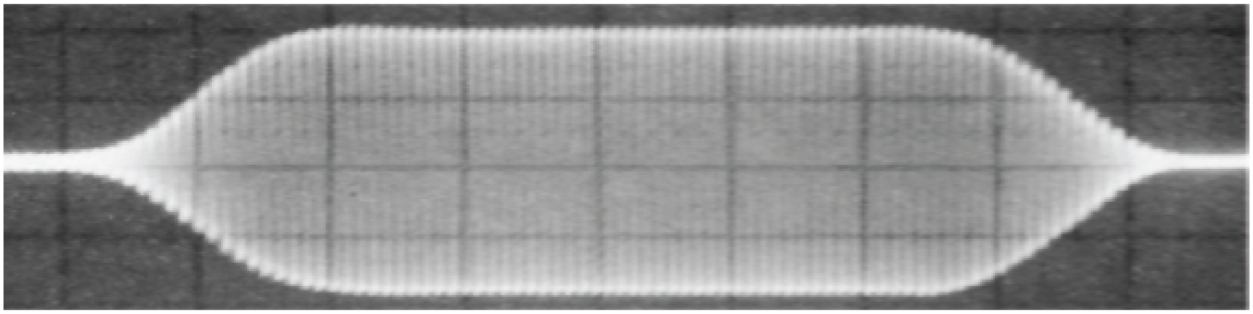

Figure 3.5: A single pulse sent out from a radar containing waves (*Semeter*, 2012).

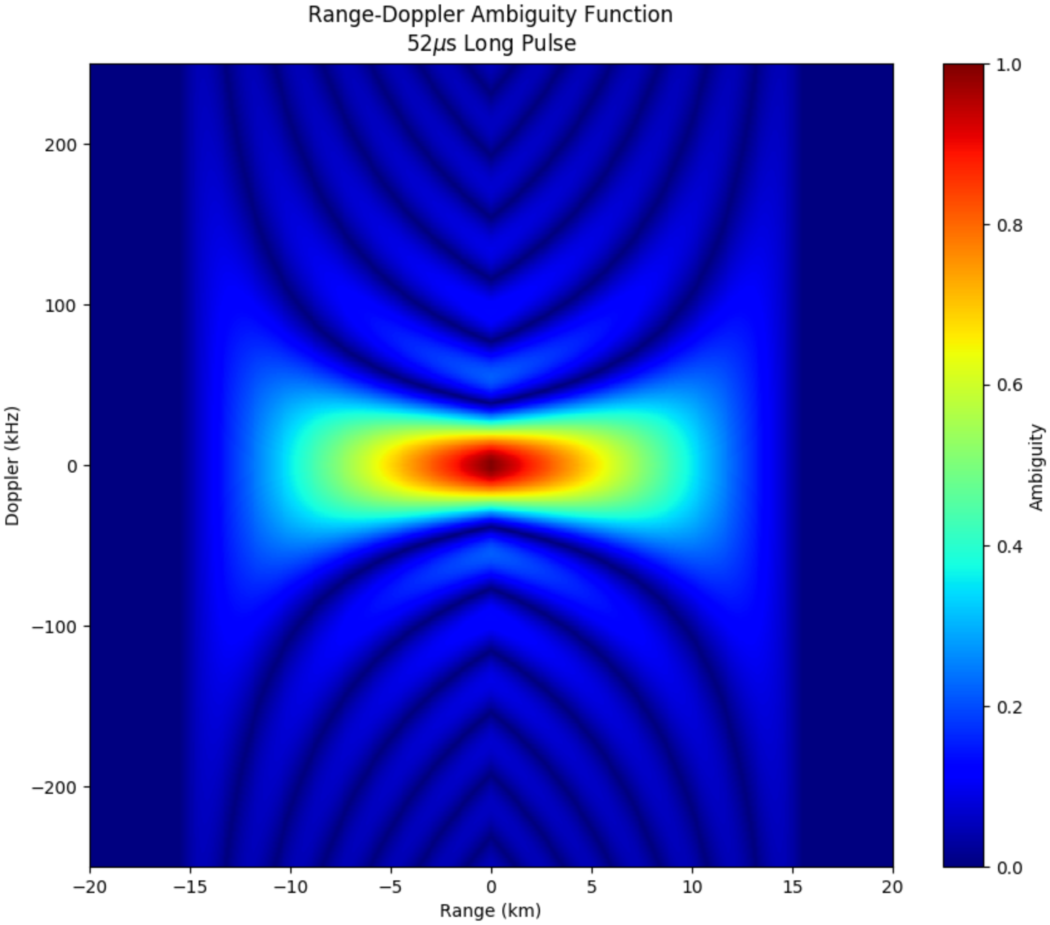

Figure 3.6: Ambiguity as a function of frequency and range for a 52 μs uncoded pulse (figure courtesy of Ashton Reimer).

Received noise, an unwanted addition to the signal received, also needs to be considered before a signal is transmitted. For example, the bandwidth of the ISR pulse affects the noise, and as the bandwidth increases, so does the noise. This means that if the pulse width is reduced to improve the range resolution, more noise appears (*Semeter*, 2012). However, the use of a "matched filter" can be used to help distinguish the signal from the noise.

3.2.3 AMISR and its characteristics

This research focuses on data from the three AMISR facilities, which are: 1) Resolute Bay Incoherent Scatter Radar-North (RISR-N) located near Resolute Bay, Nunavut, Canada, 2) Resolute Bay Incoherent Scatter Radar-Canada (RISR-C) located near Resolute Bay, Nunavut, Canada, and 3) Poker Flat Incoherent Scatter Radar (PFISR) located near Poker Flat, Alaska, United States, as seen in Figure 3.7. Figure 3.7 also shows that RISR-N and RISR-C are placed back-to-back, with RISR-N pointing northward into the polar cap, and RISR-C pointing southward over Canada. These ISRs are particularly valuable because they are some of the few ISRs to make use of a phased array design. The research presented in thesis is predominately from the RISR-N facility, therefore additional RISR-N specifications are given in Table 3.1.

.

In their typical operating modes, RISR-N, as well as RISR-C and PFISR, provide the line-of-sight ion temperature, $T_{i\phi}$, the electron temperature, the electron density, and the mean line-of-sight ion velocity, v_{ϕ}, as a function of Universal Time (UT), MLT, altitude, range, Magnetic LATitude (MLAT), corrected magnetic longitude, and aspect angle (the angle between the radar wavevector and the magnetic field). Within these parameters, uncoded (480 μs) and Alternating Code (AC) pulse measurements (*Lehtinen*, 1986) are generally taken, which vary in terms of volume of integration and the resulting noise level. Higher spatial resolution AC codes are necessary for altitudes like the E-region, where parameters change on scales of the order of a few kilometers. Given the regions being examined in the present work, the uncoded or "long" pulse measurements are typically used.

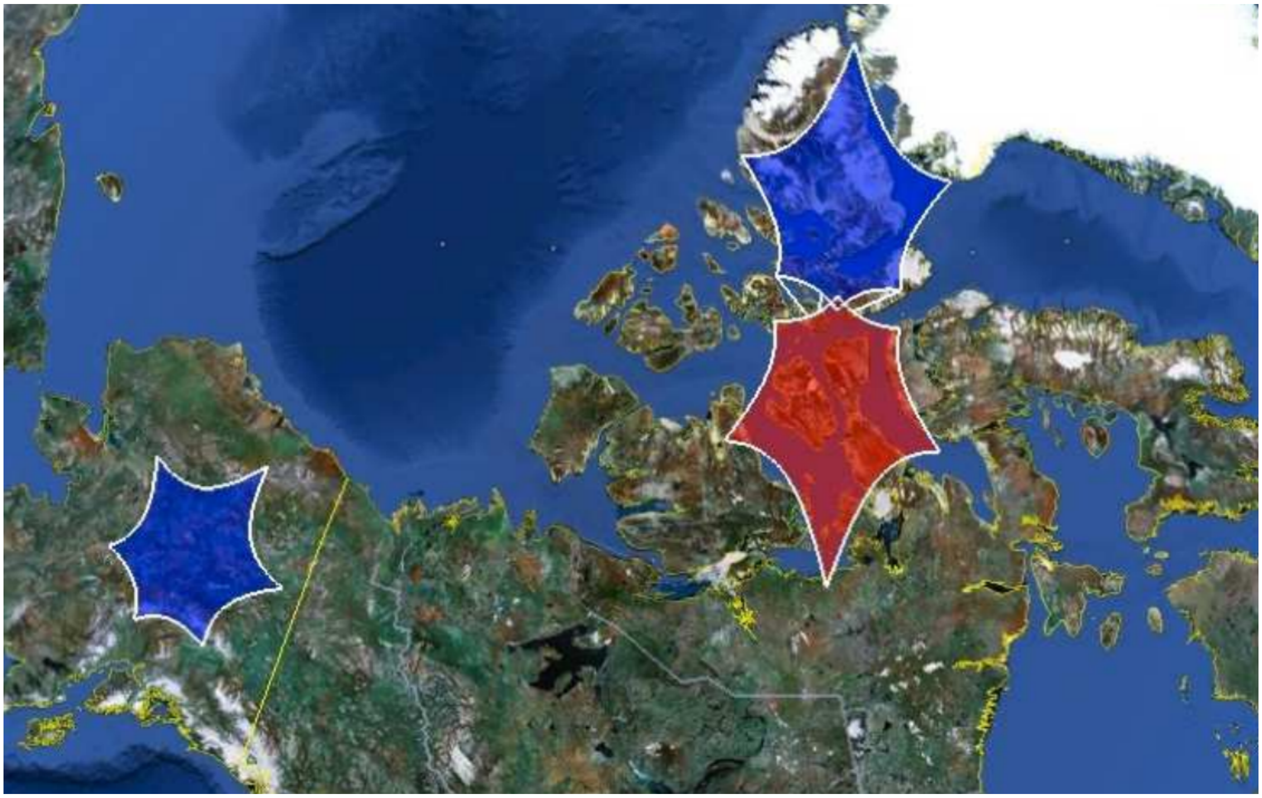

Figure 3.7: Field-of-view of the three Advanced Modular ISRs: RISR-N, RISR-C, and PFISR (*Varney*, 2016).

Location	74° 43’ 46” N, 94° 54’ 16” W
Geomagnetic Dip angle	88° 47’
Invariant Latitude	83° 37’ N
Local Time	UT - 6
Magnetic Local Time	UT - 7:45
Peak Power	2 MW
Maximum Duty Cycle	10%
Pulse Length	1 μsec - 2 msec
Transmission Frequency	430-450 MHz
Antenna Gain	Roughly 43 Decibels relative to an isotropic antenna
Antenna Aperture	Roughly 715 m^2
Beam Width	Roughly 1.1°
System Temperature	Roughly 120 K
Steering	Pulse to pulse over roughly ± 25°
Max Power Consumption	Roughly 700 KW
Plasma Parameters	n_e, T_e, $T_{i\phi}$, v_ϕ, ν_{in}

Table 3.1: Additional specification for RISR-N (*Varney*, 2016).

Chapter 4

INCOHERENT SCATTER SPECTRA BASED ON MONTE-CARLO SIMULATIONS OF ION VELOCITY DISTRIBUTIONS UNDER STRONG ION FRICTIONAL HEATING

Under strong electric fields conditions, the ion velocity distributions of weakly ionized high-latitude F-region plasma differ enough from a Maxwellian shape to introduce both ion temperature anisotropies and toroidal ion velocity distributions. This substantially changes ISR spectra and thus the analysis of those spectra, which rely on a Maxwellian description of the ion velocity distribution. Knowing this, *Akbari et al.* (2017b) used an empirical description of the ion velocity distribution and compared the resulting spectra to those found from a Maxwellian velocity distribution, as seen in Figure 4.1 (which also reflects a large change in the retrieved electron temperature when different ion velocity spectral fits are used). *Akbari et al.* (2017b) also used PFISR measurements along the magnetic field line from 3/3/2012 during a large electric field event, and found that at lower altitudes (approximately 130 km to 250 km) the line-of-sight ion temperature values obtained at relatively small aspect angles are consistent with the theoretical calculations of anisotropic NO^+ and N_2 ion velocity distributions that emerge from polarization elastic scattering, as seen in Figure 4.2. Meanwhile at higher altitudes (greater than 300 km), the IS spectra obtained at large aspect angles were qualitatively similar to those expected from toroidal ion velocity distributions, while the line-of-sight ion temperatures measured at low aspect angles exceeded those expected from ion-neutral frictional heating and RCE collisions by about 1000 K, suggesting Coulomb collisions could have been responsible for reducing the ion temperature anisotropy with altitude.

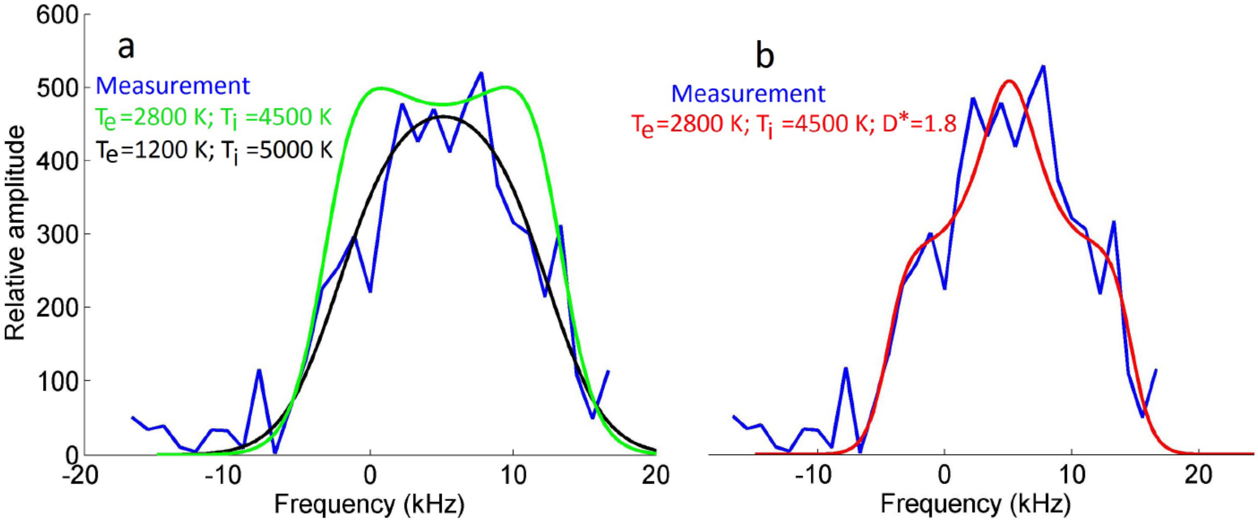

Figure 4.1: Measured and theoretical IS spectra that highlight the quality of fit using Maxwellian ion velocity distributions (left), as opposed to distorted ion velocity distributions of the kind discussed in *Raman et al.* (1981) (right). Data is taken from PFISR on 16/2/2015 at an aspect angle of 55°. Taken from *Akbari et al.* (2017b).

However, *Akbari et al.* (2017b) utilized an empirical description of the ion velocity distribution, which is strictly reliable only under limited conditions, like moderately strong electric fields. In order to provide a quantitative and reliable description of IS spectra for a range of electric fields and aspect angles, this study goes beyond the work of *Akbari et al.* (2017b) by directly using for the first time an advanced MC calculation of the ion velocity distribution to derive spectra. This study also fully characterizes the spectral shape, as well as the ion temperature and its anisotropy, for two different models of the RCE between O^+ and O, and includes a determination of the stability of the plasma against magnetic field-aligned electrostatic instabilities.

This chapter contains verbatim the work of "Incoherent scatter spectra based on Monte-Carlo simulations of ion velocity distributions under strong ion frictional heating", which has recently been accepted by *Radio Science*. Following the reproduction of the Radio Science publication is an additional section that utilizes the results of the research paper to further examine spectral features from toroidal ion velocity distributions. The supplementary material for "Incoherent scatter spectra based on Monte-Carlo simulations of ion velocity distributions under strong ion frictional heating" is provided verbatim in Appendix A and

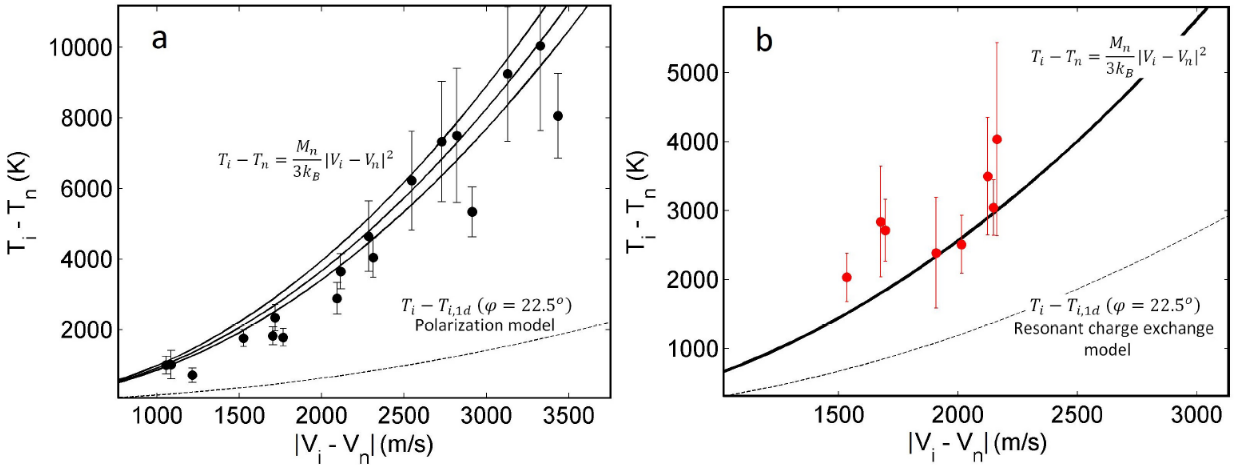

Figure 4.2: The line-of-sight ion temperatures parallel to the magnetic field, where the left panel is for measurements between approximately 130 km to 250 km and the right panel is for measurements between approximately 300 km and 400 km. The dotted lines show modifications applied to the one-dimensional temperatures in each panel (specifically, the expected difference between the line-of-sight ion temperatures at the aspect angle of 22.5° and the three-dimensional temperatures according to the appropriate collision models). The left panel has been modified based on the polarization scattering collision model, and the right panel by the resonant charge exchange collision model (in order to represent the three-dimensional ion temperatures). The solid black lines indicate theoretical curves of ion temperature with neutral temperature versus the relative drift between ions and neutrals, where the left panel shows O/N_2 composition ratios of 1/2.6, 1/1.35, 1/0.8 while the right panel only assumes 100% O. Taken from *Akbari et al.* (2017b).

refers to data files which are available online through *Radio Science*. Meanwhile, Appendix B gives additional material required for calculating spectra, and refers to data files which are available upon request. The authors and their respective institutions are:

- L. V. Goodwin (Institute of Space and Atmospheric Studies, Department of Physics and Engineering Physics, University of Saskatchewan, Saskatoon, Saskatchewan, Canada)
- J.-P. St.-Maurice (Institute of Space and Atmospheric Studies, University of Saskatchewan, Saskatoon, Saskatchewan, Canada)
- H. Akbari (Laboratory for Atmospheric and Space Physics, Boulder, Colorado, USA)
- R. J. Spiteri (Department of Computer Science, University of Saskatchewan, Saskatoon, Saskatchewan, Canada).

4.1 Abstract

Under strong electric field conditions often found at high latitudes, the ion velocity distribution of the weakly ionized F region plasma can differ enough from a Maxwellian shape to substantially change Incoherent Scatter (IS) spectra and thus the analysis of those spectra. With the goal to provide a quantitative and reliable description of the IS spectra, this study directly uses for the first time an advanced Monte-Carlo calculation of the ion velocity distribution to derive IS spectra for a range of electric fields and aspect angles. For most cases the spectra associated with NO^+ maintains a shape that closely resembles that of a spectrum derived from a Maxwellian distribution with the same line-of-sight ion temperature as the equivalent Monte-Carlo simulated distribution. This study also fully characterizes the spectral shape as well as the ion temperature and its anisotropy for two different models of the resonant charge exchange between O^+ and O. It confirms that the distortions from the Maxwellian shape can be substantial for this particular interaction. The distortions are also such that along the magnetic field direction, the extracted apparent electron temperature is always greater than the real temperature. This work also includes a determination of the stability of the plasma against magnetic field-aligned electrostatic instabilities. It is found that the NO^+ distribution is always stable, whereas the O^+ distribution may or may not

be stable, depending on the model chosen for the resonant charge exchange cross-section in collisions with the background atomic oxygen gas.

4.2 Introduction

Current Incoherent Scatter (IS) spectral analysis techniques rely heavily on the inference that ionospheric ion velocity distributions have a Maxwellian shape. However, it is well established that in the presence of strong electric fields the ion velocity distribution of the weakly ionized plasma at high latitudes can differ enough from a Maxwellian shape to substantially affect IS spectra (*Lockwood et al.*, 1987; *Raman et al.*, 1981; *Suvanto*, 1988; *Winser et al.*, 1987). This in turn is known to potentially seriously influence the analysis of those spectra and the retrieval of parameters such as the ion and electron temperatures (e.g. *Raman et al.*, 1981; *Suvanto*, 1988). Until now, studies of this topic have focused on a description of the ion velocity distribution based on a semi-empirical toroidal shape. These have proven to fit one-dimensional ion velocity distributions in the velocity plane perpendicular to the geomagnetic field but only for a limited range of conditions (*St-Maurice et al.*, 1976).

Owing in particular to the dependence of IS spectra on the derivative of the velocity distributions, a more precise description of the velocity distribution than has been characterized thus far has to be considered for the determination of IS spectra for the broad range of conditions pertaining to IS Radar (ISR) data. Most pointedly, aside from anisotropy considerations, no deviation from a Maxwellian has ever been considered, to our knowledge, for line-of-sight directions parallel or near-parallel to the magnetic field in spite of the frequent use of this direction to diagnose the various plasma properties of interest. As a typical example, in his analytical work on IS spectra based on non-Maxwellian signatures produced by the processes discussed in the present work, *Hubert* (1984) stated that at 27° to the magnetic field direction, the line-of-sight velocity distribution was ‘very nearly Maxwellian’. To remedy these shortcomings and provide the best possible tools to analyze IS spectra, results from a state-of-the-art Monte-Carlo (MC) simulation are used here to retrieve high-accuracy one-dimensional ion velocity distributions for any electric field, ion-neutral particle interaction, and direction relative to the magnetic field. From these simulated ion velocity distributions, an interpolation scheme is perfected to extract a precise characterization of the ion velocity distribution for up to two ion thermal speeds.

There are two main aspects to ion velocity distributions that must be kept in mind when strong frictional heating affects the ion velocity distribution through ion-neutral collisions. The first concerns the extent to which the distribution function is toroidal and how to characterize that toroidal shape. The second is the temperature anisotropy, which originates from the fact that during frictional heating events the temperature perpendicular to the magnetic field is greater than the temperature along the magnetic field. These are both discussed in greater detail in this section.

4.2.1 Toroidal nature of the ion velocity distribution

The toroidal shape of the ion velocity distribution is obtained when the ion collision to cyclotron frequency ratio is small, as is the case in the ionospheric F region. One example of a distorted ion velocity distribution is provided for a 150 mV/m electric field in Figure 4.3 based on the MC simulation that is used in the present work. Based on a simple Relaxation Collision Model (RCM) description of the ion-neutral collisions, distributions that are qualitatively similar to what are seen in Figure 4.3 have often been characterized in terms of a parameter D^* and an effective temperature T^* in an equation of the form (*Raman et al.*, 1981; *St-Maurice et al.*, 1976):

$$f_{0i}(\mathbf{v}_i) = \frac{n}{(2\pi k_B T^*/m_i)^{3/2}} I_0 \left(2D^* \left[\frac{|\mathbf{c}_\perp|^2}{2k_B T^*/m_i} \right]^{1/2} \right) \exp\left(-D^{*2} - \frac{|\mathbf{v}_i|^2}{2k_B T^*/m_i} \right), \qquad (4.1)$$

where n is the plasma density, k_B is the Boltzmann constant, m_i is the ion mass, $\mathbf{v}_i$ is the ion velocity, $\mathbf{c}_i = \mathbf{c}_{||} + \mathbf{c}_\perp$ is the ion velocity in the $\mathbf{E} \times \mathbf{B}$ frame of reference, and I_0 is the modified Bessel function of order zero. This expression can be modified to allow for separate parallel and perpendicular ion temperatures and to show more clearly the toroidal character of the ion velocity distribution. This means that it is useful to characterize the above empirical description through the somewhat more general expression:

$$f_{0i}(\mathbf{v}_i) = n \left(\frac{m_i}{2\pi k_B T_{\|}} \right)^{1/2} \frac{m_i}{2\pi k_B T_\perp^*} \left[e^{-2D^* C_\perp} I_0 \left(2D^* C_\perp \right) \right] \exp\left(-C_\|^2 - [C_\perp - D^*]^2 \right), \qquad (4.2)$$

where $C_\perp = c_\perp/\sqrt{2k_BT_\perp^*/m_i}$, $C_\parallel = c_\parallel/\sqrt{2k_BT_\parallel/m_i}$, and $T_\parallel$ is the temperature along the magnetic field (see below for more on this). Because the function $e^{-x}I_0(x)$ is of order 1 over a wide range of x values, the toroidal character stands out clearly from the fact that the rest of the perpendicular part of the distribution function introduces a strong peak at $C_\perp = D^*$. The parameter $T_\perp^*$ is such as to yield a perpendicular temperature $T_\perp$ that properly fits observations.

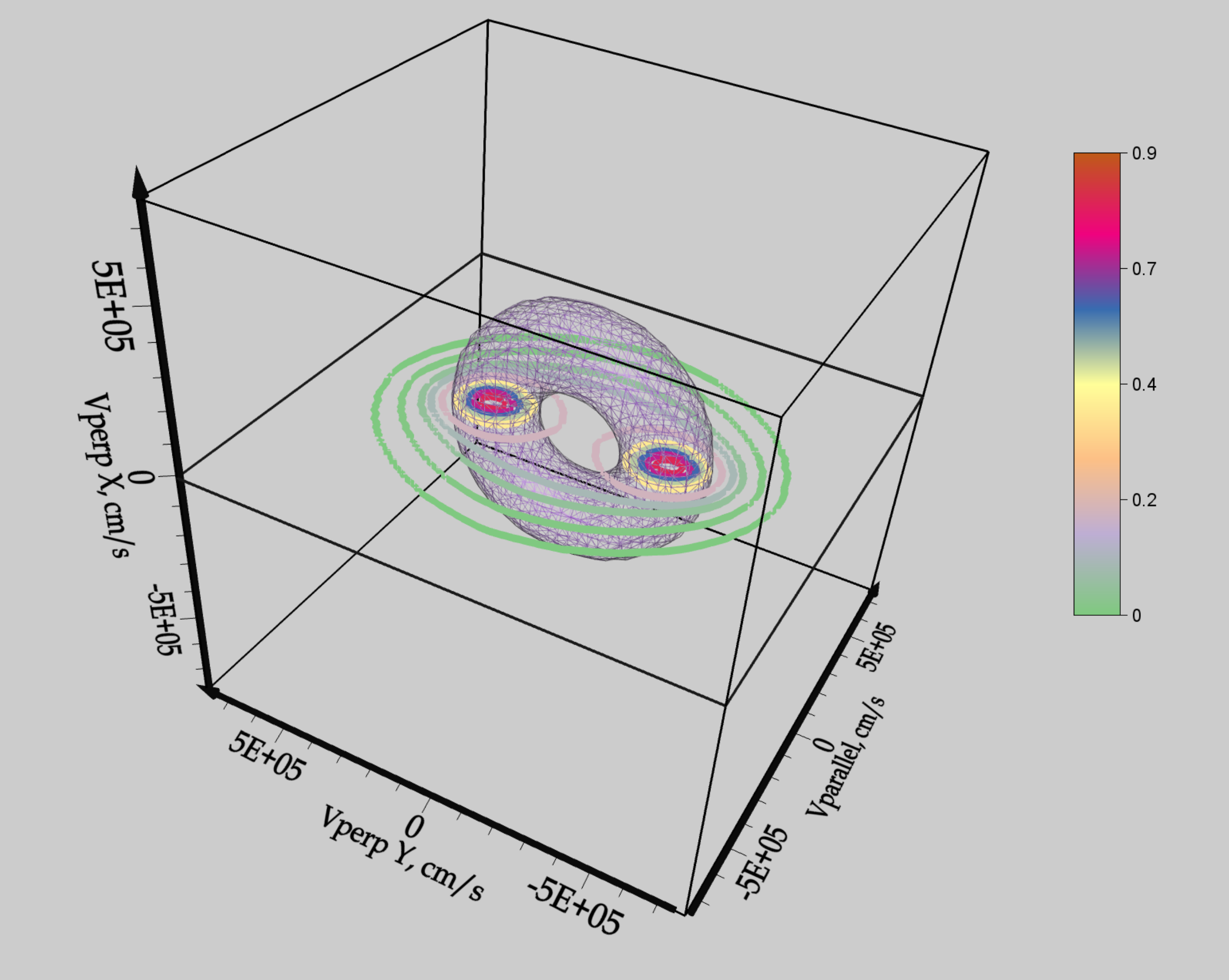

Figure 4.3: O$^+$ velocity distribution for collisions with its O parent gas. The distribution was obtained from the MC simulation of *Winkler et al.* (1992) for a 150 mV/m electric field. 'V$_{\text{perp}}$ X' and 'V$_{\text{perp}}$ Y' are velocity components perpendicular to the magnetic field, and V$_{\text{parallel}}$ is parallel to the magnetic field. The distribution was derived by a MC simulation developed by *Winkler et al.* (1992) rather than from Equation 4.2, but the results are qualitatively similar. The origin of this toroidal shape is discussed in detail in *St.-Maurice and Schunk* (1977).

The RCM-based description of the toroidal distribution function in terms of the D^* parameter has been used repeatedly in the past for ionospheric data studies. Historically, it was first used to fit and interpret satellite one-dimensional velocity distribution data in directions perpendicular to the geomagnetic field (*St-Maurice et al.*, 1976). Later, it was used to calculate how IS spectra were affected by the distorted distributions (*Raman et al.*, 1981) and also served to analyze such spectra by finding the combination of parameters in Equation 4.2 that would reproduce observed spectral shapes as closely as possible (e.g., *Akbari et al.*, 2017b; *Suvanto et al.*, 1989). The stability of the distribution function against electrostatic waves, particularly in magnetic field aligned directions, was also investigated based on the toroidal RCM-based description given by Equation 4.2. Near the F region peak, these distributions were found to be unstable for $D^* > 1.27$ (*Ott and Farley*, 1975; *St-Maurice et al.*, 1976; *Suvanto et al.*, 1989).

An advanced MC description was created by *Winkler et al.* (1992) well after the empirical D^* approach had been developed. Results from this MC code, which are used in the present work, confirmed that the distribution was qualitatively similar to the description provided by Equation 4.2. They were also used to show that when the electric field became large for any angle with respect to the geomagnetic field, it was not possible to obtain good quality fits to the one-dimensional ion velocity distributions described by D^* in Equation 4.2. Double-Maxwellians along the line-of-sight were also attempted but were not successful either. The MC was not used further after that because when this work was carried out, the simulation run-times were long. As a result the data analysis either stuck with the empirical D^* method or simply used a Maxwellian description of the ion velocity distribution along the line-of-sight. It is also noteworthy that the MC distributions were not used to test the stability of the distribution function against electrostatic waves. This is now done in the present paper.

4.2.2 Ion temperature anisotropy

Aside from the toroidal shape, an important property of the ion velocity distribution during strong frictional heating events is that it has different temperatures $T_{\|}$ and $T_{\perp}$ parallel and perpendicular to the geomagnetic field. In the context of distributions that depart considerably from thermodynamic equilibrium, we recall that the temperature is defined as the second velocity moment of the velocity distribution along a particular direction. This means that along, say, the x-direction, the temperature T_x is defined through:

$$T_x = \frac{1}{k_B n} \int d\mathbf{v} m_i (v_x - < v_x >)^2 f_{0i}, \tag{4.3}$$

where v_x is the velocity in the x-direction, n is the density given by:

$$n = \int f_{0i} d\mathbf{v}, \tag{4.4}$$

and the average velocity $< v_x >$ is given by:

$$< v_x > = \frac{1}{n} \int d\mathbf{v} v_x f_{0i}. \tag{4.5}$$

The average ion temperature T_i is related to the two temperatures via the relation (*St-Maurice and Schunk*, 1979):

$$T_i = \frac{T_{\parallel} + 2T_{\perp}}{3}. \tag{4.6}$$

The ion temperature $T_{i\phi}$ along a line-of-sight at an angle ϕ to the geomagnetic field (the 'aspect angle') becomes (*Raman et al.*, 1981):

$$T_{i\phi} = T_{\parallel} \cos^2 \phi + T_{\perp} \sin^2 \phi. \tag{4.7}$$

This relation holds as long as the distributions along the parallel and perpendicular are separable functions of $v_{\parallel}$ and $v_{\perp}$. As is presented later in this paper, the MC simulations show that this assumption, while not perfect, is reasonable. We note that from Equations 4.6 and 4.7 that the line-of-sight ion temperature is equal to the average ion temperature when the aspect angle is 54.7° (*Raman et al.*, 1981).

An additional feature of the ion temperature in the presence of ion-neutral collisions is its relation to the relative ion-neutral drift. The temperatures parallel and perpendicular to the magnetic field are given by (*St-Maurice and Schunk*, 1979; *Winkler et al.*, 1992):

$$T_{\parallel} = \frac{\beta_{\parallel} m_n | < \mathbf{v} >_i - < \mathbf{v} >_n |^2}{2k_B} + T_n \tag{4.8}$$

and

$$T_{\perp} = \frac{\beta_{\perp} m_n | < \mathbf{v} >_i - < \mathbf{v} >_n |^2}{2k_B} + T_n, \tag{4.9}$$

where T_n is the temperature of the neutral gas, m_n is the neutral mass, $< \mathbf{v} >_n$ is the mean velocity of the neutral gas, $< \mathbf{v} >_i$ is the mean velocity of the ion gas, and $\beta_{||}$ and $\beta_\perp$ are partition coefficients. It follows from Equation 4.6 and the above equations that:

$$\beta_{||} + 2\beta_\perp = 2. \tag{4.10}$$

It is also usually assumed that a good leading-order description of the ion energy balance yields (*Schunk and Nagy*, 2009):

$$T_i - T_n = \frac{m_n}{3k_B} | < \mathbf{v} >_i - < \mathbf{v} >_n |^2. \tag{4.11}$$

Various corrections from this pure quadratic dependence on the magnitude of the relative drift can be found in the literature. For example, an energy dependence associated with hard-sphere collisions has been described in *St-Maurice and Hanson* (1982), *Schunk* (1977), and *Banks and Kockarts* (1973). Independently from the quadratic dependence or lack thereof of $(T_i - T_n)$ on the relative drift, $\beta_{||}$ and $\beta_\perp$ are functions of the mean relative velocity between ions and neutrals (*Gaimard et al.*, 1998; *St.-Maurice and Schunk*, 1977; *Winkler et al.*, 1992), though Equation 4.10 still holds. In addition, if ion-ion and ion-electron collisions contribute enough to the ion energy budget, anisotropy calculations based on the sole inclusion of ion-neutral collisions require corrections. These corrections are discussed further in Section 4.3.2.

4.2.3 Outline of present work

In the present paper, the MC simulation perfected by *Winkler et al.* (1992) is used to extract the best possible information that could be retrieved about the shape of the ion velocity distribution and its anisotropy in the presence of large electric fields under a predominance of ion-neutral collisions. Various smoothing techniques are introduced and tested to filter the noise that necessarily affects the MC calculations of velocity distributions. Numerous runs are made to produce one-dimensional ion velocity distributions in terms of polynomial fits as functions of electric field strength, ion and neutral composition, and aspect angle to make the results accessible to a routine analysis of data. This work also studies the impact that a more recently published cross-section for the Resonant Charge Exchange (RCE) collisions between O and O^+ has on the ion velocity distribution, as well as the impact of both the old and new collision frequency models on the stability of the velocity distribution against electrostatic waves. Finally, we introduce a procedure to correct the velocity distribution for the influence of ion-ion and ion-electron collisions.

Section 4.3 discusses the procedure in more detail. Section 4.4 highlights the results of the smoothing technique in exploring ion temperature anisotropy and associated IS spectra. Section 4.5 discusses new findings from the calculations and offers an overview of the results. The various polynomial coefficients that were used to characterize one-dimensional ion velocity distributions for various situations are included as an online supplement to this paper.

4.3 Background and procedures

As stated in the introduction, the work presented here employs the MC simulation documented in *Winkler et al.* (1992) that uses an effective RCE cross-section given by:

$$Q_T^{ex}(E) = [A - B\log_{10}(E)]^2, \tag{4.12}$$

where E is the kinetic energy, in eV, of the relative motion between an ion and a neutral with which it collides and A and B are coefficients that reflect the ion-neutral collision cross-section. For O^+-O collisions, *Winkler et al.* (1992) used 10.99 and 0.95 for the constants A and B, respectively, as derived from the work of *Knof et al.* (1964). However, a newer study presented in *Pesnell et al.* (1993) implies 13.72 and 2.126 instead for A and B. As a result, we have considered the newer RCE cross-section introduced by *Pesnell et al.* (1993) (referred to as the 'POH cross-section', after Pesnell, Omidvar, and Hoegy) and compared the results with the cross-section from *Knof et al.* (1964) (referred to as the 'KMV cross-section', after Knof, Mason, and Vanderslice) used in *Winkler et al.* (1992).

The work presented here also uses a number of collisions that is high enough to characterize the ion velocity distribution up to two thermal speeds with good accuracy. The resulting distributions have been smoothed to eliminate the effects of increased statistical fluctuations in the tails of the distributions. From the resulting one-dimensional ion velocity distributions, theoretical IS spectra have been constructed. In the process, we have also fully characterized the anisotropy of the ion temperature and its variations along any line of sight. Furthermore, and as explained in Section 4.2.1, we have queried the stability of the attending velocity distribution against field-aligned electrostatic waves expected to be of the 'loss-cone' (or 'Post-Rosenbluth') type (*Ott and Farley*, 1975; *St-Maurice*, 1978).

4.3.1 Computation of high quality IS spectra and related properties based on MC simulations

In order to obtain good statistics up to two ion thermal speeds, the number of collisions has been increased from the two million seen in *Winkler et al.* (1992) to 40 million. In addition, necessitated by the fact that spectra depend strongly on the derivative of the velocity distribution (see subsection 4.3.1), extra smoothing and interpolation techniques were used before the necessary calculations to characterize the IS spectra could be carried out.

Polynomial smoothing techniques

As explained in Section 4.2.1, previous studies have used the D^* parameter to describe the distorted MC ion velocity distributions (*Akbari et al.*, 2017b; *Raman et al.*, 1981; *Suvanto et al.*, 1989; *Winkler et al.*, 1992). However, the work of *Winkler et al.* (1992) shows that such fits are not terribly accurate, particularly when the electric field is stronger than 35 mV/m. To improve the quality of the functions that should be used in spectral calculations, we used a special polynomial technique to describe a particular velocity distribution. As a first step towards our goal, a 6-point bivariate interpolation scheme was applied to the MC output to obtain the distribution function at specific velocities and to describe the distribution from the MC more continuously than given by *Winkler et al.* (1992). After that, we performed a multinomial least squares fit not on the smoothed distribution but, rather, on its logarithm so as to avoid dealing with negative numbers for the reconstructed distribution anywhere. A chi-squared optimization scheme was used to find the ideal degree of least squares fit. The procedure was carried out until the distribution was smaller than the maximum by a factor 1.5×10^{-8}, where the noise was typically becoming strong. After exponentiating the resulting polynomial, we had a highly accurate representation of the velocity distribution up to the point where the distribution was 1.5×10^{-8} times smaller than the maximum, which was typically beyond our nominal two ion thermal speeds.

However, there could be cases where a smooth description of the velocity distribution would be needed beyond two thermal speeds, particularly if the electron temperature was to be more than twice the ion temperature. For the purpose of introducing a smooth (but admittedly more qualitative) description for the far tail of the distribution under such conditions, the multinomial fit was merged smoothly with a v^2 quadratic fit of the logarithm of the distribution over the region representing greater than two thermal speeds. The qualitative nature of this procedure should have little consequence in practice because it is usually the case that, when ions are frictionally heated by strong electric fields, the electron temperature is typically smaller, or at least not much larger, than the ion temperature. This means that a $T_e > 2T_{i\phi}$ situation should rarely be met — if ever — during strong frictional heating situations, consistent with the notion that large electric fields are found mostly in regions of smaller plasma densities, i.e., regions devoid of electron precipitation and attendant electron heating.

Although the above method describes the ion velocity distribution well enough to obtain accurate IS spectra, one disadvantage is that the MC simulation and the fitting procedure must be repeated every time the electric field or the aspect angle is changed. Using a modern computer, the MC simulates 40 million collisions in only 2.5 minutes, but to obtain a fit to a spectrum observed by an ISR calls must be made to a program that calculates the spectrum from the ion and electron velocity distributions for a number of ion and electron temperatures. Therefore, MC simulations are too time-consuming and impractical even for modern IS spectral analysis techniques. To greatly accelerate the process, ion velocity distributions were simulated by steps of 10 mV/m between 20 mV/m and 200 mV/m and by steps of 10° aspect angles between 0 and 90°. A continuous description of every resulting distribution was obtained using the procedure described above. After that, Legendre polynomials were fitted to the smoothened continuous distribution found after taking the exponential of a polynomial fit to the logarithm of the distribution. Each distribution is described by a sum of Legendre polynomials going up to order 50 (but only the even-numbered coefficients are needed, given the symmetry of the situation). By using these 50 coefficients, our procedure cuts the amount of time required to get a spectrum from toroidal velocity distributions by two orders of magnitude. The resulting 50 orthogonal polynomial coefficients could then be interpolated to compute the required coefficients for arbitrary electric fields and aspect angles of interest for which MC simulations had not been performed.

Spectral calculations

For a stable plasma, the spectrum of scattered radar waves is given by the expression (*Sheffield*, 1975):

$$S(\mathbf{k},\omega) = \frac{2\pi}{k}\left|\frac{1+G_i}{\epsilon}\right|^2 g_{0e} + \frac{2\pi}{k}\left|\frac{G_e}{\epsilon}\right|^2 g_{0i}, \tag{4.13}$$

where ϵ is the longitudinal dielectric function given by

$$\epsilon(\mathbf{k},\omega) = 1 + G_e(\mathbf{k},\omega) + G_i(\mathbf{k},\omega), \tag{4.14}$$

and $\mathbf{k}$ is the difference between the incident wavevector and the scattered wavevector, ω is the Doppler shifted angular frequency (i.e., the difference between the incident radar frequency and the scattered radar frequency), g_{0i} and g_{0e} are the one-dimensional velocity distributions of ions and electrons, respectively, evaluated at the velocity $\mathbf{k}\omega/k^2$, and G_e and G_i are the electron and ion dielectric functions, respectively.

As has been done in the past, we used the standard magnetized collision-free expressions for the electron dielectric function, and we neglected ion gyro-resonances and the effects of collisions in our calculations of the ion dielectric function (e.g., *Raman et al.*, 1981). Note that this procedure is not strictly valid if the radar line-of-sight is within 3° from perpendicularity to the magnetic field (e.g., *Sheffield*, 1975; *Woodman*, 2004, and references therein).

For the singly ionized species of interest here, the ion dielectric function was computed from the expression

$$G_i\left(\mathbf{k},\omega\right) = \frac{4\pi e^2 n_{0i}}{m_i k^2}\int_{-\infty}^{\infty} d\mathbf{v}\frac{\mathbf{k}\cdot\dfrac{\partial f_{0i}}{\partial \mathbf{v}}}{\omega - \mathbf{k}\cdot\mathbf{v} - i\gamma}, \tag{4.15}$$

where e is the elementary charge, we recall that f_{0i} is the ion velocity distribution, and n_{0i} is the plasma density. Here, γ is asymptotically small, real, and positive and is used to describe analytically continuous functions that give rise to Landau damping effects.

Defining the x-direction to be along the scattered wavevector, the above can be rewritten as:

$$G_i\left(k,\omega\right) = \frac{\omega_{pi}^2}{k^2}\int_{-\infty}^{\infty} dv_x \frac{k\dfrac{\partial g_{0i}}{\partial v_x}}{\omega - kv_x - i\gamma}, \tag{4.16}$$

where $\omega_{pi}^2 = \dfrac{4\pi n_{0i}e^2}{m_i}$ is the square of the ion plasma frequency. This function is obtained by integrating the velocity distributions over the two velocity components perpendicular to a line-of-sight direction defined by $\mathbf{k}$ (in this case, the x-direction).

Finally, after defining the non-dimensional parameters $x_i = \dfrac{\omega}{bk}$ and $y = \dfrac{v_x}{b}$, where b is the ion thermal speed, G_i is evaluated through the computation:

$$G_i\left(x_i\right) = \frac{\omega_{pi}^2}{bk^2}\left(\mathcal{P}\int_{-\infty}^{\infty} dy \frac{\dfrac{\partial g_{0i}}{\partial y}}{x_i - y} + i\pi \left.\frac{\partial g_{0i}(y)}{\partial y}\right|_{y=x_i}\right), \tag{4.17}$$

where $\mathcal{P}$ indicates the principal value integral and contains the derivative of the one-dimensional distribution function. The imaginary part of this expression likewise requires the evaluation of a derivative. Although working with the derivative appears at first sight easy to do numerically, it does require a noise-free description of the velocity distribution. This is why this work went to quite an extent to carefully smooth the MC output.

In addition to the noise-removal for the calculation of the derivative, there was the challenge of evaluating the real part of G_i, which contains a singularity at $x_i = y$. Following a technique introduced by *Raman et al.* (1981), we first introduced a change of variables to move the singularity to the origin, letting $c = y - x_i$ so as to write:

$$G_{iR} = \frac{\omega_{pi}^2}{bk^2}\mathcal{P}\int_{-\infty}^{\infty} \frac{dc}{-c}\frac{\partial g_{0i}}{\partial c}. \tag{4.18}$$

The integration was then performed through an even-numbered Gaussian quadrature, namely, an expression of the form:

$$\int_{x_1}^{x_2} f(x)dx = \sum_{j=1}^{N} w_j f(x_j), \tag{4.19}$$

where x_1 and x_2 are limits of integration, which were set to be at numbers considered to have a large magnitude in the present context, namely, ±6. In this expression, we also have $f(x)$ as the function being integrated, N the number of quadrature points, and w_j a weight attributed to the evaluation of f at the location x_j. The advantage of using an even-numbered Gaussian quadrature is that the function was never evaluated at the singularity $c = 0$. Still, the numerical quadrature occasionally ended up with an isolated spike or two due to surviving noise at some specific locations of x_i. When this happened, the number of quadrature points was simply increased by an additional two points to prevent the quadrature from sampling the previous bad point or points. At a bad point, the result from the first quadrature was then replaced by the value at that point that came from the new quadrature. This provided a final filter by which to remove residual noise effects.

The numerical evaluation of the ion dielectric function was tested against the analytical result based on MC runs for which the electric field was set to zero. In that case, the solution was found to agree perfectly with the analytical solution G_{iM} for G_i, namely, with the plasma dispersion function (*Sheffield*, 1975):

$$G_{iM} = \frac{T_e}{T_i k^2 \lambda_D^2} \left[1 - 2x_i \exp\left(-x_i^2\right) \int_0^{x_i} \exp(p^2) dp - x_i i \pi^{1/2} \exp(-x_i^2) \right]. \tag{4.20}$$

where λ_D is the Debye length.

4.3.2 Incorporating Ion-Ion and Ion-Electron Collisions

In general, it should not be assumed that ion-electron and ion-ion collisions in the F region play a completely negligible role. For instance, in the absence of frictional heating, even for ordinary situations, the ion temperature starts to depart from the neutral temperature typically at 300 km or above because of heat exchange with hotter electrons (e.g., *Schunk and Nagy* (2009)). Likewise, the ion-ion collision frequency starts to be comparable to the ion-neutral collision frequency by a height of 300 km if the ion temperature is comparable to the neutral temperature. The role of ion-ion collisions in the context of the present paper is to rebuild an isotropic Maxwellian ion velocity distribution.

We used a simple empirical modification to incorporate the corrections due to ion-ion and ion-electron collisions through the equation:

$$\nu_T f_T = \nu_{in} f_{in} + \nu_{ie} f_{1i} + \nu_{ii} f_{2i}, \tag{4.21}$$

where $\nu_T = \nu_{in} + \nu_{ie} + \nu_{ii}$ and ν_{in}, ν_{ie}, and ν_{ii} are the ion-neutral, ion-electron, and ion-ion momentum transfer collision frequencies, respectively. Here, f_T is the 'total' (or final) ion velocity distribution, f_{in} is the MC simulated distribution, f_{1i} is an isotropic Maxwellian velocity distribution with a temperature equal to the electron temperature, and f_{2i} is an isotropic Maxwellian velocity distribution with a temperature equal to the average ion temperature. A similar procedure was followed by *Tereshchenko et al.* (1991) to describe the effect of ion-ion collisions. However, these authors used D^* (or RCM) distributions instead of the far more accurate MC distributions. They also did not include the effect of ion-electron collisions.

In Equation 4.21, the collision frequencies presented in *Schunk and Nagy* (2009) for ν_{ie}, ν_{ii}, and ν_{in} were used. For the first two, we assumed that O^+ ions dominated above 250 km and that NO^+ dominated below that altitude. For the POH RCE collision frequency in s^{-1} between O^+ and O, we used

$$\nu_{in} = 3.0 \times 10^{-11} n(O) T_r^{1/2} (1 - 0.135 \log_{10}(T_r/1000))^2 \tag{4.22}$$

where $n(O)$ is the density of O in cm^{-3}, and $T_r = (T_i + T_n)/2$. For the KMV RCE collision frequency, we used (*Schunk and Walker*, 1973):

$$\nu_{in} = 3.69 \times 10^{-11} n(O) T_r^{1/2} (1 - 0.065 \log_{10} T_r)^2 \tag{4.23}$$

4.3.3 Validation of Results

Details of the MC simulation are given in *Winkler et al.* (1992), along with its validation techniques. As for the present work, additional software was needed to create IS spectra from an MC output because IS spectral calculations involve not just the derivative of the distribution function (which is noisy owing to statistical fluctuations), but also a principal value integral of that derivative over a singularity, as seen through Equation 4.17. For IS spectra, the derivative must be handled particularly well near the ion thermal speed because ion-acoustic speeds often dominate the spectrum. This requires a smooth high-accuracy description of the derivative of the distribution up to two ion thermal speeds, and the Gaussian integration techniques used in this work further require the distribution to be described continuously. To create this description, the number of collisions was increased by a factor of eight over *Winkler et al.* (1992) to reduce the 10% statistical fluctuation level found for two million collisions at two thermal speeds to 3% (as per $\sqrt{N}$, where N is the number of collisions). Smoothing techniques discussed in Section 4.3.1 were used to remove remnant fluctuations in the tail of the distribution. These smoothing and numerical integrations recover the expected theoretical spectra for a Maxwellian velocity distribution when the electric field is 0 mV/m for artificial neutral temperatures ranging from 1000 K to 10000 K. The differences were barely visible, and were far less than any noise measurement.

4.4 Results

The use of MC simulations has allowed us to revisit: (1) the question of the plasma stability against field-aligned electrostatic instabilities of the loss-cone (or Post-Rosenbluth) type, (2) the dependence of the ion temperature and its anisotropy on the effective electric field strength, and (3) the IS spectral shape as functions of electric field strength and aspect angle for applications to the analysis of data during strong electric field episodes. We present the key findings from the MC simulations in this section.

The simulations described in this report can be applied to regions for which the ion-neutral collision frequency is smaller than 0.2 times the cyclotron frequency, i.e., regions typically above 135 km. However, as the altitude changes, the collision model and the results change. Above 300 km, ion-ion collisions start to become important if the plasma density is elevated and the ion temperature is low. Above 400 km, vertical transport must be taken into account, and the distributions undergo transient signatures of the kind described by *Loranc and St-Maurice* (1994). In that case, there can be many different solutions, depending on how long a magnetic field tube has been in a fast convecting region. Therefore, these simulations are only valid between 130 km and 400 km. Above this, they are only valid if the magnetic field line has been heated for a few minutes.

The following are results from two specific altitude regions of the ionosphere: 1) the NO^+ dominant region between approximately 150 and 200 km, and 2) the O^+ dominant region above 250 km. Between 150 to 200 km the neutral population is dominated by O and N_2; hence an O and N_2 neutral background concentration is used for the NO^+ calculations. Meanwhile, O is dominant above 250 km; hence only an O background is used for O^+

calculations. At high latitudes, the Mass Spectrometer IS radar (MSIS) model gives a neutral density of 2.0×10^{15} m^{-3} for the NO$^+$ region and a neutral density of 1.8×10^{14} m^{-3} for the O$^+$ region (*Hedin*, 1991). Given the variability in plasma density, this work assumes a 1.0×10^{11} m^{-3} plasma density for both NO$^+$ and O$^+$. For the spectral calculations, a radar frequency of 440×10^6 Hz is assumed, consistent with the three Advanced Modular ISRs located near Resolute Bay (Nunavut, Canada) and near Poker Flat (Alaska, Canada).

4.4.1 Plasma Stability

The question of plasma stability is of interest for two reasons. First, it is useful to know if the plasma becomes unstable under strong electric field conditions in that it might create field-aligned irregularities that could be observed by rockets or radars in the F region. Second, if the plasma is unstable, there is a chance, as originally argued by *Ott and Farley* (1975), that the perpendicular part of the velocity distribution could be rearranged by the ensuing structures to maintain the plasma configuration in a near-marginally stable state. This might impact the large aspect angle results of the present work, which assumes that the MC results are fully applicable, once small corrections due to ion-ion and ion-electron collisions are included. In that context, the wave-particle interactions in the presence of an instability could be viewed as akin to having much stronger ion-ion interactions than anticipated.

One way to test the stability of the plasma against electrostatic waves is to develop a Nyquist diagram in which the imaginary part of the plasma dispersion relation is plotted against its real part in the complex plane. If the resulting diagram circles the origin, the plasma is unstable (*St-Maurice*, 1978; *Stix*, 1992). Any contribution from Maxwellian electrons moving at the same bulk velocity stabilizes the plasma. However, at zero aspect angles (field-aligned structures), the electron contribution to the dispersion relation vanishes (*St-Maurice*, 1978). If, for that case at least, the diagram circles the origin, the simulated plasma is unstable. Therefore, the calculations of the imaginary and real parts of the ion dielectric function G_i are used here to check the plasma stability.

It has been shown by *St-Maurice* (1978) and *Suvanto et al.* (1989) that the toroidal distribution in terms of D^* is actually unstable to field-aligned structures if $D^* > 1.27$ when RCE collisions are dominant for O$^+$ ions and a Relaxation Collision Model (RCM) is used. This stated, the RCM is an extreme model where there is never any ordinary elastic scattering involving partial exchange of energy and momentum between the colliding partners and where the collision frequency is independent of energy (*St.-Maurice and Schunk*, 1977). Even after scaling the resulting velocity distributions to fit observations as well as possible, the description given by an RCM remains extreme. It is therefore of interest to see if the MC results also produce unstable plasmas. As illustrated in Figure 4.4, the stability of the plasma depends on the choice of RCE cross-section. The POH cross-section, published in *Pesnell et al.* (1993), is used for the green curve in Figure 4.4. For the blue curve, the older KMV cross-section published by *Knof et al.* (1964) is used. This cross-section has been the basis for much of the work on F region ion-neutral collisions until the mid-1990s. Both cases include elastic scattering from polarization interactions and hard core repulsion. Interestingly, Figure 4.4 shows that the POH cross-section produces stable distributions, whereas the KMV cross-section (like the RCM distributions with $D^* > 1.27$) produces unstable distributions for the 100 mV/m case shown. Similar O^+-O collision results were found for electric fields up to 200 mV/m.

4.4.2 Temperature Anisotropy

Figure 4.5 shows the line-of-sight ion temperature found for O^+-O collisions using the POH RCE cross-section for a variety of electric fields and aspect angles. As expected, the line-of-sight ion temperature increases with electric field strength and aspect angle. These results correspond closely to those based on Equation 4.7, implying that the distribution function is indeed well described by the product of separate functions of $v_\parallel$ and $v_\perp$. There is nevertheless an interesting small deviation from separability that comes across near 30° when the electric field strength exceeds 100 mV/m. This is shown through Figure 4.6, which shows the ratio of the results presented in Figure 4.5 to what is inferred from Equation 4.7. Differences of up to 15% are seen but only if the electric field exceeds 150 mV/m. Nonetheless, it should be noted that, at 15%, the actual difference between the calculated and actual line-of-sight temperatures are as much as 1200 K. This stated, it is interesting to note that only aspect angles of the order of 30° are affected by the lack of perfect separability. Furthermore, when these calculations are performed for molecular ions, the deviations from Equation 4.7 are less

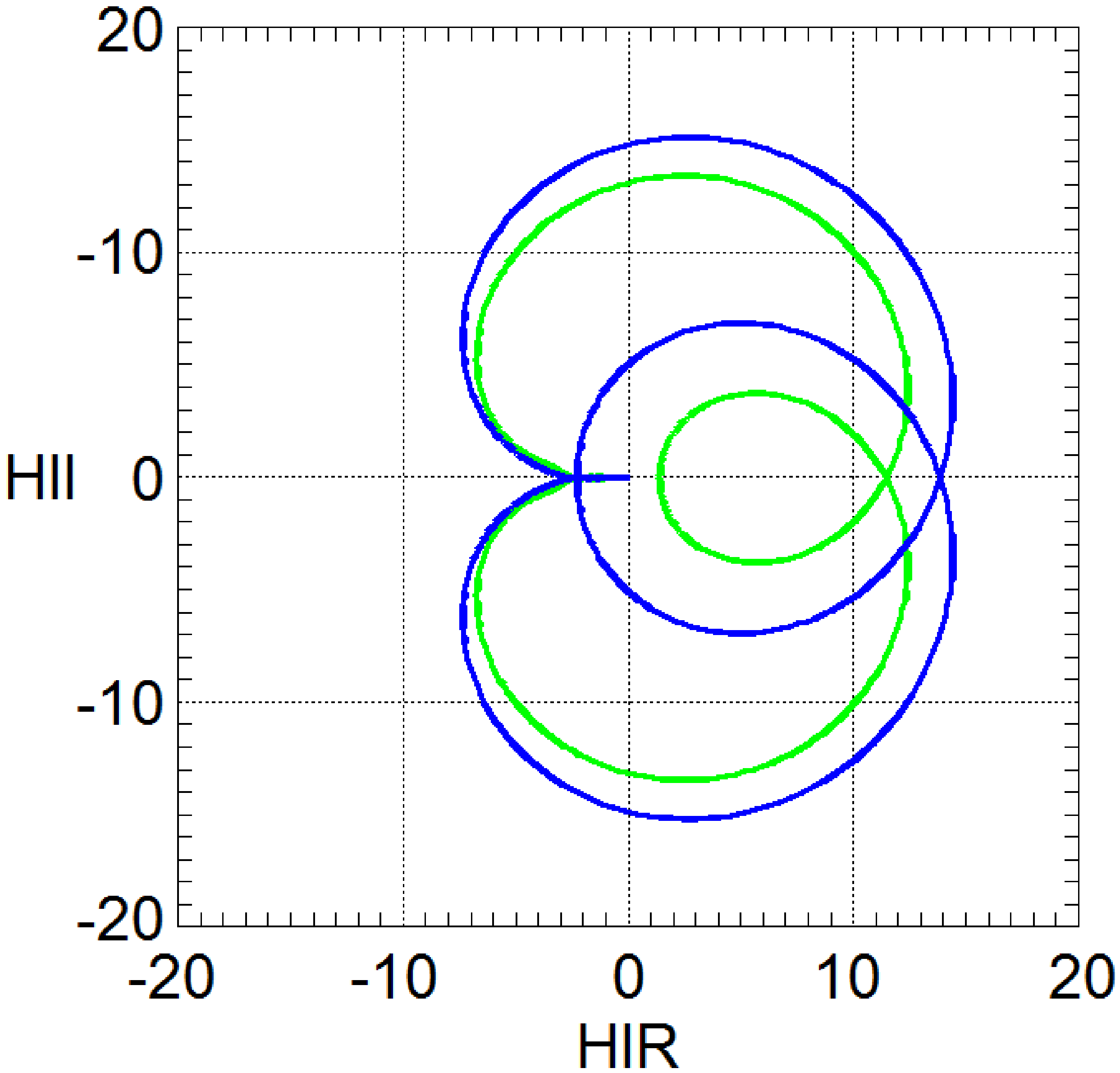

Figure 4.4: Nyquist diagram of the ion dielectric function at 100 mV/m. Green curve not circling the origin: POH cross-section result. Blue curve circling the origin: KMV cross-section result.

than the 2% temperature uncertainty.

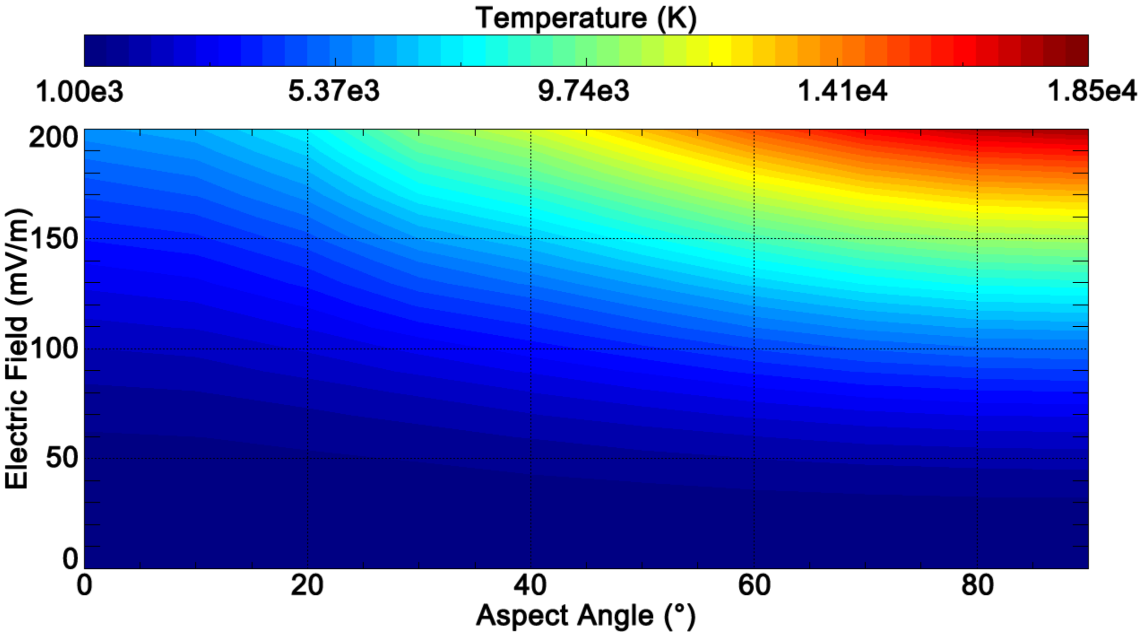

Figure 4.5: Line-of-sight O^+ temperature as a function of electric field and aspect angle, based on the MC simulation of O^+-O collisions using the POH RCE cross-section.

Figure 4.7 examines more precisely the behavior of the ion temperature by producing line plots of the relative ion-neutral temperature difference as a function of the relative ion-neutral drift for a chosen set of aspect angles. This figure is produced using O^+-O collisions with the POH RCE cross-section. It also reflects the effect of collisions with other charged particles by producing the temperature results both with and without the influence of ion-ion and ion-electron collisions. In addition, the figure clearly shows that the ion-neutral temperature difference increases in parabolic-like fashion, and that, in agreement with Figure 4.5, for a given relative drift, the ion-neutral temperature difference increases with increasing aspect angle.

As discussed in Section 4.2.2 and confirmed by Figure 4.6, the ion temperature at an aspect angle close to 55° is basically equal to the average ion temperature. This allows for a comparison between the average ion temperature, inferred from the 55° angle, and Equation 4.11, which is based on the Maxwell molecule approximation, namely, on a collision frequency that does not depend on energy. The latter is shown by the black curve in Figure 4.7. There is clearly a noticeable difference between the Maxwell molecule approximation and the actual

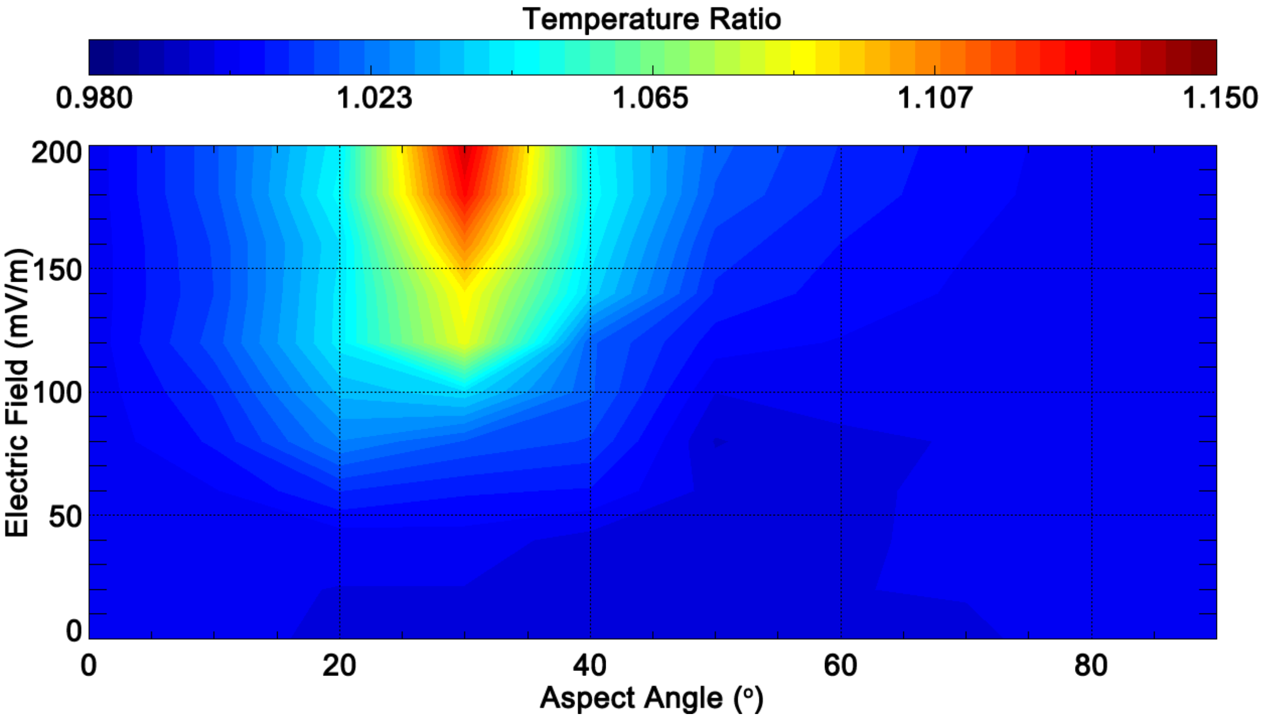

Figure 4.6: Ratio between the MC simulated results of Figure 4.5 and the predictions from Equation 4.7.

energy-dependent result in the case of RCE collisions and the temperature from the MC simulations is several thousand kelvin higher than the Maxwell molecule prediction when the electric field is very strong.

The solid lines in Figure 4.7 give the results when only ion-neutral collisions are considered, whereas the dashed lines illustrate the influence of ion-ion and ion-electron collisions, using a 2000 K electron temperature, a 1.8×10^{14} m^{-3} neutral density, and a plasma density of 10^{11} m^{-3}. The neutral density is based on the Mass Spectrometer Incoherent Scatter 90 (MSIS-90) model, and corresponds to quiet ($F_{10.7} = 74$), winter conditions at an altitude of roughly 320 km (*Hedin*, 1991). This neutral density was chosen because it is roughly where Coulomb collisions begin to have an appreciable impact (more than 500 K).

In Figure 4.8, the RCE calculations for O-O^+ collisions are repeated, this time for the KMV cross-section. Although the overall results are similar, at lower aspect angles the POH cross-section produces larger relative temperature differences than the KMV cross-section, whereas, consistent with Equation 4.10, at higher aspect angles the KMV cross-section produces larger ion-neutral temperature differences. Additionally, the average ion temperature is greater for the KMV cross-section. This differences may be large enough to be measurable and allow one, based on observations, to identify which cross-section is closer to reality. Lastly, the impact of Coulomb collisions is slightly greater for the KMV cross-section than the POH cross-section.

Figure 4.9 examines the ion temperature anisotropy for NO^+ instead of O^+ ions, with a 50% O and 50% N_2 neutral mixture (other background concentrations involving NO^+ are shown in the supplementary material). As with the O^+ case, the temperature difference increases in parabolic-like fashion with the magnitude of the relative drift. The temperature differences in Figure 4.9 are larger than those in Figure 4.7, particularly at smaller aspect angles. As the O concentration decreases and the N_2 concentration increases, the ion-neutral temperature difference also increases. This is a result of the influence of the neutral mass on the heating rate (see Equations 4.8, 4.9, or 4.11). This stated, there is a very strong agreement at 55° with the Maxwell molecule approximation for any neutral mixture (not shown). This contrasts sharply with the strongly energy-dependent RCE process observed in the O^+-O temperature plots. Finally, Figure 4.9 shows the impact of ion-ion and ion-electron collisions to be negligible when compared to Figure 4.7. This is because the ion-neutral collision frequency is much larger at the lower altitudes for which molecular ions dominate the plasma composition. The much larger ion-neutral collision frequency means a considerable reduction of the influence of Coulomb collisions on the ion velocity distribution.

4.4.3 Spectra

As stated in Section 4.2, two signatures to the ion velocity distribution need to be considered: its anisotropy, just discussed above, and the extent to which its shape is toroidal. In this subsection, we study the extent to which the toroidal form can influence IS spectral shapes.

The IS spectra were derived from the MC simulations by following the methodology described in Section 4.3.1. Figures 4.10 through 4.15 show a variety of those spectra as a function of x_i. All instances are compared with their 'effective' (same line-of-sight ion temperature) Maxwellian counterparts and include ion-ion and ion-electron collisions for a plasma density of 10^{11} m^{-3}. The panels on the left-hand-side are for $T_e = 2000$ K, while those on the right-hand-side are for $T_e = 4000$ K. Each figure describes results for aspect

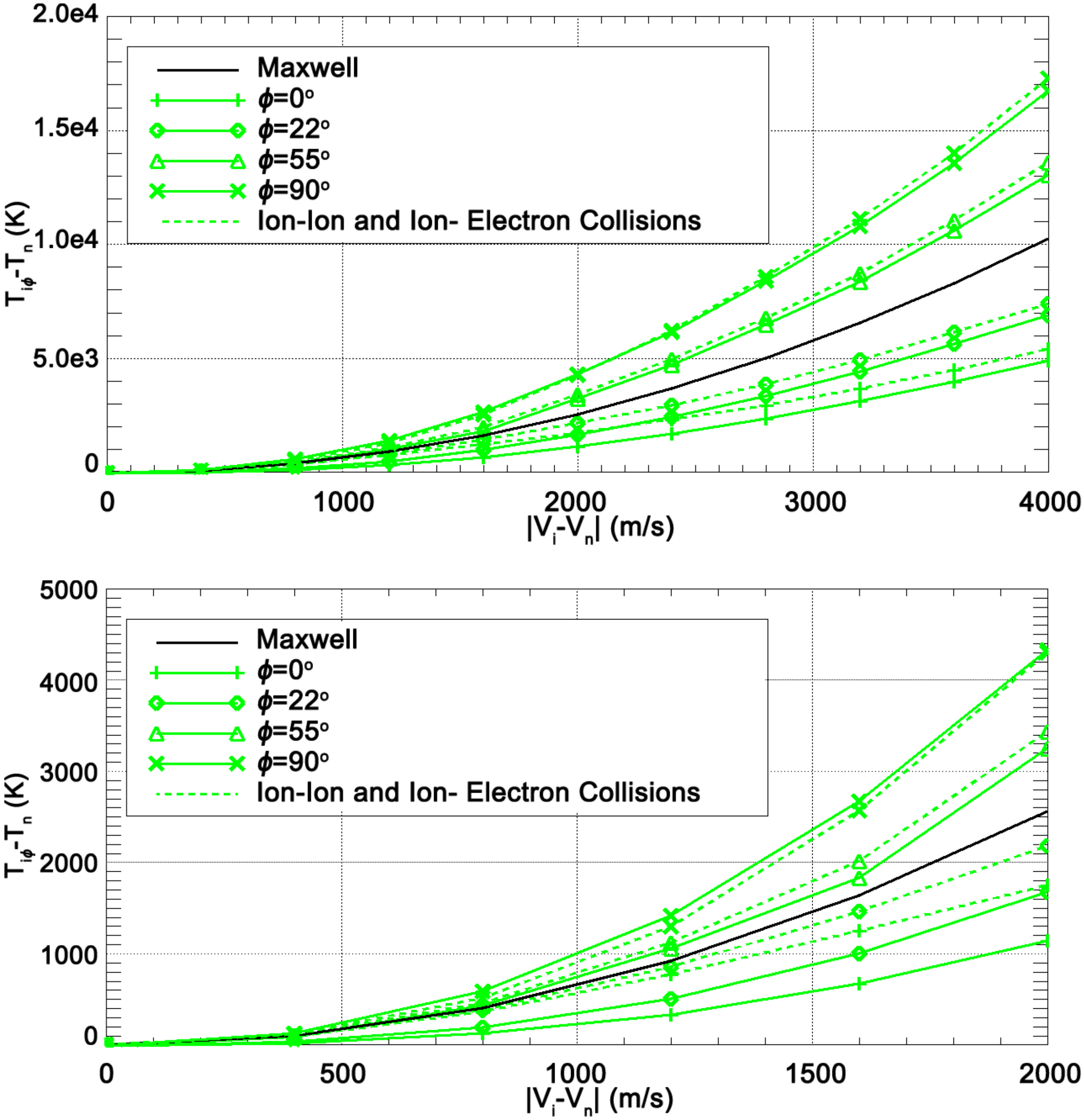

Figure 4.7: Difference between the line-of-sight ion temperature and the neutral temperature as a function of relative drift for O^+-O collisions at various aspect angles. Green lines: POH RCE cross-section. Black line: Maxwell molecule average ion temperature given by Equation 4.11. Solid lines: pure ion-neutral particle interactions. Dashed lines: ion-ion and ion-electron collisions included. Top panel: relative ion-neutral drift between 0 m/s and 4000 m/s. Bottom panel: relative ion-neutral drift between 0 m/s and 2000 m/s.

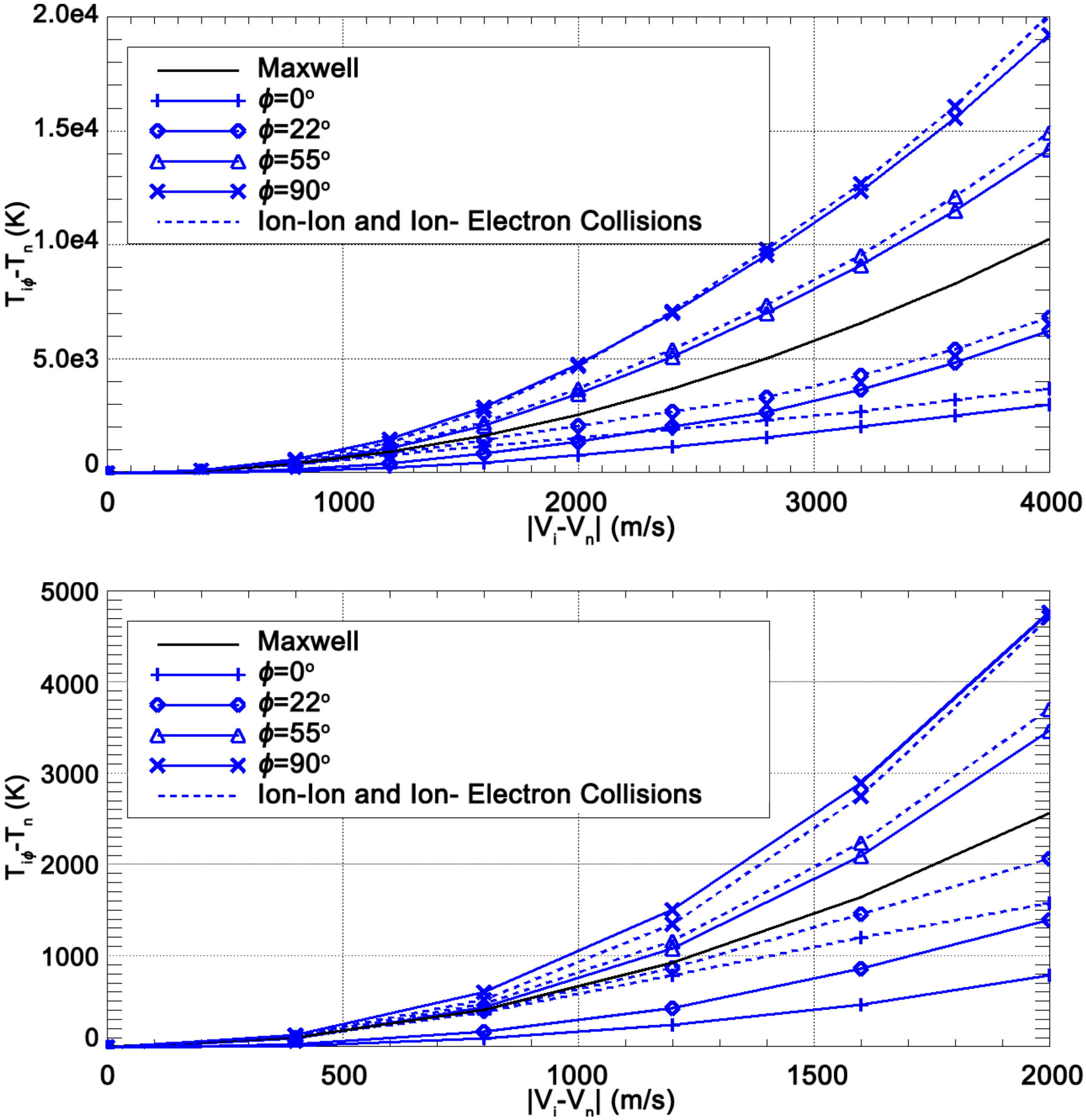

Figure 4.8: Same as Figure 4.7 but for the KMV RCE cross-section.

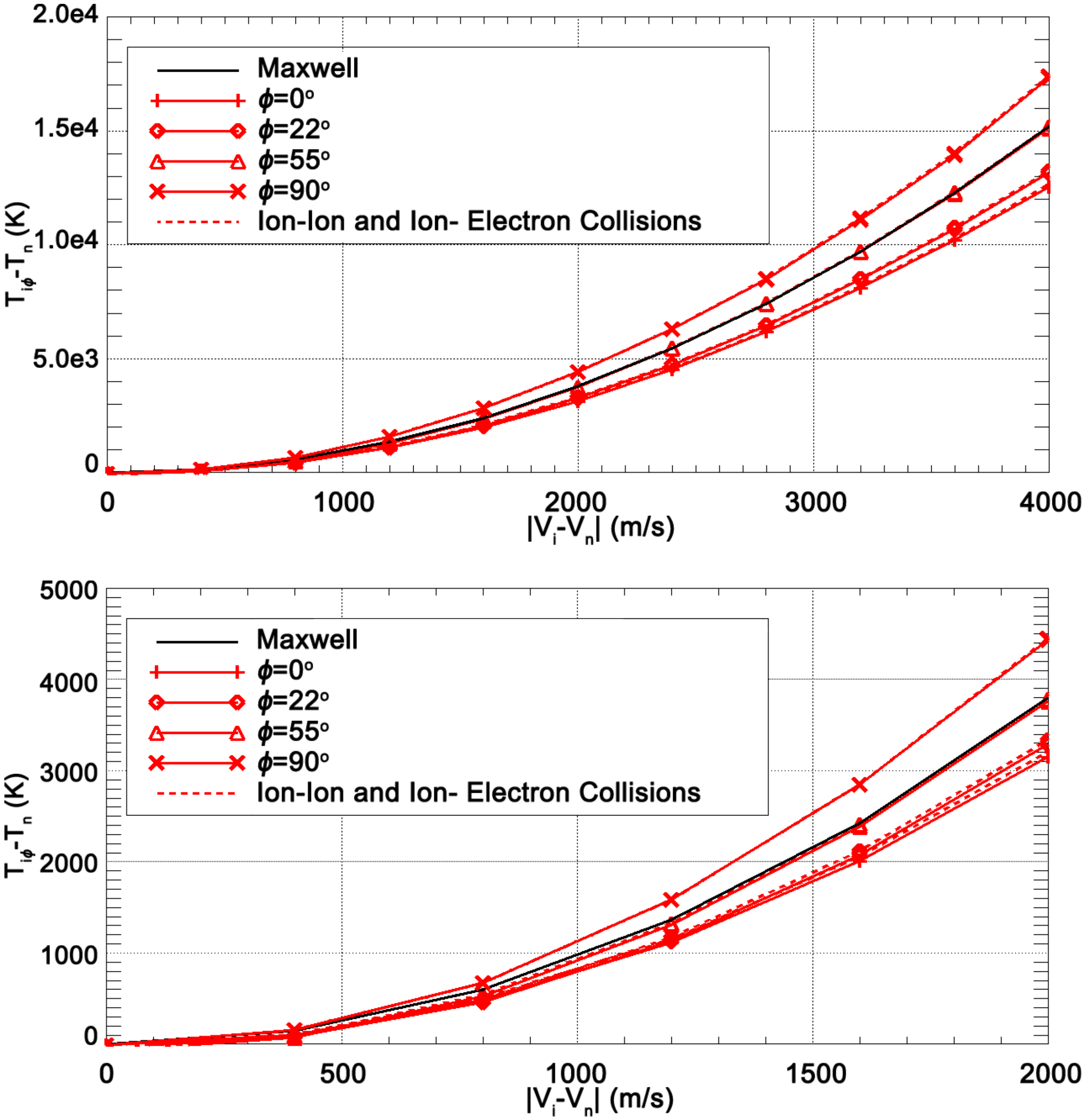

Figure 4.9: Same as in Figure 4.7 but for NO^+ collisions with 50% O and 50% N_2.

angles of 0°, 22°, 55°, and 90°. Only the results for electric fields of 50 mV/m or greater are shown because the spectra are nearly identical to equivalent Maxwellian spectra when the electric field is weak.

4.4.4 O^+ spectra

Figures 4.10 through 4.12 show the spectra created for O^+ ions colliding with O, based on the POH RCE cross-section, for electric fields of 50 mV/m, 100 mV/m, and 170 mV/m, respectively. The figures show that even for a 'moderate' electric field of 50 mV/m, the MC-derived ion velocity distributions are capable of creating spectra that differ substantially from those derived from Maxwellian ion velocity distributions at the same effective ion temperature. In qualitative agreement with earlier work on the subject (e.g., *Raman et al.*, 1981) for strong electric fields and large aspect angles, the spectra become triple-humped. A new feature from the present work, furthermore, is that in the magnetic field direction, the MC-derived spectra are similar to Maxwellian spectra, but with electron to ion temperature ratios that look larger than they actually are (as seen through the peak-to-trough ratio of a given spectrum). The origin of this new feature is rooted with the use of the second velocity moment in the definition of temperature. For the particular situation at hand, along the magnetic field direction, the bulk of the distribution is narrower than that of a Maxwellian with the same line-of-sight ion temperature because there are more particles in the high velocity tail of the velocity distribution. The figures also show the substantial influence of ion-ion and ion-electron collisions on the O^+ spectra. The results are similar if the KMV cross-section for collisions is used instead of the POH cross-section.

4.4.5 NO^+ spectra

Figures 4.13 through 4.15 show NO^+ spectra for collisions in a 50% O and 50% N_2 mixture (other background concentrations are shown in the supplementary material). As expected from the discussion in Section 4.4.2, these spectra are minimally influenced by ion-ion and ion-electron collisions. Compared to the O^+-O spectra, the MC simulated NO^+ spectra are actually quite similar to those obtained from an effective Maxwellian ion velocity distribution,

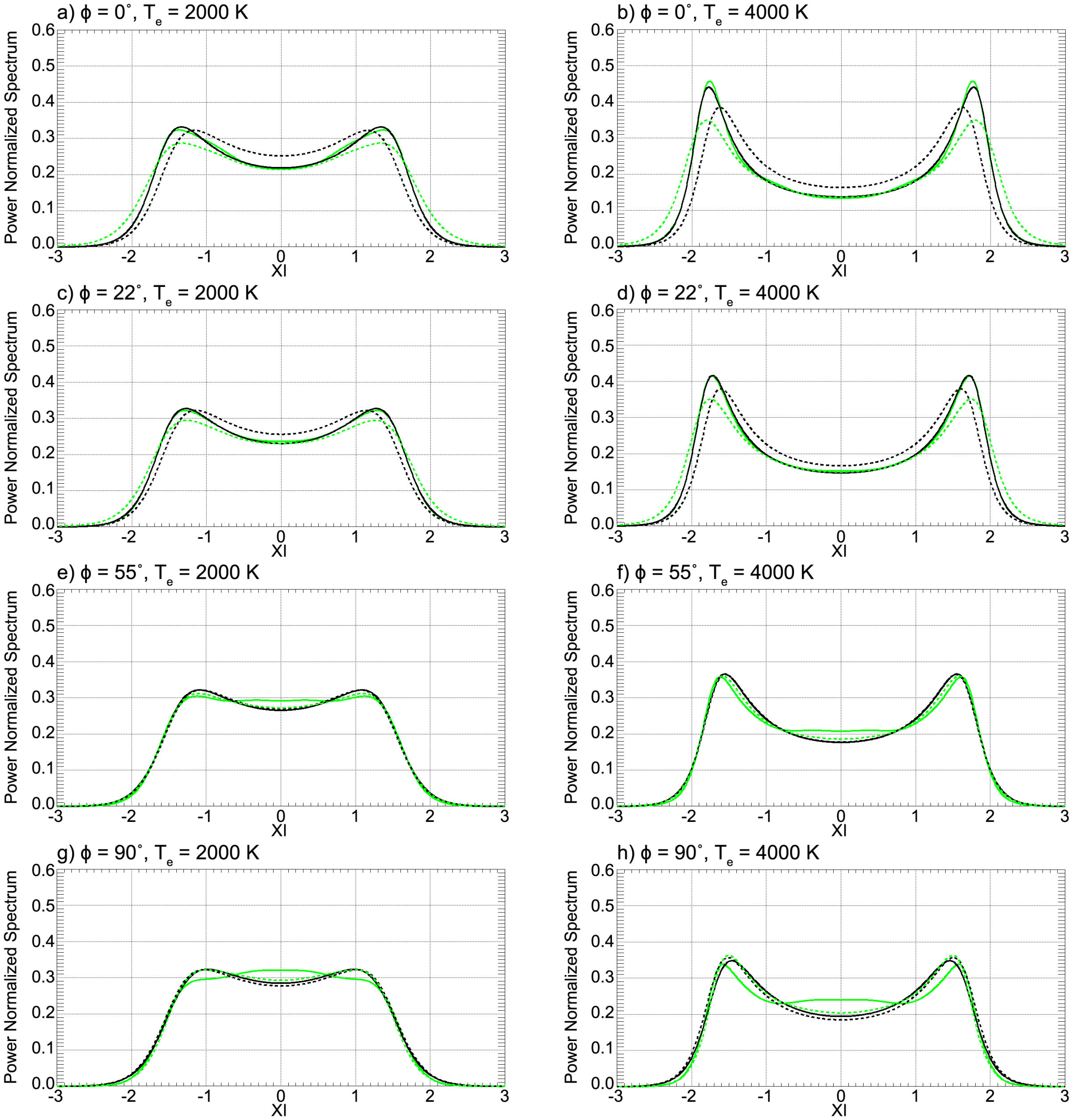

Figure 4.10: IS spectra for O^+-O collisions with a 50 mV/m electric field. First row from the top: 0° aspect angle. Second row from the top: 22° aspect angle. Third row from the top: 55° aspect angle. Bottom row: 90° aspect angle. Left-hand-side: 2000 K electron temperature. Right-hand-side: 4000 K electron temperature. Green curves: MC simulated spectra. Black curves: Maxwellian spectra with the same line-of-sight ion temperature. Dashed lines: with ion-ion and ion-electron collisions added in.

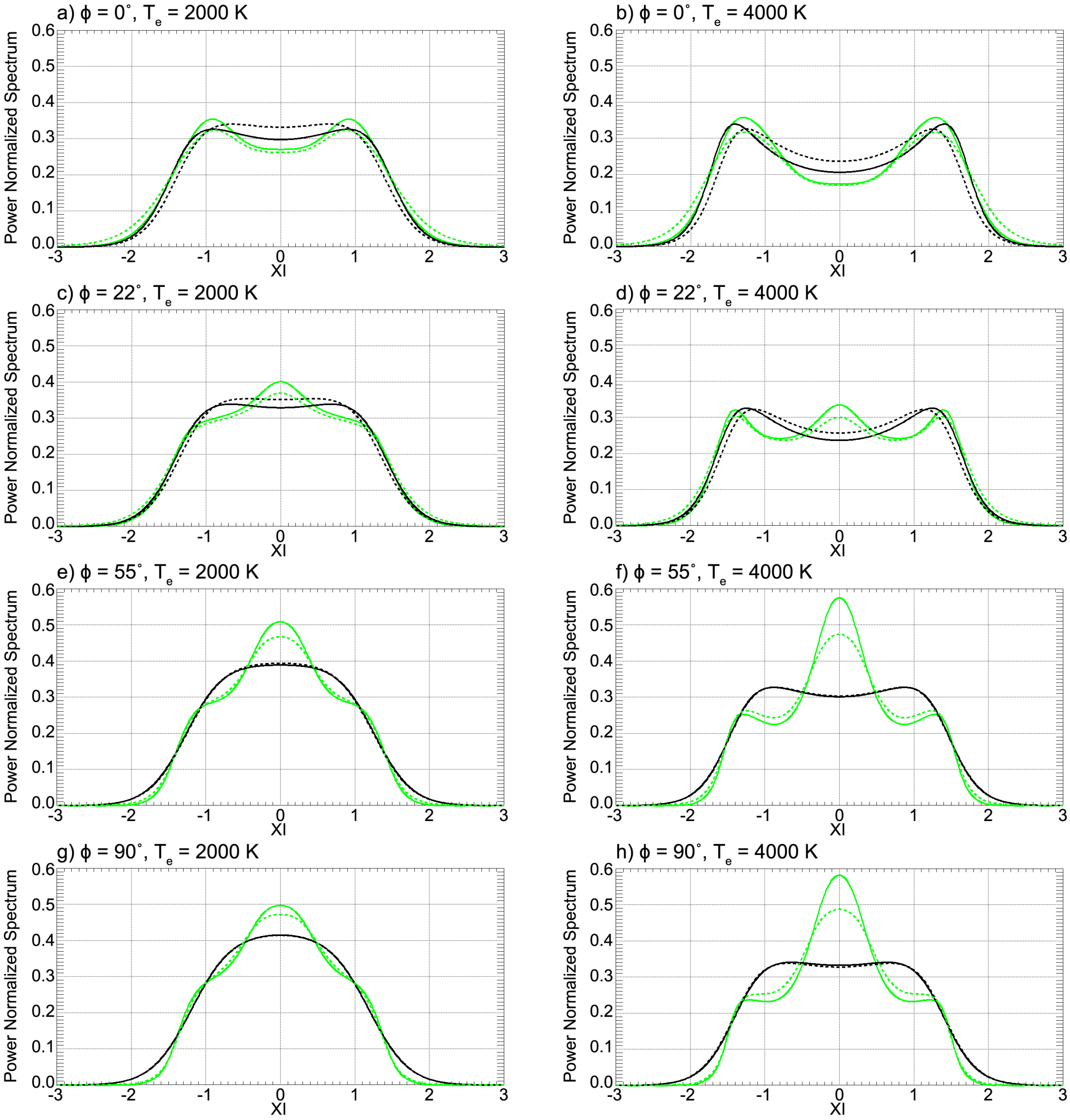

Figure 4.11: Same as in Figure 4.10 but for a 100 mV/m electric field.

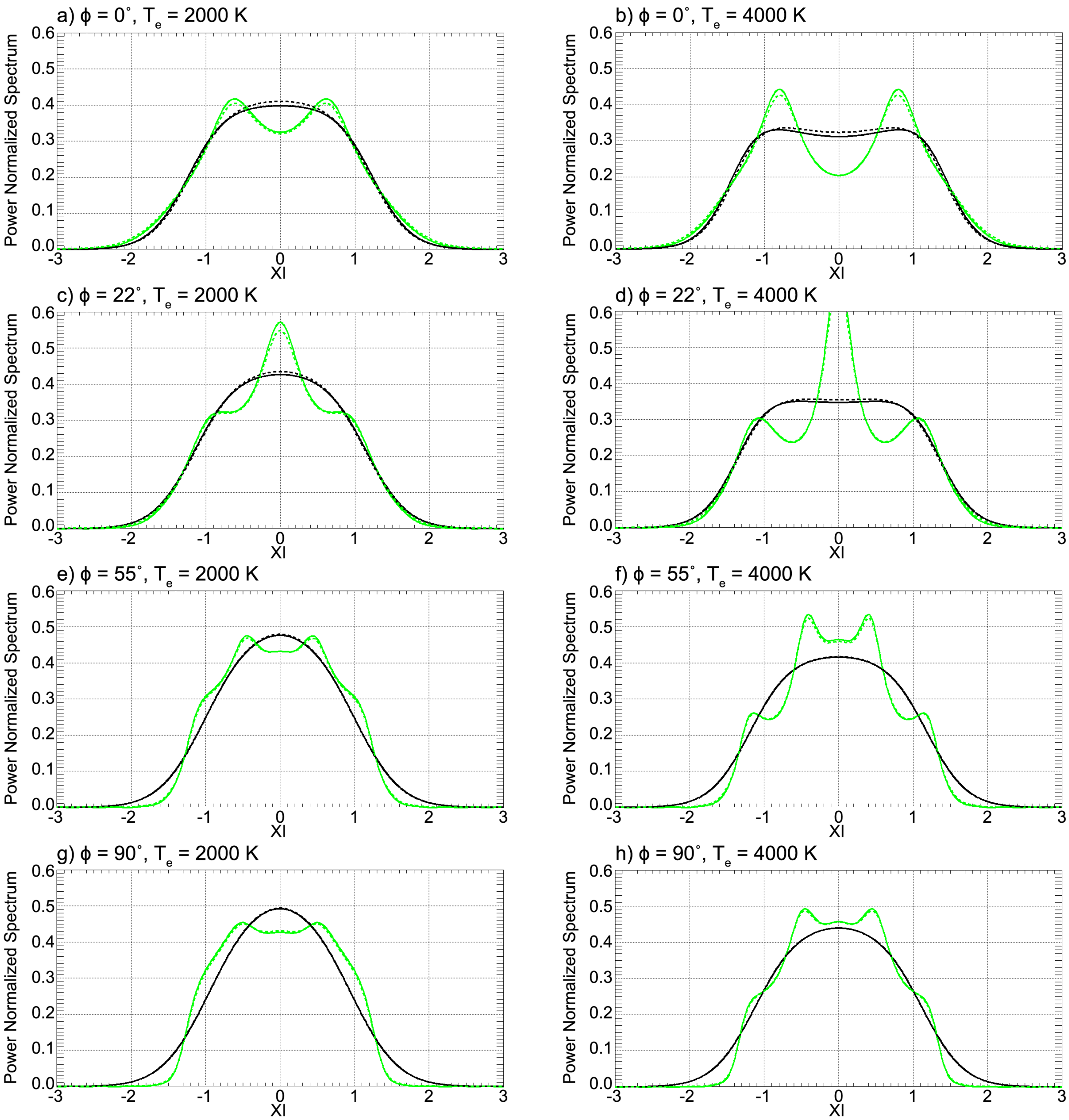

Figure 4.12: Same as in Figure 4.10 but for a 170 mV/m electric field.

particularly for the lower electron temperature at 2000 K. In addition, for a given electric field, aspect angle, and electron temperature, there is little variation as a function of the O to N_2 concentration ratio. Interestingly, the molecular ion spectra undergo their largest distortions at 100 mV/m in the figures shown here, whereas the spectra at 50 mV/m and 170 mV/m reveal hardly any detectable departure from their equivalent Maxwellian counterparts.

4.5 Summary and conclusion

The ion contribution to the plasma dielectric function has been calculated directly from MC simulations for the first time, using an advanced smoothing and fitting technique. The MC code developed by *Winkler et al.* (1992) has been the basis for these calculations, and corrections from the effect of collisions with other charged particles have been added. Based on these calculations, this study was able to (1) determine the response of the ion temperature along various lines-of-sight and for a wide range of electric field strengths, (2) determine the response for the shape of IS spectra, and (3) study the stability of the velocity distributions against electrostatic field-aligned instabilities.

4.5.1 Ion temperature results

We need to consider two factors affecting the ion temperature in the presence of strong electric fields, namely, its anisotropy and its departure from a pure parabolic dependence on the magnitude of the relative drift between ions and neutrals. It is important to consider these effects for a proper characterization of frictional heating in Joule heating studies.

Given the anisotropy in the ion temperatures, we have studied the dependence of the MC calculated line-of-sight ion temperature $T_{i\phi}$ on the aspect angle. We have found that when corrections due to Coulomb collisions can be neglected, $T_{i\phi}$ is for the most part well described by its dependence on the parallel and perpendicular temperature through Equation 4.7, implying for one thing that the temperature at 55° aspect angle is the same as the average ion temperature needed for Joule heating rate studies. As expected from previous work on the subject, the temperature anisotropy was found to be much stronger for O^+ ions than for NO^+ ions, owing to O^+-O RCE collisions making the perpendicular temperature

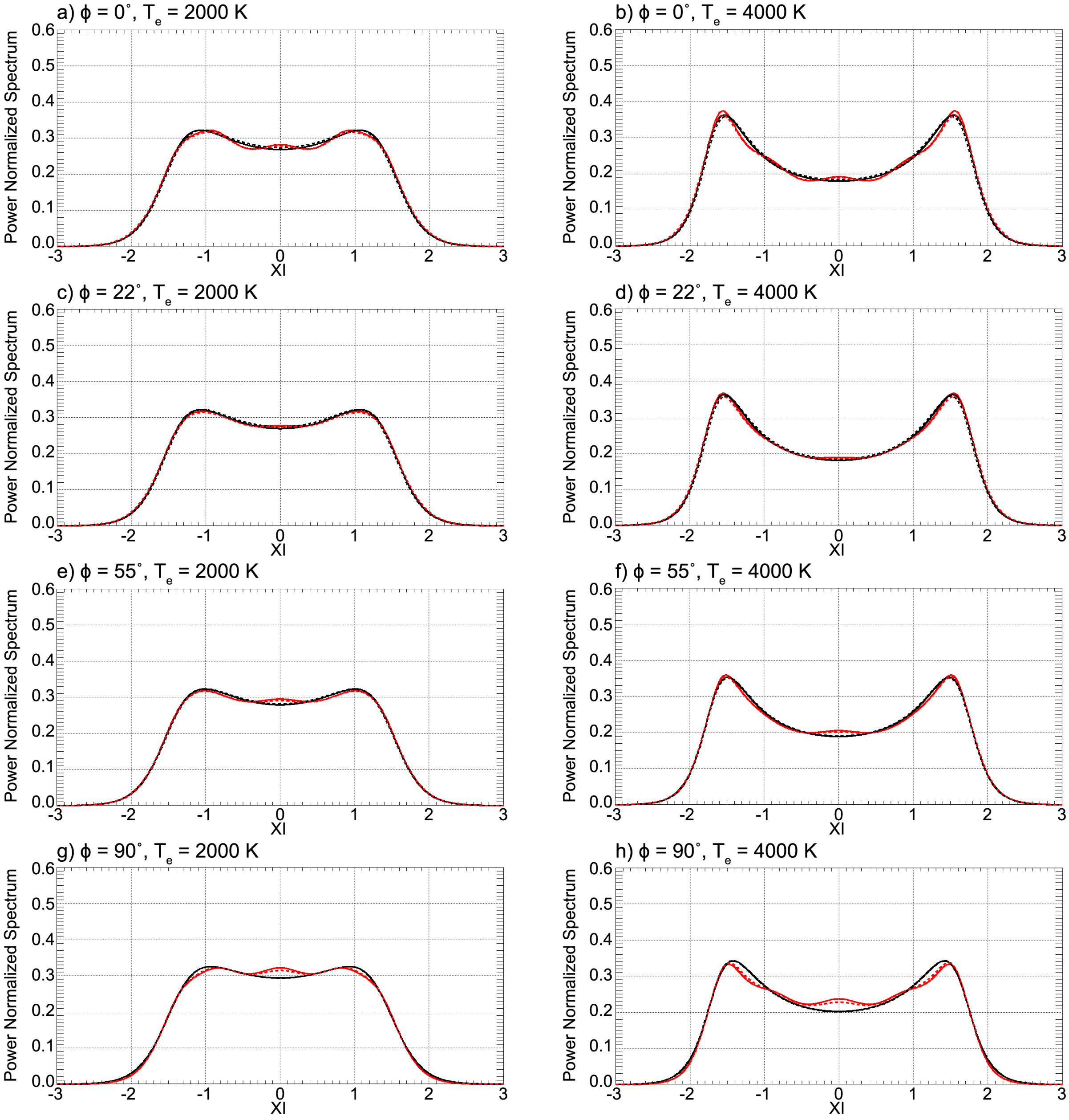

Figure 4.13: Same as in Figure 4.10 but for NO^+ ions colliding with a mixture 50% O and 50% N_2.

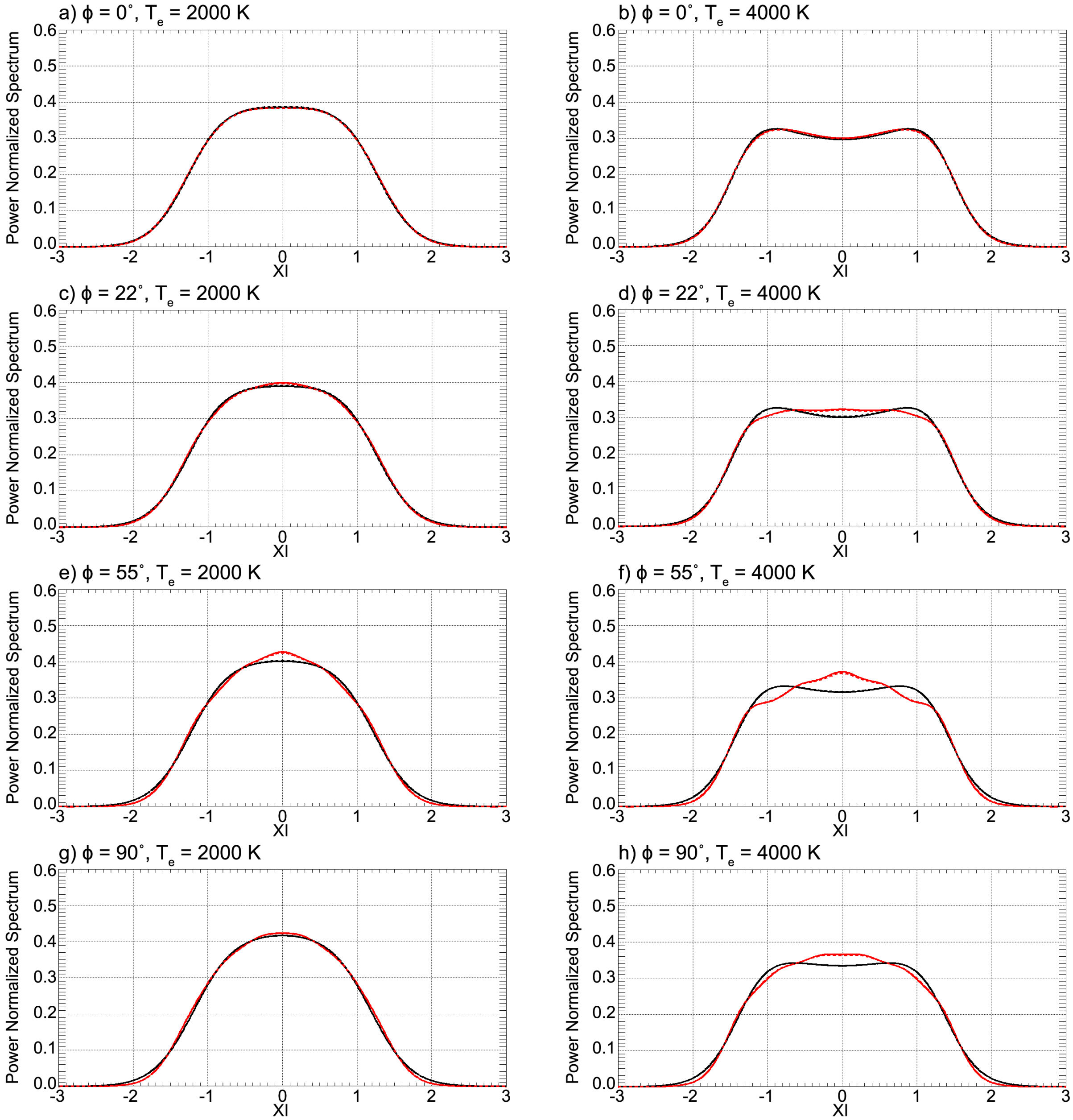

Figure 4.14: Same as in Figure 4.13 but for a 100 mV/m electric field.

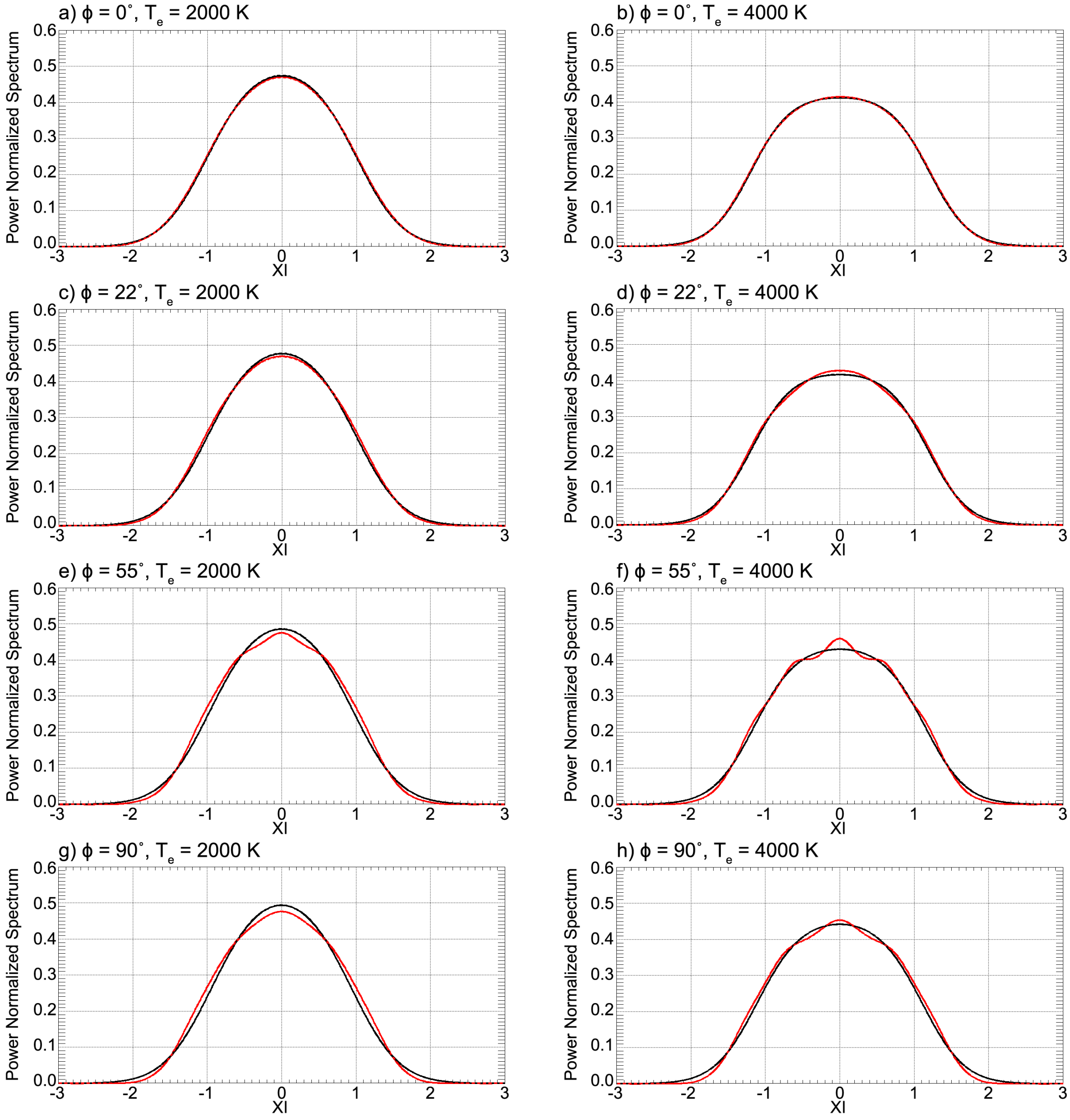

Figure 4.15: Same as in Figure 4.13 but for a 170 mV/m electric field.

much larger than the parallel temperature. We also found that the anisotropy is larger and significant enough to be measurable if we use the KMV RCE collision cross-section as opposed the more recently published POH RCE cross-section. It should be noted, however, that corrections due to Coulomb collisions have measurable effects on the O^+ ions. Note that as the altitude increases, the influence of Coulomb collisions also increases: as the neutral density decreases, the corresponding ion-neutral collision frequency lowers, thereby increasing the impact of Coulomb collisions in Equation 4.21. This explains the increase in line-of-sight ion temperature with altitude seen in real ISR data, such as in *Goodwin et al.* (2014). This, however, does not change the fact that $T_{i\phi}$ at 55° is equal to the average T_i. Also, unlike their O^+ counterparts, NO^+ ions are unaffected by collisions with other charged particles because of their low altitude. Finally, our calculations highlight that, under very strong electric field conditions, the NO^+ temperatures can be much greater than the O^+ temperatures due to the fact that the ion-neutral temperature difference is proportional to the mean neutral mass, which is larger at the lower altitudes where NO^+ is the dominant species.

A second element of the $T_{i\phi}$ determination comes from the speed dependence of the temperature difference between ions and neutrals. Our calculations show that when collisions with atomic oxygen dominate, the average O^+ temperature undergoes significant departures from the pure parabolic Maxwell molecule dependence on the magnitude of the relative ion-neutral drift that is widely used in the literature. By contrast, there is essentially no such deviation from a Maxwell molecule behavior for NO^+ ions colliding with any neutral atmospheric mix.

4.5.2 IS spectral calculations

As expected from previous work, we have found from the MC simulated velocity distributions that spectral differences between non-Maxwellian plasmas and equivalent (same line-of-sight ion temperature) Maxwellian plasmas are far greater for O^+ ions above 250 km than for NO^+ ions at lower altitudes. As far as NO^+ ions are concerned, the spectral shapes are for the most part so similar to those associated with a Maxwellian velocity distribution with the same line-of-sight temperature that there is apparently little need to analyze NO^+ spectra with non-Maxwellian ion dielectric functions. One exception is electric field of the order of 100 mV/m. In that case, the NO$^+$ spectral shape does have visible departures from its Maxwellian counterpart. These differences are greater for larger electron temperatures and for aspect angles of the order of 55° or greater.

The situation for the O$^+$ spectral shape is very different and far more complex than has been inferred in previous work based on fits to RCM solutions. For instance, for electric fields of the order of 100 mV/m or greater, unless the line-of-sight is very close to the magnetic field direction, the spectra from the MC simulations contain multi-peaked shapes that are rather different from those expected from earlier work (e.g., *Raman et al.* (1981); *Suvanto et al.* (1989)). Parallel or nearly parallel to the magnetic field direction, the spectra coming from MC velocity distribution simulations are similar to those from effective Maxwellian distributions but with the important caveat that they point to a larger $T_e/T_{i\phi}$ ratio than is actually present. This feature comes from an elongated high-energy tail in the ion velocity distribution relative to a Maxwellian with the same temperature, meaning that the bulk of the distribution has to be narrower than the equivalent Maxwellian.

4.5.3 Plasma stability

The ion velocity distributions coming from the MC simulations of the POH cross-section are more stable than what has been inferred from RCM models in the past. This means that the loss-cone (or Post-Rosenbluth) instability requires a larger electric field to be excited than assumed in the past. Moreover, we found that the instability may not be triggered at all — at least not for electric fields less than 200 mV/m — if we use the more recent POH RCE cross-section, whereas the older KMV cross-section does give rise to the instability.

4.5.4 Access to the simulated ion velocity distributions

A central goal of the present work has been to make it practical to process ISR data with a proper allowance for strong departures of the ion velocity distribution from the Maxwellian shape. To make it feasible to analyze the data with a fast computation of the ion dielectric function, we have produced a large number of ion velocity distribution simulations for various aspect angles and effective electric field strengths. For each electric field and aspect angle computation, a set of 50 Legendre polynomial coefficients was computed to provide a smooth, accurate, and continuous description of the distribution as a function of y (recall $y = v_x/b$) along the line-of-sight for effective electric fields in the range of 20 mV/m to 200 mV/m by steps of 10 mV/m and for aspect angles between 0 and 90° by steps of 10°. We have found that various suitable interpolation schemes could be used on each of the 50 polynomial coefficients to produce velocity distributions at non-tabulated values of the effective electric field and aspect angles. Additional aspect angles and electric fields could also be handled under request as well.

In supplementary material, we offer a listing of the 50 polynomial coefficients with an explicit description of how to use them to recreate the ion velocity distribution for a posted electric field and aspect angle. A user with a standard analysis program can substitute an interpolated ion velocity distribution in place of a Maxwellian to construct spectra for any electron temperature, plasma density, radar frequency, neutral density, electric field, and aspect angle. Software used to reconstruct the ion dielectric function from these velocity distributions is also available upon request, as well as the coefficients for different collision types. Only one neutral temperature is used for these distributions, namely, 1000 K. A change in that temperature by a few hundred K can be handled by adding that difference to the ion temperatures. For example, if the desired neutral temperature is 1300 K, an ion temperature of 2000 K translates to a 700 K difference between the line-of-sight ion temperature and the neutral temperature, instead of 1000 K. For NO^+ with a 50% O and 50% N_2 neutral mixture, this would mean that the velocity distribution would be associated with a relative ion-neutral drift of 820 m/s instead of 1000 m/s (as per Figure 4.9), and the non-Maxwellian signature would be accordingly somewhat smaller.

Finally, we note that our simulated velocity distribution determination at 90° should be most useful in particularly strong electric field situations for Retarding Potential Analyzer data studies of the type undertaken by *St-Maurice et al.* (1976).

4.6 Acknowledgments

This study is sponsored by the Canada Research Chair (CRC) Program and by the Natural Sciences and Engineering Research Council of Canada (NSERC). MSIS data were taken from https //omniweb.gsfc.nasa.gov/vitmo/msis_vitmo.html. In the supplementary material, a listing of the 50 polynomial coefficients is offered with an explicit description of how to use them to recreate the ion velocity distribution for a posted electric field and aspect angle. Software used to reconstruct the ion dielectric function from these velocity distributions is also available upon request.

4.7 Additional Material

This section details additional work performed outside of the submitted "Incoherent scatter radar spectra based on Monte-Carlo simulations of ion velocity distributions under strong ion frictional heating". However, Figure 4.16 has been submitted to Radio Science as a potential cover image.

For a global look at the spectral signatures the evolution of IS spectra for a POH O^+-O cross-section is shown in Figure 4.16 as a function of electric field strength and aspect angle for a 3000 K electron temperature. This figure highlights many of the features seen previously, but in particular this figure shows the evolution of a central (low frequency) feature as a function of the electric field strength and of the aspect angle. This central peak becomes particularly noticeable at 100 mV/m and higher, but is most unique at approximately 20°. To both test the dependency of this feature on electron temperature, and further analyze the dependency of this feature on aspect angle, Figures 4.17 through 4.19 show the evolution of an IS spectra for a POH O^+-O cross-section as a function of electric field strength and electron temperature for aspect angles 10°, 20°, and 30°. Here, 20° still shows a much more pronounced central peak than either 10° or 30° (or even similar figures at aspect angles 0°, 40°, 50°, 60°, 70°, 80°, and 90°), regardless of electron temperature. Not only is this feature most distinct at 20°, it is also the least likely to be confused with the spectral features seen from Maxwellian ion velocity distributions, regardless of the electron-ion temperature ratio.

This leads us to conclude that the spectra stemming from toroidal velocity distributions at 100 mV/m and higher are particularly identifiable at approximately 20° aspect angle, which is not what was expected when this research was started.

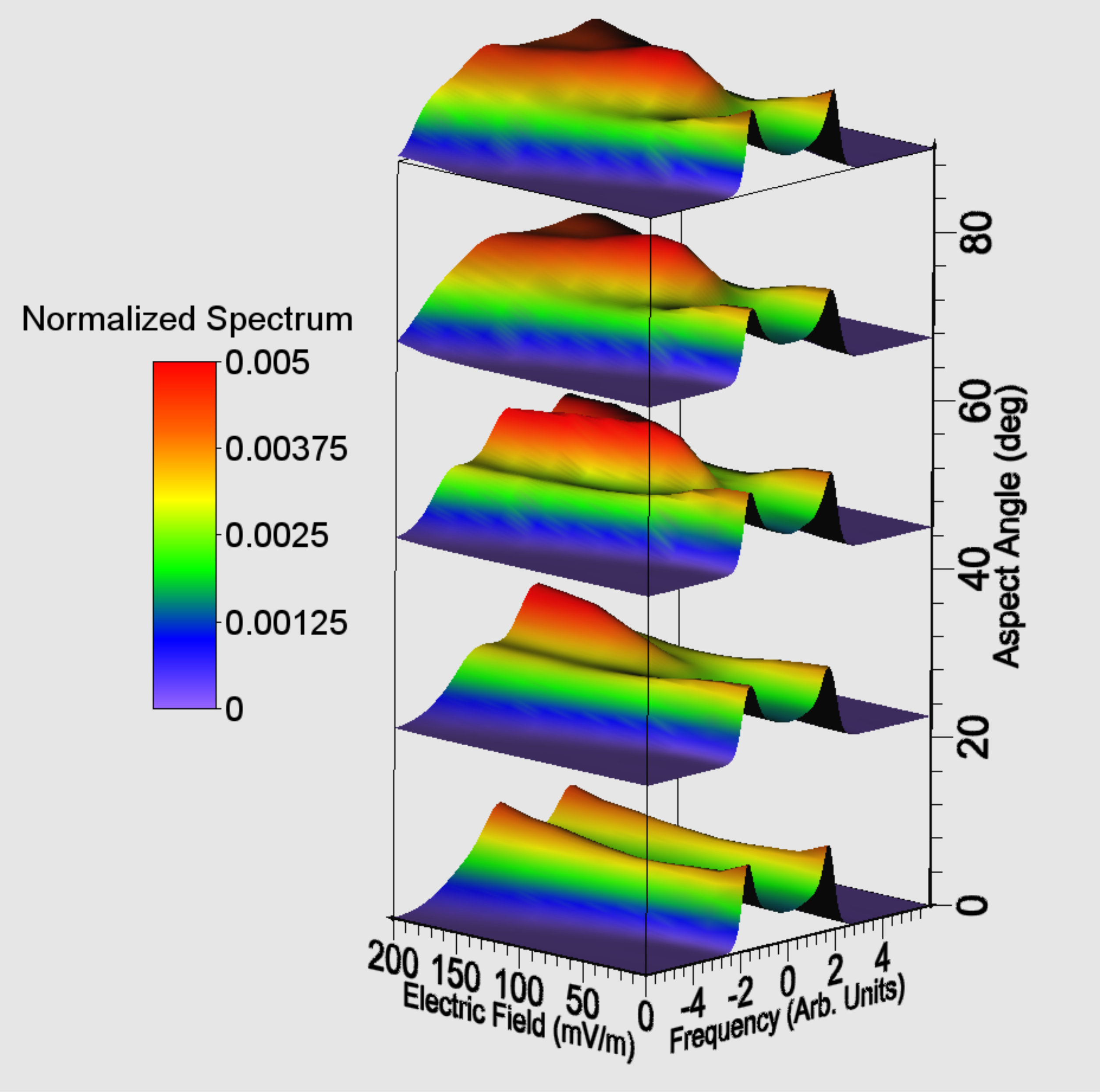

Figure 4.16: Evolution of theoretical IS spectra for a POH O^+ ionosphere as a function of electric field strength and aspect angle. Electron temperature taken to be 3000K. All spectra normalized with respect to their total power.

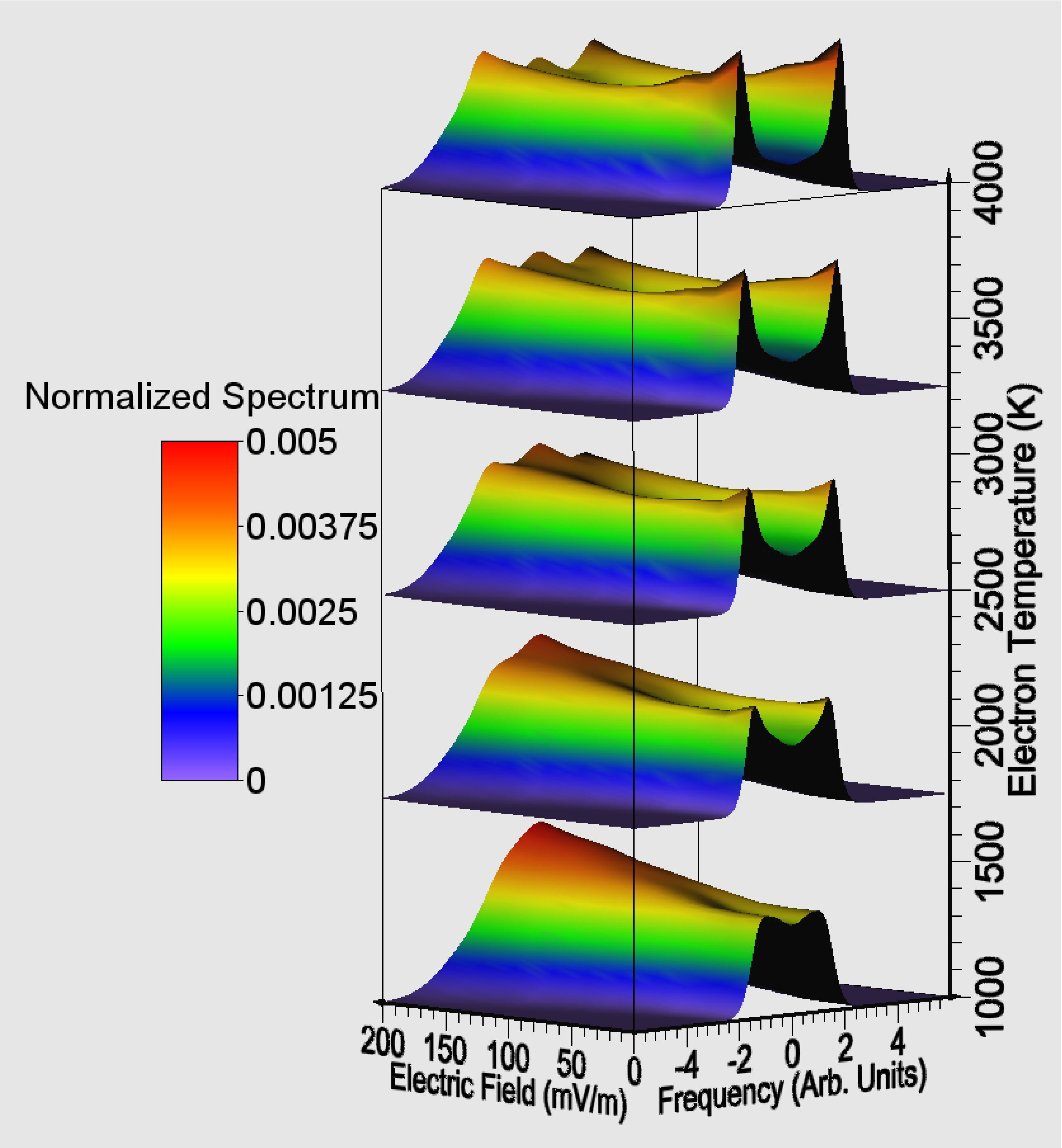

Figure 4.17: Evolution of theoretical IS spectra for a POH O^+ ionosphere as a function of electric field strength and electron temperature. The aspect angle is taken to be 10°. All spectra normalized with respect to their total power.

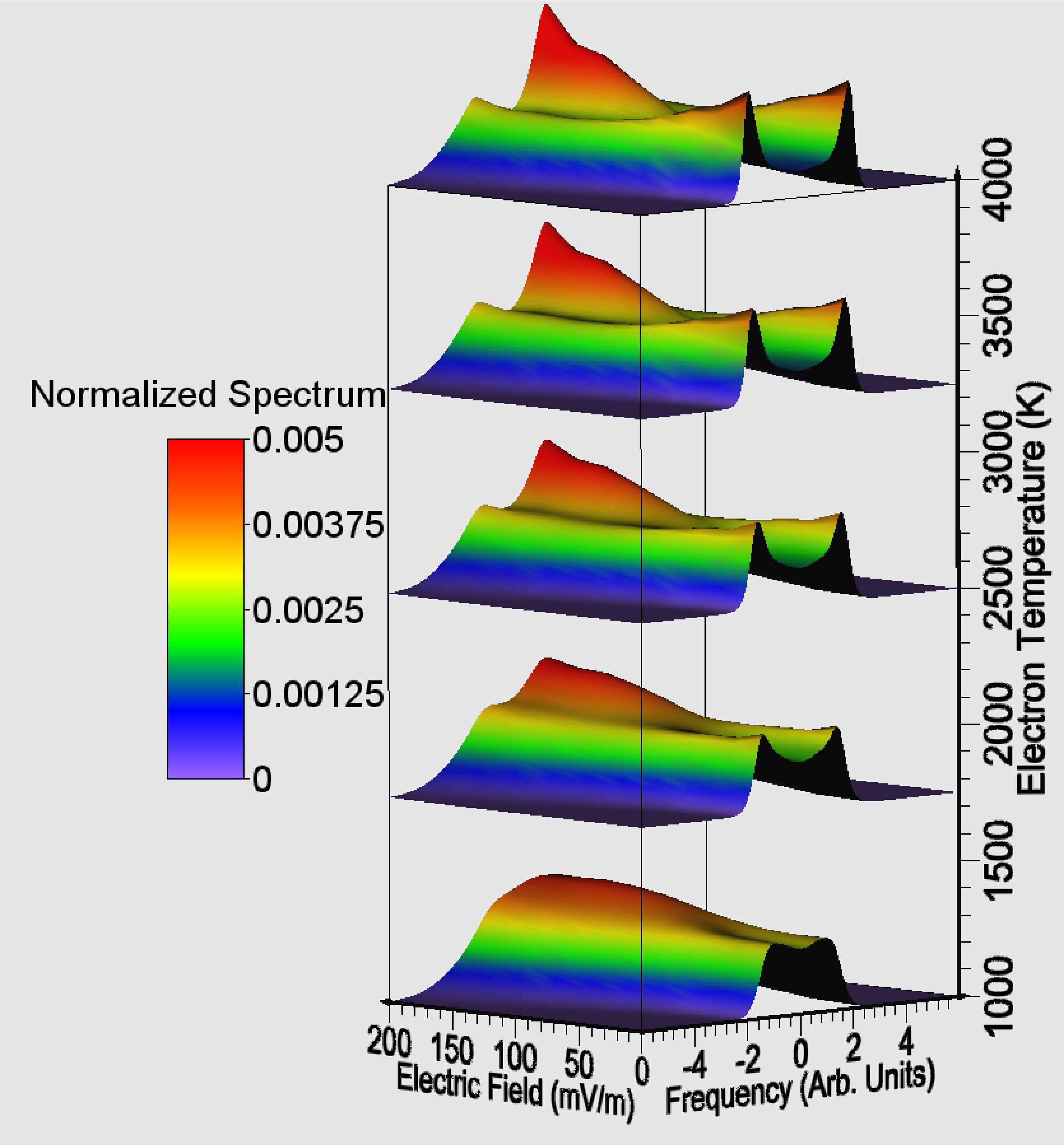

Figure 4.18: Evolution of theoretical IS spectra for a POH O^+ ionosphere as a function of electric field strength and electron temperature. The aspect angle is taken to be 20°. All spectra normalized with respect to their total power.

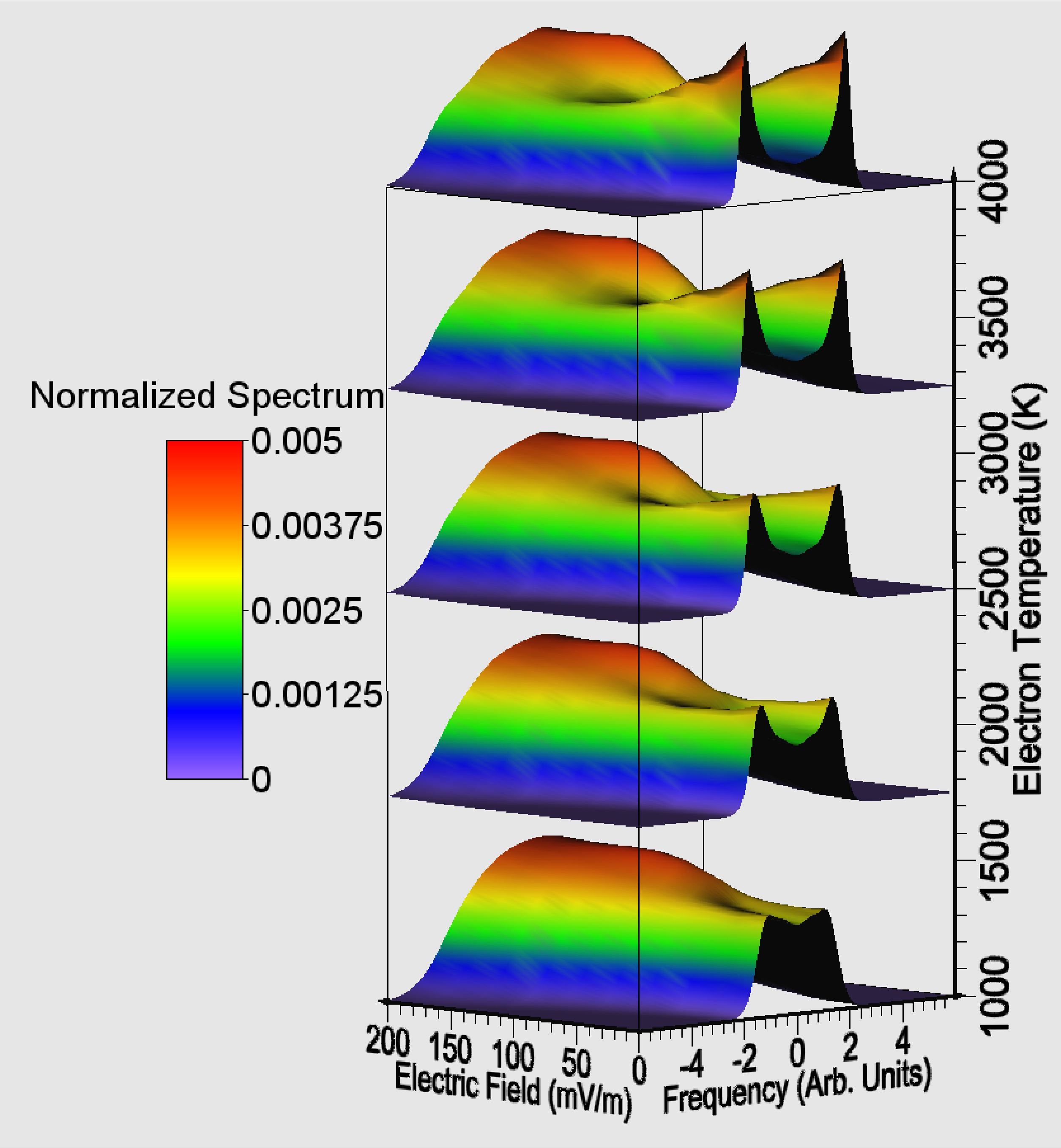

Figure 4.19: Evolution of theoretical IS spectra for a POH O^+ ionosphere as a function of electric field strength and electron temperature. The aspect angle is taken to be 30°. All spectra normalized with respect to their total power.

Chapter 5

CHARACTERIZING ION TEMPERATURE ANISOTROPY AND THE ELECTRIC FIELD VECTOR USING RISR-N OBSERVATIONS

Chapter 4 uses simulations of ion-neutral collisions in a magnetized environment to characterize the ion temperature anisotropy. Using instruments to do this requires multiple measurements at different aspect angles of the same ion velocity distribution. This is relatively simple to do with in situ instruments, such as with the EFI on the Swarm spacecraft (*Archer et al.*, 2015), but this is more challenging to do with a single ground-based ISR because each beam probes a different region. This stated, it is still possible to characterize ion temperature anisotropy using ISRs, but strong electric field events and specific beam arrangements are required.

For similar reasons, it is also challenging to characterize the electric field vector in a given location using an ISR. The Madrigal database (an online geospace database) provides a calculation of the electric field vector as a function of latitude along a direct path towards the geomagnetic north pole using a Bayesian approach (*Heinselman and Nicolls*, 2008). However, even though these calculations are shown to agree with rocket observations, this technique requires multiple measurements that are separated by several degrees of longitude. This technique therefore misses smaller scale structures in the electric field and can be fraught with difficulty at times.

This chapter continues the electric field and ion temperature anisotropy studies of *Akbari et al.* (2017b) and Chapter 4 by using RISR-N plasma parameters to characterize both the ion temperature anisotropy and the electric field vector. This chapter first discusses the special ISR beam arrangement used in this research, as well as a specific"experiment" (a beam pattern) which had this beam arrangement during a strong electric field event. Next, the results of characterizing the ion temperature anisotropy and the electric field vector from this arrangement are discussed. Lastly, a summary of this research is given, along with a list of the future goals of this work.

However, note that since Chapter 4 highlights the importance of using complete descriptions of ion velocity distribution based on MC simulations in IS spectral fitting techniques, meaning that the results of this chapter are only preliminary because this data is inferred using Maxwellian spectral fitting techniques. Therefore, the work presented in this chapter will ultimately be reprocessed to improve the quality of the results.

5.1 ISR Experiment Setup and Observations

In order to characterize the ion temperature anisotropy, multiple measurements of the same ion velocity distribution are needed at different aspect angles. This can be arranged with multiple, independent ISRs, but it is usually not possible to use more than one ISR, due to the current space distribution of such radars. However, this can be done with simultaneous measurements from multi-beam radars, like AMISR. Figure 5.1 shows a cartoon of RISR-N making measurements with two beams, both pointing towards the geomagnetic north pole at different elevation angles. Even though line-of-sight measurements of the drift are not necessarily measurements of the $\mathbf{E} \times \mathbf{B}$ drift, multiple beam measurements can help infer the $\mathbf{E} \times \mathbf{B}$ drift if there are no large changes with azimuth or altitude in the electric field. In Figure 5.1, the beams overlap within the same flux tube and are taking nearby measurements of the weakly-ionized, magnetized O^+ plasma between roughly 200 km and 400 km. In this figure, beam 1 is measuring the line-of-sight velocity, $v_{\phi 1}$, at one altitude and beam 2 is measuring the line-of-sight velocity, $v_{\phi 2}$ at a slightly different altitude. When the parallel electric field is negligible the north-south $\mathbf{E} \times \mathbf{B}$ drift, $v_{\perp los}$, is the dominant process determining both v_{ϕ} values, so that for either beam:

$$v_{\perp los} = \frac{v_{\phi}}{\sin \phi} \tag{5.1}$$

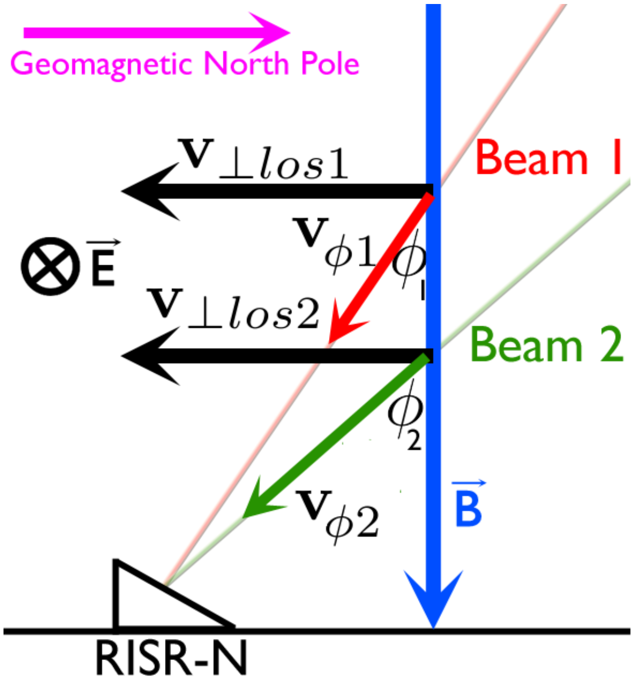

Figure 5.1: A cartoon of RISR-N probing the ionosphere with two different beams. The red and green lines show two different beams, the red and green arrows show the two respective line-of-sight velocity measurements, the blue arrow is the magnetic field, the purple arrow indicates the location of the geomagnetic north pole relative to the experiment, and the black arrows represent the component of the $\mathbf{E} \times \mathbf{B}$ drift resolved from the line-of-sight ion velocity measurements. ϕ_1 and ϕ_2 are the aspect angles of beam 1 and beam 2. As indicated, for this geometry the electric field is into the page.

where ϕ is the aspect angle of a given beam. Therefore, if the two $v_{\perp los}$ measurements in Figure 5.1 are close together and nearly identical, then both measurements are examining similar ion velocity distributions from different aspect angles. Although there are several experiments frequently running on RISR-N that contain beam arrangements conducive to this study, the real challenge is having this beam arrangement run during a period of extreme heating between 200 to 400 km.

In the WorldDay66m beam arrangement there are four beams pointing towards the geomagnetic north pole at different elevation angles, as shown in Figure 5.2. Between 11 September 2014 and 15 September 2014 this beam arrangement ran on RISR-N and measured a strong heating event on 12 September 2014 between 18 and 20 UT. This heating event is the focus of the work by *Clauer et al.* (2016), which uses these measurements to examine ionospheric data near local noon within unusually strong reverse convection cells that developed during a period of very strong (28 nT) northward IMF.

The plasma parameters during this period, including $v_{\perp los}$, are given in Figures 5.3 and 5.4 as a function of UT and altitude. These figures only focus on the 55° and 75° elevation angles because: 1) their measurements are close in magnetic latitude and therefore these beams measure similar (if not the same) flux tubes, 2) these two beams have the highest signal-to-noise ratio between 200 km and 400 km, and 3) they are close to each other between 200 km and 400 km, which reduces altitudinal variations in the ion velocity distribution. Figures 5.3 and 5.4 show a large line-of-sight ion temperature coincident with a strong negative north-south component of the $\mathbf{E} \times \mathbf{B}$ drift, indicating a 3 km/s sunward drift. Figure 5.5 shows that these strong drifts are coincident with large electric fields inferred by RISR-N using the *Heinselman and Nicolls* (2008) approach. During this period there is also an elevated plasma density. Meanwhile, the electron temperature is rather uneventful between 200 km and 400 km during this time, but *Clauer et al.* (2016) highlights electron temperature enhancements in the *E*-region around 110 km, which is expected from strong electric fields (*Foster and Erickson*, 2000). Figure 5.6 shows that parallel to the magnetic field the drifts are less than 200 m/s in magnitude. This not only implies that the electric field parallel to the magnetic field is small, but also that the vertical drifts are negligible compared the electric fields perpendicular to the magnetic field that drive the $v_{\perp los}$ values found from the 55° and 75° elevation angle beams.

To show that $v_{\perp los}$ is nearly identical for both the 55° and 75° beams, measurement "pairs" between roughly 200 km and 400 km are designated. In each pair, measurements are separated by less than 10 km in altitude, one measurement is taken from the 55° beam, and one measurement is from the 75° beam. Figures 5.7 to 5.9 show line plots of $v_{i\phi}$ and $v_{\perp los}$ for several pairs as a function of UT. Both measurements in a pair show similar $v_{i\phi}$ values, but when Equation 5.1 is used the $v_{\perp los}$ values resolved from either measurement are almost identical, and often even contain the same fine details. Figure 5.10 further emphasizes the similarities in $v_{\perp los}$ by taking the values inferred from the 55° beam against those inferred simultaneously from the 75° beam. In each figure an orthogonal least-squares fit is performed, that is, a least-squares fit in which regression considers both dependent and independent variables. The slope of the fit performed for each pair is close to one, implying that each

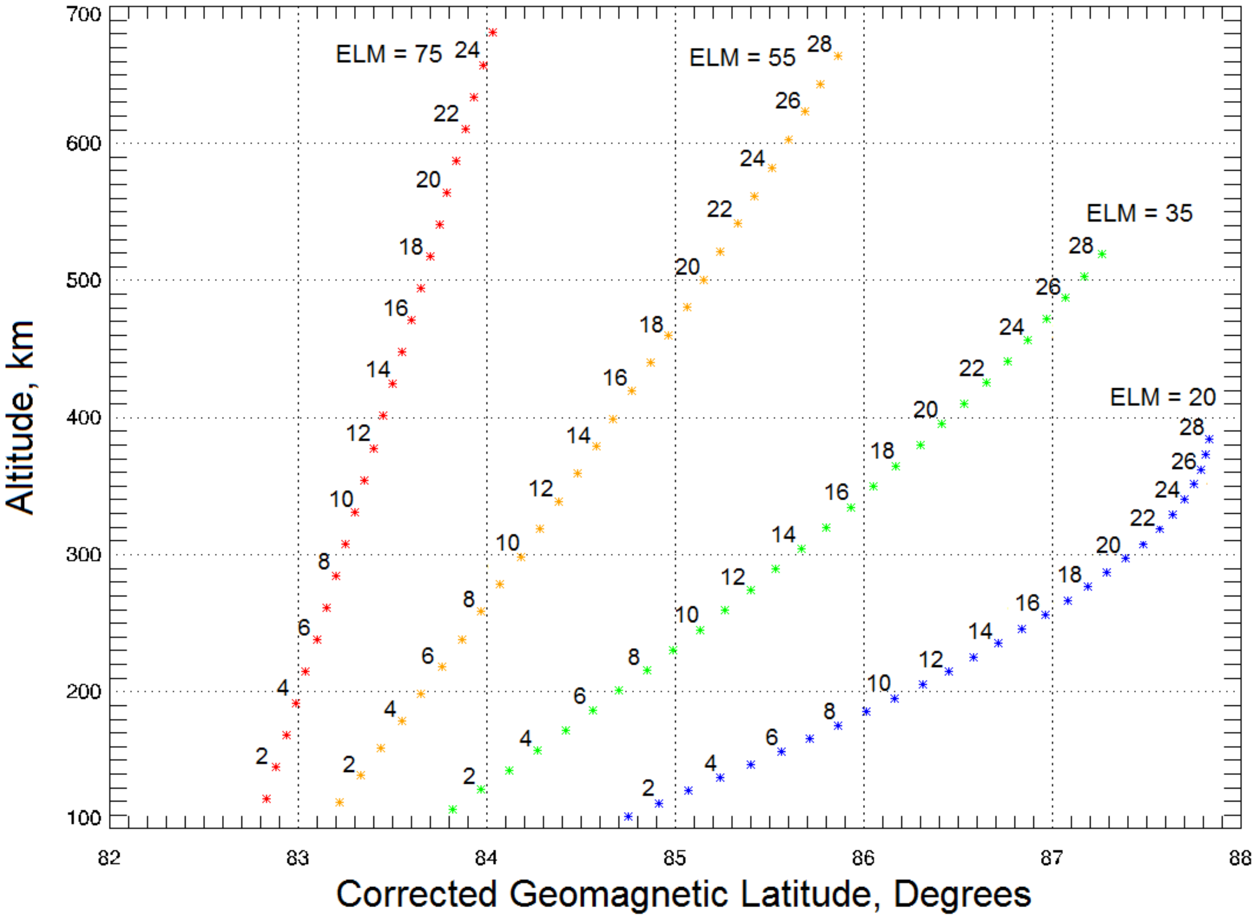

Figure 5.2: The beam arrangement for the WorldDay66m experiment, which ran from 21.5 UT 11 September 2014 to 0.01 UT 15 September 2014. The blue range gates indicate beam 55748, which has an elevation angle of 20° and an aspect angle ranging between 111.66° and 117.98°. The green range gates indicate beam 56954, which has an elevation angle of 35° and an aspect angle ranging between 125.19° and 130.43°. The orange range gates indicate beam 60617, which has an elevation angle of 55° and an aspect angle ranging between 144.23° and 147.50°. The red range gates indicate beam 64280, which has an elevation angle of 75° and an aspect angle ranging between 163.55° and 164.36°. All beam depicted are at an azimuth of 26°, which is towards the geomagnetic north pole (other beams are available, but are not the focus of this research).

.

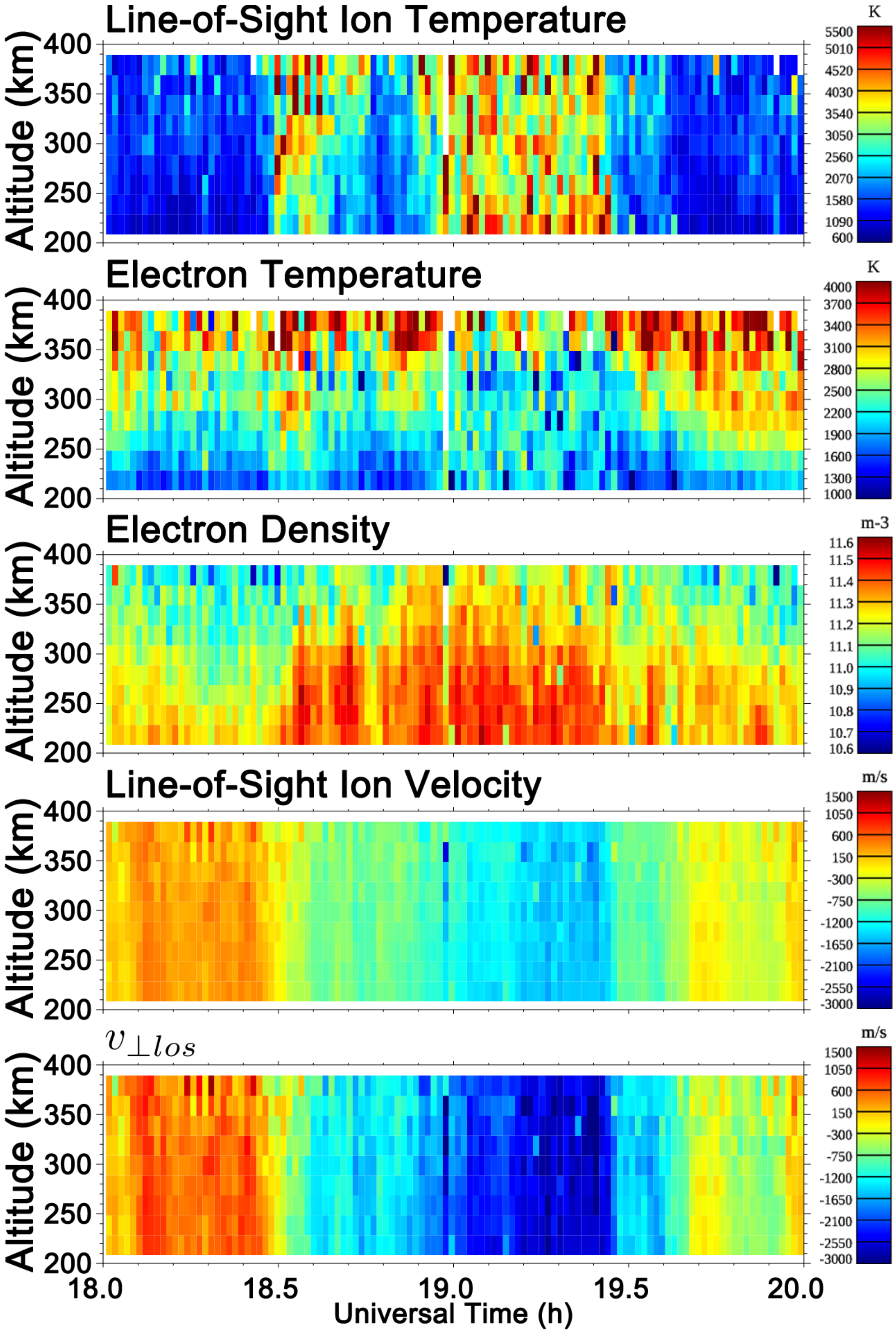

Figure 5.3: Plasma parameters captured by RISR-N on the 55° elevation beam during the 18 UT to 20 UT heating event on 12 September 2014. Equation 5.1 is used to calculate $v_{\perp los}$. Note that negative velocities are towards the radar, and positive are away.

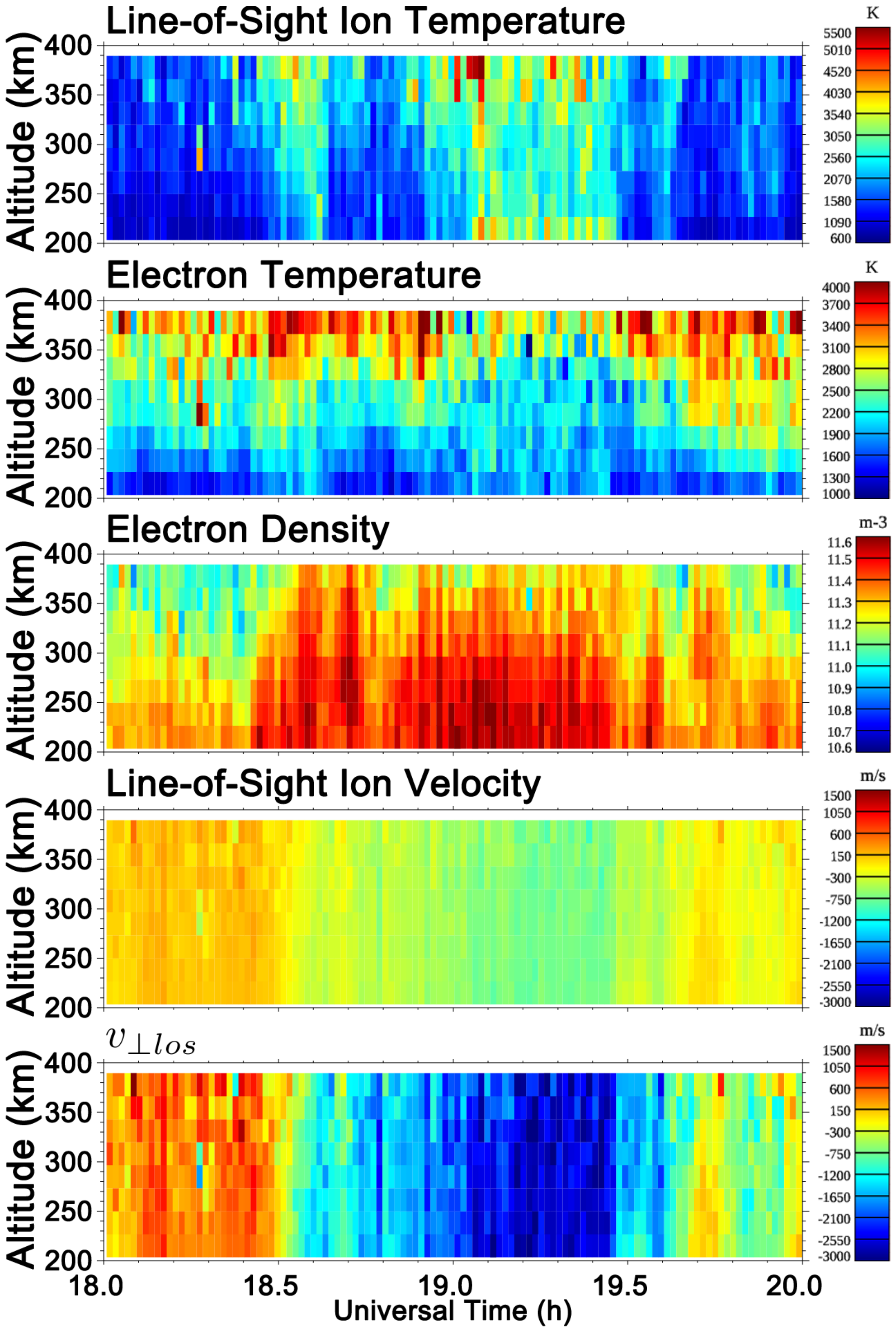

Figure 5.4: Plasma parameters captured by RISR-N on the 75° elevation beam during the 18 UT to 20 UT heating event on 12 September 2014. Equation 5.1 is used to calculate $v_{\perp los}$. Note that negative velocity values are towards the radar, and positive are away.

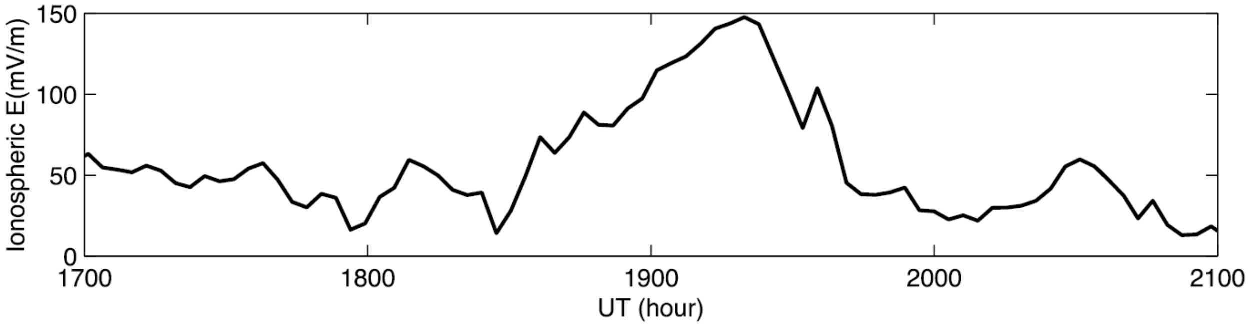

Figure 5.5: Ionospheric horizontal electric field inferred from RISR-N at 84° geomagnetic latitude on 12 September 2014. Figure taken from *Clauer et al.* (2016).

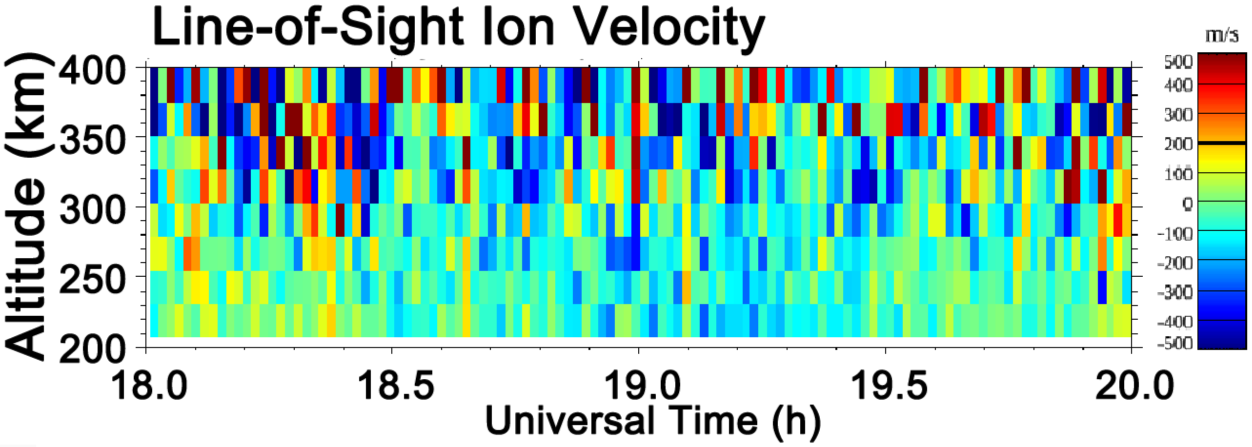

Figure 5.6: The line-of-sight ion velocity captured by RISR-N on a beam nearly parallel to the magnetic field during the 18 UT to 20 UT heating event on 12 September 2014. Negative velocities are towards the radar, and positive ones are away.

measurement in a pair is examining a similar ion velocity distribution from a different aspect angle.

5.2 Data Analysis

Knowing the temperature anisotropy present in the ionosphere, the effective electric field (namely the relative ion-neutral drift) can be resolved through Equation 2.6. If the electric field (the ion drift) is then known, it is possible to resolve the neutral wind at a given time and space. Given the ideal beam arrangement and the strong electric field event present, this section first compares this strong temperature event to the POH and KMV collision cross-sections discussed in Chapter 4, in order to characterize the ion temperature anisotropy and therefore the average temperature of the ionosphere. After this a new technique for resolving the electric field vector at a given latitude is presented, which can be used at a later date to constrain the F-region neutral wind.

In spite of the fact that this has not been analyzed with toroidal based spectra, this preliminary study is based on the notion that the ion temperature is not too strongly affected by toroidal distributions (*Akbari et al.*, 2017b) so that the results should be considered as correct to first order.

5.2.1 ISR Temperature Anisotropy Calculations

Figures 5.11 to 5.13 show the line-of-sight ion temperature as a function of UT for the designated pairs, and Figures 5.14 to 5.18 show the difference between the line-of-sight ion temperature and the base-line neutral temperature (the approximate average temperature in Figures 5.11 to 5.13 before heating occurred) from the 55° beam against those from the 75° beam. From these figures it is clear that the values from the 55° elevation angle are higher. This is consistent with Chapter 4, which shows an increase in line-of-sight ion temperature as the aspect angle increases. Figures 5.14 to 5.18 also reflect the anisotropy found from the different collision cross-sections discussed in Chapter 4. In general the data agrees best with the KMV O^+-O collision cross-section, which confirms that this region is populated by O^+ and suggests that ionospheric temperature anisotropy follows the KMV O^+-O collision

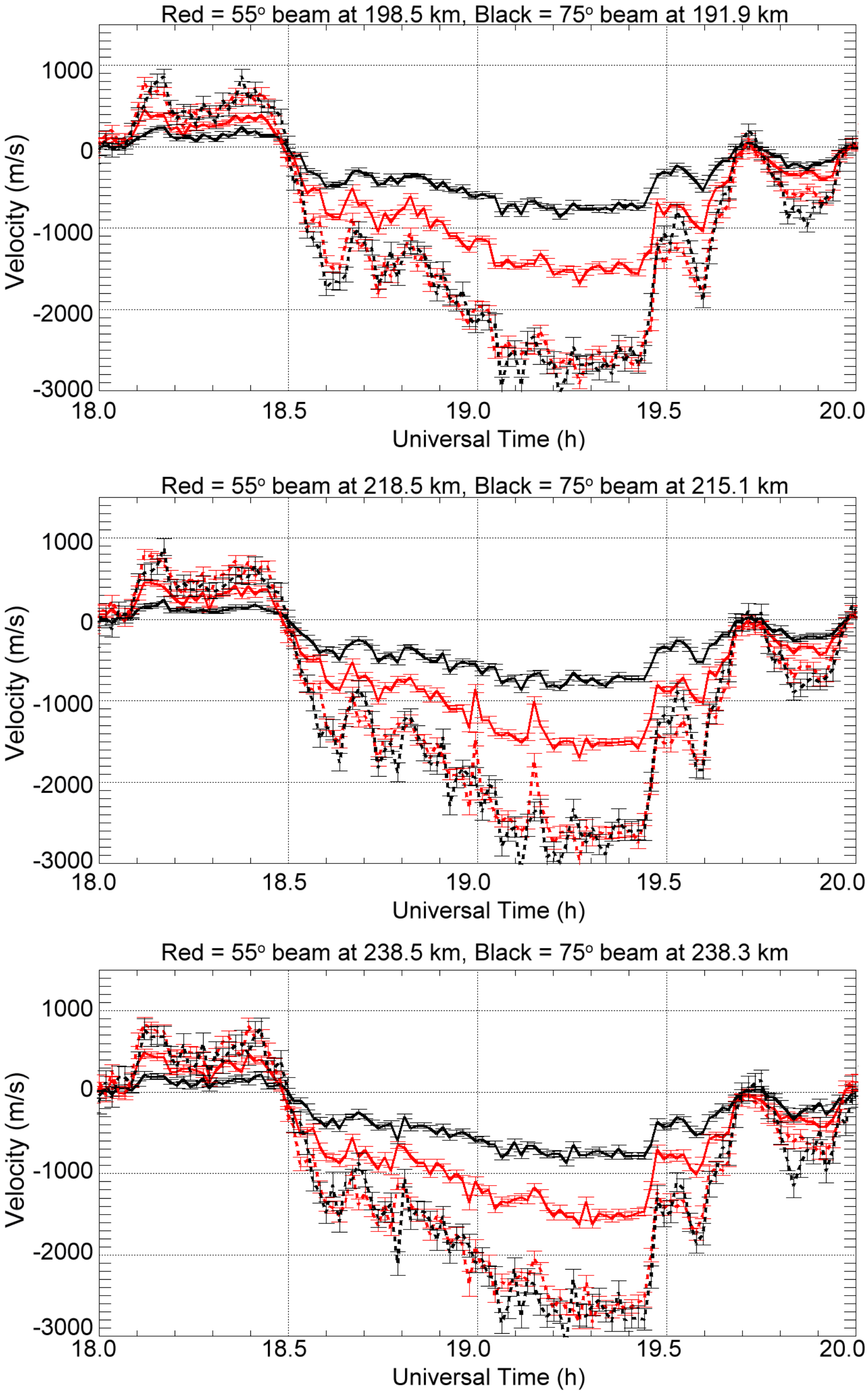

Figure 5.7: Velocity values between 18 UT and 20 UT on 12 September 2014 for an assortment of RISR-N measurement "pairs" between roughly 200 km and 400 km. Each pair has one measurement from the 55° elevation beam, and one from the 75° elevation beam. The measurements in a pair are less than 10 km apart from each other in altitude. The solid lines are for $v_{i\phi}$ and the dashed lines are for $v_{\perp los}$. The red lines reflect an elevation angle of 55°, and the black lines reflect an elevation angle of 75°.

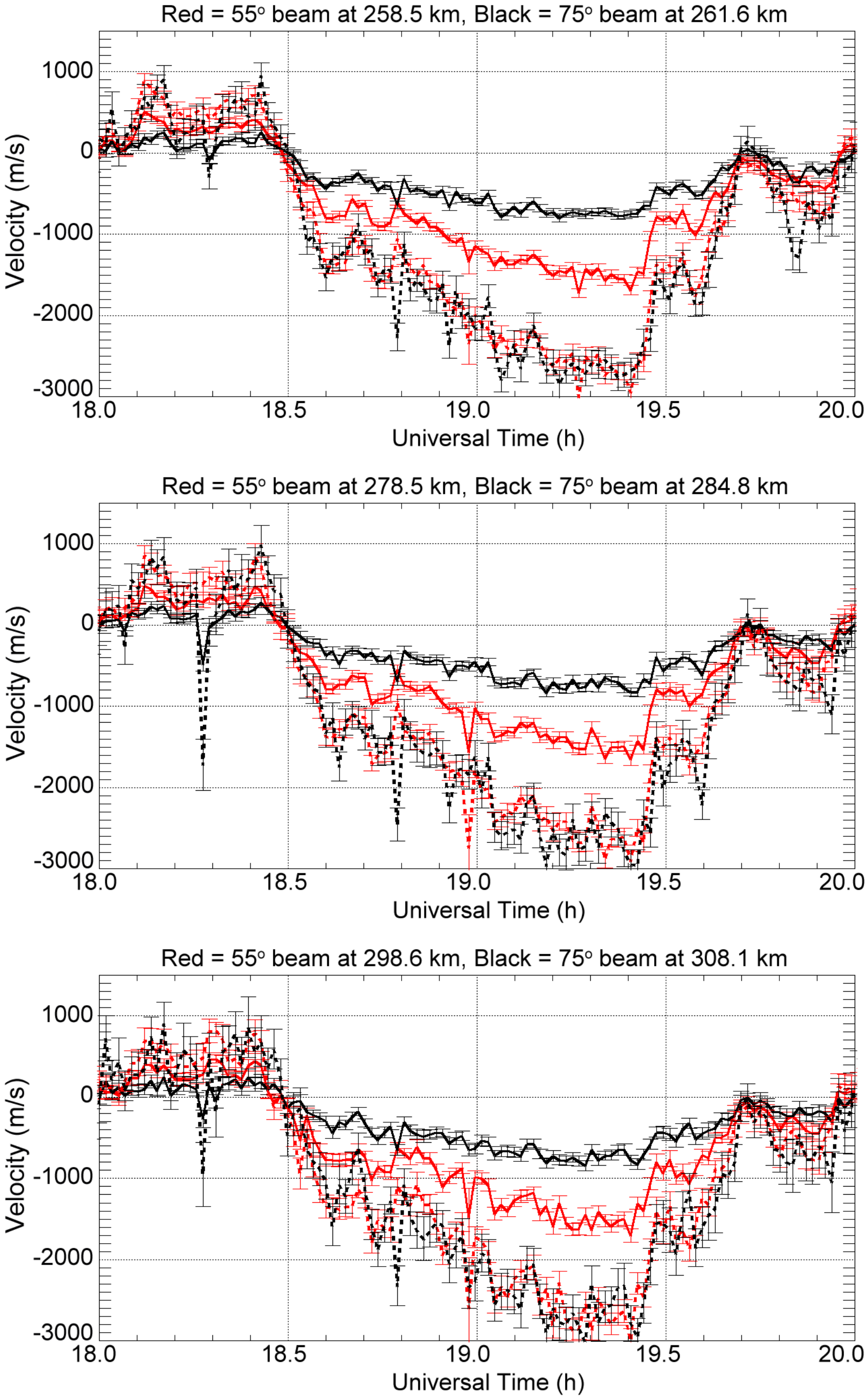

Figure 5.8: Velocity values between 18 UT and 20 UT on 12 September 2014 for an assortment of RISR-N measurement "pairs" between roughly 200 km and 400 km. Each pair has one measurement from the 55° elevation beam, and one from the 75° elevation beam. The measurements in a pair are less than 10 km apart from each other in altitude. The solid lines are for $v_{i\phi}$ and the dashed lines are for $v_{\perp los}$. The red lines reflect an elevation angle of 55°, and the black lines reflect an elevation angle of 75°.

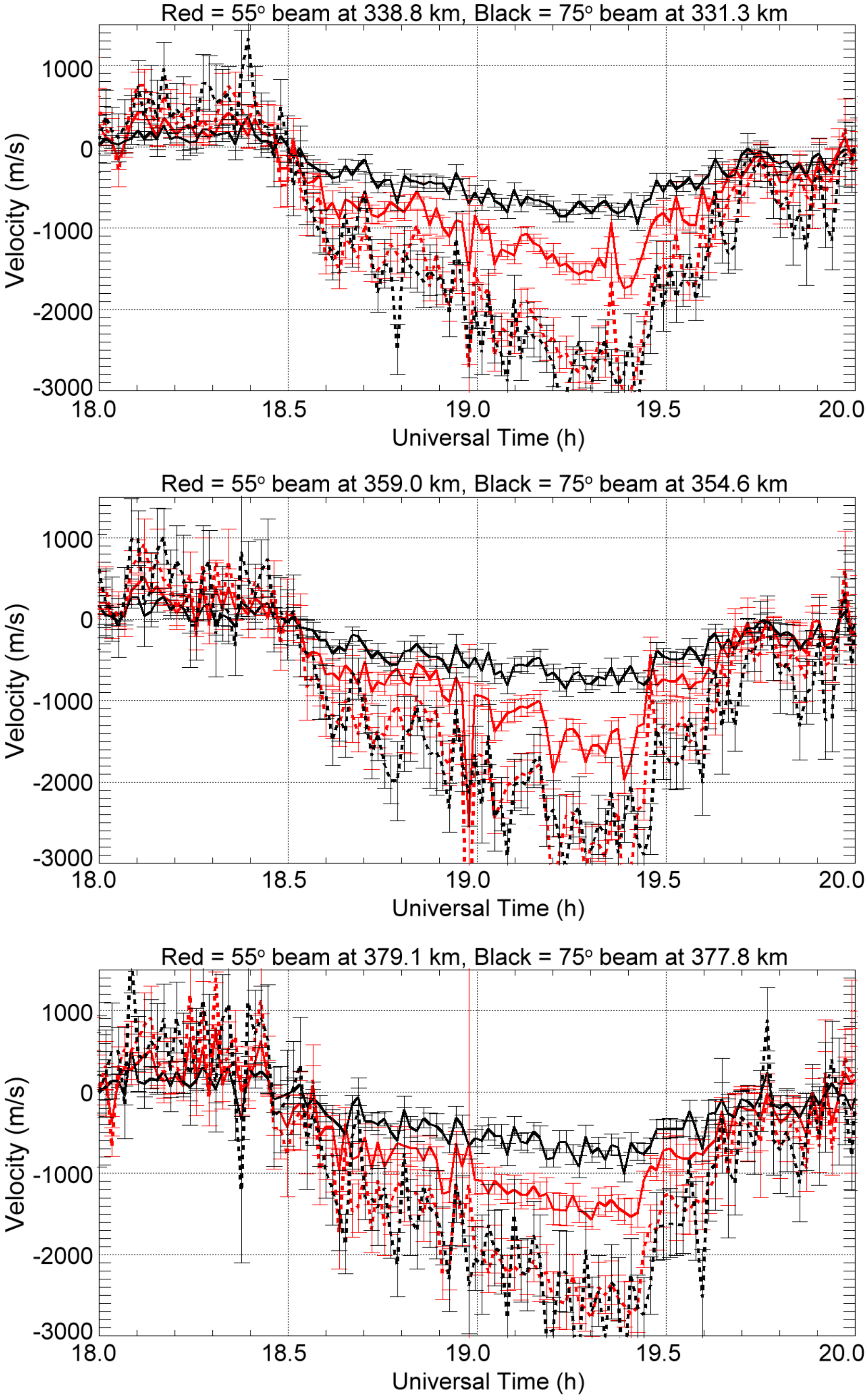

Figure 5.9: Velocity values between 18 UT and 20 UT on 12 September 2014 for an assortment of RISR-N measurement "pairs" between roughly 200 km and 400 km. Each pair has one measurement from the 55° elevation beam, and one from the 75° elevation beam. The measurements in a pair are less than 10 km apart from each other in altitude. The solid lines are for $v_{i\phi}$ and the dashed lines are for $v_{\perp los}$. The red lines reflect an elevation angle of 55°, and the black lines reflect an elevation angle of 75°.

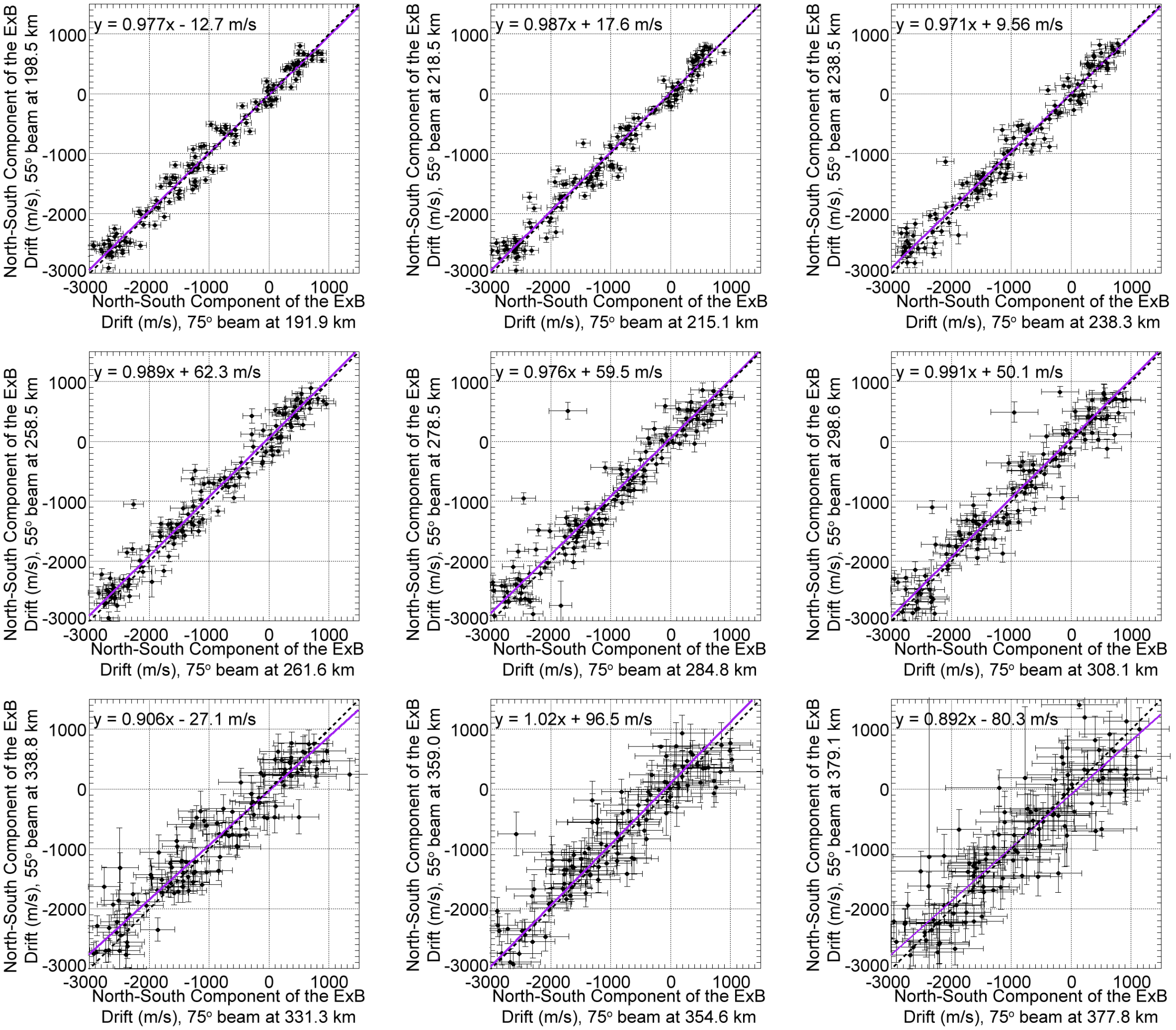

Figure 5.10: $v_{\perp los}$ values at an elevation angle of 55° against simultaneous measurements of $v_{\perp los}$ values at an elevation angle of 75° between 18 UT and 20 UT on 12 September 2014 for the same pairs shown in Figures 5.7 through 5.9. The purple line is an orthogonal least-squares fit to the $v_{\perp los}$ values whose equation is given, and the black dashed line is the 45° line.

cross-section. At lower altitudes the data tends more towards the POH curve, but it is important to emphasize that at lower altitudes the neutral mass is larger due to N_2 populations, which serve to both increase the line-of-sight ion temperature and decrease the anisotropy. Additionally, the error bars show that altitudes above 320 km are noisy and therefore less reliable, suggesting the KMV represents the data best between about 220 km and 320 km. The KMV curve indicates a few of the corresponding effective electric field values used in the MC simulation. Here, the effective electric field of the ISR data generally increases beyond 120 mV/m, reaching almost 140 mV/m for certain pairs. This is consistent with Figure 5.5, which shows the electric field reaching 150 mV/m within the throat of the reverse convection cells, as discussed in *Clauer et al.* (2016).

Knowing that the ISR observations lie the closest to the KMV collision cross-section is arguably enough to characterize ion temperature anisotropy. However, an alternative approach is to resolve $\beta_{||}/\beta_{\perp}$ from these results, and compare them to $\beta_{||}/\beta_{\perp}$ values from Chapter 4. From Equation 4.7, for a given measurement:

$$T_{\phi_1} = T_{||} \cos^2 \phi_1 + T_{\perp} \sin^2 \phi_1 \tag{5.2}$$

which is rewritten as:

$$T_{||} = \frac{T_{\phi_1} - T_{\perp} \sin^2 \phi_1}{\cos^2 \phi_1} \tag{5.3}$$

Meanwhile, for the other measurement in a given pair:

$$T_{\phi_2} = T_{||} \cos^2 \phi_2 + T_{\perp} \sin^2 \phi_2 \tag{5.4}$$

Combining Equations 5.3 and 5.4 gives:

$$T_{\perp} = \frac{T_{\phi_2} - \dfrac{T_{\phi_1} \cos^2 \phi_2}{\cos^2 \phi_1}}{\sin^2 \phi_2 - \tan^2 \phi_1 \cos^2 \phi_2} \tag{5.5}$$

The perpendicular temperature is then used to find the parallel temperature. However, assuming each measurement in a pair has the same m_n and $| \langle \mathbf{v} \rangle_i - \langle \mathbf{v} \rangle_n |^2$, Equations 4.8 and 4.9 yield:

$$T_{||} - T_n = \frac{\beta_{||} m_n | \langle \mathbf{v} \rangle_i - \langle \mathbf{v} \rangle_n |^2}{2k_B} \tag{5.6}$$

and:

$$T_{\perp} - T_n = \frac{\beta_{\perp} m_n | \langle \mathbf{v} \rangle_i - \langle \mathbf{v} \rangle_n |^2}{2k_B} \tag{5.7}$$

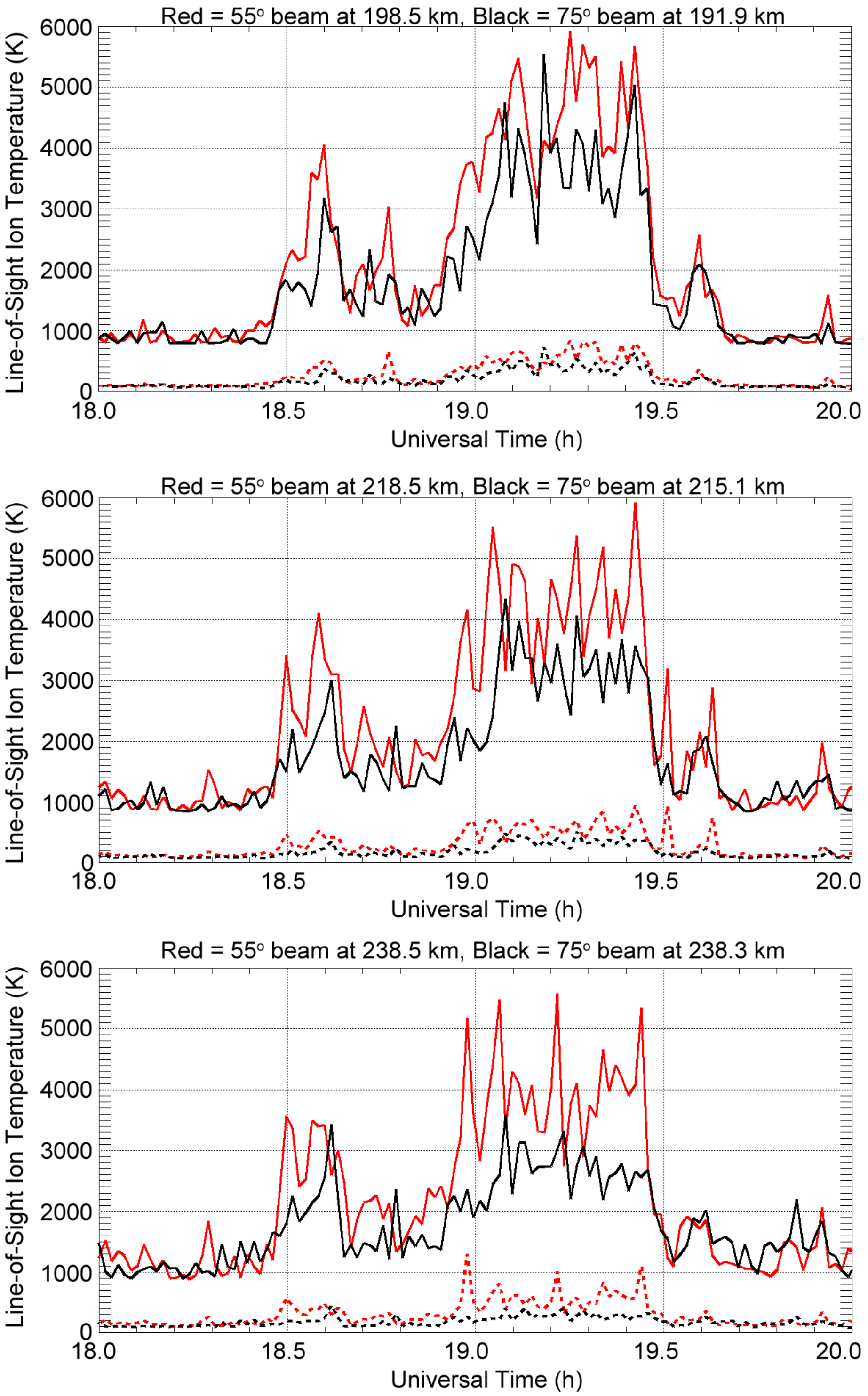

Figure 5.11: Line-of-sight ion temperatures between 18 UT and 20 UT on 12 September 2014 for the same RISR-N pairs shown in Figure 5.7. The red line is for an elevation angle of 55°, and the black line is for an elevation angle of 75°. The dashed lines indicate the error associated with a respective colour.

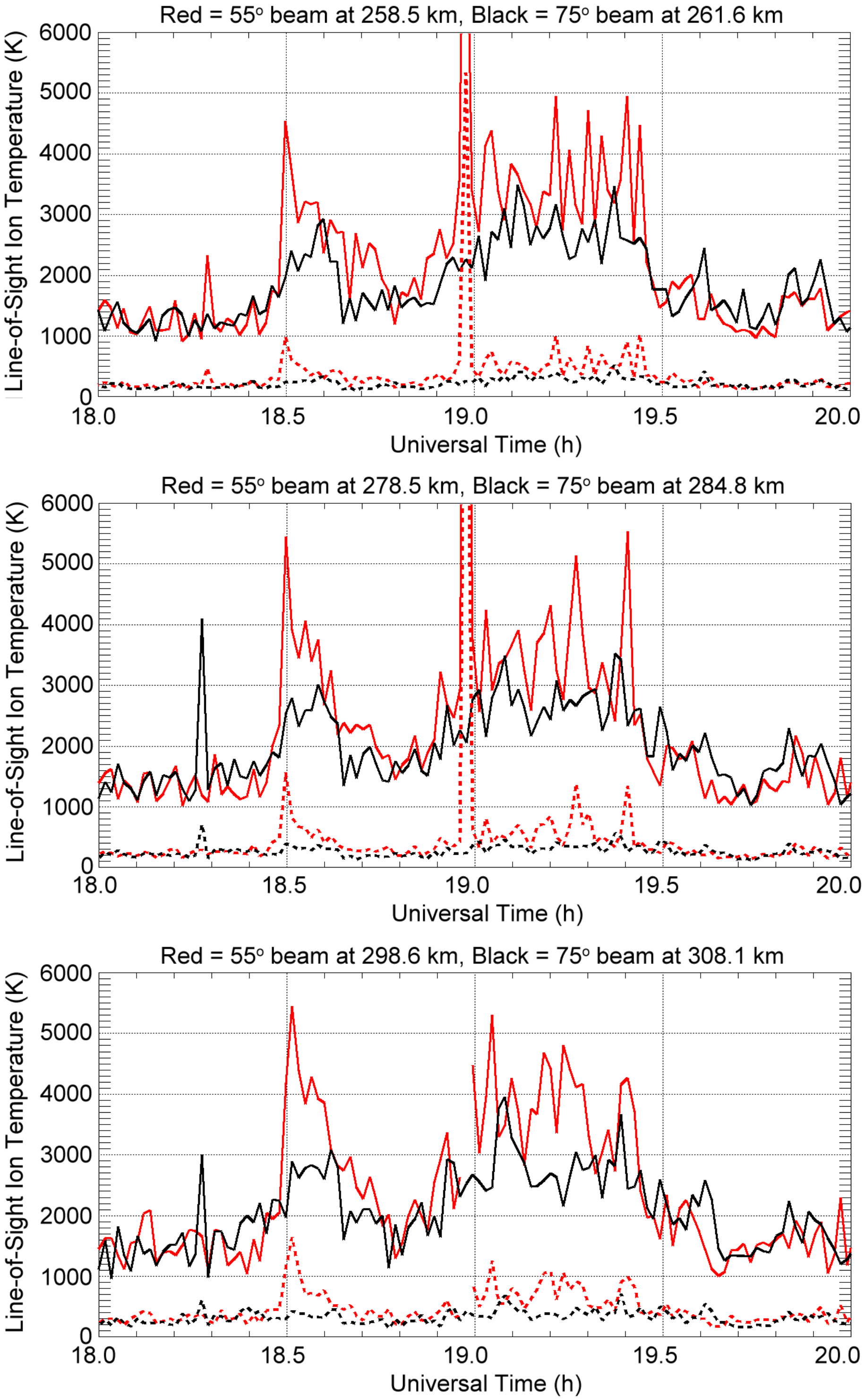

Figure 5.12: Line-of-sight ion temperatures between 18 UT and 20 UT on 12 September 2014 for the same RISR-N pairs shown in Figure 5.8. The red line is for an elevation angle of 55°, and the black line is for an elevation angle of 75°. The dashed lines indicate the error associated with a respective colour.

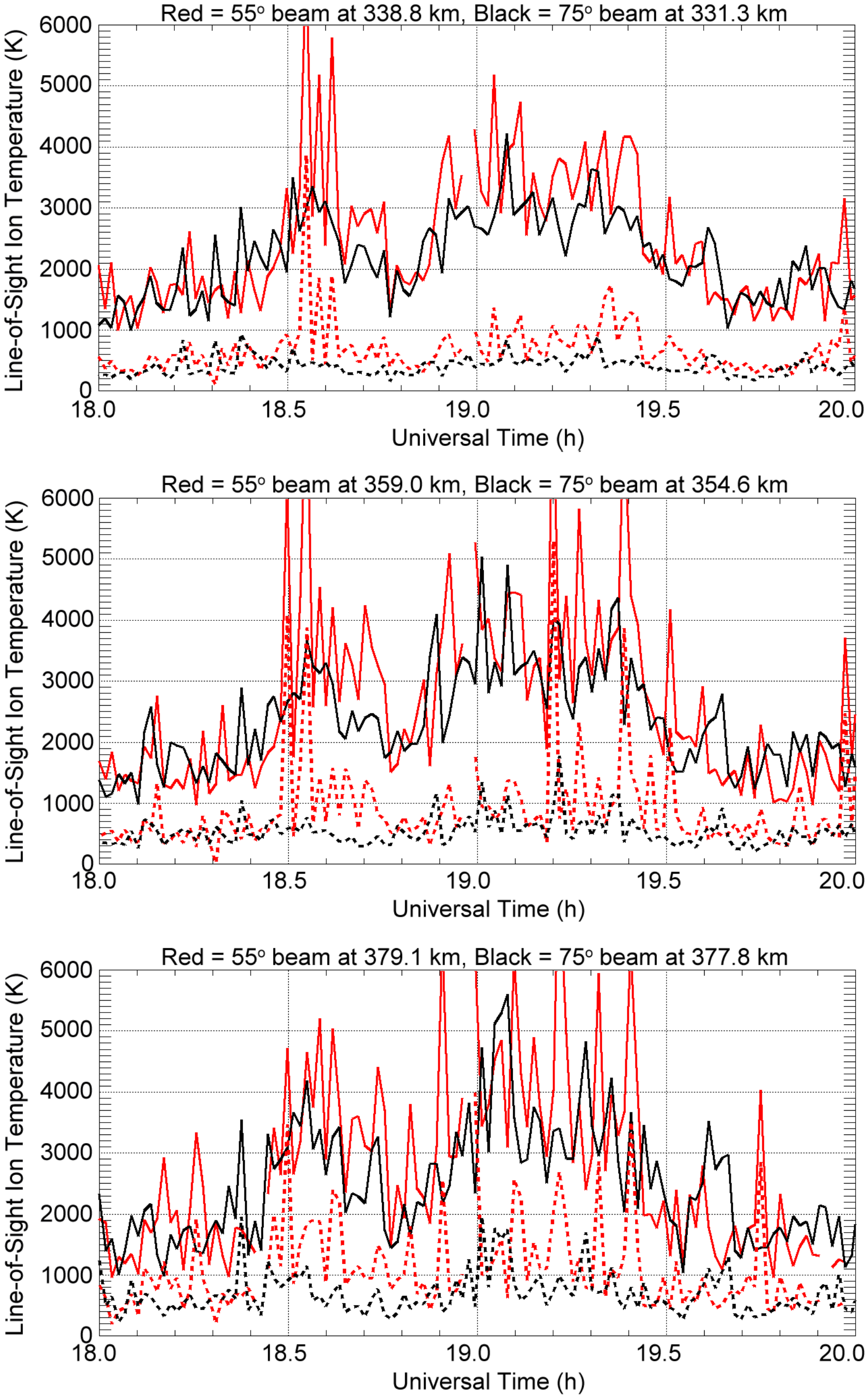

Figure 5.13: Line-of-sight ion temperatures between 18 UT and 20 UT on 12 September 2014 for the same RISR-N pairs shown in Figure 5.9. The red line is for an elevation angle of 55°, and the black line is for an elevation angle of 75°. The dashed lines indicate the error associated with a respective colour.

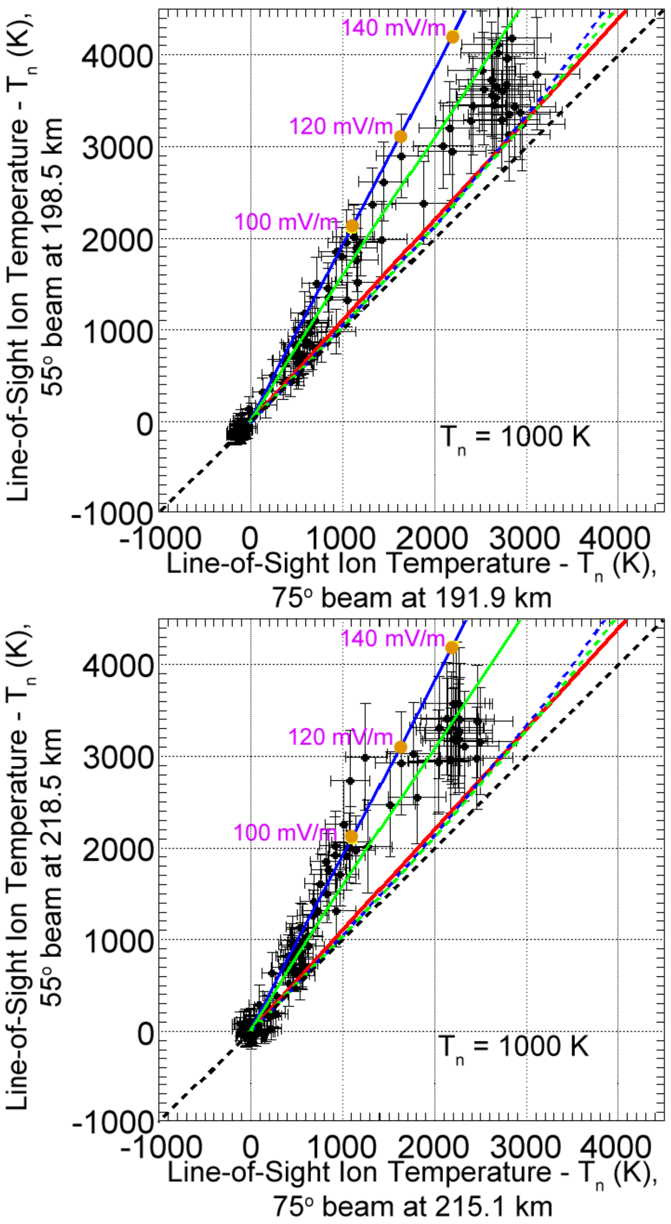

Figure 5.14: $T_{i\phi} - T_n$ values between 18 UT and 20 UT on 12 September 2014 at an elevation angle of 55° against simultaneous measurements of $T_{i\phi}$ values at an elevation angle of 75° for two of the pairs shown in Figures 5.7 through 5.9. T_n is taken to be the base-line temperatures seen in Figures 5.11 to 5.13. The green, blue, and red lines use Equation 4.7 and the $T_{||}$ and $T_\perp$ values found in Chapter 4 along with a T_n of 1000 K (the temperature used in all the MC simulations). The green line is found using the POH cross-section, the blue line is found using the KMV cross-section, and the red line is found using NO$^+$ with 50% O and 50% N$_2$. The green and blue dashed lines included Coulomb collisions, while the black dashed line is the 45° line. The dots on the blue line indicate a given effective electric field used in the MC simulation. Note that a seven-point running average in UT is performed for both beams.

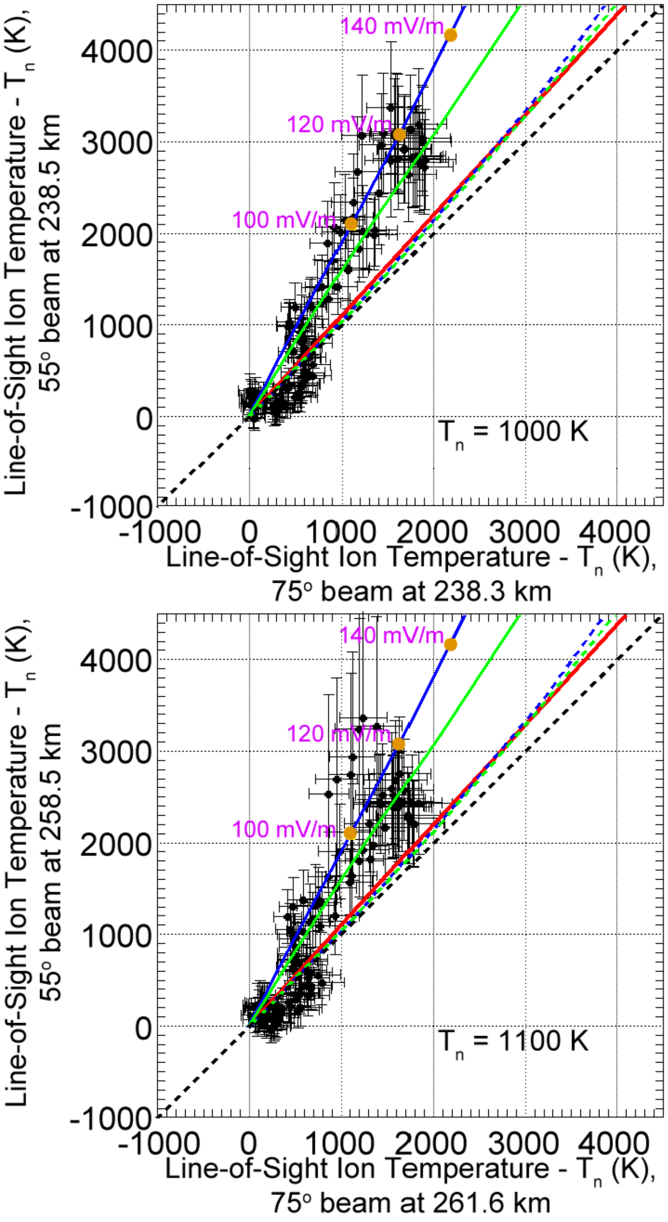

Figure 5.15: $T_{i\phi}-T_n$ values between 18 UT and 20 UT on 12 September 2014 at an elevation angle of 55° against simultaneous measurements of $T_{i\phi}$ values at an elevation angle of 75° for two of the pairs shown in Figures 5.7 through 5.9. T_n is taken to be the base-line temperatures seen in Figures 5.11 to 5.13. The green, blue, and red lines use Equation 4.7 and the $T_{||}$ and $T_{\perp}$ values found in Chapter 4 along with a T_n of 1000 K (the temperature used in all the MC simulations). The green line is found using the POH cross-section, the blue line is found using the KMV cross-section, and the red line is found using NO$^+$ with 50% O and 50% N$_2$. The green and blue dashed lines included Coulomb collisions, while the black dashed line is the 45° line. The dots on the blue line indicate a given effective electric field used in the MC simulation. Note that a seven-point running average in UT is performed for both beams.

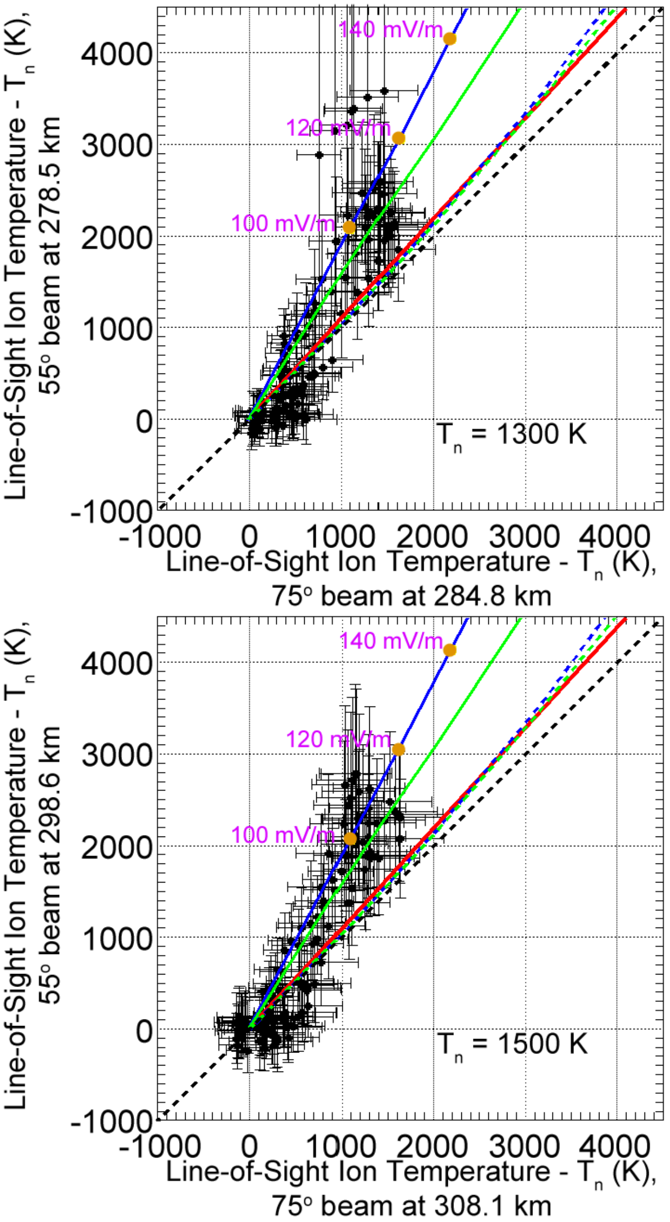

Figure 5.16: $T_{i\phi} - T_n$ values between 18 UT and 20 UT on 12 September 2014 at an elevation angle of 55° against simultaneous measurements of $T_{i\phi}$ values at an elevation angle of 75° for two of the pairs shown in Figures 5.7 through 5.9. T_n is taken to be the base-line temperatures seen in Figures 5.11 to 5.13. The green, blue, and red lines use Equation 4.7 and the $T_{||}$ and $T_{\perp}$ values found in Chapter 4 along with a T_n of 1000 K (the temperature used in all the MC simulations). The green line is found using the POH cross-section, the blue line is found using the KMV cross-section, and the red line is found using NO^+ with 50% O and 50% N_2. The green and blue dashed lines included Coulomb collisions, while the black dashed line is the 45° line. The dots on the blue line indicate a given effective electric field used in the MC simulation. Note that a seven-point running average in UT is performed for both beams.

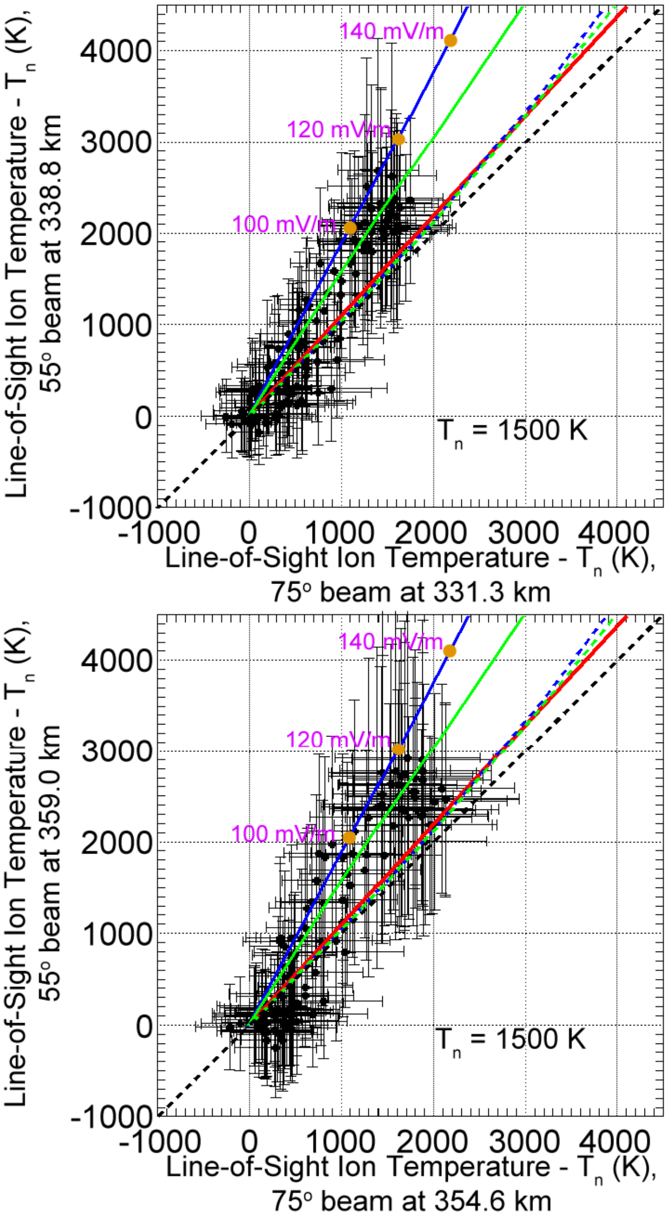

Figure 5.17: $T_{i\phi} - T_n$ values between 18 UT and 20 UT on 12 September 2014 at an elevation angle of 55° against simultaneous measurements of $T_{i\phi}$ values at an elevation angle of 75° for two of the pairs shown in Figures 5.7 through 5.9. T_n is taken to be the base-line temperatures seen in Figures 5.11 to 5.13. The green, blue, and red lines use Equation 4.7 and the $T_{||}$ and $T_{\perp}$ values found in Chapter 4 along with a T_n of 1000 K (the temperature used in all the MC simulations). The green line is found using the POH cross-section, the blue line is found using the KMV cross-section, and the red line is found using NO$^+$ with 50% O and 50% N$_2$. The green and blue dashed lines included Coulomb collisions, while the black dashed line is the 45° line. The dots on the blue line indicate a given effective electric field used in the MC simulation. Note that a seven-point running average in UT is performed for both beams.

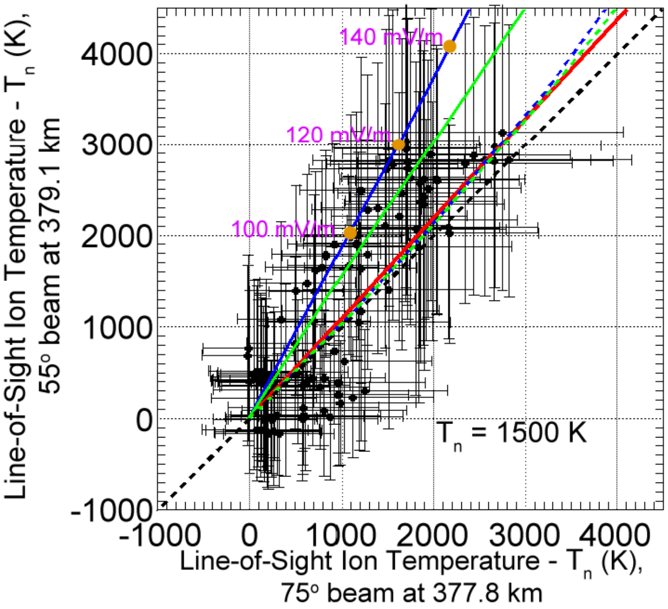

Figure 5.18: $T_{i\phi} - T_n$ values between 18 UT and 20 UT on 12 September 2014 at an elevation angle of 55° against simultaneous measurements of $T_{i\phi}$ values at an elevation angle of 75° for one of the pairs shown in Figures 5.7 through 5.9. T_n is taken to be the base-line temperatures seen in Figures 5.11 to 5.13. The green, blue, and red lines use Equation 4.7 and the $T_{||}$ and $T_{\perp}$ values found in Chapter 4 along with a T_n of 1000 K (the temperature used in all the MC simulations). The green line is found using the POH cross-section, the blue line is found using the KMV cross-section, and the red line is found using NO^+ with 50% O and 50% N_2. The green and blue dashed lines included Coulomb collisions, while the black dashed line is the 45° line. The dots on the blue line indicate a given effective electric field used in the MC simulation. Note that a seven-point running average in UT is performed for both beams.

combining these gives:

$$T_{||} = (\beta_{||}/\beta_{\perp})T_{\perp} + T_n\left(1 - \beta_{||}/\beta_{\perp}\right) \tag{5.8}$$

showing that $\beta_{||}/\beta_{\perp}$ is the slope in parallel versus perpendicular temperature plots. Figures 5.19 to 5.21 show the parallel temperature against the perpendicular temperature at the same time for a given pair. At high energies, the perpendicular temperature is larger than the parallel temperature. The slopes of the orthogonal least-squares fits in Figures 5.19 to 5.21 agree best with the KMV curve, particularly between 220 km and 320 km (where measurements are not subject to N_2 populations and the error measurements are reasonable). This finding agrees well with Figures 5.14 to 5.18, in spite of the large error (which this method amplifies). At lower altitudes $\beta_{||}/\beta_{\perp}$ is larger due to the increased N_2 populations, while the increase in $\beta_{||}/\beta_{\perp}$ with the 338.8 km - 331.3 km pair and the 359.0 km - 354.6 km pair is likely the result of Coulomb collisions.

The $\beta_{||}/\beta_{\perp}$ values from Figures 5.19 to 5.21 are compared to those found using Equation 5.8 and the parallel and perpendicular temperatures resolved for the KMV and POH cross-sections in Chapter 4. Figure 5.22 shows the resulting KMV and POH $\beta_{||}/\beta_{\perp}$ values as a function of effective electric field. As the effective electric field increases $\beta_{||}/\beta_{\perp}$ for the POH cross-section increases, but the $\beta_{||}/\beta_{\perp}$ for the KMV stays constant. Between 220 km and 320 km the $\beta_{||}/\beta_{\perp}$ values from Figures 5.19 to 5.21 agree the most with the KMV cross-section, where the average $\beta_{||}/\beta_{\perp}$ for the KMV cross-section is 0.162 and the average $\beta_{||}/\beta_{\perp}$ for the POH cross-section is 0.269. However, these results still show the KMV $\beta_{||}/\beta_{\perp}$ to be generally higher than the approximate 0.1 value found from the heating event between 220 km and 320 km, suggesting the KMV cross-section underestimates the anisotropy. However, recall that these results must be re-analyzed once distorted Maxwellian fits are incorporated in spectral fitting techniques.

5.2.2 Electric Field Determination

As shown in Figures 5.7 through 5.9 and 5.10, the $\mathbf{E} \times \mathbf{B}$ drift is a dominant process in the F-region, but it is also an important process in the E-region. From *Schunk and Nagy* (2009)

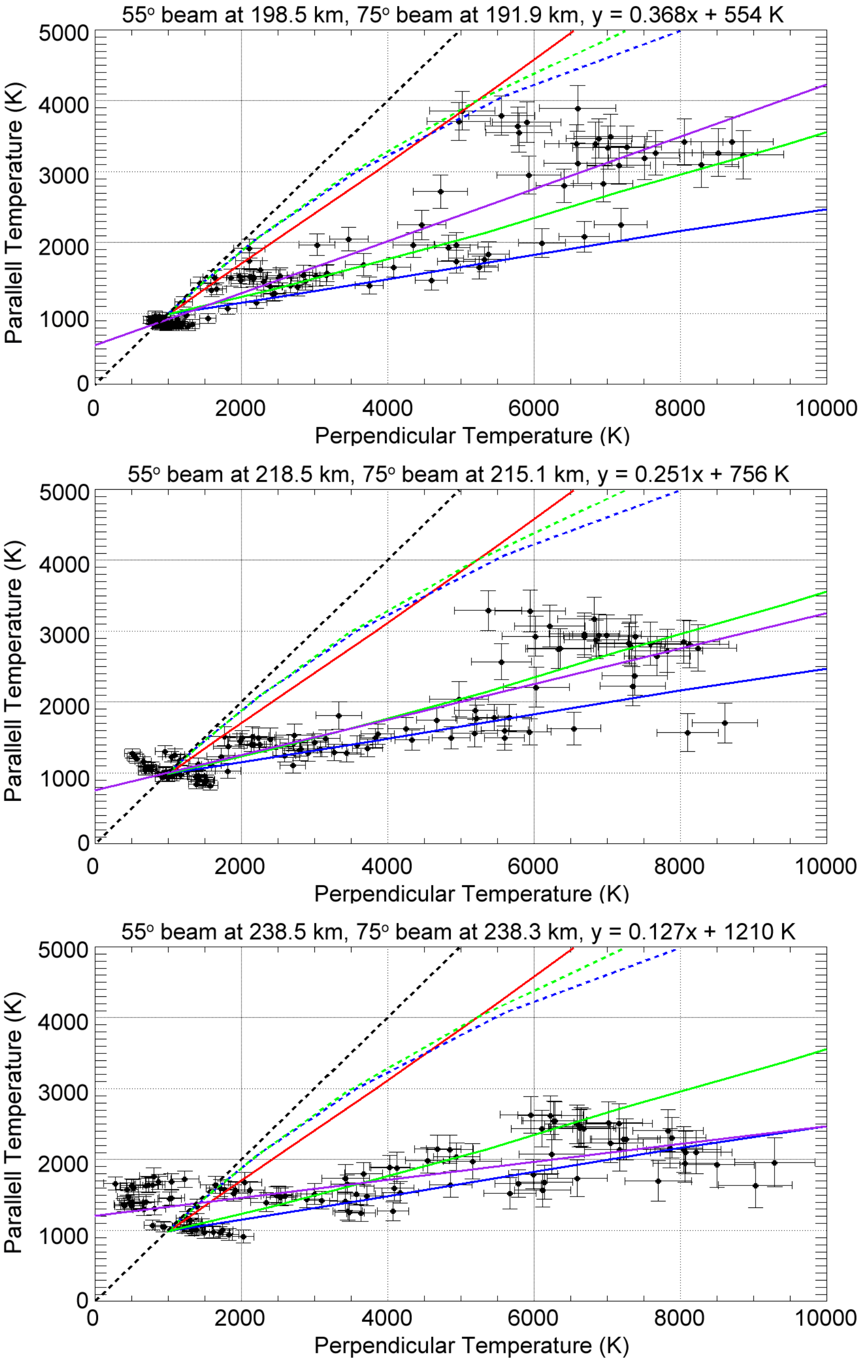

Figure 5.19: $T_{||}$ against $T_{\perp}$ between 18 UT and 20 UT on 12 September 2014 for the pairs shown in Figures 5.7. These values are resolved from Equations 5.3 and 5.5, and the averaged $T_{i\phi}$ values used in Figures 5.14 to 5.18. The purple line is an orthogonal fit to the data (whose equation is given), while the green, blue, and red lines use the $T_{||}$ and $T_{\perp}$ values found in Chapter 4 along with a T_n of 1000 K (the temperature used in all the MC simulations). The green line is found using the POH cross-section, the blue line is found using the KMV cross-section, and the red line is found using NO^+ with 50% O and 50% N_2. The green and blue dashed lines included Coulomb collisions, while the black dashed line is the 45° line. Note that the error bars are divided by a factor of 5 for the sake of clarity.

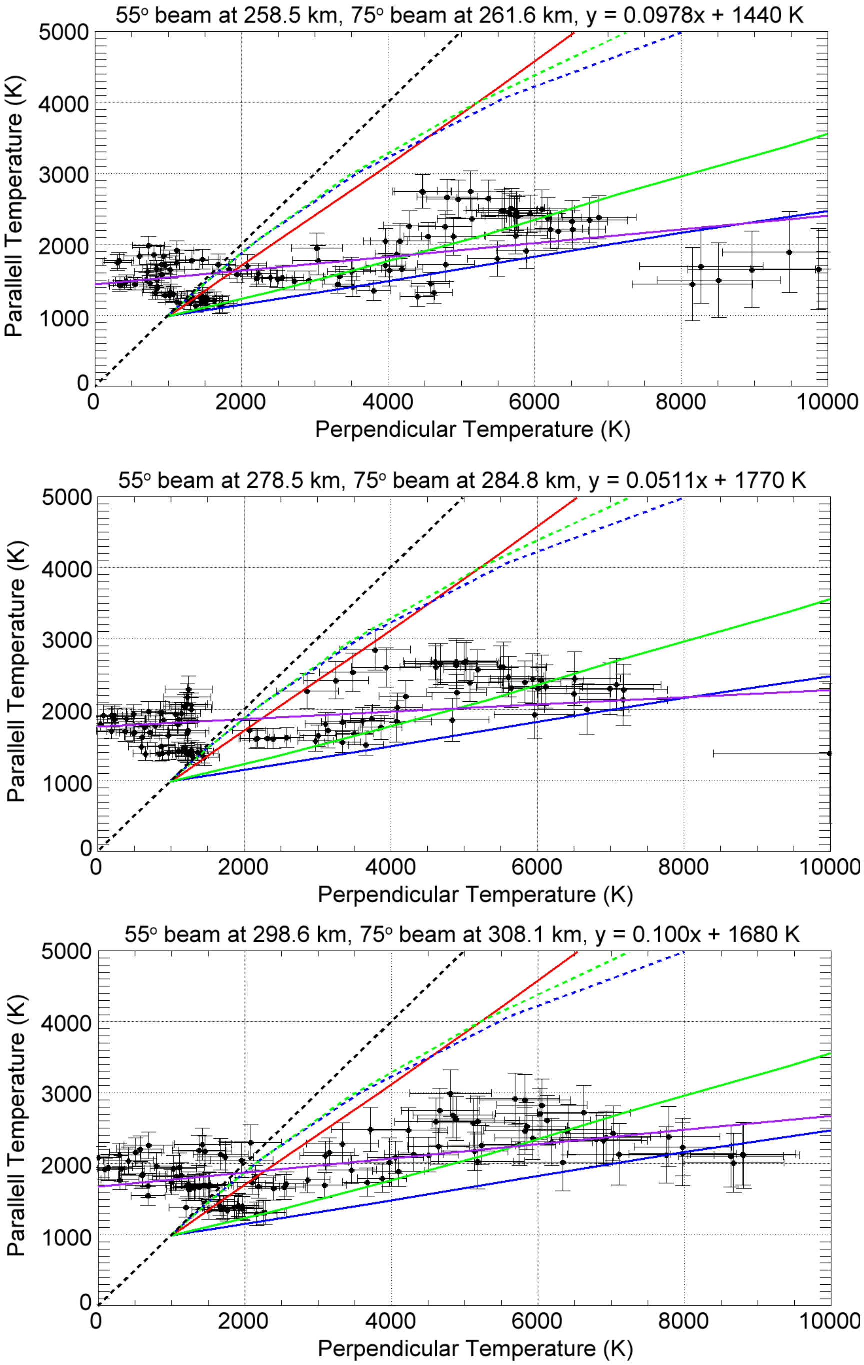

Figure 5.20: $T_{||}$ against $T_{\perp}$ between 18 UT and 20 UT on 12 September 2014 for the pairs shown in Figures 5.8. These values are resolved from Equations 5.3 and 5.5, and the averaged $T_{i\phi}$ values used in Figures 5.14 to 5.18. The purple line is an orthogonal fit to the data (whose equation is given), while the green, blue, and red lines use the $T_{||}$ and $T_{\perp}$ values found in Chapter 4 along with a T_n of 1000 K (the temperature used in all the MC simulations). The green line is found using the POH cross-section, the blue line is found using the KMV cross-section, and the red line is found using NO^+ with 50% O and 50% N_2. The green and blue dashed lines included Coulomb collisions, while the black dashed line is the 45° line. Note that the error bars are divided by a factor of 5 for the sake of clarity.

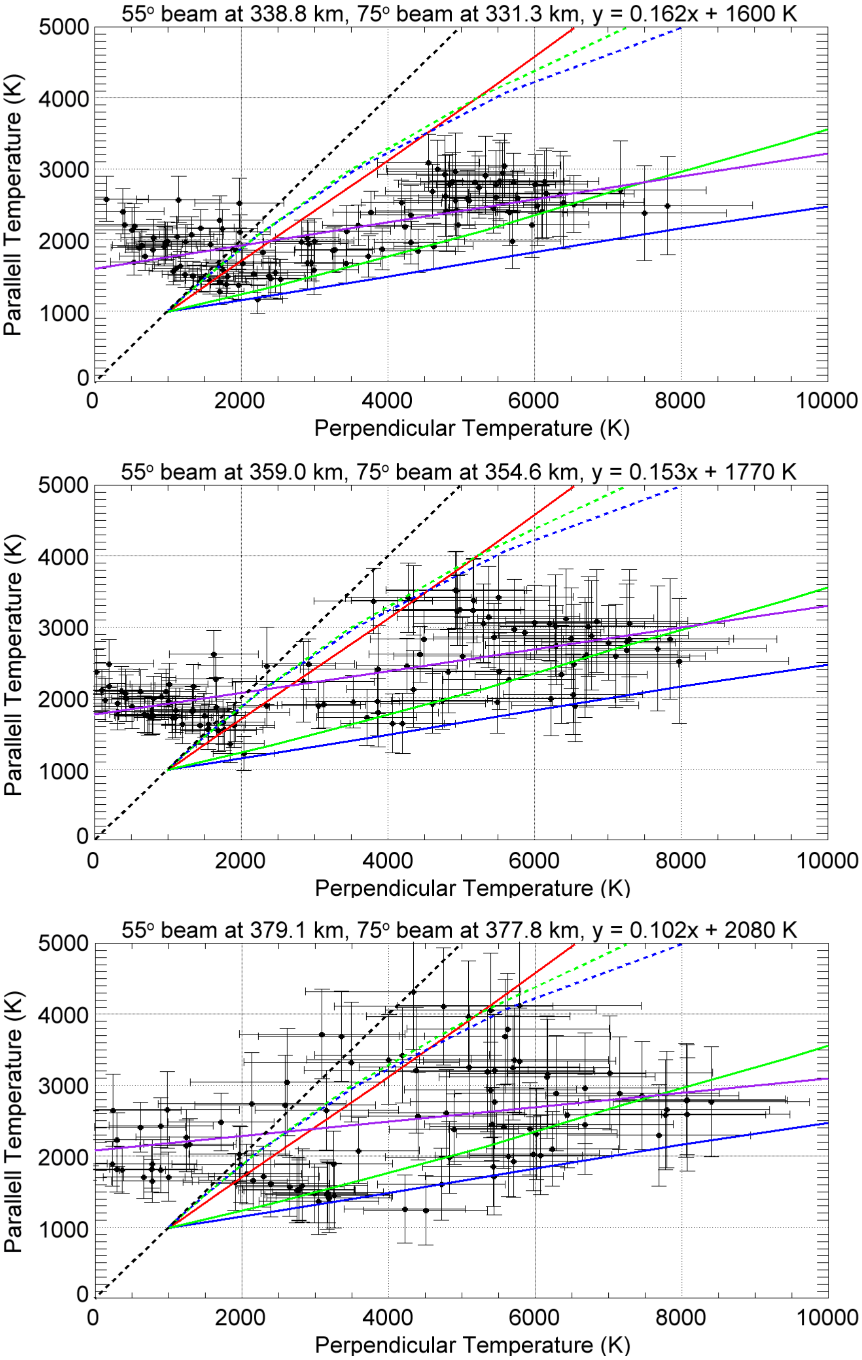

Figure 5.21: $T_{||}$ against $T_{\perp}$ between 18 UT and 20 UT on 12 September 2014 for the pairs shown in Figures 5.9. These values are resolved from Equations 5.3 and 5.5, and the averaged $T_{i\phi}$ values used in Figures 5.14 to 5.18. The purple line is an orthogonal fit to the data (whose equation is given), while the green, blue, and red lines use the $T_{||}$ and $T_{\perp}$ values found in Chapter 4 along with a T_n of 1000 K (the temperature used in all the MC simulations). The green line is found using the POH cross-section, the blue line is found using the KMV cross-section, and the red line is found using NO^+ with 50% O and 50% N_2. The green and blue dashed lines included Coulomb collisions, while the black dashed line is the 45° line. Note that the error bars are divided by a factor of 5 for the sake of clarity.

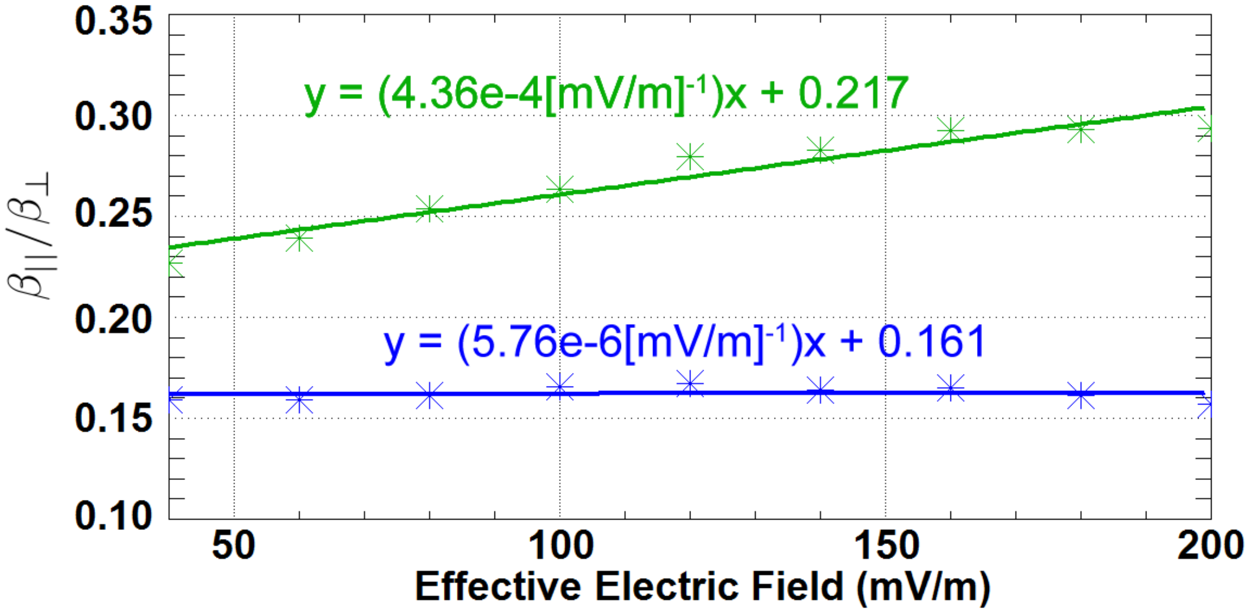

Figure 5.22: $\beta_{||}/\beta_{\perp}$ as a function of the effective electric field for the POH collision cross-section (green) and the KMV collision cross-section (blue).

the average ion velocity in the ionosphere is:

$$\mathbf{v}_i = \frac{\nu_{in}/\Omega_i}{\nu_{in}^2/\Omega_i^2+1}\frac{\mathbf{E}'}{B} + \frac{1}{1+\nu_{in}^2/\Omega_i^2}\frac{\mathbf{E}'\times\hat{b}}{B} + \mathbf{v}_n \tag{5.9}$$

where $\mathbf{E}'$ is the effective electric field. For the F-region, to order ν_{in}/Ω_i :

$$v_{\perp losF} = \frac{E}{B}\cos\theta \tag{5.10}$$

where θ is the angle between the $\mathbf{E}\times\mathbf{B}$ and line-of-sight. However, in the E-region ν_{in}/Ω_i is not negligible, giving:

$$v_{\perp losE} = \frac{\nu_{in}/\Omega_i}{\nu_{in}^2/\Omega_i^2+1}\frac{E'}{B}\sin\theta + \frac{1}{1+\nu_{in}^2/\Omega_i^2}\frac{E}{B}\cos\theta + \mathbf{v}_n\frac{\nu_{in}^2/\Omega_i^2}{1+\Omega_i^2/\nu_{in}^2} \tag{5.11}$$

By ignoring the negligible change in magnetic field strength from the E-region to the F-region ionosphere, assuming the contribution from the E-region neutral wind to be small compared to $\frac{E}{B}$, and by taking measurements of $v_{\perp losF}$ and $v_{\perp losE}$ at approximately the same geomagnetic latitudes, Equations 5.10 and 5.11 give:

$$\frac{E}{B} = \sqrt{v_{\perp losF}^2 + \left(v_{\perp losE}\frac{\nu_{in}^2/\Omega_i^2+1}{\nu_{in}/\Omega_i} - \frac{v_{\perp losF}}{\nu_{in}/\Omega_i}\right)^2} \tag{5.12}$$

as well as:

$$\tan\theta = \frac{(\nu_{in}^2/\Omega_i^2 + 1)v_{\perp losE} - v_{\perp losF}}{v_{\perp losF}\nu_{in}/\Omega_i} \tag{5.13}$$

Using the MSIS-90 atmospheric model (*Hedin*, 1991) ν_{in}/Ω_i values are found as a function of altitude and time, allowing for preliminary calculations of the electric field vector during the heating event discussed in *Clauer et al.* (2016). Figure 5.23 shows one such calculation for a pair of measurements located at approximately 83.2° geomagnetic latitude. The F-region measurement of $v_{\perp los}$ comes from the 75° beam at 284.8 km, and the E-region measurement of $v_{\perp los}$ comes from the 55° beam at 119.0 km. For convenience, Figure 5.5 is superimposed on the calculated electric field.

Figure 5.23 shows that between 18 and 20 UT $v_{\perp losE}$ is almost 2 km/s southward and $v_{\perp losF}$ is almost 3 km/s southward. The strongest drifts occur during a period of particularly strong heating. Within the same period the electric field grows to approximately 180 mV/m between 19.2 UT and 19.7 UT, which is similar but larger than what is inferred through the multi-beam ISR reconstruction. These electric field measurements are also greater than what is inferred for the effective electric field in Figures 5.14 to 5.18, suggesting the presence of a neutral wind that could be as large as 800 m/s. The angle between the $\mathbf{E} \times \mathbf{B}$ and line-of-sight fluctuates but is near 180° during the period of extreme heating. Given that RISR-N is in the polar cap and that this time period corresponds with approximately 10.25 MLT and 12.25 MLT (noon), this angle indicates a sunward $\mathbf{E} \times \mathbf{B}$ drift and dusk-to-dawn electric field, which is consistent with the reversed convection cell mentioned in *Clauer et al.* (2016). The errors propagated for the electric field and the angle are large, but reasonable.

5.3 Summary and Discussion

By characterizing the ion temperature anisotropy in the ionosphere, as well as the electric field, it is possible to resolve the neutral wind and better understand ionospheric Joule heating. Here, overlapping northward pointing RISR-N beams were used to characterize both the high-latitude ion temperature anisotropy and the electric field vector during a strong heating event on 12 September 2014, in which the parallel drift is small and the $\mathbf{E} \times \mathbf{B}$ drift dominates plasma motion.

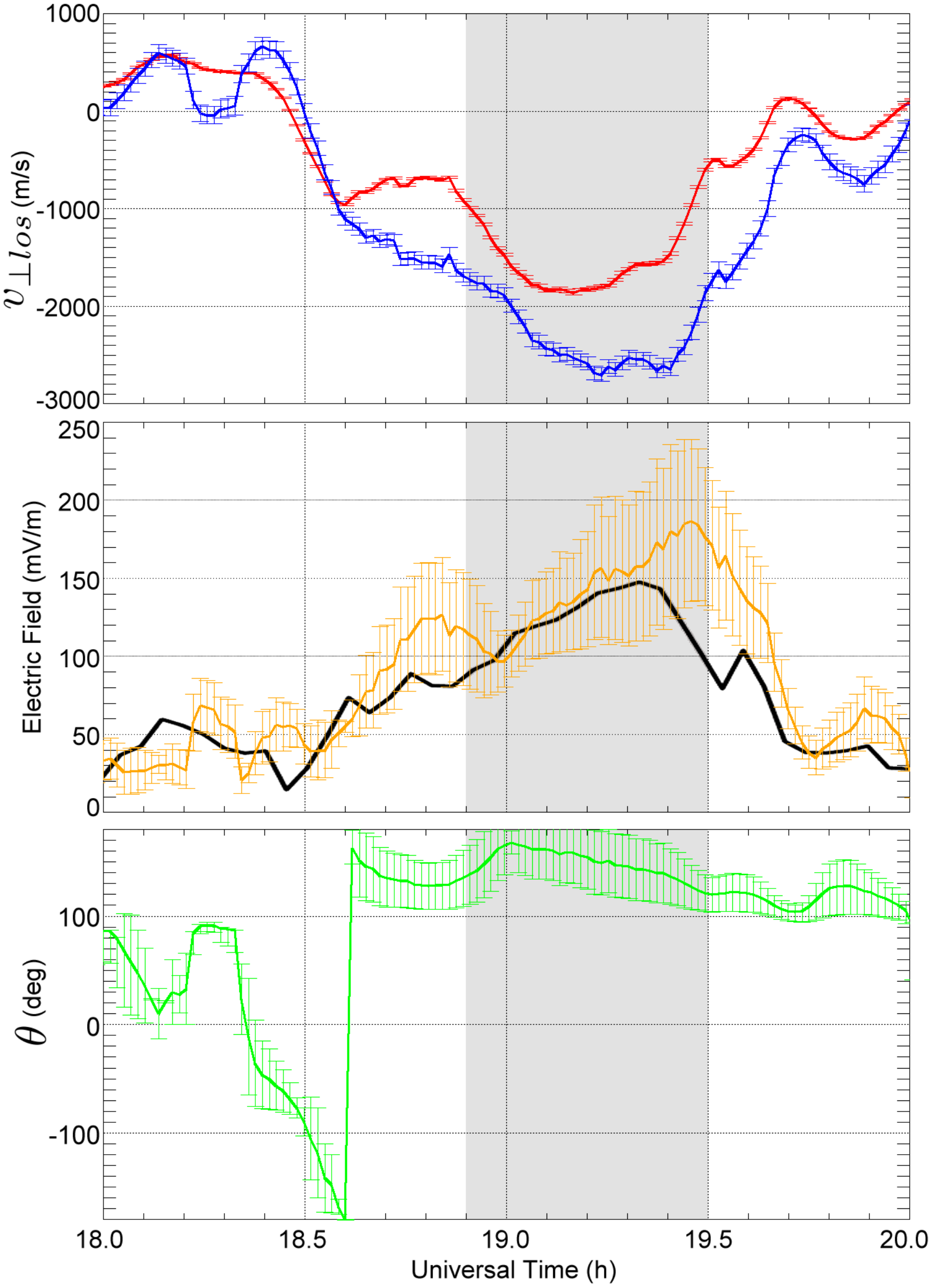

Figure 5.23: Early results from resolving the electric field vector at 83.2° geomagnetic latitude using RISR-N data between 18 UT and 20 UT on 12 September 2014. a) The perpendicular component of the line-of-sight ion velocities used in calculating E/B. The blue line is the F-region reading (75° beam, altitude of 284.8 km) and the red line is the E-region reading (55° beam, altitude of 119.0 km). Note that a seven point running average in time is performed. b) The calculated E magnitude, assuming a B of 5×10^{-5} T, in orange, and the ionospheric horizontal electric field measured by RISR-N at 84° geomagnetic latitude (taken from *Clauer et al.* (2016)). c) The calculated angle between the $\mathbf{E} \times \mathbf{B}$ and line-of-sight, where 0° is along the line-of-sight. The gray region indicates a period of particularly strong heating, as inferred from Figures 5.11 to 5.13. Error calculations are performed assuming a 20% in ν_{in}/Ω_i.

By plotting the line-of-sight ion temperature from one high elevation beam against the line-of-sight ion temperature from another near-by (in terms of altitude and latitude) high elevation beam, the ion temperature anisotropy was found to follow the KMV O^+-O RCE cross-section description discussed in Chapter 4 between 220 km and 320 km. Through the KMV description the line-of-sight ion temperatures implied a 120 mV/m to 140 mV/m electric field to be present, somewhat less than inferred through a Bayesian approach in *Clauer et al.* (2016) (*Heinselman and Nicolls*, 2008). An alternative method to characterize ion temperature anisotropy was used, in which $\beta_{||}/\beta_{\perp}$ was found from calculated parallel and perpendicular temperatures. At high-energies the perpendicular temperature was consistently larger than the parallel temperature, as expected from Chapter 4. The $\beta_{||}/\beta_{\perp}$ values found agreed most closely with the KMV cross-section between 220 km and 320 km, but still appeared to be even more anisotropic.

Meanwhile, E-region readings and F-region readings were used in a preliminary study of the electric field vector. The electric field was found to reach roughly 180 mV/m at 83.2° geomagnetic latitude, which is larger than that discussed in *Clauer et al.* (2016) at 84°. Comparing the approximate 180 mV/m electric field measurement to the 140 mV/m effective electric field measurement found using the KMV O^+-O RCE cross-section results in an approximate 40 mV/m difference that translates into a 800 m/s neutral wind, which is large but has been seen for very large electric field conditions of the kind found in *Killeen et al.* (1984). The angle of the $\mathbf{E} \times \mathbf{B}$ with respect to the line-of-sight was consistent with the reverse convection cell analysis of *Clauer et al.* (2016).

To continue this research, the Special Study of E/B and Ion Temperature (SSEBIT) experiment has been designed from this work and runs fairly frequently on both RISR-N and RISR-C. Although the exact beam arrangement is still being refined, this experiment has several overlapping northward beams on RISR-N and several overlapping southward beams on RISR-C at similar aspect angles.

One flaw with the present results is that Chapter 4 showed the importance of using spectral fitting routines based on toroidal velocity distributions for ISR data taken during strong electric field events in the O^+ dominated regions. The dataset that had to be used was based on spectral fitting routines that relied on Maxwellian velocity distributions. This data will need to be reprocessed in accordance with Chapter 4 before firmer conclusions can be realized. This new interpretation is currently underway but requires time to be inserted into the current analysis scheme.

Chapter 6

MODELING HIGH-ALTITUDE PLASMA TRANSPORT USING MONTE-CARLO SIMULATED ION VELOCITY DISTRIBUTIONS

As mentioned in Chapter 5, anisotropic ion temperatures can be inferred with spacecraft instruments and not just with ground-based instruments like ISRs. Figure 6.1 shows one such case of anisotropic temperatures taken from *Archer et al.* (2015), which used the three identical Swarm spacecraft (*Friis-Christensen et al.*, 2008), orbiting at 500 km altitude. Each satellite possesses two Thermal Ion Imagers (TIIs), which are oriented in the horizontal and vertical directions. These instruments use microchannel-plate-intensified phosphor screens imaged by a charge-coupled device to generate two-dimensional images of low-energy, high-resolution (66 × 40 pixels) ion distribution functions at a rate of 16 Hz. These images are down-sampled to 2 Hz measurements of the ion flow (where Langmuir probes are used to correct for the spacecraft potential), the electric field, and the ion temperature (as discussed in relation to Equation 4.3 in Chapter 4) (*Knudsen et al.*, 2017).

In this case, the Swarm spacecraft observed large perpendicular to parallel temperature ratios (as large as five) at 550 km during strong, localized electric fields. These ratios were at the time thought to exceed the values predicted by collisional heating by a factor of two (which Chapter 5 indicates may well be the case for very strong electric fields). This led *Archer et al.* (2015) to conclude that the temperature anisotropy observed through the Swarm spacecraft is not simply a function of the electric field strength, but also results through the motion of hot plasma from strongly collisional regions to weakly-collisional regions.

In order to give more insights into the satellite results, this chapter revisits *Loranc and*

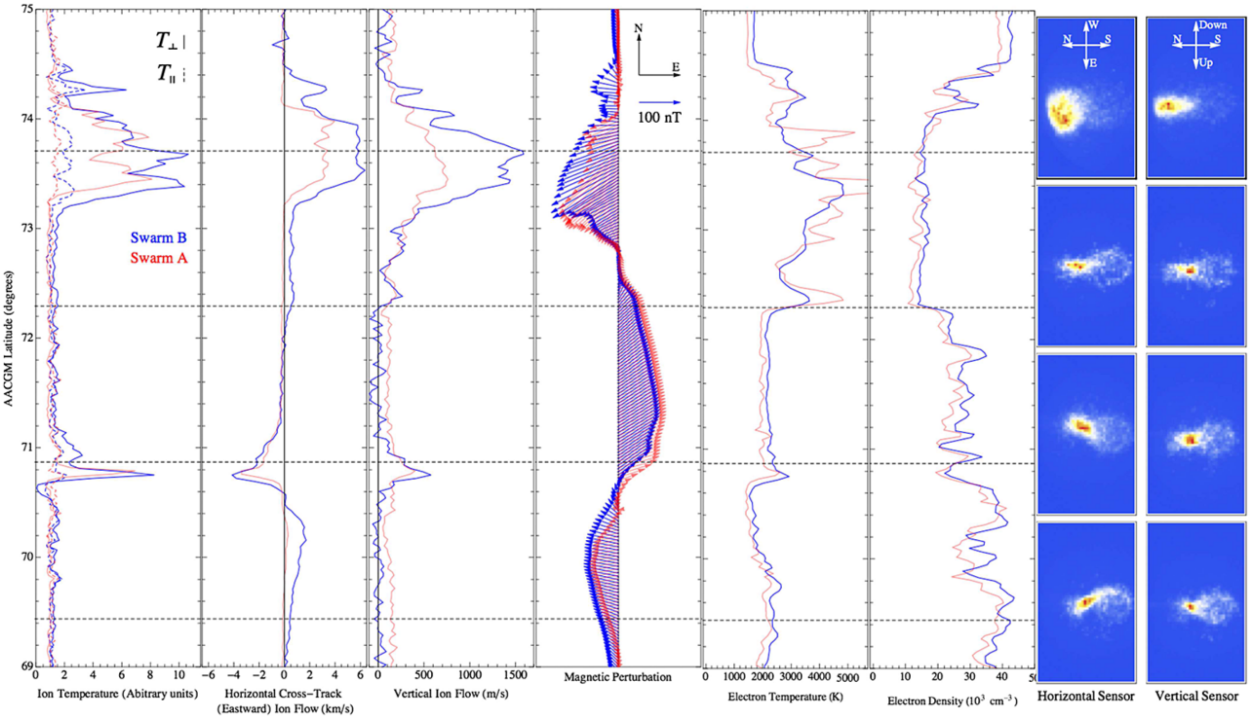

Figure 6.1: Anisotropic ion temperature heating event, taken directly from *Archer et al.* (2015). The blue lines indicate values inferred from Swarm B, and the red lines indicate values inferred from Swarm A roughly 30 s later. Swarm B is traveling antisunward around 01:42 MLT on 13 December 2013 between 04:52:05 UT and 4:54:46 UT. Ion temperature, horizontal flow, upward flow, and horizontal/vertical sensor images are measured by the TII, while magnetic variations are determined using the Vector Field Magnetometer (VFM) and electron temperature and electron density are measured by the Langmuir probe. The TII raw images are taken coincident with dashed black lines.

St-Maurice (1994), given that fluid theory is unable to reproduce the observed features of ionospheric ion upflows along flux tubes on short transition time scales. *Loranc and St-Maurice* (1994) formulated an analytical theory of the response of the high-latitude F-region to frictional heating using a time-dependent gyro-kinetic O^+ model across a discontinuous boundary between fully collisional and collisionless plasmas. By assuming a constant and uniform polarization electric field to reduce the calculation of the ion guiding center motion in the frame of a convecting flux tube to simply one-dimensional ballistic trajectories, they obtained the ion velocity distribution function, ion density, parallel velocity, parallel and perpendicular temperature, and parallel flux as a function of time and altitude. Their work showed that the velocity distributions are often distorted and formed from multiple populations in the initial steps of the evolution following the onset of a frictional heating event. *Loranc and St-Maurice* (1994) also found initial perturbations to propagate rapidly up the flux tube, observed periods in which the parallel temperature decreased to only a few hundred Kelvins, and saw large parallel temperatures and large downward parallel velocities develop as the flux tube returned to diffusive equilibrium. *Wilson* (1994) also modeled the evolution of ionospheric O^+ field-aligned upflows generated from high-latitude ion-neutral frictional heating, using a numerical semikinetic, collisional model. He also found distorted ion velocity distributions, but used discrete steps in electric field on the way to a steady state, and required stepping in both time and space. His results did not differ too markedly from the simpler formulation by *Loranc and St-Maurice* (1994), in spite of the far greater complexity of their calculations.

In this upgraded model of the weakly collisional altitude region based on the *Loranc and St-Maurice* (1994) approach, the effects of changing the electric field strength and the ion velocity distribution at the collisional boundary are studied. That is to say: O^+ ions are taken to be described by MC results at the collisional boundary and are assumed to be collisionless above it. The velocity distribution then evolves as a result of the vertical transport along a flux tube of newly heated ions, with the fastest ions being the first to reach a particular altitude. Unlike *Loranc and St-Maurice* (1994), this model: 1) includes the effect of temporal electric field changes on a convecting magnetic field line by incorporating the smooth descriptions of the ion velocity distributions developed in Chapter 4 using the POH

O^+-O cross-section, 2) does not use step-wise increments in the parallel and perpendicular temperatures to create boundary ion velocity distribution functions, and 3) includes the effect of changing densities at the boundary. From this analysis, variable anisotropic temperature ratios, changing plasma densities, ion heat flows, and ion upflows are obtained as a function of time and altitude for a variety of trigger conditions and a variety of possible ion-neutral cross-sections. This chapter first discusses the software behind the work in more detail, before outlining the findings. A number of possible future improvements are listed at the end.

6.1 Modeling High Altitude Ion Distributions

Weakly collisional regions of the ionosphere are subject to the vertical transport of plasma from highly collisional O^+ regions, making the plasma at Swarm altitudes (550 km) strongly dependent on the time history of a sampled flux tube. As ions move according to a given velocity distribution and travel into weakly-collisional regions, they are subject to the combined acceleration of the polarization electric field and gravity, which both act along the magnetic field at high-latitudes. As time goes on, these particles travel upwards and then fall back down into strongly-collisional regions. To determine the two-dimensional ion velocity distribution at a specific altitude above the boundary layer and a specific time relative to changing conditions at the boundary layer, this work first determines the number of particles traveling at a given final velocity at a specific time and altitude relative to the boundary distribution it originated from.

For a given final altitude relative to the boundary and a final parallel (to the magnetic field) velocity, the initial parallel velocity for a group of moving particles is found from:

$$v_{||0} = \sqrt{v_{||f}^2 - 2a_{gp}\Delta z} \tag{6.1}$$

where $v_{||f}$ is a chosen velocity at some particular altitude above the boundary, a_{gp} is the combined acceleration of gravity and the polarization electric field, and Δz is the altitude above the boundary. In this work the acceleration is simply taken to be 5 m/s^2 to approximate the combined effect of gravity and polarization electric fields due to electrons (see Section 6.3

for more). The length of time this population has spent traveling to Δz is then found using:

$$\Delta t = (v_{||f} - v_{||0})a_{gp}^{-1} \tag{6.2}$$

Knowing Δt and the time-history of the boundary layer (which is chosen before the simulation runs), the electric field and density from when the population left the boundary is recovered, which in turn reveals the two-dimensional distribution the particle population originated from. By then taking a slice through this distribution at $v_{||0}$, the relative number of particles traveling at the given $v_{||f}$ is found, as well as the perpendicular (to the magnetic field) distribution. Repeating this process for a series of $v_{||f}$ values reveals the total two-dimensional distribution present at a given Δz and time. Since this motion follows a magnetic field line, the variable electric field changes the ion velocity distribution at the collisional boundary, before it moves upward.

The approach first described provides a noise-free determination of the ion velocity distribution at a given time and location, and it does not require marching in time and tracking the motion of particles over a series of altitudes. As mentioned, a similar technique is used by *Loranc and St-Maurice* (1994) to develop an O^+ time-dependent gyro-kinetic model of the high-latitude F-region. However, due to the analytical nature of their calculations *Loranc and St-Maurice* (1994) use a time-dependent ion velocity distribution function at the boundary that is described by a simple bi-Maxwellian characterized by different parallel and perpendicular ion temperatures, mainly:

$$f(\mathbf{v}, z=0, t) = n_0 \left[\frac{m_i}{2\pi k_b T_\perp(0,t)}\right] e^{-m_i v_\perp^2/2k_b T_\perp(0,t)} \times \left[\frac{m_i}{2\pi k_b T_{||}(0,t)}\right]^{1/2} e^{-m_i v_{||}^2/2k_b T_{||}(0,t)} \tag{6.3}$$

where n_0 is the boundary plasma density. *Loranc and St-Maurice* (1994) then used step changes to determine the ion velocity distribution above $z = 0$. In the work presented here the shape of the boundary distribution is instead determined by the electric field, specifically the MC results characterized in Chapter 4 using the POH O^+-O RCE collision cross-section (see Appendix B for more information). Specifically a six degree polynomial fit is used to provide a smooth description of the coefficients as a function of electric field, allowing for the boundary electric field to be any magnitude between 0 mV/m (a Maxwellian distribution) and 200 mV/m (highly toroidal distribution). Meanwhile, the magnitude of the boundary distribution is determined by the plasma density, and as the plasma density at the boundary increases/decreases the overall magnitude of the boundary ion velocity distribution also increases/decreases.

6.2 Sample Runs

The output from two sample runs is shown to provide insights into the observations by *Archer et al.* (2015). Sample run 1 focuses on the effect an elevated boundary electric field has on the weakly-collisional region, while sample run 2 focuses on a boundary plasma depletion. This second run is performed in order to: 1) examine the role of the boundary plasma density in creating ion temperature anisotropies in the F-region, and 2) qualitatively characterize the effects of an increased recombination rate that results from elevated ion-neutral frictional heating in strongly-collisional regions during moderate to strong electric fields. This recombination is through:

$$\mathrm{O^+ + N_2 \rightarrow NO^+ + N}$$

due to its sensitivity to the ion and neutral particle energy (*Banks et al.*, 1974). Enhanced recombination rates of this nature are discussed extensively in *Schunk et al.* (1975), but are not fully implemented in this work because knowledge of the ion and neutral density profiles are required. Since it is challenging to determine from Swarm observations the degree of recombination being observed (which likely changes on a case-by-case basis), it is not realistic or practical to fully characterize the effects of enhanced recombination rates in this model. Thus, only a simple study of boundary plasma depletion is performed.

Any altitude is easily examined with this model, but since the focus of this work is the Swarm spacecraft, which is roughly 100 km to 150 km above the approximate boundary between fully collisional and collisionless plasmas, this work will focus on the region 100 km above the boundary.

6.2.1 Sample Runs 1A and 1B: Changing Electric Field

To make a qualitative comparison with the kinds of observations made by *Archer et al.* (2015), the boundary electric field is linearly increased by 1 mV/m per second from 0 mV/m (equivalent to a Maxwellian ion velocity distribution) to 100 mV/m and then decreased at the same rate back to 0 mV/m, while the boundary plasma density is kept constant at 1×10^{12} m^{-3}. Letting t_s be the beginning of the electric field increase, Figure 6.2 shows the ion velocity distribution as it evolves over time 100 km above the boundary layer. Here the recovered velocity distribution is a superposition of various time histories. For example, at $t_s = 250s$ a central plasma depletion is seen at approximately $v_{||f} = 400$ m/s, which originates from a toroidal boundary velocity distribution. Meanwhile, the surrounding features are from more Maxwellian boundary distributions. As time goes on, the toroidal ion velocity distributions from the boundary sweep through the 100 km two-dimensional ion velocity distribution from high to low $v_{||f}$ values, leaving behind the original Maxwellian distribution.

Using these ion velocity distributions and Equations 4.3 through 4.5, Figure 6.3 shows how the plasma density, parallel velocity, and both the parallel and perpendicular temperatures all changed as functions of time at 100 km. At 40 s the plasma density starts to increase, with a 19% increase by $t_s = 160$ s. The density then decreases to about 3% above the original density over 320 s, after which the plasma density continues to stay slightly elevated for over 1000 s, slowly and gently increasing and then decreasing back to the original plasma density at $t_s = 0$ s. The average parallel velocity also begins to increase at 40 s, and experiences a 270 s long upflow that reaches 230 m/s slightly before the plasma density reaches its maximum. After this upflow, the parallel velocity becomes negative, gradually extending to -40 m/s at $t_s = 700$ s. This downflow then becomes less negative, and ultimately returns to zero.

Before 40 s, the parallel and perpendicular temperatures are approximately equal (to within the 2% uncertainty mentioned in Chapter 4). The parallel temperature then begins to increase from 1000 K to a maximum of 1600 K by $t_s = 140$ s. After this, the parallel temperature decreases back down to its original value by 230 s, decreases further, and then gradually increases back to 1100 K, ultimately decreasing back to its original temperature after 1000 s. However, the perpendicular ion temperature begins to increase at 210 s, reaching

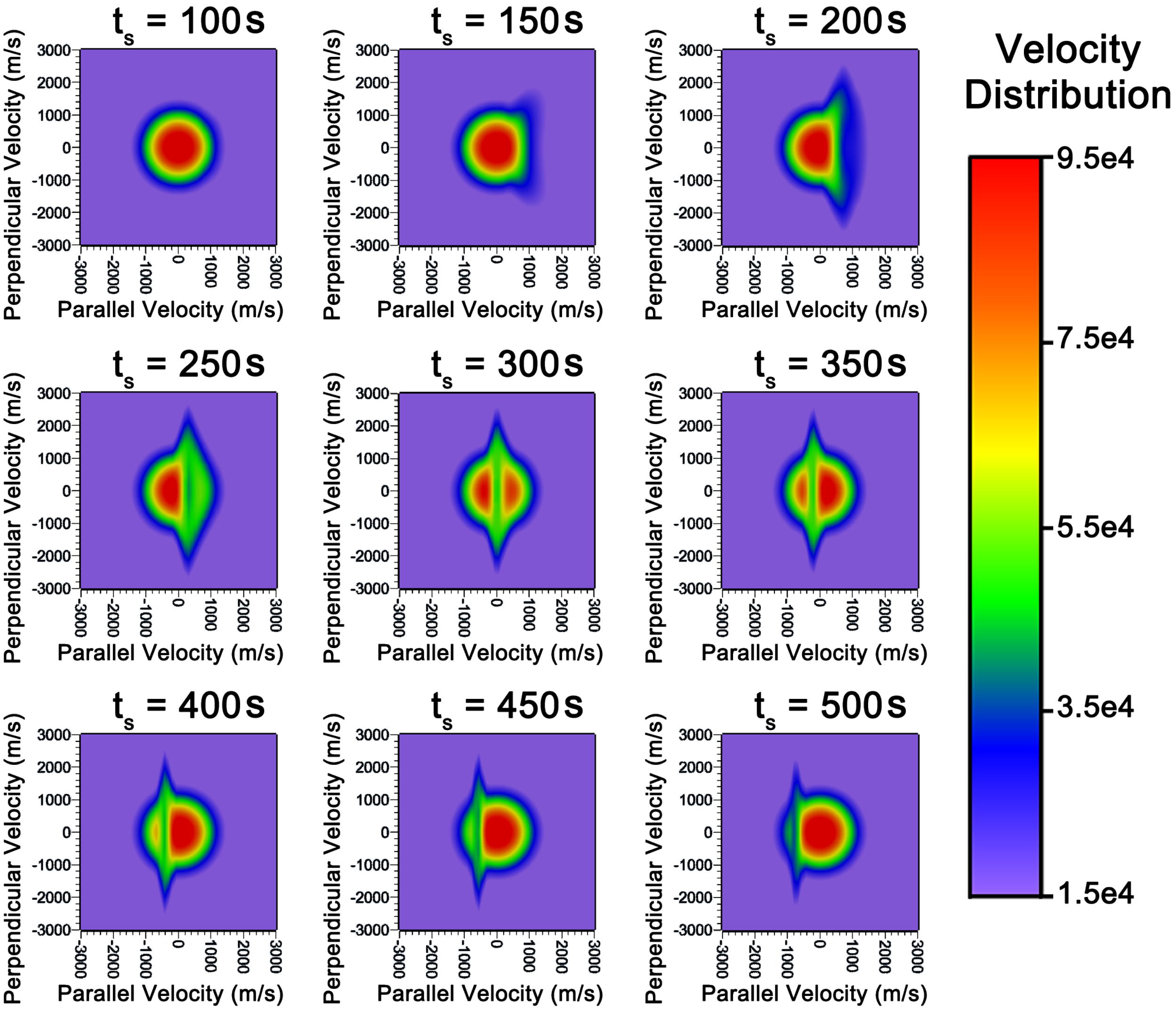

Figure 6.2: The velocity distribution 100 km above the boundary layer as the boundary electric field changes. Here, the boundary electric field is linearly increased by 1 mV/m per 1 second from 0 mV/m (equivalent to a Maxwellian ion velocity distribution) to 100 mV/m and then decreased at the same rate back to 0 mV/m, while the boundary plasma density is kept at a constant 1×10^{12} m^{-3}. $t_s = 0$ s is when the boundary electric field began to increase.

a maximum temperature of 5300 K at 300 s, then returns back to 1000 K by 390 s.

To explore the effects of changing the scale height (the distance over which the density depletes by a factor of e), Figure 6.4 shows a figure similar to Figure 6.3, but 100 km higher (200 km above the boundary). Around 130 s the plasma density increases and reaches a 30% increase by $t_s = 240$ s. At this point the density begins to decrease back to the original value, decreasing more gradually with time. The average parallel velocity begins to increase at 120 s, remaining elevated for 260 s and reaching a maximum of 320 m/s, 60 s before the plasma density maximum. The upflow then becomes a downflow, extending to -81 m/s at $t_s = 690s$ before ultimately returning to zero. At 110 s the parallel temperature increases from 1000 K to 1800 K by $t_s = 180s$. The parallel temperature then decreases back to 1000 K by 280 s, gradually decreases further to 880 K, then increases to 1190 K before ultimately returning to its original value. The perpendicular ion temperature begins to increase at 290 s, reaching a maximum temperature of 5050 K at 380 s. then returns back to 1000 K by 480 s.

Just like the 100 km altitude case, the ion temperature at 200 km becomes highly anisotropic due to transport from strongly-collisional regions. Although the perpendicular temperature is smaller at higher altitudes, ion upwelling is 100 m/s larger at 200 km than at 100 km. The higher altitude achieves a 5.7 perpendicular to parallel temperature ratio at 380 s, 180 s after the peak average parallel ion velocity, while the lower altitude reaches a 5.4 perpendicular to parallel temperature ratio at 300 s, 150 s after the peak average parallel ion velocity. Meanwhile, the peak density at 200 km occurs 40 s after the peak upwelling, while the peak density at 100 km occurs only 10 s after the peak upwelling.

6.2.2 Sample Run 2: Changing Boundary Density

For this run, the plasma density is exponentially decreasing at the boundary over 200 s (the same amount of time the electric field is elevated in sample run 1) from 1×10^{12} m^{-3} to 0.5×10^{12} m^{-3}. Figure 6.5 shows the ion velocity distribution that results at 100 km due to the boundary plasma density depletion. This ion velocity distribution is a superposition of various time histories in which the plasma density becomes lower. As this depletion sweeps through the distribution from high to low $v_{||f}$ values, the distribution returns to a Maxwellian ion velocity distribution, but with a lower overall density.

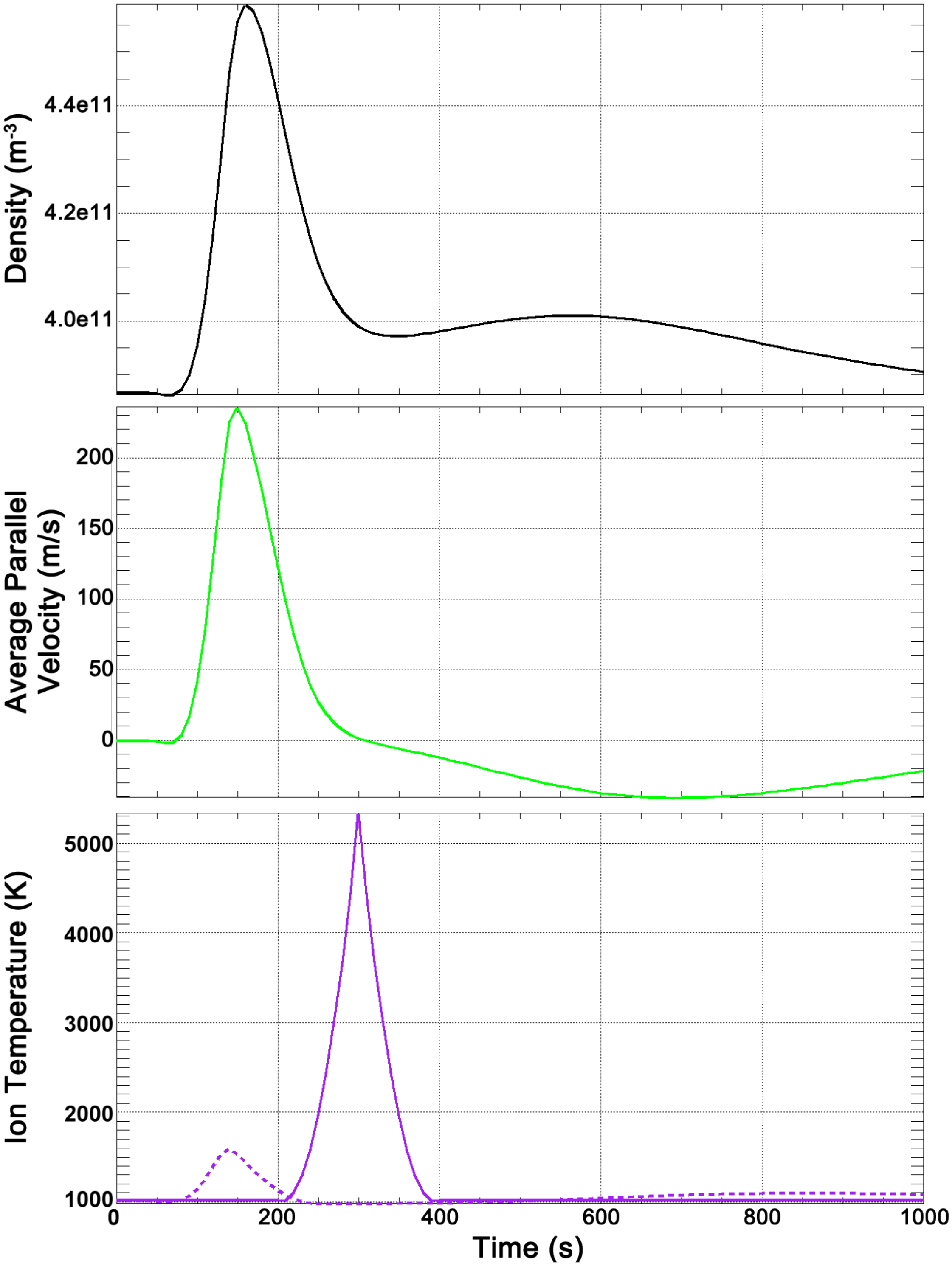

Figure 6.3: Velocity distribution moments calculated from the two-dimensional distribution featured in Figure 6.2. The top panel is the plasma density, the second panel is the average parallel ion velocity, and the bottom panel is the ion temperature, where the dashed line is the temperature parallel to the magnetic field and the solid line is the temperature perpendicular to the magnetic field.

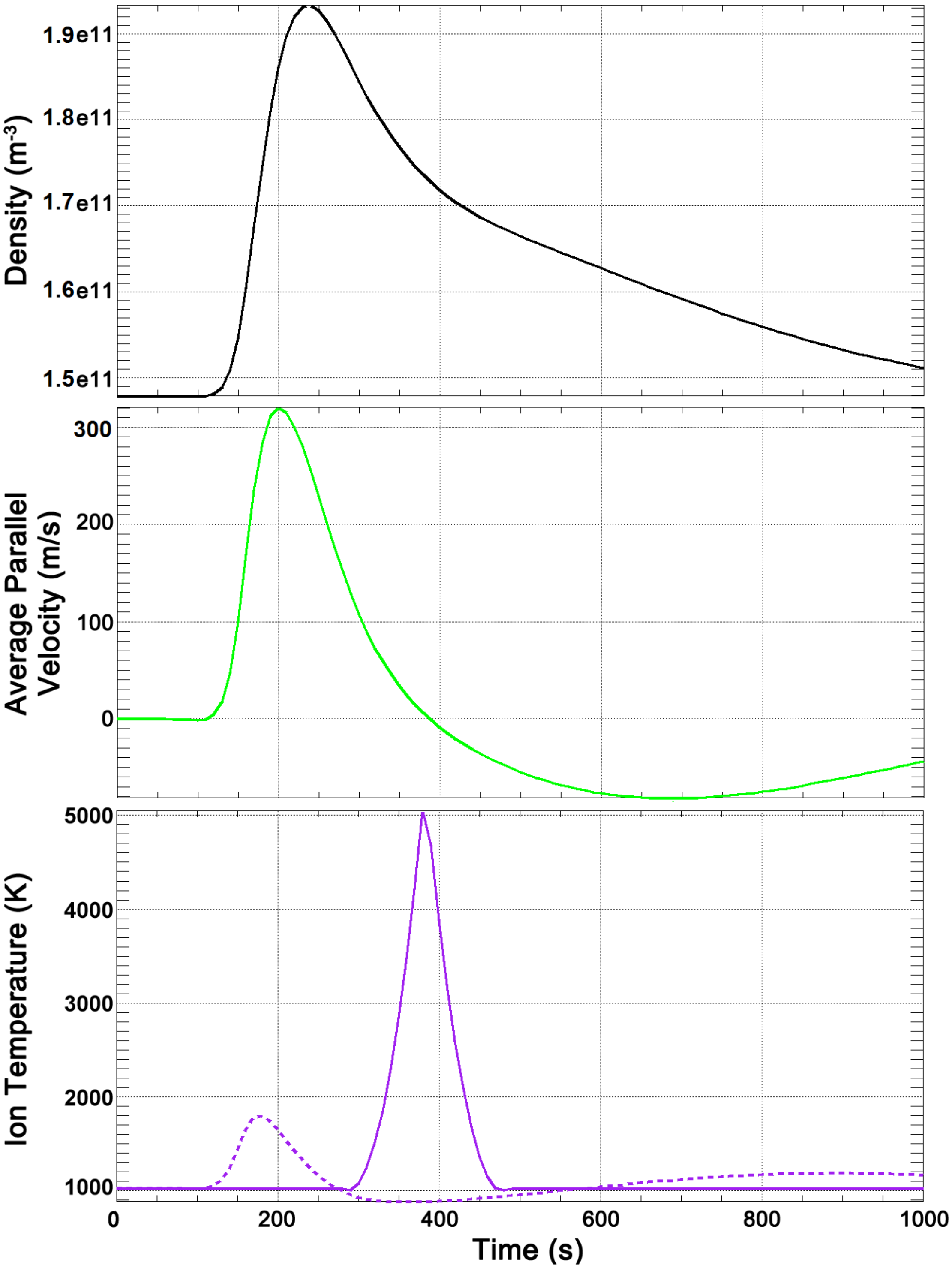

Figure 6.4: Velocity distribution moments 100 km above the two-dimensional distribution featured in Figure 6.2. The top panel is the plasma density, the second panel is the average parallel ion velocity, and the bottom panel is the ion temperature, where the dashed line is the temperature parallel to the magnetic field and the solid line is the temperature perpendicular to the magnetic field.

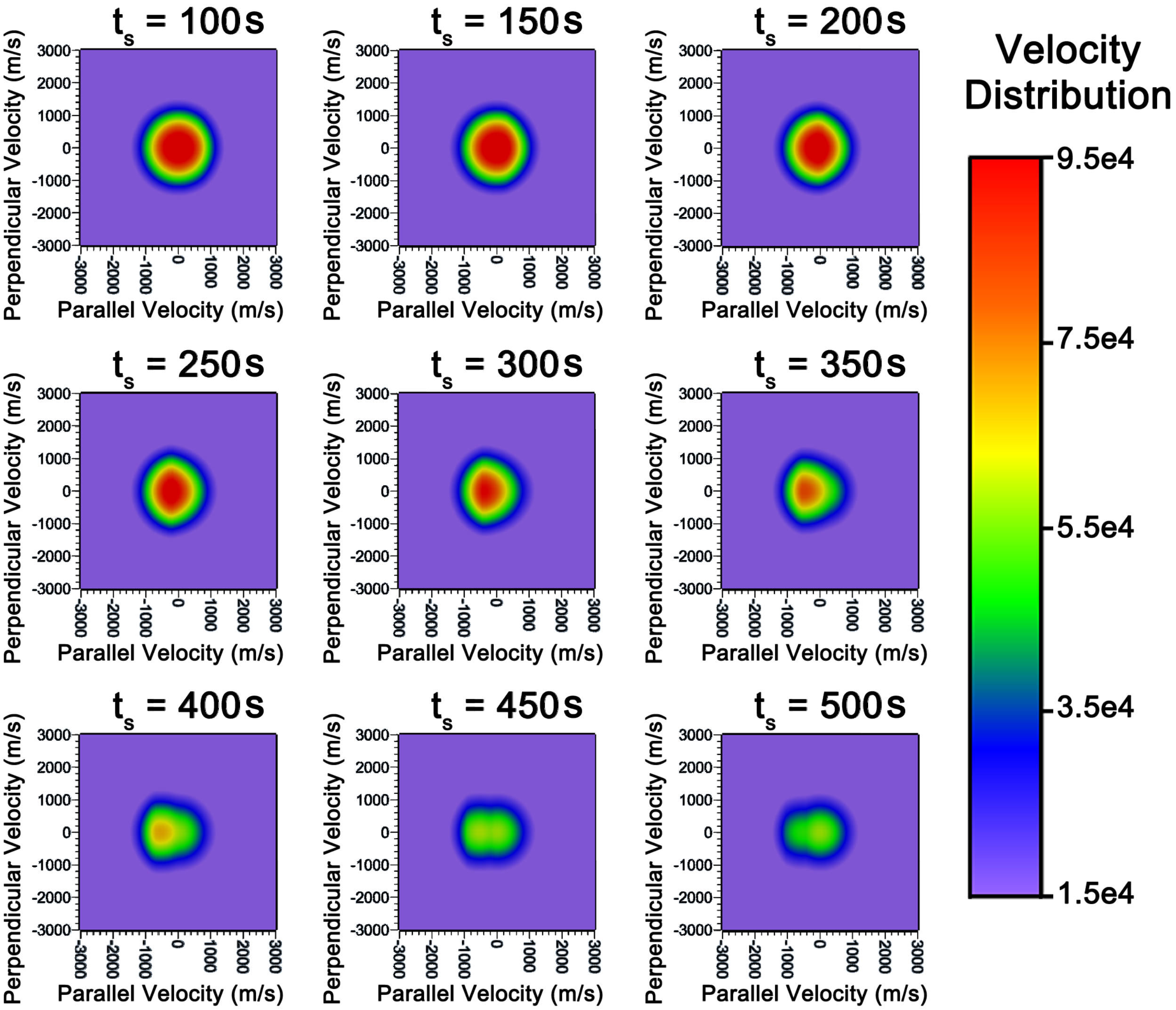

Figure 6.5: The velocity distribution 100 km above the boundary layer as the boundary density decreases exponentially from 1×10^{12} m^{-3} to 0.5×10^{12} m^{-3} over 200 s. $t_s = 0$ is when the boundary density begins to decrease.

Figure 6.6 shows the plasma density, average parallel velocity, parallel temperature, and perpendicular ion temperature at 100 km as a function of time. As expected, the plasma density decreases over the course of approximately 1000 s by 50%. The average parallel velocity experiences an overall down-flow, which agrees with the relative decrease in plasma at 100 km. This downflow reaches -190 m/s at 350 s before gradually returning back to zero. The parallel temperature experiences a decrease from approximately 1000 K to almost 900 K before becoming enhanced to nearly 1200 K. Meanwhile, the perpendicular ion temperature experiences no change from its original value, as expected.

6.3 Discussion

This work improves upon the techniques used in *Loranc and St-Maurice* (1994) by including the effect of temporal electric field changes on a convecting magnetic field line, as well as the effect of variable boundary densities and realistic temporal variations in the ion velocity distribution at the boundary. The results of this work indicate that the observations seen at Swarm altitudes depend heavily on the time history of a given flux tube and the transport of plasma from strongly-collisional regions, making the parallel to perpendicular temperature ratios unpredictable at times.

Here, two sample runs were emphasized, one in which the shape of the boundary velocity distribution changes as a function of the electric field, and one in which the boundary density depletes over time. Both of these sample runs agree qualitatively with the results of *Loranc and St-Maurice* (1994) and *Wilson* (1994), who saw distorted ion velocity distributions at high altitudes as a result of changing boundary conditions propagating upwards along a given flux tube from strongly-collisional regions. In the first sample run a strong upflow is seen, as well as anisotropic ion temperatures. However, at the same time the first sample run shows enhanced plasma densities. Meanwhile, in the second sample run a plasma depletion mechanism at the boundary leads to a depleted density at Swarm altitudes, suggesting that the plasma depletion seen in *Archer et al.* (2015) is possibly related to the enhanced recombination rates that result from strong frictional heating lower down.

This simulation shows that changes in the ion-neutral frictional heating in collisional

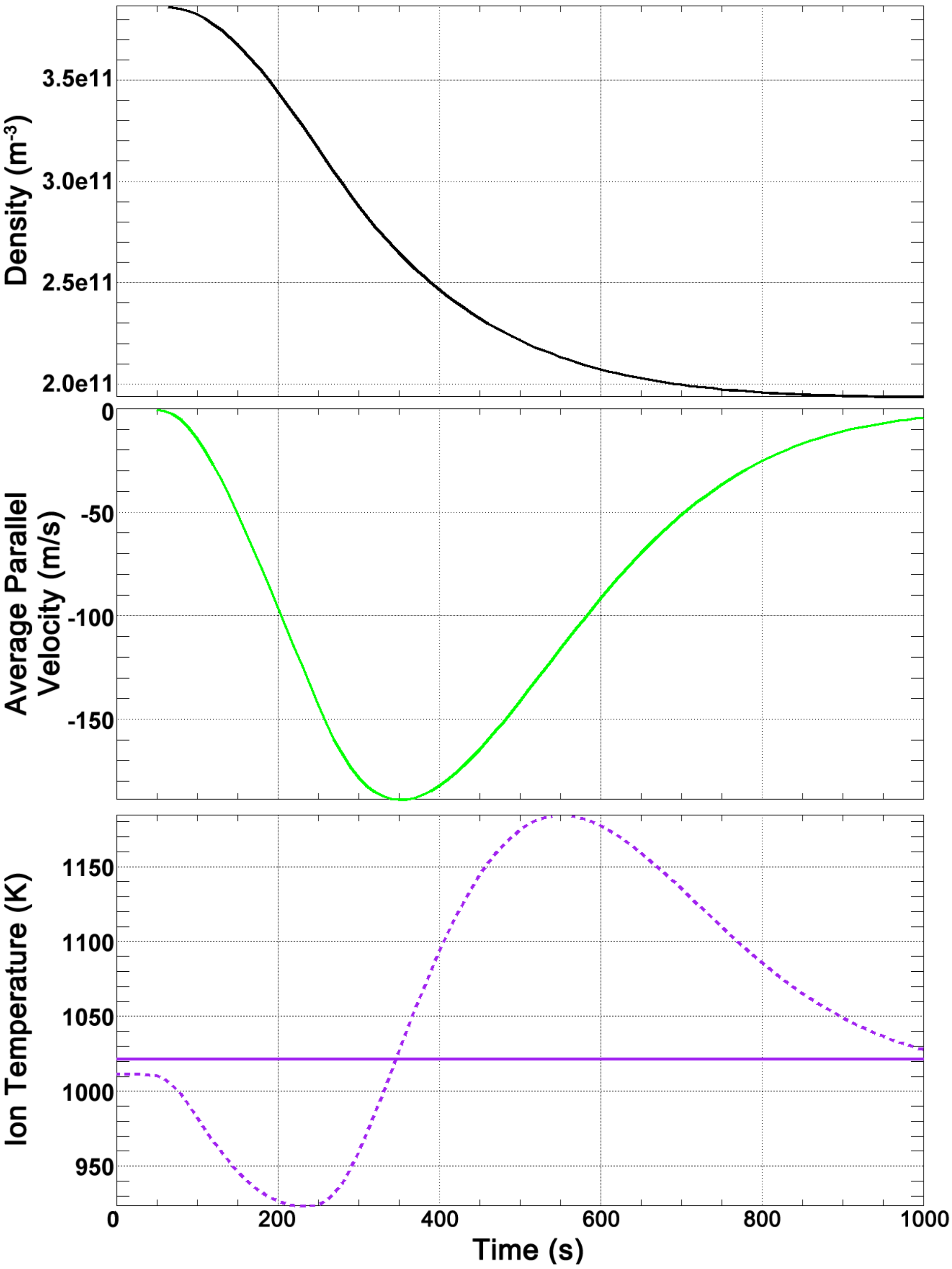

Figure 6.6: Velocity distribution moments calculated from the two-dimensional distribution featured in Figure 6.5. The top panel is the plasma density, the second panel is the average parallel ion velocity, and the bottom panel is the ion temperature, where the dashed line is the temperature parallel to the magnetic field and the solid line is the temperature perpendicular to the magnetic field. Note the scale changes between this figure and Figure 6.3.

regions easily accounts for the variability seen in the perpendicular to parallel ion temperature ratios at higher altitudes. These results also show that the observations from *Archer et al.* (2015) depend strongly on how long ago heating in a given flux tube began, and where Swarm is relative to the heating region. This is because temperature changes introduce vertical upward motion until, for a steady state solution, the parallel to perpendicular temperature ratio is the expected ratio for the collisional region. If Swarm observations are nowhere near that ratio, it has to mean the flux tube has not been heated for long. Additionally, this leads to periods where the parallel temperature is greater than perpendicular temperature.

This work also compared the impact of changing the boundary electric field and changing the boundary plasma density. Here, even when the density decreases by a factor of two in a small amount of time, the temperature anisotropy resulting is relatively minimal. At any rate, it is also interesting to point out in the second sample run that down-welling results through diffusive equilibrium, but this doesn't compare in magnitude with upwelling due to friction.

Although the results presented here are already insightful, many more simulation runs are required to fully understand the observations made by the Swarm spacecraft. For example, even though the runs presented already show that this work is able to create varying perpendicular to parallel temperature ratios and distorted ion velocity distributions, the upwelling seen through frictional heating in sample run 1 is out of phase with the perpendicular ion temperature, which is inconsistent with *Archer et al.* (2015) and Swarm observations. However, future work will use *Loranc and St-Maurice* (1994) and *Wilson* (1994) as a guide to make specific runs that replicate Swarm observations more closely.

An important advantage of the technique used in this work is that it is capable of finding the ion velocity distribution at a given time and altitude without tracking the evolution of the collisional-less region over time. However, this ultimately means that this technique is unable to properly incorporate the polarization electric field as a function of time and altitude. When the polarization electric field is considered properly, the ion equation of motion in this region becomes (in the absence of magnetic mirror effects):

$$\frac{\partial v_{||}}{\partial t} = -g - \frac{e}{m_i}\frac{\partial \phi_E}{\partial z} \tag{6.4}$$

where g is gravity. Considering:

$$n = n_0 \exp\left(\frac{e\phi_e}{k_B T_e}\right) \tag{6.5}$$

this gives:

$$\frac{\partial v_{||}}{\partial t} = -g - \frac{k_b T_e}{m_i}\frac{\partial}{\partial z}\ln\left(\frac{n}{n_0}\right) \tag{6.6}$$

which is written as:

$$v_{f||} = \sqrt{v_{0||}^2 - 2gz - \frac{2k_b T_e}{m_i}\ln\left(\frac{n}{n_0}\right)} \tag{6.7}$$

This shows the dependency of the final velocity on the plasma density, which is a function of altitude. As transport changes the density profile, the motion of the charges also changes. Furthermore, the change in time is now given by:

$$\Delta t = \int_0^z \frac{dz}{v_{f||}} \tag{6.8}$$

To implement Equations 6.7 and 6.8 correctly into this work requires tracking the density as a function of altitude and time, meaning the simulation must step in time and altitude. Note that for a diffusive equilibrium situation:

$$v_{f||} = \sqrt{v_{0||}^2 - \frac{2gz}{1 + T_e/T_{||}}} \tag{6.9}$$

In addition to correctly incorporating a polarization electric field, a more accurate transition between strongly-collisional and collisionless regions is required, particularly if the desired altitude is within two scale heights from the collisional boundary. This means simulating multiple regions that become progressively less collisional with altitude. Chapter 4 also shows the importance of Coulomb collisions and the O^+-O RCE cross-section on the ion velocity distribution. For this reason it would be beneficial to extend the present work to include Coulomb collisions as a function of altitude. As well, once the observations in Chapter 5 are calibrated with spectral fitting routines that incorporate toroidal ion velocity distributions, and the correct O^+-O RCE cross-section is determined, the cross-section used in this work may need to be altered if proven to be inaccurate.

CHAPTER 7

SUMMARY AND FUTURE WORK

In this thesis the joint impact of electric field strength and ion-neutral collisions on the high-latitude ionosphere has been explored. In researching this topic, several new discoveries have been made, in parallel with the development of several new techniques by which to improve future studies of ISR- and satellite-inferred plasma parameters, including the electric fields themselves.

Chapter 4 focuses on a manuscript that has recently been accepted for publication in *Radio Science*. This manuscript presents the first comprehensive calculation of IS spectra from quantitative, MC based, distorted ion velocity distributions. The anisotropy of the ion velocity distribution was fully characterized for all possible interactions between atomic and molecular ions and neutrals throughout the F-region. It was found, to start with, that the line-of-sight ion temperature is for the most part well described by its dependence on the parallel and perpendicular temperature through Equation 4.7, implying that the line-of-sight ion temperature at 55° (with respect to the magnetic field) is the same as the average ion temperature. This finding is important for Joule heating studies, which rely on the average ion temperature.

The second aspect of Chapter 4 is the calculated spectral shapes, where several new results were obtained. First, as an important point for practical applications, it was found that NO^+ spectral shapes are for the most part so similar to those associated with equivalent (same line-of-sight ion temperature) Maxwellian velocity distributions, that there is no real need to analyze NO^+ spectra with non-Maxwellian ion dielectric functions, except near 100 mV/m and for aspect angles of the order of 55° or greater. However, for O^+ ions the spectral shape is so distorted from the Maxwellian description for electric fields stronger than 40 mV/m that its impact cannot be ignored, as the retrieval of the plasma parameters in standard analysis programs (particularly the electron temperature) will most assuredly be affected. It was found in the present work that particularly for electric fields in excess of 100 mV/m, the O^+ spectral shapes are multi-peaked and rather different from those expected from earlier work (e.g., *Raman et al.* (1981); *Suvanto et al.* (1989)), except for directions parallel or near-parallel to the magnetic field. Parallel or near-parallel to the magnetic field, spectra from MC simulated velocity distributions are similar to those from effective Maxwellian distributions, but indicate a larger electron to line-of-sight ion temperature ratio than expected from actual Maxwellians. In what turned out to be a bit of a surprise, this study also found strong signatures of toroidal ion velocity distributions at 20° with respect to the magnetic field, showing that the best viewing angle to identify toroidal distributions might be near 20°. This is particularly interesting for RISR-N and RISR-C, which offer optimal signal-to-noise ratios at this angle compared to lower elevation angles looking closer to the perpendicular to the magnetic field.

A third aspect of the Chapter 4 calculations dealt with the stability of the ion velocity distribution against the generation of magnetic field-aligned instabilities. From the use of simple Nyquist diagrams based on the calculated ion velocity distributions and their dielectric functions, the stability was compared for two competing models of the RCE cross sections, one by *Pesnell et al.* (1993) and the other by *Knof et al.* (1964). The distributions obtained with the former cross-section were found to actually be stable, contrary to the cross-sections associated with the latter.

A final aspect of Chapter 4 dealt with the handling of velocity distribution corrections due to Coulomb collisions. The corrections have measurable effects on the O^+ ions, and as the altitude increases, the influence of Coulomb collisions also increases, explaining the increase in line-of-sight ion temperature with altitude seen in ISR data that had been presented in *Goodwin et al.* (2014). The corrections were applied not just to the temperature anisotropies but also to the spectra shapes.

The first part of Chapter 5 used the insights gained from Chapter 4 to seek a method by which to determine the ion temperature anisotropy from actual ISR observations. Using observations from overlapping northward pointing RISR-N beams during a strong heating event on 12 September 2014, in which the parallel drift was relatively small and the $\mathbf{E} \times \mathbf{B}$

drift dominated the full plasma motion, two techniques were presented to characterize the anisotropy above 220 km, where O^+-O collisions dominated. They gave similar results and indicated that the temperature anisotropy was close to following the *Knof et al.* (1964) O^+-O RCE cross-section description discussed in Chapter 4 between 220 km and 320 km. This stated, however, the results also indicated that the ionospheric ion temperature may actually be more anisotropic than the *Knof et al.* (1964) description, even though it is a closer fit than the alternative *Pesnell et al.* (1993) fit. However, these results will have to be recalculated after a full spectral analysis based on Chapter 4 is implemented in the data analysis scheme.

From the anisotropy the average ion temperature could also be determined, meaning that the magnitude of the effective electric field (i.e., the electric field in the neutral atmospheric frame of reference) could be inferred. The line-of-sight ion temperatures that were inferred from the data implied the presence of a 120 mV/m to 140 mV/m effective electric field, which is less than the electric field inferred from the Bayesian approach in discussed in *Clauer et al.* (2016) (*Heinselman and Nicolls*, 2008). This led to a second section in Chapter 5 which was concerned with a determination of the actual electric field vector using a novel approach which compared E- and F- region drifts on magnetic field lines close to one another. This new technique yielded even stronger electric fields than those inferred from the Bayesian approach, with an electric field strength that reached roughly 180 mV/m at 83.2° geomagnetic latitude. This implied a 800 m/s neutral wind when compared to the 140 mV/m effective electric field, assuming the motion was along the ion drift (as is usually found). The direction of the $\mathbf{E}\times\mathbf{B}$ was consistent with the reverse convection cell analysis of *Clauer et al.* (2016). It should be noted that the observations were accompanied by large E-region electron temperatures of the order of 3500 K, as reported by *Clauer et al.* (2016). This will provide a possible tool to see which of the two electric field determinations is more trustworthy, at least for the event studied in Chapter 5.

Chapter 6 revisited a time-dependent gyro-kinetic O^+ model originally formulated by *Loranc and St-Maurice* (1994). Here, the response to the high-latitude F-region frictional heating in a strongly-collisional region is simulated by assuming a discontinuous boundary between fully collisional and collisionless plasmas. Unlike the simulation presented in *Loranc and St-Maurice* (1994), this updated model includes arbitrary temporal boundary electric field and plasma density changes, as well as realistic temporal variations of the ion velocity distribution at the boundary. This provides fast simulations of velocity distributions and their moments above the collisional regions without the need for oversimplified temporal changes at the boundary. The earlier results of *Loranc and St-Maurice* (1994) and of *Wilson* (1994) were reproduced, namely, highly distorted ion velocity distributions were found at high altitudes, as well as unpredictable anisotropic ion temperatures, as a result of changing boundary conditions propagating upwards along a given flux tube from strongly-collisional regions.

This part of the study has provided an explanation for the variability seen in the perpendicular to parallel ion temperature ratios at higher altitudes and for their connections to ion upflows, as seen through Swarm observations at 550 km (e.g. *Archer et al.* (2015)). The present study shows that Swarm observations depend heavily on the time history of a given flux tube and the transport of plasma from strongly-collisional regions, making the parallel to perpendicular temperature ratios unpredictable at times. This thesis has also shown that the effects of density changes at the boundary are typically smaller than those induced by strong frictional heating.

From this research stems much more work that needs to be done to evaluate the role electric field strength has in changing the high-latitude ionosphere. Arguably the most important result of Chapter 4 is the production of a complete description of the ion velocity distribution for a variety of electric fields and aspect angles. Given this, it is critical to incorporate these descriptions into ISR spectral fitting routines that currently assume ion velocity distributions to be Maxwellian. The implementation of a new procedure based on Chapter 4 is currently underway using the observations presented in Chapter 5 and *Clauer et al.* (2016), but will ultimately be automated for other datasets. Our simulated velocity distribution determination at 90° should be most useful in particularly strong electric field situations for RPA data studies of the type undertaken by *St-Maurice et al.* (1976), as mentioned in Chapter 4. As shown in Chapter 5, the results of Chapter 4 can then also be used to characterize the ion temperature anisotropy of the ionosphere and determine the correct O^+-O RCE collision cross-section. Once distorted ion velocity distributions are incorporated into IS spectral fitting routines, experiments of the kind discussed in Chapter 5, such as the

SSEBIT experiment (which runs frequently on both RISR-N and RISR-C), can be used to determine convection uniformity in space in F-region observations.

Lastly, the results of Chapter 6 have so far been revealing, but many more simulations runs are required to better understand the observations seen by the Swarm spacecraft, using *Loranc and St-Maurice* (1994) and *Wilson* (1994) as a guide. Although the initial simulation presented in this thesis is useful because it quickly provides the ion velocity distribution and the distribution moments at a given time and altitude, it would ultimately require the inclusion of a self-consistent polarization electric field, which unfortunately would require systematically stepping in time and space. Furthermore, a more gradual transition to collision-free would improve the model results, particularly if the desired altitude is within two plasma scale heights from the collisional boundary. The effect of Coulomb collisions should also be considered, as per Chapter 4.

REFERENCES

Akasofu, S. I. (1976), Recent progress in studies of DMSP auroral photographs, *Space Science Reviews*, *19*(2), 169–215.

Akbari, H., A. Bhatt, C. La Hoz, and J. L. Semeter (2017a), Incoherent Scatter Plasma Lines: Observations and Applications, *Space Science Reviews*, pp. 1–46.

Akbari, H., L. V. Goodwin, J. Swoboda, J.-P. St-Maurice, and J. L. Semeter (2017b), Extreme plasma convection and frictional heating of the ionosphere: ISR observations, *Journal of Geophysical Research: Space Physics*.

Alfvén, H. (1986), *Plasma universe*, KTH Royal Institute of Technology.

Archer, W. E., D. J. Knudsen, J. K. Burchill, M. R. Patrick, and J. P. St-Maurice (2015), Anisotropic core ion temperatures associated with strong zonal flows and upflows, *Geophysical Research Letters*, *42*(4), 981–986.

Banks, P., R. Schunk, and W. Raitt (1974), NO+ and O+ in the high latitude F-region, *Geophysical Research Letters*, *1*(6), 239–242.

Banks, P. M. (1980), Energy sources of the high latitude upper atmosphere, in *Exploration of the polar upper atmosphere*, pp. 113–127, Springer.

Banks, P. M., and G. Kockarts (1973), *Aeronomy*, Academic, New York.

Barakat, A. R., R. W. Schunk, and J. P. St-Maurice (1983), Monte Carlo calculation of the O+ velocity distribution in the auroral ionosphere, *Journal of Geophysical Research*, *88*, 3237–3241.

Bernstein, I. B. (1958), Waves in a plasma in a magnetic field, *Physical Review*, *109*(1), 10–21.

Bhatnagar, P. L., E. P. Gross, and M. Krook (1954), A model for collision processes in gases. i. Small amplitude processes in charged and neutral one-component systems, *Physical Review*, *94*(3), 511.

Chau, J. L., C. J. Heinselman, and M. J. Nicolls (2012), Phased Arrays Radars, `https://www.scribd.com/document/325933206/11-Chau-Phased-Arrays-pdf`.

Chen, F. F. (2006), *Introduction to Plasma Physics and Controlled Fusion*, Springer.

Clauer, R. C., Z. Xu, M. Maimaiti, M. J. Ruohoneimi, W. Scales, M. D. Hartinger, M. J. Nicolls, S. Kaeppler, F. D. Wilder, and R. E. Lopez (2016), Investigation of a rare event where the polar ionospheric reverse convection potential does not saturate during a period of extreme northward IMF solar wind driving, *Journal of Geophysical Research: Space Physics*, *121*(6), 5422–5435.

Collis, P. N., and I. Häggström (1988), Plasma convection and auroral precipitation processes associated with the main ionospheric trough at high latitudes, *Journal of Atmospheric and Terrestrial Physics*, *50*(4-5), 389–404.

Dougherty, J. P., and D. T. Farley (1960), A theory of incoherent scattering of radio waves by a plasma, in *Proceedings of the Royal Society of London A: Mathematical, Physical and Engineering Sciences*, vol. 259, pp. 79–99, The Royal Society.

Dougherty, J. P., and D. T. Farley (1963), A theory of incoherent scattering of radio waves by a plasma: 3. Scattering in a partly ionized gas, *Journal of Geophysical Research*, *68*(19), 5473–5486.

Evans, J. V. (1972), Ionospheric movements measured by incoherent scatter: A review, *Journal of Atmospheric and Terrestrial Physics*, *34*(2), 175–209.

Farley, D. T., J. P. Dougherty, and D. W. Barron (1961), A theory of incoherent scattering of radio waves by a plasma ii. Scattering in a magnetic field, in *Proceedings of the Royal Society of London A: Mathematical, Physical and Engineering Sciences*, vol. 263, pp. 238–258, The Royal Society.

Fejer, J. A. (1960), Scattering of radio waves by an ionized gas in thermal equilibrium, *Canadian Journal of Physics*, *38*(8), 1114–1133.

Fejer, J. A. (1961), Scattering of radio waves by an ionized gas in thermal equilibrium in the presence of a uniform magnetic field, *Canadian Journal of Physics*, *39*(5), 716–740.

Foster, J. C., and P. J. Erickson (2000), Simultaneous observations of E-region coherent backscatter and electric field amplitude at F-region heights with the Millstone Hill UHF radar, *Geophysical Research Letters*, *27*(19), 3177–3180.

Fried, B. D., and S. D. Conte (1961), *The Plasma Dispersion Relation*, Academic Press, New York.

Friis-Christensen, E., H. Lühr, D. Knudsen, and R. Haagmans (2008), Swarm–an Earth observation mission investigating geospace, *Advances in Space Research*, *41*(1), 210–216.

Fukunishi, H. (1975), Dynamic relationship between proton and electron auroral substorms, *Journal of Geophysical Research*, *80*(4), 553–574.

Gaimard, P., J.-P. St-Maurice, C. Lathuillere, and D. Hubert (1998), On the improvement of analytical calculations of collisional auroral ion velocity distributions using recent Monte Carlo results, *Journal of Geophysical Research: Space Physics*, *103*(A3), 4079–4095.

Goodwin, L., J.-P. St-Maurice, P. Richards, M. Nicolls, and M. Hairston (2014), F region dusk ion temperature spikes at the equatorward edge of the high-latitude convection pattern, *Geophysical Research Letters*, *41*(2), 300–307.

Gordon, W. E. (1958), Incoherent scattering of radio waves by free electrons with applications to space exploration by radar, *Proceedings of the IRE*, *46*(11), 1824–1829.

Gross, E. P. (1951), Plasma oscillations in a static magnetic field, *Physical Review*, *82*(2), 232.

Hagfors, T. (1961), Density fluctuations in a plasma in a magnetic field, with applications to the ionosphere, *Journal of Geophysical Research*, *66*(6), 1699–1712.

Hagfors, T. (1995), Plasma fluctuations excited by charged particle motion and their detection by weak scattering of radio waves, *INCOHERENT SCATTER*, pp. 1–32.

Hagfors, T., and R. A. Brockelman (1971), A theory of collision dominated electron density fluctuations in a plasma with applications to incoherent scattering, *The Physics of Fluids*, *14*(6), 1143–1151.

Häggström, I. (2012), Incoherent and coherent scatter radars, `https://www.espas-fp7.eu/trac/raw-attachment/wiki/PublicPages/TrainingPresentations/IngemarHaggstrom_Incoherent_and_Coherent_Scatter_Radars.pdf`.

Harra, L. K., and K. O. Mason (2004), *Space science*, World Scientific Publishing Company.

He, H., J. Li, and P. Stoica (2012), *Waveform design for active sensing systems: A computational approach*, Cambridge University Press.

Hedin, A. E. (1991), Extension of the MSIS thermosphere model into the middle and lower atmosphere, *Journal of Geophysical Research: Space Physics*, *96*(A2), 1159–1172.

Hedin, M., I. Häggström, A. Pellinen-Wannberg, L. Andersson, U. Brändström, B. Gustavsson, Å. Steen, A. Westman, G. Wannberg, T. Aso, et al. (2000), 3-D extent of the main ionospheric trough–a case study, *arXiv preprint physics/0001043*.

Heelis, R. A. (1984), The effects of interplanetary magnetic field orientation on dayside high-latitude ionospheric convection, *Journal of Geophysical Research: Space Physics*, *89*(A5), 2873–2880.

Heelis, R. A., J. K. Lowell, and R. W. Spiro (1982), A model of the high-latitude ionospheric convection pattern, *Journal of Geophysical Research: Space Physics*, *87*(A8), 6339–6345.

Heelis, R. A., J. J. Sojka, M. David, and R. W. Schunk (2009), Storm time density enhancements in the middle-latitude dayside ionosphere, *Journal of Geophysical Research: Space Physics*, *114*(A3).

Heinselman, C. J., and M. J. Nicolls (2008), A Bayesian approach to electric field and E-region neutral wind estimation with the Poker Flat Advanced Modular Incoherent Scatter Radar, *Radio Science*, *43*(5).

Hubert, D. (1984), Non-Maxwellian velocity distribution functions and incoherent scattering of radar waves in the auroral ionosphere, *Journal of atmospheric and terrestrial physics*, *46*(6-7), 601–611.

Ichimaru, S. (1973), *Basic principles of plasma physics: A statistical approach*, Benjamin.

Iijima, T., and T. A. Potemra (1978), Large-scale characteristics of field-aligned currents associated with substorms, *Journal of Geophysical Research: Space Physics*, *83*(A2), 599–615.

Iijima, T., T. A. Potemra, L. J. Zanetti, and P. F. Bythrow (1984), Large-scale Birkeland currents in the dayside polar region during strongly northward IMF: A new Birkeland current system, *Journal of Geophysical Research: Space Physics*, *89*(A9), 7441–7452.

Istomin, V. G. (1966), Observational results on atmospheric ions in the region of the outer ionosphere, in *Symposium d'Aéronomie Communications*, vol. 4, p. 185.

Jackson, J. D. (2007), *Classical electrodynamics*, John Wiley & Sons.

Johnson, C. Y. (1969), Ion and neutral composition of the ionosphere., *Annals of the IQSY*, *5*, 197–213.

Jones, A. V., F. Creutzberg, R. L. Gattinger, and F. R. Harris (1982), Auroral studies with a chain of meridian-scanning photometers: 1. Observations of proton and electron aurora in magnetospheric substorms, *Journal of Geophysical Research: Space Physics*, *87*(A6), 4489–4503.

Kelley, M. C. (2009), *The Earth's ionosphere: plasma physics and electrodynamics*, vol. 96, Academic press.

Killeen, T. L., P. B. Hays, G. R. Carignan, R. A. Heelis, W. B. Hanson, N. W. Spencer, and L. H. Brace (1984), Ion-neutral coupling in the high-latitude F region: Evaluation of ion heating terms from Dynamics Explorer 2, *Journal of Geophysical Research: Space Physics*, *89*(A9), 7495–7508.

Knof, H., E. A. Mason, and J. T. Vanderslice (1964), Interaction Energies, Charge Exchange Cross Sections, and Diffusion Cross Sections for N+–N and O+–O Collisions, *The Journal of Chemical Physics*, *40*(12), 3548–3553.

Knudsen, D. J., J. K. Burchill, S. C. Buchert, A. I. Eriksson, R. Gill, J.-E. Wahlund, L. Åhlen, M. Smith, and B. Moffat (2017), Thermal ion imagers and Langmuir probes in the Swarm electric field instruments, *Journal of Geophysical Research: Space Physics*, *122*(2), 2655–2673.

Knudsen, W. C. (1974), Magnetospheric convection and the high-latitude F 2 ionosphere, *Journal of Geophysical Research*, *79*(7), 1046–1055.

Kudeki, E., S. Bhattacharyya, and R. F. Woodman (1999), A new approach in incoherent scatter F region E× B drift measurements at Jicamarca, *Journal of Geophysical Research: Space Physics*, *104*(A12), 28,145–28,162.

Landau, L. D. (1946), On the vibrations of the electronic plasma, *Journal of Physics*, *10*, 25.

Le, G., J. A. Slavin, and R. J. Strangeway (2010), Space technology 5 observations of the imbalance of regions 1 and 2 field-aligned currents and its implication to the cross-polar cap Pedersen currents, *Journal of Geophysical Research: Space Physics*, *115*(A7).

Lehtinen, M. S. (1986), *Statistical theory of incoherent scatter radar measurements*, MS Lehtinen.

Lockwood, M., B. J. I. Bromage, R. B. Horne, J.-P. St-Maurice, D. M. Willis, and S. W. H. Cowley (1987), Non-Maxwellian ion velocity distributions observed using EISCAT, *Geophysical Research Letters*, *14*(2), 111–114.

Loranc, M., and J.-P. St-Maurice (1994), A time-dependent gyro-kinetic model of thermal ion upflows in the high-latitude F region, *Journal of Geophysical Research: Space Physics*, *99*(A9), 17,429–17,451.

Lühr, H., M. Rother, W. Köhler, P. Ritter, and L. Grunwaldt (2004), Thermospheric upwelling in the cusp region: Evidence from CHAMP observations, *Geophysical Research Letters*, *31*(6).

Mason, E. A. (1970), Estimated ion mobilities for some air constituents, *Planetary and Space Science*, *18*(2), 137–144.

Mason, E. A., and H. W. Schamp Jr (1958), Mobility of gaseous Ions in weak electric fields, *Annals of Physics*, *4*(3), 233–270.

Montbriand, L. E. (1971), The proton aurora and auroral substorm, in *The Radiating Atmosphere*, vol. 24, p. 366.

Muldrew, D. B. (1965), F-layer ionization troughs deduced from Alouette data, *Journal of Geophysical Research*, *70*(11), 2635–2650.

Ott, E., and D. T. Farley (1975), Microinstabilities and the production of short-wavelength irregularities in the auroral F region, *Journal of Geophysical Research*, *80*(34), 4599–4602.

Park, C. G. (1976), Downward mapping of high-latitude ionospheric electric fields to the ground, *Journal of Geophysical Research*, *81*(1), 168–174.

Perkins, F. W., E. E. Salpeter, and K. O. Yngvesson (1965), Incoherent scatter from plasma oscillations in the ionosphere, *Physical Review Letters*, *14*(15), 579.

Pesnell, W. D., K. Omidvar, and W. R. Hoegy (1993), Momentum transfer collision frequency of O+-O, *Geophysical Research Letters*, *20*(13), 1343–1346.

Pitout, F., and P. L. Blelly (2003), Electron density in the cusp ionosphere: increase or depletion?, *Geophysical Research Letters*, *30*(14).

Press, W. H., S. A. Teukolsky, W. T. Vetterling, and B. P. Flannery (1992), Numerical recipes in FORTRAN 77, vol. 1, *New York, NY: Press Syndicate of the University of Cambridge.*

Pudovkin, M. I. (1974), Electric fields and currents in the ionosphere, *Space Science Reviews*, *16*(5-6), 727–770.

Raman, R. S., J. P. St-Maurice, and R. S. B. Ong (1981), Incoherent scattering of radar waves in the auroral ionosphere, *Journal of Geophysical Research: Space Physics*, *86*(A6), 4751–4762.

Reber, C. A., and M. Nicolet (1965), Investigation of the major constituents of the April–May 1963 heterosphere by the Explorer XVII satellite, *Planetary and Space Science*, *13*(7), 617–646.

Rees, M. H. (1989), *Physics and chemistry of the upper atmosphere*, vol. 1, Cambridge University Press.

Reiff, P. H. (1982), Sunward convection in both polar caps, *Journal of Geophysical Research: Space Physics*, *87*(A8), 5976–5980.

Reiff, P. H., and J. L. Burch (1985), IMF By-dependent plasma flow and Birkeland currents in the dayside magnetosphere: 2. A global model for northward and southward IMF, *Journal of Geophysical Research: Space Physics*, *90*(A2), 1595–1609.

Richards, P. G., M. J. Nicolls, J.-P. St-Maurice, L. Goodwin, and J. Ruohoniemi (2014), Investigation of sudden electron density depletions observed in the dusk sector by the Poker Flat, Alaska incoherent scatter radar in summer, *Journal of Geophysical Research: Space Physics*, *119*(12).

Rishbeth, H., and W. B. Hanson (1974), A comment on plasma 'pile-up' in the F-region, *Journal of Atmospheric and Terrestrial Physics*, *36*(4), 703–706.

Rosenbluth, M. N., and N. Rostoker (1962), Scattering of electromagnetic waves by a nonequilibrium plasma, *The Physics of Fluids*, *5*(7), 776–788.

Salpeter, E. E. (1960), Electron density fluctuations in a plasma, *Physical Review*, *120*(5), 1528.

Salpeter, E. E. (1961a), Plasma density fluctuations in a magnetic field, *Physical Review*, *122*(6), 1663.

Salpeter, E. E. (1961b), Effect of the magnetic field in ionospheric backscatter, *Journal of Geophysical Research*, *66*(3), 982–984.

Sangalli, L., D. J. Knudsen, M. F. Larsen, T. Zhan, R. F. Pfaff, and D. Rowland (2009), Rocket-based measurements of ion velocity, neutral wind, and electric field in the collisional transition region of the auroral ionosphere, *Journal of Geophysical Research: Space Physics*, *114*(A4).

Schunk, R., and A. Nagy (2009), *Ionospheres: physics, plasma physics, and chemistry*, Cambridge university press, Cambridge UK.

Schunk, R. W. (1975), Transport equations for aeronomy, *Planetary and Space Science*, *23*(3), 437–485.

Schunk, R. W. (1977), Mathematical structure of transport equations for multispecies flows, *Reviews of Geophysics*, *15*(4), 429–445.

Schunk, R. W., and A. F. Nagy (1978), Electron temperatures in the F region of the ionosphere: Theory and observations, *Reviews of Geophysics*, *16*(3), 355–399.

Schunk, R. W., and J. J. Sojka (1982), Ion temperature variations in the daytime high-latitude F region, *Journal of Geophysical Research: Space Physics*, *87*(A7), 5169–5183.

Schunk, R. W., and J. C. G. Walker (1973), Theoretical ion densities in the lower ionosphere, *Planetary and Space Science*, *21*(11), 1875–1896.

Schunk, R. W., W. J. Raitt, and P. M. Banks (1975), Effect of electric fields on the daytime high-latitude E and F regions, *Journal of Geophysical Research*, *80*(22), 3121–3130.

Schunk, R. W., P. M. Banks, and W. J. Raitt (1976), Effects of electric fields and other processes upon the nighttime high-latitude F layer, *Journal of Geophysical Research*, *81*(19), 3271–3282.

Sedgemore-Schulthess, F., and J.-P. St-Maurice (2001), Naturally enhanced ion-acoustic spectra and their interpretation, *Surveys in Geophysics*, *22*(1), 55–92.

Semeter, J. (2012), Basic Radar Signal Processing, `https://eiscat3d.se/drupal/sites/default/files/IISRWS2011/08-Semeter_Radar_Signal_Processing.pdf`.

Sharp, G. W. (1966), Midlatitude trough in the night ionosphere, *Journal of Geophysical Research*, *71*(5), 1345–1356.

Sheffield, J. (1975), *Plasma Scattering of Electromagnetic Radiation*, Academic, New York.

Sheffield, J., D. Froula, S. H. Glenzer, and N. C. Luhmann Jr (2010), *Plasma scattering of electromagnetic radiation: theory and measurement techniques*, Academic press.

Solomon, S. (2007), Ionospheres of the Terrestrial Planets.

Solomon, S. C., and L. Qian (2005), Solar extreme-ultraviolet irradiance for general circulation models, *Journal of Geophysical Research: Space Physics*, *110*(A10).

Spiro, R. W., R. A. Heelis, and W. B. Hanson (1978), Ion convection and the formation of the mid-latitude F region ionization trough, *Journal of Geophysical Research: Space Physics*, *83*(A9), 4255–4264.

St-Maurice, J.-P. (1978), On a mechanism for the formation of VLF electrostatic emissions in the high latitude F-region, *Planetary and Space Science*, *26*(9), 801–816.

St-Maurice, J.-P., and W. B. Hanson (1982), Ion Frictional Heating at High Latitudes and Its Possible Use for an In Situ Determination of Neutral Thermospheric Winds and Temperatures, *Journal of Geophysical Research*, *87*(A9), 7580–7602.

St-Maurice, J.-P., and W. B. Hanson (1984), A statistical study of F region ion temperatures at high latitudes based on Atmosphere Explorer C data, *Journal of Geophysical Research: Space Physics*, *89*(A2), 987–996.

St-Maurice, J.-P., and P. J. Laneville (1998), Reaction rate of O+ with O2, N2, and NO under highly disturbed auroral conditions, *Journal of Geophysical Research: Space Physics*, *103*(A8), 17,519–17,521.

St.-Maurice, J.-P., and R. W. Schunk (1977), Auroral ion velocity distributions for a polarization collision model, *Planetary and Space Science*, *25*, 243–260.

St-Maurice, J.-P., and R. W. Schunk (1979), Ion velocity distributions in the high-latitude ionosphere, *Reviews of Geophysics*, *17*(1), 99–134.

St-Maurice, J.-P., and D. G. Torr (1978), Nonthermal rate coefficients in the ionosphere: The reactions of O+ with N2, O2, and NO, *Journal of Geophysical Research: Space Physics*, *83*(A3), 969–977.

St-Maurice, J. P., W. B. Hanson, and J. C. G. Walker (1976), Retarding potential analyzer measurement of the effect of ion-neutral collisions on the ion velocity distribution in the auroral ionosphere, *Journal of Geophysical Research*, *81*(31), 5438–5446.

Stix, T. H. (1992), *Waves in plasmas*, Springer Science & Business Media, New York, USA.

Suvanto, K. (1988), Incoherent scattering of radar waves from nonthermal F region plasma: Analytical methods of spectrum synthesis, *Radio Science*, *23*(6), 989–996.

Suvanto, K., M. Lockwood, K. J. Winser, A. D. Farmer, and B. J. I. Bromage (1989), Analysis of incoherent scatter radar data from non-thermal F-region plasma, *Journal of Atmospheric and Terrestrial Physics*, *51*(6), 483–495.

Sydorenko, D., and R. Rankin (2013), Simulation of O+ upflows created by electron precipitation and Alfvén waves in the ionosphere, *Journal of Geophysical Research: Space Physics*, *118*(9), 5562–5578.

Tereshchenko, V. D., E. D. Tereshchenko, and H. Kohl (1991), The incoherent scattering of radio waves in a non-Maxwellian plasma: The effects of Coulomb collisions, *Journal of Geophysical Research: Space Physics*, *96*(A10), 17,591–17,598, doi:10.1029/91JA01571.

Varney, R. H. (2016), Advanced modular incoherent scatter radar, `https://eiscat3d.se/drupal/sites/default/files/ISRSchool2016/24-Varney-AMISR_open_me_in_adobe_for_movies.pdf`.

Wand, R. H., and F. W. Perkins (1968), Radar Thomson scatter observations of temperature and ion-neutral collision frequency in the E region, *Journal of Geophysical Research*, *73*(19), 6370–6372.

Weimer, D. R. (1995), Models of high-latitude electric potentials derived with a least error fit of spherical harmonic coefficients, *Journal of Geophysical Research: Space Physics*, *100*(A10), 19,595–19,607.

Wickwar, V. B., C. Lathuillere, W. Kofman, and G. Lejeune (1981), Elevated electron temperatures in the auroral E layer measured with the Chatanika radar, *Journal of Geophysical Research: Space Physics*, *86*(A6), 4721–4730.

Wilson, G. R. (1994), Kinetic modeling of O+ upflows resulting from E× B convection heating in the high-latitude F region ionosphere, *Journal of Geophysical Research: Space Physics*, *99*(A9), 17,453–17,466.

Winkler, E., J. P. St-Maurice, and A. R. Barakat (1992), Results from improved Monte Carlo calculations of auroral ion velocity distributions, *Journal of Geophysical Research*, *97*, 8399–8423.

Winser, K. J., M. Lockwood, and G. O. L. Jones (1987), Non-thermal plasma observations using EISCAT: Aspect angle dependence, *Geophysical Research Letters*, *14*(9), 957–960.

Woodman, R. F. (1967), Incoherent scattering of electromagnetic waves by a plasma, Ph.D. thesis.

Woodman, R. F. (1971), Inclination of the geomagnetic field measured by an incoherent scatter technique, *Journal of Geophysical Research*, *76*(1), 178–184.

Woodman, R. F. (2004), On a proper electron collision frequency for a Fokker–Planck collision model with Jicamarca applications, *Journal of Atmospheric and Solar-Terrestrial Physics*, *66*(17), 1521–1541.

Woodward, P. M. (2014), *Probability and Information Theory, with Applications to Radar: International Series of Monographs on Electronics and Instrumentation*, vol. 3, Elsevier.

Zarka, P. (2011), Magnetosphere, in *Encyclopedia of Astrobiology*, pp. 950–956, Springer.

Appendix A

SUPPLEMENTARY INFORMATION FOR "INCOHERENT SCATTER SPECTRA BASED ON MONTE-CARLO SIMULATIONS OF ION VELOCITY DISTRIBUTIONS UNDER STRONG ION FRICTIONAL HEATING"

Contents of this file

Figures A.1 to A.8.

Table A.1.

Additional Supporting Information (located in zip file)

1. "1-E_20.DAT" is an ASCII file that contains the O^+-O collision information for an electric field of 20 mV/m using the cross-section inferred from *Pesnell et al.* (1993). Rows 2 to 29 have ten columns, each for a different aspect angle in steps of 10° between 0° and 90°. The rows are:

   - Row 1: Parallel ion temperature in Kelvin using the Monte-Carlo simulation output (purely ion-neutral collisions), then the perpendicular ion temperature in Kelvin using the Monte-Carlo simulation output (purely ion-neutral collisions).
   - Row 2: Aspect angle, the angle with respect to the magnetic field.
   - Row 3: Ion thermal speed in m/s, based on the line-of-sight ion temperature given by the Monte-Carlo simulation. This value is used to find ω from x_i and/or v_x from y.
   - Row 4 - 29: The even numbered polynomial coefficients from 0 to 50 (i.e. coefficient 0, coefficient 2, coefficient 4, coefficient 6,..., coefficient 48, coefficient 50). These polynomial coefficients describe the ion velocity distribution from -4 thermal speeds to 4 thermal speeds.

2. "1-E_30.DAT", is the same as "1-E_20.DAT" but for 30 mV/m.

3. "1-E_40.DAT", is the same as "1-E_20.DAT" but for 40 mV/m.

4. “1-E_50.DAT”, is the same as “1-E_20.DAT” but for 50 mV/m.
5. “1-E_60.DAT”, is the same as “1-E_20.DAT” but for 60 mV/m.
6. “1-E_70.DAT”, is the same as “1-E_20.DAT” but for 70 mV/m.
7. “1-E_80.DAT”, is the same as “1-E_20.DAT” but for 80 mV/m.
8. “1-E_90.DAT”, is the same as “1-E_20.DAT” but for 90 mV/m.
9. “1-E_100.DAT”, is the same as “1-E_20.DAT” but for 100 mV/m.
10. “1-E_110.DAT”, is the same as “1-E_20.DAT” but for 110 mV/m.
11. “1-E_120.DAT”, is the same as “1-E_20.DAT” but for 120 mV/m.
12. “1-E_130.DAT”, is the same as “1-E_20.DAT” but for 130 mV/m.
13. “1-E_140.DAT”, is the same as “1-E_20.DAT” but for 140 mV/m.
14. “1-E_150.DAT”, is the same as “1-E_20.DAT” but for 150 mV/m.
15. “1-E_160.DAT”, is the same as “1-E_20.DAT” but for 160 mV/m.
16. “1-E_170.DAT”, is the same as “1-E_20.DAT” but for 170 mV/m.
17. “1-E_180.DAT”, is the same as “1-E_20.DAT” but for 180 mV/m.
18. “1-E_190.DAT”, is the same as “1-E_20.DAT” but for 190 mV/m.
19. “1-E_200.DAT”, is the same as “1-E_20.DAT” but for 200 mV/m.

Introduction

In this document, we present the additional figures and files mentioned in the main body of “Incoherent scatter spectra based on Monte-Carlo simulations of ion velocity distributions under strong ion frictional heating”.

In the main article, it is mentioned that as the O concentration decreases and the N_2 concentration increases, the ion-neutral temperature difference also increases as a result of the influence of the neutral mass on the heating rate. This is reflected in Figures A.1 and A.2, which examine the ion temperature anisotropy for NO^+ with a background neutral concentration of 33% O and 66% N_2 and a concentration of 25% O and 75% N_2, respectively. The spectra for these different concentrations are also presented in Figures A.3 to A.8 for various electric fields and aspect angles.

The ASCII files accompanying this document allow for the reconstruction of one dimensional velocity distributions, g_{0i}, for a number of electric fields and for 10 different aspect angles for each electric field. Specifically, high-quality Legendre polynomial fits to the one-dimensional velocity distributions have been acquired through the formula:

$$g_{0i}(y) = \sum_{j=0}^{D} n_j P_j^0, \tag{A.1}$$

where D is the desired degree chosen to perform the fit around its drift point and P_j^0 are the Legendre polynomials. We used $D = 50$; however, it should be noted that only even-numbered polynomials contributions need to be considered because of the symmetry of the velocity distributions about their drift point. We therefore have listed 26 values for n_j associated with the Legendre polynomials of degree 0, 2, 4, etc., all the way to degree 50.

Each ASCII .DAT file is for a different electric field, but all are for O^+ with O collisions with the cross-section inferred from *Pesnell et al.* (1993). From these values, the ion velocity distribution is found at a specific y value (recall that y is v_x/b, where v_x is the line-of-sight speed and b is the ion thermal speed). A sample Fortran 77 code is provided below (note that the function "plgndr.for" from *Press et al.* (1992) is required and provided).

```
!!!!!!!!!!!!!!!!!!!!!!!!!!!!!!!!!!!!!!!!!!!!
! RECONSTRUCTION.FOR
!!!!!!!!!!!!!!!!!!!!!!!!!!!!!!!!!!!!!!!!!!!!
! IN THIS CODE, LEGENDRE POLYNOMIALS ARE USED TO RECONSTRUCT THE
! ION VELOCITY DISTRIBUTION FOR A GIVEN ASPECT ANGLE AND ELECTRIC FIELD
!!!!!!!!!!!!!!!!!!!!!!!!!!!!!!!!!!!!!!!!!!!!
      REAL TPARA,TPERP,LIM,PHI,Y,FIT,B
      REAL BARR(0:9),COEFF(0:50),COEFFALL(0:50,0:9)
      INTEGER I,J,DEG,ELEN
      CHARACTER E*3
! LIM = THE +/- INTERVAL OVER WHICH THE ION VELOCITY DISTRIBUTION
!       IS DESCRIBED BY POLYNOMIAL COEFFICIENTS, GIVEN AS A
!       NUMBER OF THERMAL SPEEDS. THIS IS 4.
! E=DESIRED ELECTRIC FIELD IN mV/m IN QUOTES (OPTIONS:’20’,’30’,’40’,’50’,’60’,
!’70’,’80’,’90’,’100’,’110’,’120’,130’,’140’,150,’160’,’170’,’180’,’190’,OR’200’)
! PHI = DESIRED ASPECT ANGLE WITH RESPECT TO THE MAGNETIC FIELD
!       (OPTIONS: 0, 10, 20, 30, 40, 50, 60, 70, 80, 90)
! Y = A DESIRED Vx/(ION THERMAL SPEED)
! DEG = DEGREE OF ORTHOGONAL FIT TO THE DISTRIBUTION (BETWEEN 0 AND 50)
! COEFFALL = LEGENDRE POLYNOMIAL COEFFICIENTS FOR A GIVEN ELECTRIC FIELD
! COEFF = LEGENDRE POLYNOMIAL COEFFICIENTS FOR A GIVEN ELECTRIC FIELD AND PHI.
! TPARA = PARALLEL ION TEMPERATURE.
! TPERP = PERPENDICULAR ION TEMPERATURE.
! BARR = ARRAY HOLDING THE ION THERMAL SPEEDS.
! B = ION THERMAL SPEED FOR A DESIRED PHI.
! FIT = THE DISTRIBUTION AT Y, I.E. g(Y)
      LIM = 4.
! FIRST, THE USER CREATES AN INPUT FILE THAT LISTS ’E’, ’PHI’, ’Y’, AND ’DEG’
      OPEN(UNIT=15,FILE=’input.dat’,STATUS=’OLD’)
      READ(15,*) E
      READ(15,*) PHI
      READ(15,*) Y
      READ(15,*) DEG
      CLOSE(15)
! THIS READS IN THE CORRECT DATA FOR A GIVEN ELECTRIC FIELD
      ELEN = 0
      DO 11 I = 1, LEN(E)
        IF ( E(I:I) .NE. ’ ’ ) THEN
          ELEN = ELEN + 1
        END IF
 11   CONTINUE
      OPEN(UNIT=15,FILE=’1-E_’//E(1:ELEN)//’.DAT’,STATUS=’OLD’)
      READ(15,*) TPARA, TPERP
      READ(15,*)
      READ(15,*) BARR(0),BARR(1),BARR(2),BARR(3),BARR(4),BARR(5),
```

```
     >     BARR(6),BARR(7),BARR(8),BARR(9)
      DO 12 I  = 0, DEG
        IF (mod(I,2).eq.0) THEN
          READ(15,*) COEFFALL(I,0),COEFFALL(I,1),COEFFALL(I,2),
     >     COEFFALL(I,3),COEFFALL(I,4),COEFFALL(I,5),COEFFALL(I,6),
     >     COEFFALL(I,7),COEFFALL(I,8),COEFFALL(I,9)
        ENDIF
 12   CONTINUE
      CLOSE(15)
      B = BARR(INT(PHI)/10)
! THE COEFFICIENTS FOR A GIVEN PHI ARE SELECTED
      DO 20 I  = 0, DEG
        COEFF(I) = COEFFALL(I,INT(PHI)/10)
 20   CONTINUE
      FIT = 0.
! THE VELOCITY DISTRIBUTION IS FOUND
      DO 10 J  = 0, DEG
! ONLY THE EVEN NUMBERED COEFFICIENTS ARE NEEDED BECAUSE THE VELOCITY
! DISTRIBUTION IS SYMMETRIC
        IF (mod(J,2).eq.0) THEN
          FIT=COEFF(J)*DBLE(plgndr(J,0,Y/LIM))+FIT
        ENDIF
 10   continue
! THE VELOCITY DISTRIBUTION IS WRITTEN TO AN OUTPUT FILE
      OPEN(UNIT=15,FILE='output.dat')
      WRITE(15,*) Y, FIT
      CLOSE(15)
      END
```

```
!/////////////////////////////////////////////////////////////
  FUNCTION plgndr(l,m,x)
  INTEGER l,m
  REAL plgndr,x
cComputes the associated Legendre polynomial P m l (x). Here m and l are integers
c satisfying 0 = m = l, while x lies in the range -1 = x = 1.
  INTEGER i,ll
  REAL fact,pll,pmm,pmmp1,somx2
c   if(m.lt.0.or.m.gt.l.or.abs(x).gt.1.) write(15,*) 'bad'
  pmm=1.
cCompute P mm .
  if(m.gt.0) then
    somx2=sqrt((1.-x)*(1.+x))
    fact=1.
    do 11 i=1,m
      pmm=-pmm*fact*somx2
      fact=fact+2.
 11   CONTINUE
  endif
  if(l.eq.m) then
    plgndr=pmm
  else
    pmmp1=x*(2*m+1)*pmm
cCompute P m
c     m+1.
    if(l.eq.m+1) then
      plgndr=pmmp1
    else
cCompute P m
c     l , l>m + 1.
      do 12 ll=m+2,l
        pll=(x*(2*ll-1)*pmmp1-(ll+m-1)*pmm)/(ll-m)
        pmm=pmmp1
        pmmp1=pll
 12       CONTINUE
      plgndr=pll
    endif
  endif
  return
  END
```

As mentioned in the main text, the NO^+ spectra can be reproduced using Maxwellian ion velocity distributions. For this reason, Table A.1 supplies the ion temperatures parallel and perpendicular to the magnetic field for Monte-Carlo simulations of NO+ with a background of 50% O and 50% N2. The ion temperatures for a variety of aspect angles can be found using Equation 4.7 from the main text.

Lastly, it should be noted that the neutral temperature used in every Monte-Carlo run presented in this work is 1000 K. For electric fields less than 20 mV/m the velocity distributions of both O+ and NO+ can be approximated well with a bi-Maxwellian velocity distribution having ion temperatures that are well described by Model A in *St.-Maurice and Schunk* (1977).

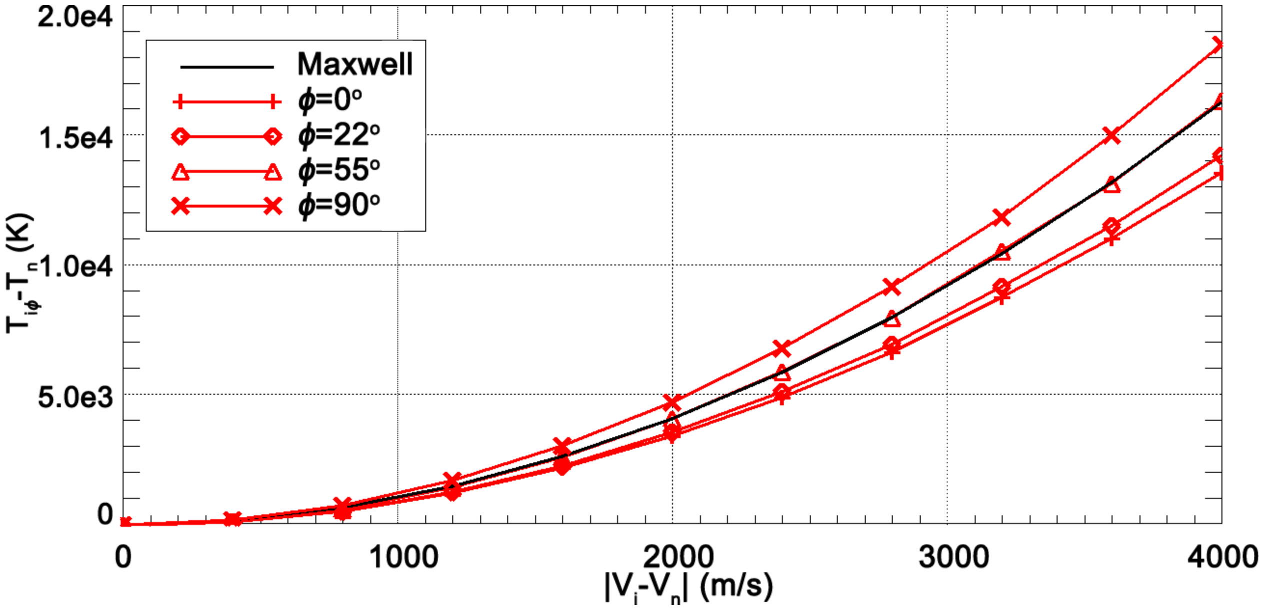

Figure A.1: Same as in Figure 4.9 but for NO^+ collisions with 33% O and 66% N_2

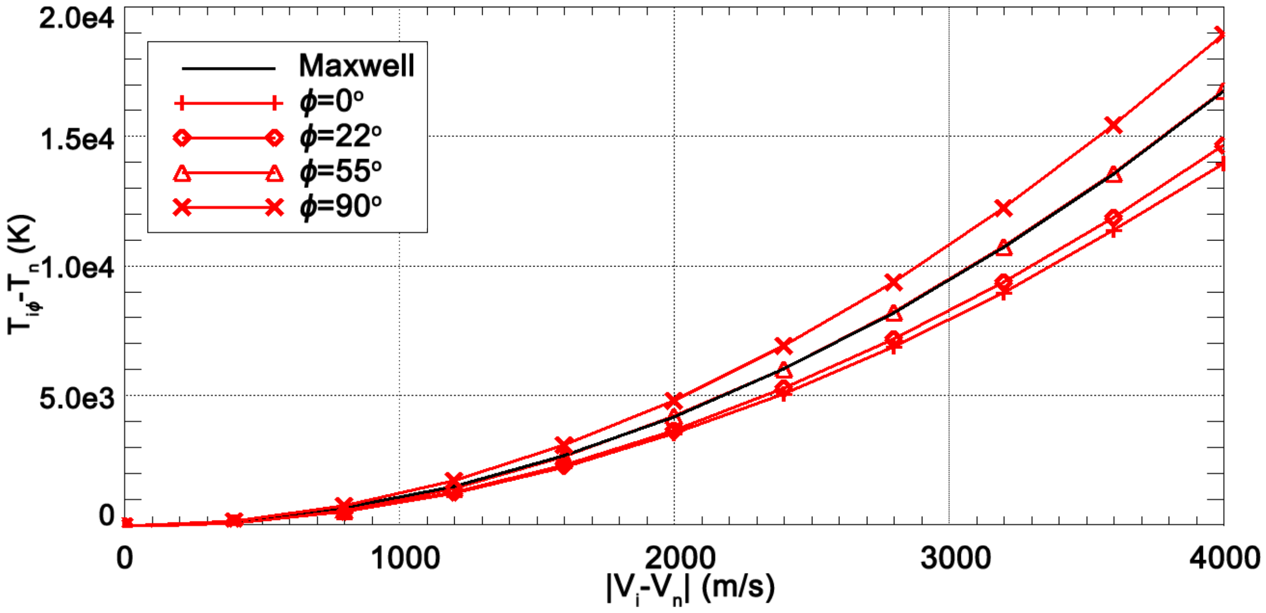

Figure A.2: Same as in Figure 4.9 but for NO$^+$ collisions with 25% O and 75% N$_2$

Electric Field (mV/m)	Parallel Temperature (K)	Perpendicular Temperature (K)
20	1.10e3	1.16e3
30	1.25e3	1.38e3
40	1.48e3	1.68e3
50	1.75e3	2.09e3
60	2.11e3	2.58e3
70	2.52e3	3.16e3
80	3.01e3	3.85e3
90	3.57e3	4.58e3
100	4.16e3	5.39e3
110	4.83e3	6.32e3
120	5.55e3	7.31e3
130	6.34e3	8.40e3
140	7.19e3	9.50e3
150	8.08e3	1.08e4
160	9.12e3	1.21e4
170	1.01e4	1.35e4
180	1.12e4	1.50e4
190	1.23e4	1.66e4
200	1.36e4	1.83e4

Table A.1: Ion temperatures needed to produce Maxwellian NO$^+$ velocity distributions, where the neutral background is 50% O and 50% N$_2$.

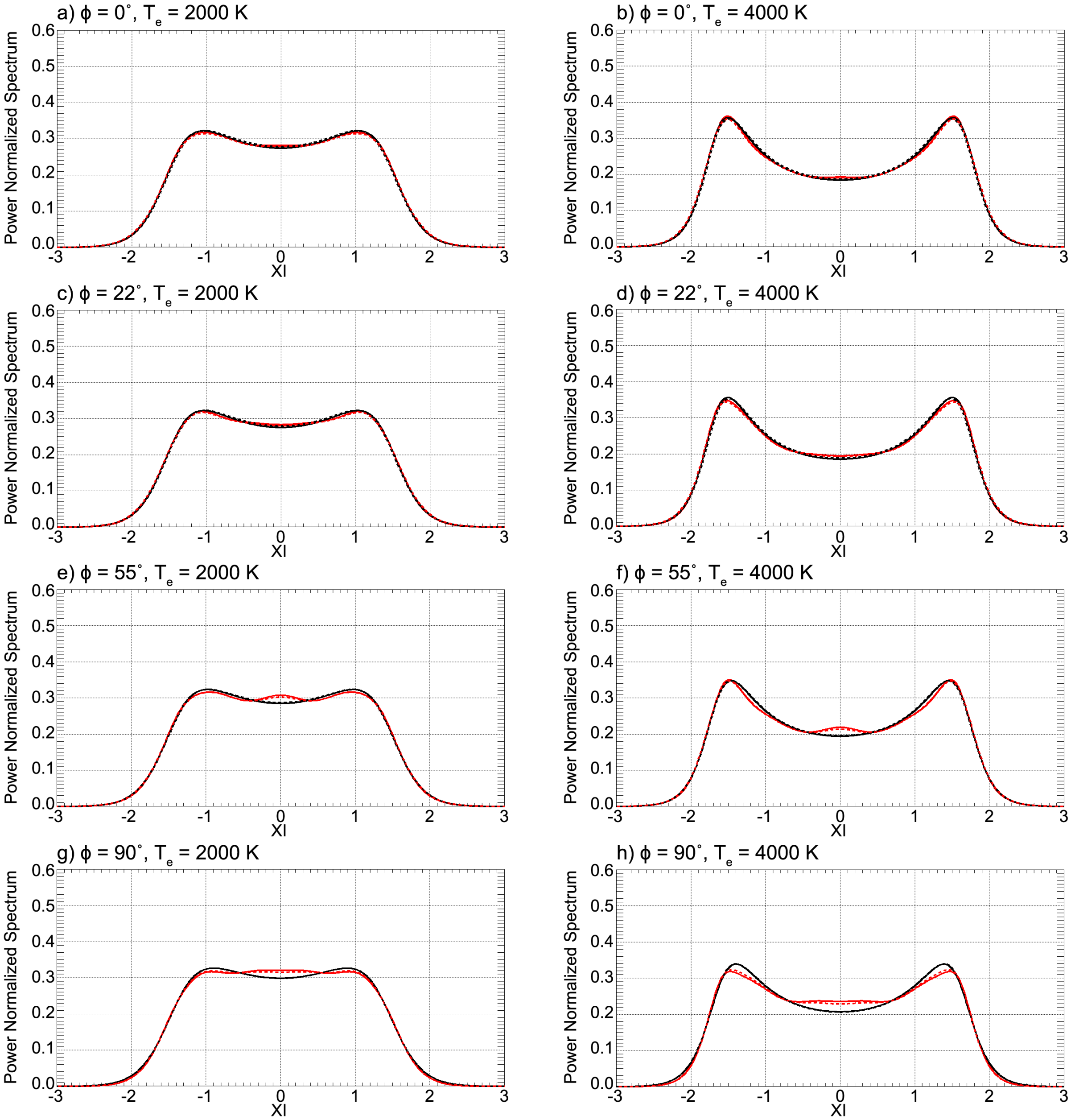

Figure A.3: Same as in Figure 4.13 but for NO^+ in a mixture 33% O and 66% N_2

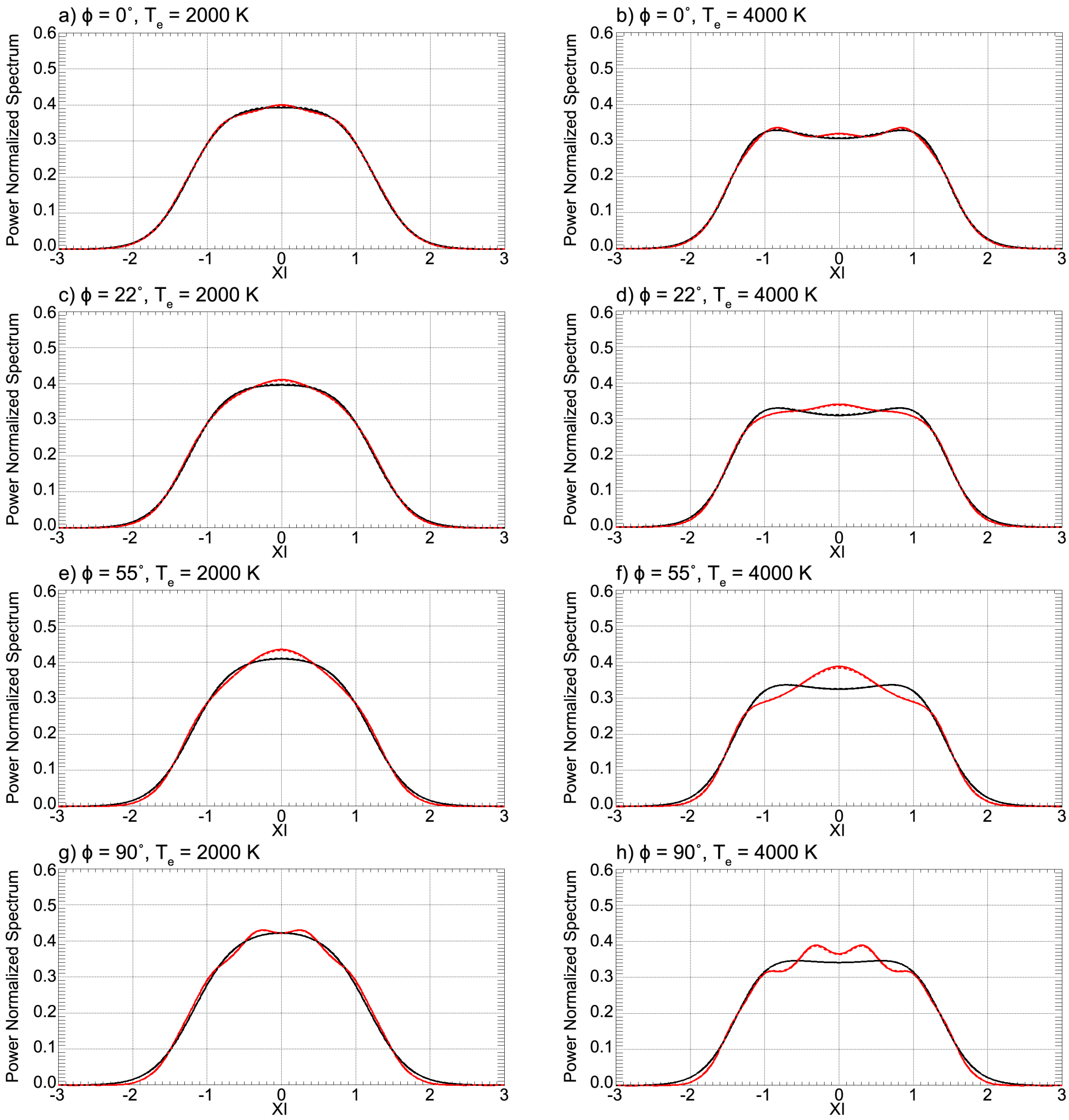

Figure A.4: Same as in Figure A.3 but for a 100 mV/m electric field

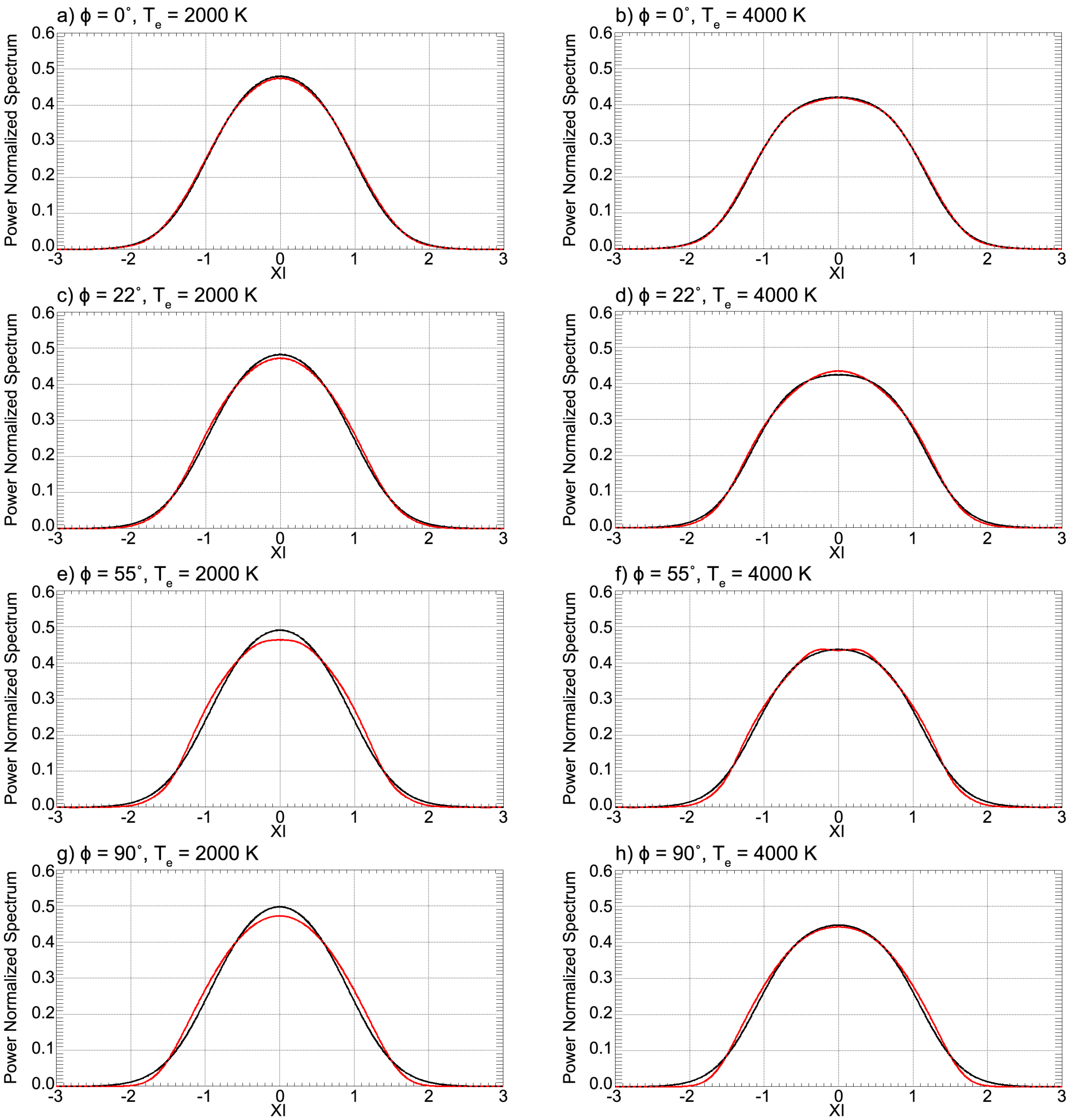

Figure A.5: Same as in Figure A.3 but for a 170 mV/m electric field

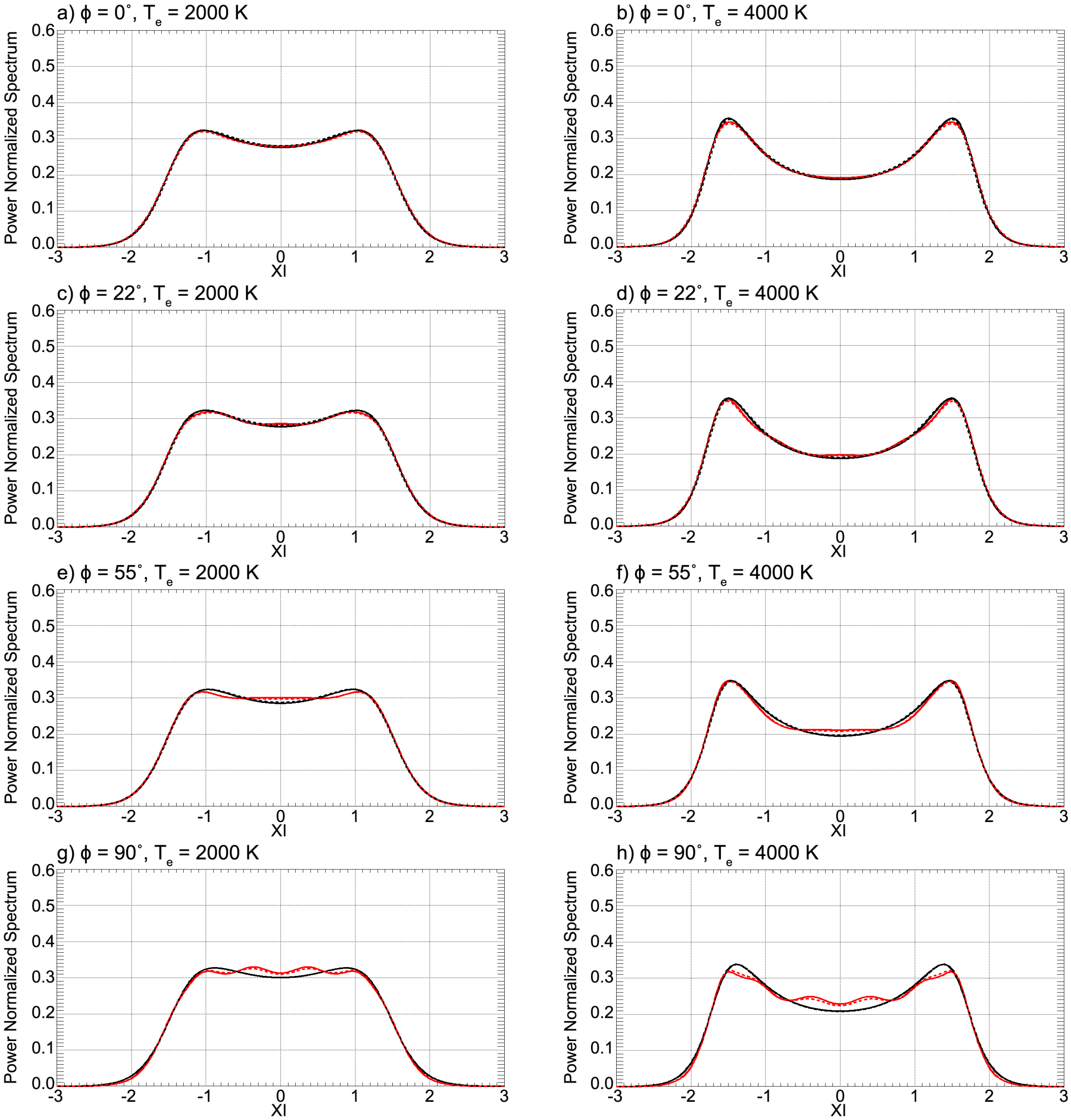

Figure A.6: Same as in Figure 4.13 but for NO^+ in a mixture 25% O and 75% N_2

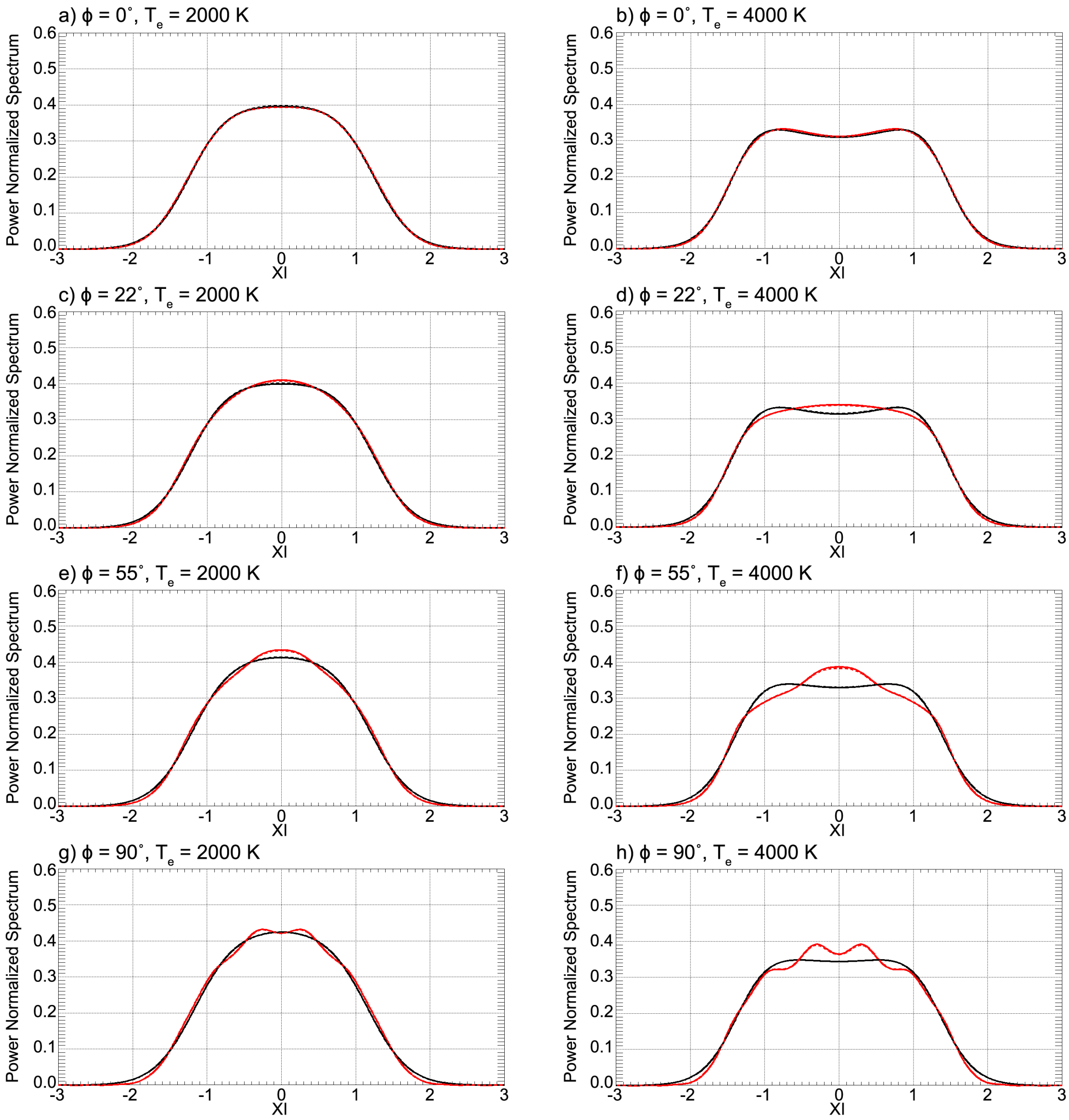

Figure A.7: Same as in Figure A.6 but for a 100 mV/m electric field

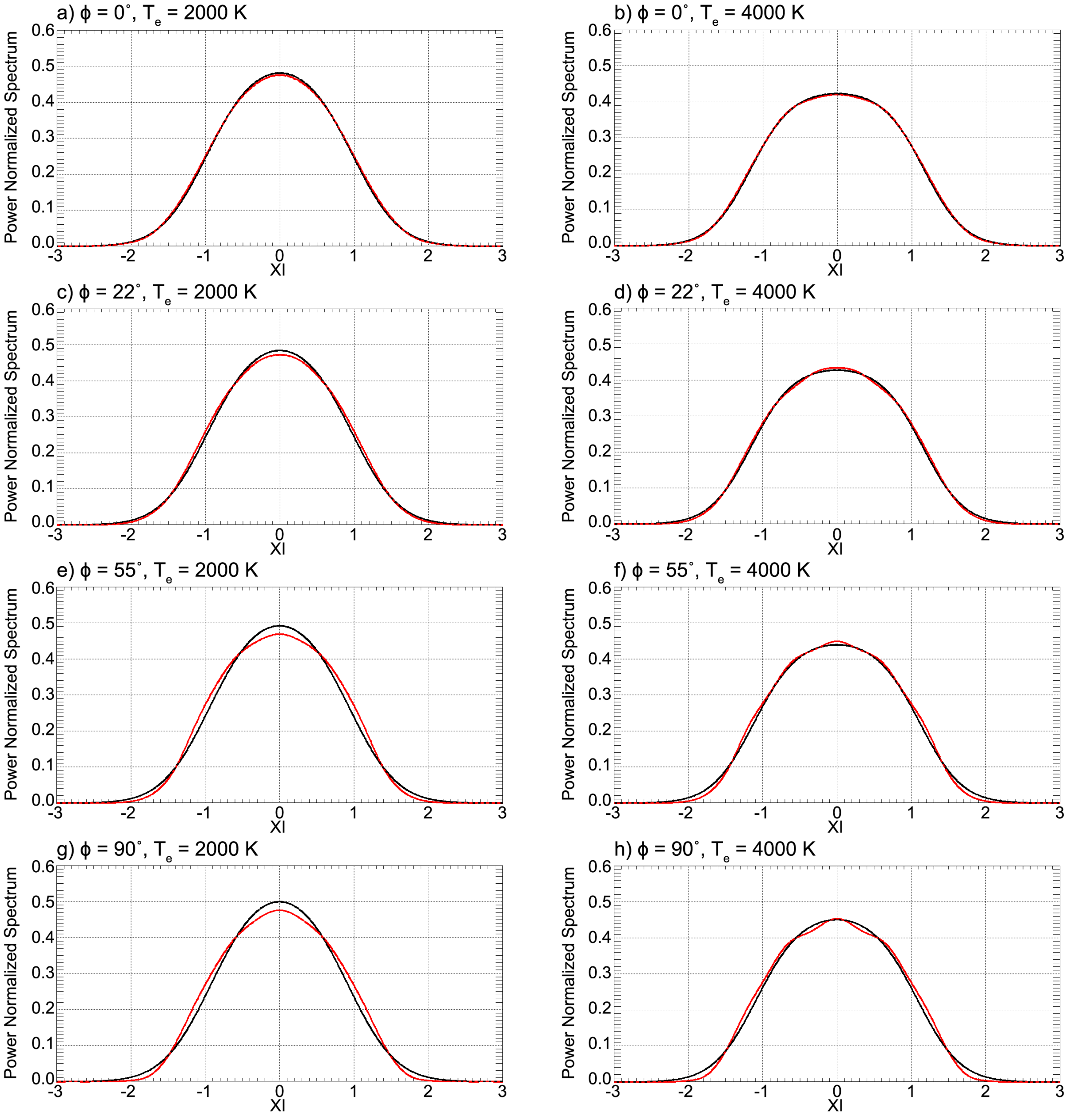

Figure A.8: Same as in Figure A.6 but for a 170 mV/m electric field

Appendix B

SPECTRA SIMULATION SOFTWARE

This appendix lists the F77 software needed to construct the one dimensional ion velocity distributions, the ion dielectric functions, and the spectra for a number of electric fields (every 10 mV/m from 0 mV/m to 200 mV/m) and aspect angles (every 10° from 0° to 90°) for the POH O^+-O collision cross-section and the NO^+ with a 50% O and 50% N_2 background. Section B.1 contains the input file referred to by the software, which is the only file the requires user input. Sections B.2 to B.10 contain the software itself, with the main program (“SPECFNMAIN.FOR”) being in Section B.10. The last section of this appendix discusses the data files needed, which are different from the data files associated with Chapter 4 or Appendix A.

Lastly, please note that Section B.4 has been passed on to me from Jean-Pierre St-Maurice who received it as part of a package, while Sections B.6 and B.9 are from *Press et al.* (1992). All other files listed in this appendix were generated specifically for this research.

B.1 input.dat

```
'TEST'   FILENAME, TAG ASSOCIATED WITH THE OUTPUT FILES
4000.    TE, ELECTRON TEMPERATURE (K)
1.e11    ANOMN, PLASMA DENSITY (m-3)
220.E6   FREQ, RADAR FREQUENCY (Hz)
1.8E14   NN, NEUTRAL DENSITY (m-3)
'100'    ELEC, ELECTRIC FIELD IN QUOTES (mV/m), OPTIONS: '0','10',...,'190','200'
0        PHI, ASPECT ANGLE, OPTIONS: 0, 10, 20, 30, 40, 50, 60, 70, 80, OR 90
1        COLLISION, OPTIONS: 1=PESNELL O+O, 2=NO+ W/ 50% O AND 50% N2
```

B.2 ANAELECT.FOR

```
C   ANAELECT.FOR
C*******************************************************************************C
          SUBROUTINE ANAELECT(XI,TI,TE,ALPHA,K,AMASSI,HER,HEI,AME)
C*******************************************************************************C
C    ANALYTICAL CALCULATION OF THE ELECTRON FUNCTIONS AND SPECTRUM FOR A MAXWELLIAN
C    VELOCITY DISTRIBUTION AT XE [SHEFFIELD 1975, 6.3.7]
C
C    LINDSAY GOODWIN 14/08/2017
C
      DOUBLE PRECISION MI,ME,K,TE,B,A,XI,XE,RWXE,IWXE,DRE,
     @ALPHA,DIE,AMASSI,TI,HEI,AME,HER,BOLT,AMU,PI
      DATA BOLT,ME,AMU,PI/1.380E-23,9.109E-31,1.661E-27,3.1415927/
! XE = OMEGA/(K*A), WHERE OMEGA IS THE ANGULAR FREQUENCY FOR ELECTRONS
! MI = ION MASS (kg)
! TI = ION TEMPERATURE (K)
! ME = ELECTRON MASS (kg)
! AMU = ONE ATOMIC MASS UNIT
! A = ELECTRON THERMAL SPEED
      MI = AMASSI*AMU
      A = SQRT(2.*BOLT*TE/ME)
      B = SQRT(2.*BOLT*TI/MI)
C THE XE FOR THE GIVEN XI IS FOUND
      XE = XI*B/A
C DRE AND DIE ARE USED BY DISP TO FIND RWXE AND IWXE FROM SHEFFIELD (1975), 6.3.7
      call DISP(XE,DRE,DIE)
      RWXE = DRE+1.
      IWXE = -DIE
      HEI = -(ALPHA**2)*IWXE
      HER = (ALPHA**2)*RWXE
      AME = EXP(-XE**2)/(A*SQRT(PI))
      RETURN
      END
```

B.3 ANAION.FOR

```
C   ANAION.FOR
C****************************************************************************C
          SUBROUTINE ANAION(XI,TI,TE,ALPHA,K,AMASSI,HIR,HII,AMI)
C***********************************************************************c****C
C    ANALYTICAL CALCULATION OF THE ION FUNCTIONS AND SPECTRUM FOR A MAXWELLIAN
C    VELOCITY DISTRIBUTION AT XI [SHEFFIELD 1975, 6.3.8]
C
C    LINDSAY GOODWIN 14/08/2017
C
      DOUBLE PRECISION MI,TI,TE,B,RWXI,IWXI,DRI,DII,K,ALPHA,AMASSI,
     @HII,AMI,HIR,XI,BOLT,AMU,PI
      DATA BOLT,AMU,PI/1.381E-23,1.661E-27,3.1415927/
! MI = ION MASS (kg)
! TI = ION TEMPERATURE (K)
! AMU = ONE ATOMIC MASS UNIT
      MI = AMASSI*AMU
      B = SQRT(2.*BOLT*TI/MI)
! DRI AND DII ARE USED BY DISP TO FIND RWXE AND IWXE FROM SHEFFIELD (1975), 6.3.8
      call DISP(XI,DRI,DII)
      RWXI = DRI+1.
      IWXI = -DII
      HII = -(ALPHA**2)*(TE/TI)*IWXI
      HIR = (ALPHA**2)*(TE/TI)*RWXI
      AMI = EXP(-XI**2)/(B*SQRT(PI))
      RETURN
      END
```

B.4 DISP.FOR

```
C   DISP.FOR
C******************************************************************************C
      SUBROUTINE DISP(Y,DR,DI)
C******************************************************************************C
C     THIS SUBROUTINE EVALUATES Y TIMES THE FRIED AND CONTE PLASMA
C     DISPERSION FUNCTION OF Y. THE SUBROUTINE IS VALID ONLY FOR REAL
C     VALUES OF THE ARGUMENT
C     Y=ARGUMENT
C     DI=IMAGINARY PART
C     DR=REAL PART
C     THE EVALUATION OF DR INVOLVES THE DETERMINATION OF THE ERROR
C     FUNCTION FOR A PURE IMAGINARY ARGUMENT, THIS IS DONE BY USING AN
C     INFINITE SERIES. THE NUMBER OF TERMS IS GIVEN BY NMAX=4*ABS(Y)+4,
C     BUT IF ABS(Y) IS LESS THAN 1.0 NMAX=10
C     REF.  ABRAMOWITZ AND STEGUN
C
      DOUBLE PRECISION Y,DR,DI
          NMAX=4*ABS(Y)+4
C
C  ON NOV 28,87  I CHANGED LIMIT FOR TEST TO 4 INSTEAD OF 5 TO
C  AVOID OVERFLOW ARGS ON EXP ON PC
C
      IF (ABS(Y) .GT. 4.0) GO TO 20
      IF (ABS(Y) .LE. 1.0) NMAX=10
             B=Y/2.0
      DO 10 N=1,NMAX
             B=B+SINH(N*Y)*EXP(-(N**2)/4.0)/N
 10   CONTINUE
C
C   I MULTIPLIED FOLL LINES BY y ON 11/27/87....JPSTM
C
            DR=Y*(-2/1.772454)*EXP(-Y*Y)*B
            DI=-Y*1.772454*EXP(-Y*Y)
      GO TO 90
 20         Y2=Y**2
      IF (Y2 .GT. 175.0) GO TO 80
             B=0.0
      DO 70 N=1,NMAX
             E=N*Y-N**2/4.0-Y2
      IF (-E .GT. 175.0) GO TO 30
            E1=EXP(E)
      GO TO 40
 30         E1=0.0
```

```
40          F=-N*Y-N**2/4.0-Y2
     IF (-F .GT. 175.0) GO TO 50
           F1=EXP(F)
     GO TO 60
50         F1=0.0
60          B=B+(E1-F1)/(2*N)
70   CONTINUE
           DR=(-2/1.772454)*Y*(B+EXP(-Y2)*Y/2.0)
           DI=1.772454*Y*EXP(-Y2)
     GO TO 90
80         YY=1/(2*Y*Y)
           DR=-(((15*YY+3)*YY+1)*YY+1)
           DI=0.0
90   RETURN
     END
```

B.5 DISTORTED.FOR

```
C   DISTORTED.FOR
C*******************************************************************************C
        SUBROUTINE DISTORTED(XI,K,deltax,AMASSI,HIR,HII,AMI,ANOMN,
     >   COEFF,LIM,DEG,SETR,normin,normi,norme,B,TPERP,TPARA,TE,num)
C***********************************************************************c****C
C    NUMERICAL CALCULATION OF THE ION FUNCTIONS AND SPECTRUM FOR A DISTORTED
C    VELOCITY DISTRIBUTION AT XI
C
C    LINDSAY GOODWIN 14/08/2017
C
      INTEGER Ngauleg,num,DEG
      DOUBLE PRECISION B,PI,C,K,MI,XI,XPOS,DGDP,G,G1,G2,
     @AMASSI,HIR,HII,AMI,deltax,ANOMN,ELCH,fit,SETR,normin,
     @normi,norme,TPERP,TPARA,TE,AMU,PERM,OMEGAPSQ
      DOUBLE PRECISION COEFF(0:DEG)
      REAL gaulegx(1:52),gaulegw(1:52),LIM
      DATA ELCH,AMU,PI,PERM/1.602E-19,1.661E-27,
     @3.1415927,8.854E-12/
! DGDP = THE DERIVATIVE OF THE VELOCITY DISTRIBUTION AT A GIVEN LOCATION
! G/G1/G2 = THE VELOCITY DISTRIBUTION AT A GIVEN LOCATION DIRECTLY FROM
! THE ORTHOGONAL POLYNOMIALS
! AMU = ONE ATOMIC MASS UNIT
! MI = ION MASS (kg)
      MI = AMASSI*AMU
  OMEGAPSQ = (4.*PI*ANOMN*ELCH**2)/MI
! GAUSSIAN QUADRATURE WEIGHTS ARE FOUND:
      Call gauleg(-LIM,LIM,gaulegx,gaulegw,num)
! HIR IS CALCULATED
      HIR = 0.
      DO 30 Ngauleg=1,num
! CHANGE IN VARIABLES FROM XI TO C
        C = DBLE(gaulegx(Ngauleg))
        XPOS = C + XI
        DGDP = 0.
        G1 = fit((XPOS+deltax),COEFF,LIM,DEG,
     >      SETR,SETR,normin,normi,norme,B,TPERP,TPARA,TE,AMASSI)
        G2 = fit((XPOS-deltax),COEFF,LIM,DEG,
     >      SETR,SETR,normin,normi,norme,B,TPERP,TPARA,TE,AMASSI)
        if (G1 .eq. 0. .or.  G2 .eq. 0.) GO TO 87
        DGDP = (G1-G2)/(2.*deltax)
 87     HIR= HIR-DBLE(gaulegw(Ngauleg))*DGDP/C
 30   CONTINUE
      HIR=(2.*OMEGAPSQ/(4.*PI*PERM*(B*K)**2))*HIR/3.545
```

```
! DGDP AT A GIVEN XI IS FOUND FOR THE HII CALCULATION
      DGDP = 0.
      G1 = fit((XI+deltax),COEFF,LIM,DEG,SETR,SETR,
     >      normin,normi,norme,B,TPERP,TPARA,TE,AMASSI)
      G2 = fit((XI-deltax),COEFF,LIM,DEG,SETR,SETR,
     >      normin,normi,norme,B,TPERP,TPARA,TE,AMASSI)
      if (G1 .eq. 0. .or.  G2 .eq. 0.) GO TO 88
      DGDP = (G1-G2)/(2.*deltax)
! HII IS CALCULATED/NORMALIZED
 88   HII=(2.*OMEGAPSQ/(4.*PI*PERM*(B*K)**2))*PI*dgdp/3.545
! AMI IS CALCULATED/NORMALIZED
      AMI=0.
      G = fit(XI,COEFF,LIM,DEG,SETR,SETR,normin,
     >      normi,norme,B,TPERP,TPARA,TE,AMASSI)
! AMI INCLUDES SQRT(PI)/(K*B) IN ORDER TO MATCH THE DEFINITION GIVEN BY
! NUMMAXWELL AND ANAION
      AMI = G/(B*SQRT(PI))
 89   end
```

B.6 gauleg.FOR

```
C   gauleg.FOR
C*************************************************************************C
        SUBROUTINE gauleg(x1,x2,x,w,n)
C*************************************************************************C
C       THIS IS TAKEN STRAIGHT FROM THE FORTRAN 77 NUMERICAL RECIPES
C        [PRESS ET AL., 1992]
        INTEGER n
        REAL x1,x2,x(n),w(n)
        DOUBLE PRECISION EPS
        PARAMETER (EPS=3.d-14)
C       EPS is the relative precision.
C     Given the lower and upper limits of integration x1 and x2, and given n,
C     this routine returns arrays x(1:n) and w(1:n) of length n, containing the
C     abscissas and weights of the GaussLegendre n-point quadrature formula.
        INTEGER i,j,m
        DOUBLE PRECISION p1,p2,p3,pp,xl,xm,z,z1
C       High precision is a good idea for this routine.
        m=(n+1)/2
C       The roots are symmetric in the interval, so we only have to find
C       half of them.
        xm=0.5d0*(x2+x1)
        xl=0.5d0*(x2-x1)
        do 12 i=1,m
C       Loop over the desired roots.
          z=cos(3.141592654d0*(i-.25d0)/(n+.5d0))
C       Starting with the above approximation to the ith root, we enter the
C       main loop of refinement by Newtons method.
1         continue
          p1=1.d0
          p2=0.d0
          do 11 j=1,n
C       Loop up the recurrence relation to get the Legendre polynomial
C       evaluated at z.
            p3=p2
            p2=p1
            p1=((2.d0*j-1.d0)*z*p2-(j-1.d0)*p3)/j
11        continue
C       p1 is now the desired Legendre polynomial. We next compute pp, its
C       derivative, by a standard relation involving also p2, the polynomial
C       of one lower order.
          pp=n*(z*p1-p2)/(z*z-1.d0)
          z1=z
          z=z1-p1/pp
```

```
C       Newtons method.
          if(abs(z-z1).gt.EPS)goto 1
          x(i)=xm-xl*z
C       Scale the root to the desired interval,
          x(n+1-i)=xm+xl*z
C       and put in its symmetric counterpart.
          w(i)=2.d0*xl/((1.d0-z*z)*pp*pp)
C       Compute the weight
          w(n+1-i)=w(i)
C       and its symmetric counterpart.
12      continue
        return
        END
```

B.7 MOMENTS.FOR

```
C   MOMENTS.FOR
C*******************************************************************************C
          SUBROUTINE MOMENTS(COEFF,MOMVAVE,MOMTEMP,AMASSI,NORM,LIM,B,
     >      DEG,SETM,NORMIN,NORMI,NORME,TPERP,TPARA,TE)
C*************************************************************************c****C
c THIS CALCULATES THE VELOCITY MOMENTS OF A GIVEN DISTRIBUTION
C
C    LINDSAY GOODWIN 14/08/2017
C
      DOUBLE PRECISION BOLT,MOMDEN,MOMVAVE,MOMTEMP,AMU,SETM,VPHI,AMASSI,
     @MI,NORM,fit,B,NORMIN,NORMI,NORME,SET0,SET1,TPERP,TPARA,G,TE
      REAL gaulegx(1:40),gaulegw(1:40),LIM
      INTEGER NGAULEG,NUM,DEG
      DOUBLE PRECISION COEFF(0:DEG)
      DATA BOLT,AMU/1.381E-23,1.661E-27/
! G = THE VELOCITY DISTRIBUTION AT A GIVEN LOCATION DIRECTLY FROM THE
!        ORTHOGONAL POLYNOMIALS
! VPHI = VELOCITY IN A GIVEN DIRECTION
! SET0 = VARIABLE SET TO 0
! SET1 = VARIABLE SET TO 1
! AMU = ONE ATOMIC MASS UNIT
! MI = ION MASS (kg)
! NORMIN = NORMALIZATION CONSTANT FOR THE ION-NEUTRAL COLLISION DISTRIBUTION
! NORMI = NORMALIZATION CONSTANT FOR THE ION-ION COLLISION DISTRIBUTION
! NORME = NORMALIZATION CONSTANT FOR THE ION-ELECTRON COLLISION DISTRIBUTION
      MI = AMASSI*AMU
! A 40 POINT GAUSSIAN QUADRATURE IS USED TO FIND THE AREA UNDER AN ASSORTMENT
! OF CURVES
      NUM = 40
C GAUSSIAN QUADRATURE WEIGHTS ARE FOUND
      Call gauleg(-LIM,LIM,gaulegx,gaulegw,NUM)
      SET0=0.
      SET1=1.
  IF (SETM.ne.-1.) THEN
! A NORMALIZATION CONSTANT FOR ION-NEUTRAL COLLISION DISTRIBUTION IS FOUND
        MOMDEN = 0.
        do 150 NGAULEG =1,NUM
          VPHI = DBLE(gaulegx(NGAULEG))
          G = fit(VPHI,COEFF,LIM,DEG,SET0,SET0,SET1,SET0,
     >      SET0,B,TPERP,TPARA,TE,AMASSI)
          MOMDEN = MOMDEN + DBLE(gaulegw(NGAULEG))*G
 150    CONTINUE
        if (MOMDEN.eq.0.) stop
```

```
        NORMIN = 1./MOMDEN
! A NORMALIZATION CONSTANT FOR ION-ION COLLISION DISTRIBUTION IS FOUND
        MOMDEN = 0.
        do 151 NGAULEG =1,NUM
          VPHI = DBLE(gaulegx(NGAULEG))
          G = fit(VPHI,COEFF,LIM,DEG,SET1,SET0,SET0,SET1,
     >      SET0,B,TPERP,TPARA,TE,AMASSI)
          MOMDEN = MOMDEN + DBLE(gaulegw(NGAULEG))*G
 151    CONTINUE
        if (MOMDEN.eq.0.) stop
        NORMI = 1./MOMDEN
! A NORMALIZATION CONSTANT FOR ION-ELECTRON COLLISION DISTRIBUTION IS FOUND
        MOMDEN = 0.
        do 152 NGAULEG =1,NUM
          VPHI = DBLE(gaulegx(NGAULEG))
          G = fit(VPHI,COEFF,LIM,DEG,SET0,SET1,SET0,SET0,
     >      SET1,B,TPERP,TPARA,TE,AMASSI)
          MOMDEN = MOMDEN + DBLE(gaulegw(NGAULEG))*G
 152    CONTINUE
        if (MOMDEN.eq.0.) stop
        NORME = 1./MOMDEN
      ENDIF
! THE VELOCITY MOMENTS ARE CALCULATED. FIRST, THE DENSITY IS FOUND.
      MOMDEN = 0.
      do 250 NGAULEG =1,NUM
        VPHI = DBLE(gaulegx(NGAULEG))
        G = fit(VPHI,COEFF,LIM,DEG,SETM,SETM,NORMIN,
     >      NORMI,NORME,B,TPERP,TPARA,TE,AMASSI)
        MOMDEN = MOMDEN + DBLE(gaulegw(NGAULEG))*G
 250  CONTINUE
      if (MOMDEN.eq.0.) stop
      NORM = 1./MOMDEN
! THE AVERAGE VELOCITY IS FOUND
      MOMVAVE = 0.
      do 350 NGAULEG =1, NUM
        VPHI = DBLE(gaulegx(NGAULEG))
        G = fit(VPHI,COEFF,LIM,DEG,SETM,SETM,NORMIN,
     >      NORMI,NORME,B,TPERP,TPARA,TE,AMASSI)
        MOMVAVE = MOMVAVE + DBLE(gaulegw(NGAULEG))*G*NORM*VPHI*B
 350  CONTINUE
! THE ION TEMPERATURE IS FOUND
      MOMTEMP = 0.
      do 450 NGAULEG =1, NUM
        VPHI = DBLE(gaulegx(NGAULEG))
        G = fit(VPHI,COEFF,LIM,DEG,SETM,SETM,NORMIN,
```

```
     >      NORMI,NORME,B,TPERP,TPARA,TE,AMASSI)
        MOMTEMP = MOMTEMP+
     >      (DBLE(gaulegw(NGAULEG))*G*NORM*(VPHI*B-MOMVAVE)**2)
 450  CONTINUE
      MOMTEMP = MI*MOMTEMP/BOLT
! This corrects the normalization factor
      Call gauleg(-6.00,6.00,gaulegx,gaulegw,NUM)
      MOMDEN = 0.
      do 455 NGAULEG =1,NUM
        VPHI = DBLE(gaulegx(NGAULEG))
        G = exp(-(VPHI)**2)
        MOMDEN = MOMDEN + DBLE(gaulegw(NGAULEG))*G
 455  CONTINUE
      NORM = MOMDEN*NORM
      end
```

B.8 NUMMAXWELL.FOR

```
C NUMMAXWELL.FOR
C*************************************************************************C
           SUBROUTINE NUMMAXWELL(XI,TI,K,deltax,AMASSI,HIR,HII,AMI,ANOMN)
C*************************************************************************C
C    NUMERICAL CALCULATION OF THE ION FUNCTIONS AND SPECTRUM FOR A MAXWELLIAN
C    VELOCITY DISTRIBUTION AT XI [SHEFFIELD 1975, 6.2.18]
C
C    LINDSAY GOODWIN 14/08/2017
C
      INTEGER Ngauleg
      DOUBLE PRECISION B,PI,C,K,MI,TI,XI,XPOS,DGDP,deltax,AMASSI,HIR,
     @HII,AMI,ANOMN,ELCH,BOLT,AMU,PERM,OMEGAPSQ
      REAL gaulegx(1:20),gaulegw(1:20)
      DATA ELCH,BOLT,AMU,PI,PERM/1.602E-19,1.381E-23,1.661E-27,
     @3.1415927,8.854E-12/
! DGDP = THE DERIVATIVE OF THE VELOCITY DISTRIBUTION AT A GIVEN LOCATION
! MI = ION MASS (kg)
! TI = ION TEMPERATURE (K)
! AMU = ONE ATOMIC MASS UNIT
      MI = AMASSI*AMU
  OMEGAPSQ = (4.*PI*ANOMN*ELCH**2)/MI
      B = SQRT(2.*BOLT*TI/MI)
! GAUSSIAN QUADRATURE WEIGHTS ARE FOUND
      Call gauleg(-6.00,6.00,gaulegx,gaulegw,20)
! HIR IS CALCULATED
      HIR = 0.
      DO 10 Ngauleg=1,20
! CHANGE IN VARIABLES FROM XI TO C
        C = DBLE(gaulegx(Ngauleg))
        XPOS = C + XI
        DGDP = (exp(-(XPOS+deltax)**2)
     >     - exp(-(XPOS-deltax)**2))/(2.*deltax)
        HIR= HIR-DBLE(gaulegw(Ngauleg))*DGDP/C
 10   CONTINUE
! DGDP AT A GIVEN XI IS FOUND FOR THE HII CALCULATION
      DGDP = (exp(-(XI+deltax)**2)
     >     - exp(-(XI-deltax)**2))/(2.*deltax)
! THE ION FUNCTIONS ARE FOUND/NORMALIZED
!      HIR = OMEGAPSQ*HIR/(B*K)**2
!      HII = OMEGAPSQ*DGDP*PI/(B*K)**2
      HIR = (2.*OMEGAPSQ/(4.*PI*PERM*(B*K)**2))*HIR/3.545
      HII = (2.*OMEGAPSQ/(4.*PI*PERM*(B*K)**2))*(PI*DGDP)/3.545
! A MAXWELLIAN VELOCITY DISTRIBUTION
```

```
AMI = EXP(-XI**2)/(B*SQRT(PI))
end
```

B.9 plgndr.FOR

```
C       THIS IS TAKEN STRAIGHT FROM THE FORTRAN 77 NUMERICAL RECIPES
C       [PRESS ET AL., 1992]
  FUNCTION plgndr(l,m,x)
  INTEGER l,m
  REAL plgndr,x
cComputes the associated Legendre polynomial P m l (x). Here m and l are
cintegers satisfying 0 = m = l, while x lies in the range -1 = x = 1.
  INTEGER i,ll
  REAL fact,pll,pmm,pmmp1,somx2
c   if(m.lt.0.or.m.gt.l.or.abs(x).gt.1.) write(15,*) 'bad'
  pmm=1.
cCompute P mm .
  if(m.gt.0) then
    somx2=sqrt((1.-x)*(1.+x))
    fact=1.
    do 11 i=1,m
      pmm=-pmm*fact*somx2
      fact=fact+2.
 11   CONTINUE
  endif
  if(l.eq.m) then
    plgndr=pmm
  else
    pmmp1=x*(2*m+1)*pmm
cCompute P m
c     m+1.
    if(l.eq.m+1) then
      plgndr=pmmp1
    else
cCompute P m
c     l , l>m + 1.
      do 12 ll=m+2,l
        pll=(x*(2*ll-1)*pmmp1-(ll+m-1)*pmm)/(ll-m)
        pmm=pmmp1
        pmmp1=pll
 12       CONTINUE
      plgndr=pll
    endif
  endif
  return
  END
```

B.10 SPECFNMAIN.FOR

```
C   SPECFNMAIN.FOR
C******************************************************************************C
C                             FINDING HII, HIR, HEI, HER, AND S                C
C******************************************************************************C
C THIS CODE FINDS:
C 1) ANALYTICAL CALCULATION OF THE ION FUNCTIONS AND SPECTRUM FOR A MAXWELLIAN
C    VELOCITY DISTRIBUTION AT XI [SHEFFIELD 1975, 6.3.8]
C 2) NUMERICAL CALCULATION OF THE ION FUNCTIONS AND SPECTRUM FOR A MAXWELLIAN
C    VELOCITY DISTRIBUTION AT XI (ONLY ION-NEUTRAL COLLISIONS ARE CONSIDERED)
C    [SHEFFIELD 1975, 6.2.18]
C 3) NUMERICAL CALCULATION OF THE ION FUNCTIONS AND SPECTRUM FOR A MAXWELLIAN
C    VELOCITY DISTRIBUTION AT XI WHEN ION-ION AND ION-ELECTRON COLLISIONS ARE
C    INCLUDED
C 4) NUMERICAL CALCULATION OF THE ION FUNCTIONS AND SPECTRUM FOR A DISTORTED
C    VELOCITY DISTRIBUTION AT XI (ONLY ION-NEUTRAL COLLISIONS ARE CONSIDERED)
C 5) NUMERICAL CALCULATION OF THE ION FUNCTIONS AND SPECTRUM  FOR A DISTORTED
C    VELOCITY DISTRIBUTION AT XI WHEN ION-ION AND ION-ELECTRON COLLISIONS ARE
C    INCLUDED
C
C THE ION FUNCTIONS INCLUDE:
C HIR - THE REAL COMPONENT OF THE ION FUNCTION
C HII - THE IMAGINARY COMPONENT OF THE ION FUNCTION
C AMI - THE VELOCITY DISTRIBUTION
C
C FOR OUR PURPOSES WE WILL BE ASSUMING A MAXWELLIAN ELECTRON VELOCITY
C DISTRIBUTION, WHICH HAS A DEFINED ANALYTICAL SOLUTION [SHEFFIELD 1975, 6.3.7]
C   LINDSAY GOODWIN     14/08/2017
C
      DOUBLE PRECISION TE,K,ALPHA,deltax,XI,EPSSQ,SA,SN,AMASSI,PHI,
     @HIRANA,HIIANA,AMIANA,HIRNUM,HIINUM,AMINUM,HERANA,HEIANA,AMEANA,
     @ELCH,VLGT,PERM,BOLT,ANOMN,MOMVAVE,MOMTEMP,NORMI,NORME,
     @FREQ,DELNEW1,DELNEW2,HIRRED1,HIRRED2,HIRRED,HIIRED,TPERP,SETM,
     @TPARA,HIRREDnew,HIRREDa,HIRREDb,AMIRED,NORM,B,NORMIN,NUII,SR,SRI,
     @NN,POWER,POWERI,HIRI1,HIRI2,HIRI,HIII,HIRINEW,HIRIA,HIRIB,AMII,
     @NUIE,NUIN,SETR,POWERM,MOMVAVEI,MOMTEMPI,NORMIE,HIRNUMi,
     @HIINUMI,AMINUMI,SNI,POWERMI,TR,PREVHIII,PREVHIIRED,OPERC,PI,
     @DBLH,NORMINNU,NORMINU,NORMENU,TN,TIN
      DOUBLE PRECISION COEFF(0:200),BARR(0:9),COEFFALL(0:200,0:9)
      INTEGER size,I,DEG,COLLISION,NUM,ELEN,J
      real LIM
      CHARACTER FILENAME*10,ELEC*3
      DATA ELCH,BOLT,PERM,PI,VLGT/1.602E-19,1.381E-23,8.854E-12,
     @3.1415927,2.998E8/
```

```
! ELCH = ELEMENTARY CHARGE (C)
! BOLT = BOLTZMANN CONSTANT (m2 kg s-2 K-1)
! PERM = PERMITTIVITY OF FREE SPACE (Fm1)
! PI = PI
! VLGT = SPEED OF LIGHT (m s-1)
!!!!!!!!!!!!!!!!!!!!!!!!!!!!!!!!!!!!!!!!!!!!
! USER DEFINED PARAMETERS ARE READ IN:
!!!!!!!!!!!!!!!!!!!!!!!!!!!!!!!!!!!!!!!!!!!!
! FILENAME = TAG ASSOCIATED WITH ALL THE OUTPUT FILES
! TE = ELECTRON TEMPERATURE (K)
! ANOMN = DESIRED PLASMA DENSITY (m-3)
! FREQ = RADAR FREQUENCY (Hz)
! NN = NEUTRAL DENSITY (m-3)
! ELEC = ELECTRIC FIELD
! PHI = ASPECT ANGLE
! COLLISION = DESIRED COLLISION TYPE (1=PESNELL O+O, 2=NO+ WITH O AND N2)
! OPERC = PERCENTAGE OF ATOMIC OXYGEN IN THE NEUTRAL POPULATION
! TPARA = TEMPERATURE PARALLEL TO THE MAGNETIC FIELD
! TPERP = TEMPERATURE PERPENDICULAR TO THE MAGNETIC FIELD
! AMASSI = ION MASS, AMU
! DEG = DEGREE OF ORTHOGONAL FIT TO THE DISTRIBUTION
! lim = NUMBER OF THERMAL SPEEDS BEING EXAMINED
! B = ION THERMAL SPEED
! COEFF = COEFFICIENTS DEVELOPED FROM CALCULATING AN ORTHOGONAL FIT TO THE
!     ONE-DIMENSION
! DISTRIBUTION
      OPEN(UNIT=15,FILE='input.dat',STATUS='OLD')
      READ(15,*) FILENAME
      READ(15,*) TE
      READ(15,*) ANOMN
      READ(15,*) FREQ
      READ(15,*) NN
      READ(15,*) ELEC
      READ(15,*) PHI
      READ(15,*) COLLISION
      CLOSE(15)
      ELEN = 0
      DO 11 I = 1, LEN(ELEC)
        IF ( ELEC(I:I) .NE. ' ' ) THEN
          ELEN = ELEN + 1
        END IF
 11   CONTINUE
      LIM = 4.00
! THIS READS IN THE CORRECT DATA FILE FOR A GIVEN ELECTRIC FIELD AND COLLISION TYPE
      IF (COLLISION.eq.1)
```

```
     >    OPEN(UNIT=15,FILE='1-E='//ELEC(1:ELEN)//'.DAT',STATUS='OLD')
      IF (COLLISION.eq.2)
     >    OPEN(UNIT=15,FILE='2-E='//ELEC(1:ELEN)//'.DAT',STATUS='OLD')
      IF (COLLISION.eq.3)
     >    OPEN(UNIT=15,FILE='3-E='//ELEC(1:ELEN)//'.DAT',STATUS='OLD')
! INFORMATION IS READ
      READ(15,*)
      READ(15,*) OPERC, TPARA,TPERP,AMASSI,DEG
      READ(15,*)
      READ(15,*) BARR(0),BARR(1),BARR(2),BARR(3),BARR(4),BARR(5),
     >     BARR(6),BARR(7),BARR(8),BARR(9)
      DO 12 I  = 0, DEG/2
        READ(15,*) COEFFALL(I,0),COEFFALL(I,1),COEFFALL(I,2),
     >     COEFFALL(I,3),COEFFALL(I,4),COEFFALL(I,5),COEFFALL(I,6),
     >     COEFFALL(I,7),COEFFALL(I,8),COEFFALL(I,9)
 12   CONTINUE
      CLOSE(15)
      B = BARR(INT(PHI)/10)
      DO 20 I  = 0, DEG/2
        J = I*2
        COEFF(J) = COEFFALL(I,INT(PHI)/10)
        COEFF(J+1) = 0.
 20   CONTINUE
!!!!!!!!!!!!!!!!!!!!!!!!!!!!!!!!!!!!!!!!!!!!
! DAT FILES ARE OPENED FOR OUTPUT
!!!!!!!!!!!!!!!!!!!!!!!!!!!!!!!!!!!!!!!!!!!!
! INPUT PARAMETERS OF INTEREST ARE WRITTEN TO FILENAME//'-INFO.DAT'
      OPEN (UNIT=20,FILE=FILENAME//'-INFO.DAT')
! ANALYTICAL SPECTRA CALCULATIONS OF THE MAXWELLIAN ELECTRON VELOCITY DISTRIBUTION
! ARE WRITTEN TO FILENAME//'MAXWELLIAN-ELECTRON.DAT'
!      OPEN (UNIT=40,FILE=FILENAME//'MAXWELLIAN-ELECTRON.DAT')
!      WRITE(40,*) 'XI       HERANA       HEIANA       AMEANA'
! ANALYTICAL SPECTRA CALCULATION OF THE MAXWELLIAN ION VELOCITY DISTRIBUTION
! ARE WRITTEN TO FILENAME//'MAXWELLIAN-ANALYTICAL.DAT'
!      OPEN (UNIT=55,FILE=FILENAME//'MAXWELLIAN-ANALYTICAL.DAT')
!      WRITE(55,*) 'XI       HIRANA       HIIANA       AMIANA       SA'
! NUMERICAL SPECTRA CALCULATIONS
      OPEN (UNIT=110,FILE=FILENAME//'-OUTPUT.DAT')
      OPEN (UNIT=112,FILE=FILENAME//'-COULOMB-OUTPUT.DAT')
      WRITE(110,*) 'XI, MAXWELLIAN AMI(N), MAXWELLIAN HIR(N),
     >     MAXWELLIAN HII(N), MAXWELLIAN SPECTRUM, TOROIDAL AMI,
     >     TOROIDAL HIR, TOROIDAL HII, TOROIDAL SPECTRUM'
      WRITE(112,*) 'XI, MAXWELLIAN AMI(N), MAXWELLIAN HIR(N),
     >     MAXWELLIAN HII(N), MAXWELLIAN SPECTRUM, TOROIDAL AMI,
     >     TOROIDAL HIR, TOROIDAL HII, TOROIDAL SPECTRUM'
```

```
!!!!!!!!!!!!!!!!!!!!!!!!!!!!!!!!!!!!!!!!!!!!
! VELOCITY DISTRIBUTION MOMENTS ARE CALCULATED
!!!!!!!!!!!!!!!!!!!!!!!!!!!!!!!!!!!!!!!!!!!!
! SETM = A PARAMETER USED TO CALCULATE MOMENTS (SETM = 0. IS FOR ION-NEUTRAL
!      COLLISIONS, SETM = -1. IS FOR ION-NEUTRAL, ION-ION, AND ION-ELECTRON
!      COLLISIONS)
! MOMVAVE = SECOND MOMENT, AVERAGE VELOCITY
! MOMTEMP = THIRD MOMENT, ION TEMPERATURE
! MOMVAVEI = SECOND MOMENT, AVERAGE VELOCITY WHEN ION-ION AND ION-ELECTRONS
!      ARE INCLUDED
! MOMTEMPI = THIRD MOMENT, ION TEMPERATURE WHEN ION-ION AND ION-ELECTRONS
!      ARE INCLUDED
! NORMIN = NORMALIZATION CONSTANT FOR THE ION-NEUTRAL COLLISION DISTRIBUTION
! NORMI = NORMALIZATION CONSTANT FOR THE ION-ION COLLISION DISTRIBUTION
! NORME = NORMALIZATION CONSTANT FOR THE ION-ELECTRON COLLISION DISTRIBUTION
! NORMINNU = NORMALIZATION CONSTANT FOR THE ION-NEUTRAL COLLISION DISTRIBUTION*NUIN
! NORMINU = NORMALIZATION CONSTANT FOR THE ION-ION COLLISION DISTRIBUTION*NUII
! NORMENU = NORMALIZATION CONSTANT FOR THE ION-ELECTRON COLLISION DISTRIBUTION*NUIE
! NUIN = ION-NEUTRAL COLLISION FREQUENCY (Hz)
! NUII = ION-ION COLLISION FREQUENCY (Hz)
! NUIE = ION-ELECTRON COLLISION FREQUENCY (Hz)
! NORM = NORMALIZATION CONSTANT FOR HIR, HII, AND AMI
! NORMIE = NORMALIZATION CONSTANT FOR HIR, HII, AND AMI WHEN ION-ION AND
!      ION-ELECTRON
! COLLISIONS ARE INCLUDED
! TN = NEUTRAL TEMPERATURE (K)
      SETM = 0.
! THE MOMENTS ARE CALCULATED AND WRITTEN TO AN OUTPUT FILE
      CALL MOMENTS(COEFF,MOMVAVE,MOMTEMP,AMASSI,norm,
     >     LIM,B,DEG,SETM,NORMIN,NORMI,NORME,TPERP,TPARA,TE)
      TN = 1000.
      TIN = (TN + ((TPARA+2.*TPERP)/3.))/2.
! THE COLLISION FREQUENCIES ARE CALCULATED BASED ON THE TYPE OF "COLLISION":
!    FOR PESNELL O+ O COLLISIONS...
      IF (COLLISION.EQ.1)THEN
        NUIN = (3.0e-11)*(NN/(100.)**3)*(TIN**0.5)*
     >     (1.-0.135*DLOG10(TIN/1000.))**2
        NUII = 0.22*(ANOMN/(100.)**3)/(((TPARA+2.*TPERP)/3.)**1.5)
      ENDIF
!    FOR NO+ WITH O AND N2...
      IF (COLLISION.EQ.2)THEN
        NUIN = (NN/(100.)**3)*
     >     (16.*OPERC*2.44e-10 + 14.*(1.-OPERC)*4.34e-10)/30.
        NUII = 0.16*(ANOMN/(100.)**3)/(((TPARA+2.*TPERP)/3.)**1.5)
      ENDIF
```

```
!    FOR KNOF O+ O COLLISIONS...
      IF (COLLISION.EQ.3)THEN
        NUIN = (3.69e-11)*(NN/(100.)**3)*(TIN**0.5)*
     >     (1.-0.065*DLOG10(TIN))**2
        NUII = 0.22*(ANOMN/(100.)**3)/(((TPARA+2.*TPERP)/3.)**1.5)
      ENDIF
      NUIE =(5.4858e-4/AMASSI)*54.5*(ANOMN/(100.)**3)/(1.41*TE**1.5)
      SETM = -1.
      NORMINNU = NORMIN*NUIN
      NORMINU = NORMI*NUII
      NORMENU = NORME*NUIE
      CALL MOMENTS(COEFF,MOMVAVEI,MOMTEMPI,AMASSI,NORMIE,LIM,B,
     >     DEG,SETM,NORMINNU,NORMINU,NORMENU,TPERP,TPARA,TE)
!!!!!!!!!!!!!!!!!!!!!!!!!!!!!!!!!!!!!!!!!!!!
! FURTHER CALCUATIONS ARE MADE, THEN ION FUNCTION AND SPECTRA VALUES ARE FOUND
! AS A FUNCTION OF XI VALUES
!!!!!!!!!!!!!!!!!!!!!!!!!!!!!!!!!!!!!!!!!!!!
! TR = TPARA*COS2(PHI)+TPERP*SIN2(PHI)
! K = WAVENUMBER (1/m)
! DBLH = DEBYE LENGTH (m)
! ALPHA = ALPHA (UNITLESS)
! POWER = AREA UNDER THE SPECTRUM RESULTING FROM THE DISTORTED VELOCITY
!     DISTRIBUTION
! POWERM = AREA UNDER THE SPECTRUM RESULTING FROM THE MAXWELLIAN VELOCITY
!     DISTRIBUTION
! POWERI = AREA UNDER THE SPECTRUM RESULTING FROM THE DISTORTED VELOCITY
!     DISTRIBUTION WHEN
! ION-ION AND ION-ELECTRON COLLISIONS ARE INCLUDED
! POWERMI = AREA UNDER THE SPECTRUM RESULTING FROM THE MAXWELLIAN VELOCITY
!     DISTRIBUTION
! WHEN ION-ION AND ION-ELECTRON COLLISIONS ARE INCLUDED
! DELTAX = A SMALL VALUE USED TO CALCULATE THE DERIVATIVE OF THE DISTRIBUTION
! SIZE = THE NUMBER OF POINTS CALCULATED FOR THE SPECTRA AND ION FUNCTIONS
! XI = OMEGA/(K*B), WHERE OMEGA IS THE ANGULAR FREQUENCY FOR IONS
! HIRANA/HIRNUM/HIRI1/HIRI2/HIRI/HIRInew/HIRIa/HIRIb/HIRNUMi/HIRRED1/HIRRED2/
! HIRRED/HIRREDnew/HIRREDa/HIRREDb = HIR, THE REAL COMPONENT OF THE ION
!     FUNCTION IN A VARIETY OF
! CASES AT A GIVEN XI
! HIIANA/HIINUM/HIIRED/HIII/HIINUMi/prevHIII/prevHIIRED = HII, THE IMAGINARY
!     COMPONENT OF THE
! ION FUNCTION IN A VARIETY OF CASES AT A GIVEN XI
! AMIANA/AMINUM/AMIRED/AMII/AMINUMi = AMI, THE ION VELOCITY DISTRIBUTION AT A
!      GIVEN XI
! HERANA = HER, THE REAL COMPONENT OF THE ELECTRON FUNCTION IN A VARIETY OF
!     CASES AT A GIVEN XI
```

```
! HEIANA = HEI, THE IMAGINARY COMPONENT OF THE ELECTRON FUNCTION IN A VARIETY OF
!     CASES AT A GIVEN XI
! AMEANA = AME, THE ELECTRON VELOCITY DISTRIBUTION AT A GIVEN XI
! SETR = A PARAMETER USED TO CALCULATE MOMENTS (SETR = 0. IS FOR ION-NEUTRAL
!     COLLISIONS,
! SETR = -1. IS FOR ION-NEUTRAL, ION-ION, AND ION-ELECTRON COLLISIONS)
! NUM = NUMBER OF GAUSSIAN QUADRATURE POINTS
! DELNEW1/DELNEW2 = PARAMETERS USED TO FILTER THE REAL COMPONENT OF THE ION FUNCTION
! EPSSQ = SQUARE OF THE LATITUDINAL DIELECTRIC FUNCTION
! SA = ANALYTICAL SPECTRUM CALCULATION FOR A MAXWELLIAN VELOCITY DISTRIBUTION AT XI
! SN = NUMERICAL SPECTRUM CALCULATION FOR A MAXWELLIAN VELOCITY DISTRIBUTION AT XI
! SNI = NUMERICAL SPECTRUM CALCULATION FOR A MAXWELLIAN VELOCITY DISTRIBUTION AT XI
! WHEN ION-ION AND ION-ELECTRON COLLISIONS ARE INCLUDED
! SR = NUMERICAL SPECTRUM CALCULATION FOR A DISTORTED VELOCITY DISTRIBUTION AT XI
! SRI = NUMERICAL SPECTRUM CALCULATION FOR A DISTORTED VELOCITY DISTRIBUTION AT XI
! WHEN ION-ION AND ION-ELECTRON COLLISIONS ARE INCLUDED
      TR = (TPARA*DCOS(PHI*PI/180.)**2)+(TPERP*DSIN(PHI*PI/180.)**2)
      DBLH=SQRT(PERM*BOLT*TE/(ANOMN*ELCH**2))
      K=4.*PI*FREQ/VLGT
      ALPHA=1./(K*DBLH)
      POWER=0.
      POWERM=0.
      POWERI=0.
      POWERMI=0.
      DELTAX = 0.0001
      SIZE = 100*6
! A VARIETY OF XI VALUES ARE EXAMINED....
      DO 40 I  = -SIZE, SIZE
        XI = I/100.
! THE ANALYTICALLY CALCULATED ELECTRON FUNCTIONS FOR A MAXWELLIAN ELECTRON
! VELOCITY DISTRIBUTION ARE FOUND
        CALL ANAELECT(XI,MOMTEMP,TE,ALPHA,K,AMASSI,HERANA,HEIANA,AMEANA)
! THE ANALYTICALLY CALCULATED ION FUNCTIONS FOR A MAXWELLIAN ION VELOCITY
! DISTRIBUTION ARE FOUND
        CALL ANAION(XI,MOMTEMP,TE,ALPHA,K,AMASSI,HIRANA,HIIANA,AMIANA)
        EPSSQ = (1.+HERANA+HIRANA)**2+(HEIANA+HIIANA)**2
        SA = (2.*PI/K)*((((HERANA**2+HEIANA**2)/EPSSQ)*AMIANA) +
     >    ((((1.+HIRANA)**2+HIIANA**2)/EPSSQ)*AMEANA))
! THE NUMERICALLY CALCULATED ION FUNCTIONS FOR A MAXWELLIAN ION VELOCITY
! DISTRIBUTION ARE FOUND
        CALL NUMMAXWELL(XI,MOMTEMP,K,DELTAX,AMASSI,HIRNUM,HIINUM,AMINUM,
     >    ANOMN)
        EPSSQ = (1.+HERANA+HIRNUM)**2+(HEIANA+HIINUM)**2
        SN = (2.*PI/K)*((((HERANA**2+HEIANA**2)/EPSSQ)*AMINUM)+
     >    ((((1.+HIRNUM)**2+HIINUM**2)/EPSSQ)*AMEANA))
```

```
! THE NUMERICALLY CALCULATED ION FUNCTIONS FOR A MAXWELLIAN ION VELOCITY
! DISTRIBUTION ARE FOUND WHEN ION-ION AND ION-ELECTRON COLLISIONS ARE INCLUDED
        CALL NUMMAXWELL(XI,MOMTEMPI,K,DELTAX,AMASSI,HIRNUMi,HIINUMi,
     >    AMINUMi,ANOMN)
        EPSSQ = (1.+HERANA+HIRNUMi)**2+(HEIANA+HIINUMi)**2
        SNi = (2.*PI/K)*((((HERANA**2+HEIANA**2)/EPSSQ)*AMINUMi)+
     >    ((((1.+HIRNUMi)**2+HIINUMi**2)/EPSSQ)*AMEANA))
! THE NUMERICALLY CALCULATED ION FUNCTIONS FOR A DISTORTED ION VELOCITY
! DISTRIBUTION ARE FOUND
        if (I.gt.-SIZE+1) HIRREDa = HIRREDb
        if (I.gt.-SIZE) HIRREDb = HIRREDnew
        SETR = 0.
! HIR IS CALCULATED FOR A 50 POINT GAUSSIAN QUADRATURE
        NUM = 50
        CALL DISTORTED(XI,K,DELTAX,AMASSI,HIRRED1,HIIRED,AMIRED,ANOMN,
     >    COEFF,LIM,DEG,SETR,NORMIN,NORMI,NORME,B,TPERP,TPARA,TE,NUM)
        HIRREDnew=HIRRED1
! HIR IS CALCULATED FOR A 52 POINT GAUSSIAN QUADRATURE
        NUM = 52
        CALL DISTORTED(XI,K,DELTAX,AMASSI,HIRRED2,HIIRED,AMIRED,ANOMN,
     >    COEFF,LIM,DEG,SETR,NORMIN,NORMI,NORME,B,TPERP,TPARA,TE,NUM)
! THE HIR VALUES FROM THE 50 POINT AND 52 POINT GAUSSIAN QUADRATURES ARE COMPARED,
! AND THE POINT MOST CONSISTANT WITH THE PREVIOUS HIR CALCULATION IS USED AS HIR
! (THIS PROCESS REMOVES MOST SUDDEN HIR "SPIKES")
        if (I.gt.-SIZE+1) then
          DELNEW1 = (HIRREDb-HIRREDa)-(HIRRED1-HIRREDb)
          DELNEW2 = (HIRREDb-HIRREDa)-(HIRRED2-HIRREDb)
          if (abs(DELNEW1).lt.abs(DELNEW2)) HIRREDnew=HIRRED1
          if (abs(DELNEW2).lt.abs(DELNEW1)) HIRREDnew=HIRRED2
        endif
! THE ION FUNCTIONS ARE NORMALIZED
        HIRRED = HIRREDnew*norm
        HIIRED = HIIRED*norm
        AMIRED = AMIRED*norm
        if (abs(XI).eq.nint(LIM*100.)/100.) HIIRED = prevHIIRED
        EPSSQ = (1.+HERANA+HIRRED)**2+(HEIANA+HIIRED)**2
! THE SPECTRUM AT XI IS CALCULATED
        SR = (2.*PI/K)*((((HERANA**2+HEIANA**2)/EPSSQ)*AMIRED) +
     >    ((((1.+HIRRED)**2+HIIRED**2)/EPSSQ)*AMEANA))
        PREVHIIRED = HIIRED
! THE NUMERICALLY CALCULATED ION FUNCTIONS FOR A DISTORTED ION VELOCITY
! DISTRIBUTION ARE FOUND WHEN ION-ION AND ION-ELECTRON COLLISIONS ARE INCLUDED
        if (I.gt.-SIZE+1) HIRIA = HIRIB
        if (I.gt.-SIZE) HIRIB = HIRINEW
        SETR = -1.
```

```
! HIR IS CALCULATED FOR A 50 POINT GAUSSIAN QUADRATURE
        NUM = 50
        CALL DISTORTED(XI,K,DELTAX,AMASSI,HIRI1,HIII,AMII,ANOMN,COEFF,
     >    LIM,DEG,SETR,NORMINNU,NORMINU,NORMENU,B,TPERP,TPARA,TE,NUM)
        HIRInew=HIRI1
! HIR IS CALCULATED FOR A 52 POINT GAUSSIAN QUADRATURE
        NUM = 52
        CALL DISTORTED(XI,K,DELTAX,AMASSI,HIRI2,HIII,AMII,ANOMN,COEFF,
     >    LIM,DEG,SETR,NORMINNU,NORMINU,NORMENU,B,TPERP,TPARA,TE,NUM)
! THE HIR VALUES FROM THE 50 POINT AND 52 POINT GAUSSIAN QUADRATURES ARE COMPARED,
! AND THE POINT MOST CONSISTANT WITH THE PREVIOUS HIR CALCULATION IS USED AS HIR
! (THIS PROCESS REMOVES MOST SUDDEN HIR "SPIKES")
        if (i.gt.-SIZE+1) then
          DELNEW1 = (HIRIb-HIRIa)-(HIRI1-HIRIb)
          DELNEW2 = (HIRIb-HIRIa)-(HIRI2-HIRIb)
          if (abs(DELNEW1).lt.abs(DELNEW2)) HIRInew=HIRI1
          if (abs(DELNEW2).lt.abs(DELNEW1)) HIRInew=HIRI2
        endif
! THE ION FUNCTIONS ARE NORMALIZED
        HIRI = HIRInew*NORMIE
        HIII = HIII*NORMIE
        AMII = AMII*NORMIE
        if (abs(XI).eq.nint(LIM*100.)/100.) HIII = prevHIII
        EPSSQ = (1.+HERANA+HIRI)**2+(HEIANA+HIII)**2
! THE SPECTRUM AT XI IS CALCULATED WHEN ION-ION AND ION-ELECTRON COLLISIONS ARE
! INCLUDED
        SRI = (2.*PI/K)*((((HERANA**2+HEIANA**2)/EPSSQ)*AMII) +
     >    ((((1.+HIRI)**2+HIII**2)/EPSSQ)*AMEANA))
! THE ANALYTICALLY CALCULATED ELECTRON FUNCTIONS FOR A MAXWELLIAN ELECTRON VELOCITY
! DISTRIBUTION ARE WRITTEN TO FILENAME//'MAXWELLIAN-ELECTRON.DAT'
!        WRITE(40,*) XI,HERANA,HEIANA,AMEANA
! THE ANALYTICALLY CALCULATED ION FUNCTIONS FOR A MAXWELLIAN ION VELOCITY
! DISTRIBUTION ARE WRITTEN TO FILENAME//'MAXWELLIAN-ANALYTICAL.DAT'
!        WRITE(55,*) XI,HIRANA,HIIANA,AMIANA,SA
! THE ION FUNCTIONS AND SPECTRA VALUES ARE WRITTEN TO FILENAME//'-OUTPUT.DAT'
        WRITE(110,*) XI,AMINUM,HIRNUM,HIINUM,SN,AMIRED,HIRRED,HIIRED,
     >    SR
        WRITE(112,*) XI,AMINUMi,HIRNUMi,HIINUMi,SNi,AMII,HIRI,HIII,SRI
        prevHIII = HIII
! POWER IS CALCULATED FROM THE FOUR SPECTRA
        POWER=POWER+SR*1.e-2
        POWERM=POWERM+SN*1.e-2
        POWERI=POWERI+SRI*1.e-2
        POWERMI=POWERMI+SNI*1.e-2
 40   CONTINUE
```

```
! ADDITIONAL INFORMATION IS WRITTEN TO FILENAME//'-INFO.DAT'
      WRITE(20,*)'INPUT PARAMETERS:'
      WRITE(20,*)'COLLISION (1=PESNELL O+O, 2=NO+, O, N2) = '
     >, COLLISION
      WRITE(20,*)'ELECTRIC FIELD (mV/m) = ', ELEC
      WRITE(20,120)'ASPECT ANGLE (DEG) = ', PHI
 120  format (A,F15.0)
      WRITE(20,120)'ION MASS (AMU) = ', AMASSI
      WRITE(20,125)'DESIRED PLASMA DENSITY (m-3) = ', ANOMN
 125  format (A,E10.3E2)
      WRITE(20,125)'RADAR FREQUENCY (Hz) = ', FREQ
      WRITE(20,130)'ELECTRON TEMPERATURE (K) = ',TE
 130  format (A,F6.0)
      WRITE(20,125)'NEUTRAL DENSITY (m^-3) = ',NN
      WRITE(20,130)'PERPENDICULAR ION TEMPERATURE (K) = ',TPERP
      WRITE(20,130)'PARALLEL ION TEMPERATURE (K) = ',TPARA
      WRITE(20,130)'THERMAL SPEED (M/S) = ', B
      WRITE(20,*)
      WRITE(20,*)'CALCULATED MOMENTS:'
      WRITE(20,130) 'ION TEMPERATURE = ', MOMTEMP
      WRITE(20,130) 'ION TEMPERATURE WITH COULOMB COLLISIONS = '
     >, MOMTEMPI
      WRITE(20,*)
      WRITE(20,*)'OTHER CALCULATED VALUES:'
      WRITE(20,125) 'ALPHA = ', ALPHA
      WRITE(20,130) 'TPERP*SIN**2(PHI)+TPARA*COS**2(PHI) = ', TR
      WRITE(20,125) 'ION-NEUTRAL COLLISION FREQUENCY (Hz) = ',NUIN
      WRITE(20,125) 'ION-ION COLLISION FREQUENCY (Hz) = ',NUII
      WRITE(20,125) 'ION-ELECTRON COLLISION FREQUENCY (Hz) = ',NUIE
      WRITE(20,125) 'POWER OF TOROIDAL DISTRIBUTION = ', POWER
      WRITE(20,125) 'POWER OF EQUIVALANT MAXWELLIAN DISTRIB. = ', POWERM
      WRITE(20,125)
     >'POWER OF TOROIDAL DISTRIBUTION WITH COULOMB COLLISIONS = '
     >, POWERI
      WRITE(20,125)
     >'POWER OF EQUIVALANT MAXWELLIAN WITH COULOMB COLLISIONS = '
     >, POWERMI
      CLOSE(20)
!      CLOSE(40)
!      CLOSE(55)
      CLOSE(110)
      END
!!!!!!!!!!!!!!!!!!!!!!!!!!!!!!!!!!!!!!!!!!!!
! ORTHOGONAL POLYNOMIALS ARE USED TO RECONSTRUCT THE ION VELOCITY
! DISTRIBUTION FOR A GIVEN ASPECT ANGLE AND ELECTRIC FIELD
```

```
!!!!!!!!!!!!!!!!!!!!!!!!!!!!!!!!!!!!!!!!!!!!
      DOUBLE PRECISION FUNCTION fit(X,coeff,lim,DEG,SETI,SETE,
     >      NORMIN,NORMI,norme,B,TPERP,TPARA,TE,AMASSI)
      REAL lim
      INTEGER J,DEG
      DOUBLE PRECISION X,coeff(0:DEG),SETI,NORMIN,XP,VT,B,NORMI,
     >      SETE,TPERP,TPARA,norme,TE,A,AMASSI,BOLT,ME
      DATA BOLT,ME/1.380E-23,9.109E-31/
! XP = XI FOR THE AVERAGE ION TEMPERATURE, (TPARA+2.*TPERP)/3.
! VT = THERMAL SPEED FOR THE AVERAGE ION TEMPERATURE, (TPARA+2.*TPERP)/3.
! A = ELECTRON THERMAL SPEED
! ME = ELECTRON MASS (kg)
! BOLT = BOLTZMANN CONSTANT (m2 kg s-2 K-1)
! THE VELOCITY DISTRIBUTION AT A GIVEN X IS FOUND
      fit = 0.
      if (abs(X).lt.lim) then
        DO 10 J  = 0, DEG
! ONLY THE EVEN NUMBERED COEFFICIENTS ARE NEEDED BECAUSE THE VELOCITY
! DISTRIBUTION IS ALWAYS SYMMETRIC
          if (mod(j,2).eq.0) then
            fit=coeff(J)*DBLE(plgndr(J,0,real(X)/lim))+fit
          endif
 10     continue
      endif
  VT=SQRT(2.*1.381E-23*((TPARA+2.*TPERP)/3.)/(AMASSI*1.661E-27))
  XP=X*B/VT
      A = SQRT(2.*BOLT*TE/ME)
  Xe=X*B/A
! IF ION-ION AND ION-ELECTRON COLLISIONS ARE BEING INCLUDED...
  if (SETI.eq.(-1.).and.SETE.eq.(-1.)) then
        fit=(fit*normin+normi*exp(-XP**2)+norme*exp(-Xe**2))/
     >      (normin+normi+norme)
      else
! IF ONLY ONE TERM IS BEING CONSIDERED...
        fit=(1.-SETI-SETE)*fit*normin+SETI*normi*exp(-XP**2)+
     >      SETE*norme*exp(-Xe**2)
      endif
      END
```

B.11 Data Files for Calculating Spectra

Each data file contains high-quality Legendre polynomial fits to the one-dimensional velocity distributions that have been acquired through the formula:

$$g_{0i}(y) = \sum_{j=0}^{D} n_j P_j^0, \tag{B.1}$$

where D is the desired degree chosen to perform the fit around its drift point and P_j are the Legendre polynomials. This work uses $D = 50$; however, it should be noted that only even-numbered polynomials contributions need to be considered because of the symmetry of the velocity distributions about their drift point. Therefore these files list 26 values for n_j associated with the Legendre polynomials of degree 0, 2, 4, etc., all the way to degree 50. From these values, the ion velocity distribution is found at a specific y value (recall that y is v_x/b, where v_x is the line-of-sight speed and b is the ion thermal speed).

Each ASCII .DAT file is for a different electric field and collision type. Note that although there are ASCII .DAT files to produce NO^+ spectra, the NO^+ with a background of 50% O and 50% N_2 spectra can also be reproduced using Maxwellian ion velocity distributions and the temperatures provided in Table A.1 (see Appendix A for more details).

Each ASCII .DAT file contains 30 rows:

- Row 1: Collisions type (this is 1 for O^+-O and 2 for NO^+ with a background of 50% O and 50% N_2).
- Row 2: a) Abundance of background atomic oxygen, b) parallel ion temperature in Kelvin using the Monte-Carlo simulation output (purely ion-neutral collisions), c) the perpendicular ion temperature in Kelvin using the Monte-Carlo simulation output (purely ion-neutral collisions), d) ion mass in atomic mass units, and e) desired degree orthogonal fit.
- Row 3: Aspect angle.
- Row 4: Ion thermal speed in m/s, based on the line-of-sight ion temperature given by the Monte-Carlo simulation. This value is used to find ω from x_i and/or v_x from y.
- Row 5 - 30: The even numbered polynomial coefficients from 0 to 50 (i.e. coefficient 0, coefficient 2, coefficient 4, coefficient 6,..., coefficient 48, coefficient 50). These polynomial coefficients describe the ion velocity distribution from -4 thermal speeds to 4 thermal speeds.

Note that each column in row 3 and onward is for a different aspect angle in steps of 10° aspect angles from 0° to 90°.

Only one file is given here."1-E=100.DAT", which contains the POH O^+-O collision information for an electric field of 100 mV/m. This file is listed below, and other files are available upon request:

```
1
1.00   2140.96 5297.04 16.00 50
0.00    10.00    20.00    30.00    40.00    50.00    60.00    70.00    80.00    90.00
1491.6600342    1532.5    1642.2900391    1779.1300049    1909.5799561    2036.0600586    2164.5100098    2263.0800781    2325.1298828    2346.3000488
1.5768479E-7    1.5358133E-7    1.4315698E-7    1.1979354E-7    1.2352662E-7      1.1371084E-7    1.0696319E-7      1.0217780E-7    9.9577179E-8      9.8833638E-8
-3.5721484E-7    -3.4777770E-7    -3.2431913E-7    -2.7139345E-7    -2.7978587E-7      -2.5757151E-7    -2.4233697E-7      -2.3154324E-7    -2.2560012E-7      -2.2373156E-7
3.8539716E-7    3.7408341E-7    3.4727890E-7    2.8971877E-7    2.9735048E-7      2.7338535E-7    2.5694987E-7      2.4547251E-7    2.3889945E-7      2.3647762E-7
-3.3159543E-7    -3.1842936E-7    -2.8841737E-7    -2.3701106E-7    -2.3791264E-7      -2.1702627E-7    -2.0241845E-7      -1.9280468E-7    -1.8683447E-7      -1.8438570E-7
2.4800124E-7    2.3196084E-7    1.9478178E-7    1.5245966E-7    1.4039905E-7      1.2387541E-7    1.1148257E-7      1.0437721E-7    9.9419431E-8      9.7551258E-8
-1.6972680E-7    -1.5077111E-7    -1.0432186E-7    -7.0091396E-8    -4.1441620E-8      -2.8495737E-8    -1.7390681E-8      -1.2012949E-8    -8.0370466E-9      -7.1011996E-9
1.1085072E-7    9.0582141E-8    3.7696882E-8    1.0317140E-8    -3.3749306E-8      -4.4008928E-8    -5.4374400E-8      -5.9173807E-8    -6.2195980E-8      -6.2360407E-8
-7.1069415E-8    -5.1874625E-8    1.0896831E-9    2.1897556E-8    7.5587302E-8      8.3026208E-8    9.1942283E-8      9.6654269E-8    9.8574240E-8      9.8524559E-8
4.4933113E-8    2.8820198E-8    -1.7837257E-8    -3.2162514E-8    -8.7360320E-8      -9.1032121E-8    -9.6927707E-8      -1.0101631E-7    -1.0167292E-7      -1.0193691E-7
-2.7428054E-8    -1.5430706E-8    2.1089630E-8    2.9809197E-8    7.8946094E-8      7.8057788E-8    7.9626950E-8      8.1976680E-8    8.1457898E-8      8.2146258E-8
1.5495848E-8    7.6725204E-9    -1.7999241E-8    -2.2893714E-8    -6.0948466E-8      -5.5622607E-8    -5.2765262E-8      -5.2553847E-8    -5.1256915E-8      -5.2023577E-8
-7.5341697E-9    -3.2274585E-9    1.3079578E-8    1.6231422E-8    4.1334971E-8      3.2670552E-8    2.6668564E-8      2.4034430E-8    2.2473742E-8      2.2812998E-8
2.5785940E-9    7.3608242E-10    -8.5526093E-9    -1.1651595E-8    -2.4566464E-8      -1.4164812E-8    -7.1336319E-9      -3.2180567E-9    -1.7510829E-9      -1.3709932E-9
1.6784397E-10    6.3923389E-10    5.1587596E-9    9.1523384E-9    1.2197384E-8      1.6440410E-9    -4.3172221E-9      -7.9300237E-9    -9.2151993E-9      -1.0239598E-8
-1.4532744E-9    -1.3363560E-9    -2.8844835E-9    -8.0078753E-9    -3.9610120E-9      5.4286922E-9    8.9291428E-9      1.0985440E-8    1.2146430E-8      1.3521475E-8
1.9144746E-9    1.4931893E-9    1.4514004E-9    7.4587119E-9    -1.2040388E-9      -8.4101899E-9    -9.0613756E-9      -9.1623944E-9    -1.0180956E-8      -1.1679142E-8
-1.9844484E-9    -1.1587585E-9    -5.8066452E-10    -6.9941013E-9    4.3864481E-9      8.6993044E-9    7.0053541E-9      5.6388911E-9    6.3086203E-9      7.9512974E-9
1.8667954E-9    5.0870175E-10    8.4191695E-11    6.3748260E-9    -6.2780350E-9      -7.4239708E-9    -4.4166728E-9      -2.5573976E-9    -2.5862554E-9      -4.5858877E-9
-1.6051847E-9    1.2117650E-10    1.4939112E-10    -5.5407821E-9    7.1182931E-9      5.4059379E-9    2.2111186E-9      7.6873446E-10    1.5278202E-11      2.5458828E-9
1.2076889E-9    -4.1560591E-10    -2.0325881E-10    4.5140078E-9    -6.9287238E-9      -3.2243297E-9    -7.1552109E-10      -1.2773019E-10    1.2169680E-9      -1.7559368E-9
-7.4120238E-10    3.0110342E-10    1.5920285E-10    -3.3491692E-9    5.8193166E-9      1.2806751E-9    -1.0264552E-10      3.8199346E-11    -1.3958088E-9      1.6102415E-9
3.3436778E-10    9.9002967E-12    -9.2322948E-11    2.1344813E-9    -4.1403103E-9      1.6915343E-10    4.2895307E-10      4.4617966E-11    9.8216768E-10      -1.4704671E-9
-1.0009481E-10    -2.0812689E-10    4.8587905E-11    -1.0030137E-9    2.3864863E-9      -1.0083873E-9    -4.6505017E-10      -3.3794451E-10    -4.0622994E-10      9.8066877E-10
5.2960018E-11    1.4428420E-10    -3.4332297E-11    1.1207001E-10    -9.6632002E-10      1.2607646E-9    3.6602521E-10      7.2892586E-10    -4.7373640E-11      -1.4834535E-10
-1.0151419E-10    7.1298960E-11    3.1074098E-11    4.2035536E-10    3.7323474E-11      -1.0738248E-9    -2.3071867E-10      -9.5928709E-10    2.6935484E-10      -7.6312012E-10
1.2551402E-10    -2.0477531E-10    -2.0736211E-11    -5.7992133E-10    4.7083915E-10      6.6958439E-10    1.1345819E-10      8.5149421E-10    -2.8851374E-10      1.4276693E-9
```